DISSERTATION

INSIGHTS INTO EXTREME SHORT-TERM PRECIPITATION ASSOCIATED WITH SUPERCELLS AND MESOVORTICES

Submitted by

Erik R. Nielsen

Department of Atmospheric Science

In partial fulfillment of the requirements

For the Degree of Doctor of Philosophy

Colorado State University

Fort Collins, Colorado

Spring 2019

Doctoral Committee:

Advisor: Russ S. Schumacher

Susan C. van den Heever
Michael M. Bell
Jeffrey D. Niemann

ABSTRACT

INSIGHTS INTO EXTREME SHORT-TERM PRECIPITATION ASSOCIATED WITH SUPERCELLS AND MESOVORTICES

Overall, this manuscript aims to holistically evaluate the relationship between rotation and extreme precipitation processes, since radar and rain-gauge observations in several flash flooding events have suggested that the heaviest short-term rainfall accumulations were associated with supercells or mesovortices embedded within larger convective systems.

A specific subclass of these events, when tornadoes and flash floods are both concurrent and collocated (referred to here at TORFF events), present a unique set of concerns, since the recommended life-saving actions for each threat are contradictory. Given this, Chapter 2 aims to evaluate the climatological and meteorological characteristics associated with TORFF events over the United States. Two separate datasets, one based on overlapping tornado and flash flood warnings and the other based on observations, were used to arrive at estimations of the instances when a TORFF event was deemed imminent and verified to have occurred, respectively. These datasets, combined with field project data, were then used to discern the geographical and meteorological characteristics of recent TORFF events. The results show that TORFF scenarios commonly occur, are not easily distinguishable from tornadic events that fail to produce collocated flash flooding, and present difficult challenges both from the perspective of forecasting and public communication.

The research in Chapter 3 strives to identify the influence that rotation has on the storm-scale processes associated with heavy precipitation. Five total idealized simulations of a TORFF event, where the magnitude of the 0–1 km shear was varied, were performed to test the sensitivity of precipitation processes to rotation. In the simulations with greater environmental low-level shear and associated rotation, more precipitation fell, both in a point maximum and area-averaged sense. Intense, rotationally induced low-level vertical accelerations associated with the dynamic nonlinear perturbation vertical pressure gradient force were found to enhance the low-to-mid level updraft strength, total vertical mass flux, and allowed access to otherwise inhibited sources of moisture and CAPE in the higher shear simulations. The dynamical accelerations, which increased with the intensity of the low-level

shear, dominated over buoyant accelerations in the low levels and were responsible for inducing more intense, low-level updrafts that were sustained despite a stable boundary layer.

Chapter 4 aims to explore how often extreme short-term rain rates in the United States are associated with storm-scale or mesoscale vortices, since significant low-level rotation does not always yield a tornado (i.e., not all extreme rainfall events are TORFFs). Five years of METAR observations and three years of Stage-IV analyses were obtained and filtered for hourly accumulations over 75 and 100 mm, respectively. Local dual-pol radar data was then obtained for the remaining events for the hour leading up to the METAR observation. Nearly 50% of the cases were associated with low-level rotation in high-precipitation supercells and/or mesoscale vortices embedded in more organized storm modes. These results support recent modeling results, presented in Chapter 3, suggesting that rotationally induced dynamic vertical pressure accelerations are important to the precipitation formation mechanisms that lead to extreme short-term rainfall rates.

The upper Texas Coast, in and around the Houston, TX area, has experienced many intense TORFF events over the recent years. The research in Chapter 5 focuses on examining the horizontally heterogeneous environmental characteristics associated with one of those events, the Tax Day flood of 2016, which was identified as a “verified” TORFF event in Chapter 2. Radar and local mesonet rain gauge observations were used to examine the storm scale characteristics to identify the locations and structures of extreme rain rate producing cells. To supplement the observational based analysis above, a WRF-ARW simulation of the Tax Day flood in 2016, based upon a real-time forecast from the HRRR, was examined. Convective cells that produced the most intense short-term (i.e., sub-hourly to hourly) accumulations within the MCS were examined for the influence of any attendant rotation on both the dynamics and microphysics of the precipitation processes. Results show that the most intense rainfall accumulations, as in the observations analysis, are associated with rotating convective elements, and the results of this chapter confirm that the processes described in Chapter 3 apply outside of the idealized framework.

ACKNOWLEDGMENTS

This research was supported by National Science Foundation Grant AGS-1359727; NOAA grants NA15OAR4590233, NA16OAR4590215, and NA18OAR4590308; and a National Science Foundation Graduate Research Fellowship Grant DGE-1321845, Amendment 3.

High-performance computing resources from Cheyenne (doi:10.5065/D6RX99HX) and Yellowstone (ark:/85065/d7wd3xhc) were provided by the National Center for Atmospheric Research's (NCAR) Computational and Information Systems Laboratory, which is sponsored by the National Science Foundation. METAR data was provided by the Iowa Environmental Mesonet. The RAP analysis was provided by the National Oceanic and Atmospheric Administration's National Centers for Environmental Prediction, and Stage-IV analyses were provided by NCAR. Observational sounding data was provided by the University of Wyoming Department of Atmospheric Science. Flood damage estimates and reported fatalities for the extreme precipitation events examined were provided by the Storm Events Database of the National Centers for Environmental Information (NCEI).

I would like to express my thanks to the members of my Ph.D. committee, Dr. Sue van den Heever, Dr. Jorge Ramirez, Dr. Michael Bell, and Dr. Jeffrey D. Niemann, for their review of this work and many helpful suggestions through the research process. Thank you for sticking with me through this long process.

I would like to especially thank my advisor Dr. Russ Schumacher for his support in this research, as well as his unwavering willingness to help with many conceptual and technical challenges that have occurred along the way. This 6 year (actually it is closer to 8 or 9 year) journey could not have been possible or anywhere near as enjoyable without your guidance. I appreciate the willingness to answer and discuss my sometimes dull-witted questions and inquiries. You have fostered an environment where scientific inquiry is welcome and encouraged, even if the project was not initially planned. It has been a pleasure working with you!

Thanks to the members, both past and present, of the Schumacher research group – Dr. Greg Herman, Dr. Stacey Hitchcock, Dr. Robert Tournay, Dr. John Peters, Vanessa Vincente, Matt Palaus, Nathan Kelly, Sam Childs, Eric James, Faith Groff, Liu Zhang, and Peter Goble – for valuable discussion, motivation, and technical assistance throughout this research. We have spent some long nights researching and launching balloons in the middle of nowhere together. I would like to especially thank Greg and

Stacey. Without their constant encouragement in both life and research, I would not be where I am now. I would also like to thank the fellow students who started this journey with me 6 years ago – Peter Marinescu, Marie McGraw, Alex Naegele, Jack Kodros, Andy Manaster, Caitlin Fine, Stephanie Pilkington, Aryeh Drager, and Brian Crow – for dependable distractions and a being a great social support system.

I also would like to profusely thank my family and friends for their constant encouragement and willingness to listen and deal with the various aspects of graduate school life. I would not have survived this journey without y'all. I love y'all. Further, I would like to express thanks to past research advisors, including Jamie R. Rhome and Dr. Don Conlee, for helping shape my thought process and research acumen. Finally, I would like to thank Timothy Theodore Duncan, Gregory Popovich, Emanuel Ginobili, Anthony Boudain, The Redass Gents, A-Vac, and J. J. Jr. for providing continued distraction, improved mental health, and many stories.

DEDICATION

"It's very important for us to see that science is done by people, not just brains but whole human beings, and sometimes at great cost." –Alan Alda

TABLE OF CONTENTS

LIST OF TABLES

LIST OF FIGURES

CHAPTER 1

INTRODUCTION[1]

Losses due to weather-related hazards have continually increased within the United States despite mitigation and advances in predictive science and technology (e.g., Changnon et al. 2000; Bouwer 2011). Among the various atmospheric hazards that can lead to loss of life and property, tornadoes and flash floods are two of the most impactful (e.g., NOAA 2011). Tornadoes occur approximately 1000 times per year in the U.S., with almost 20,000 direct fatalities reported between 1880-2005 (Ashley 2007). Though the population-normalized yearly fatality rate associated with tornadoes has been steadily decreasing during the 20th century (e.g., Brooks and Doswell 2002), it is possible that continued urbanization could lead to more catastrophic events in the future (e.g., Wurman et al. 2007). Flooding is responsible for almost 100 fatalities per year with the flash flooding archetype being the most deadly and, unlike tornado related deaths, did not see any appreciable decrease in fatality rate from 1959 to 2005 (Ashley and Ashley 2008).

Given the considerable threat tornadoes and flash floods pose individually, any simultaneous occurrence of these hazards in the same location is particularly dangerous (Rogash and Smith 2000; Rogash and Racy 2002). In the case of multi-threat scenarios, effective communication of the most pertinent threat to those in harm's way can be muddled due to differing instructions associated with each hazard. This is of particular concern for tornadoes and flash floods since the life-saving actions for each hazard are contradictory; tornado safety protocol recommends taking shelter in a low-lying interior room, whereas flood safety protocol recommends retreating to high ground. Throughout this maunscript concurrent, collocated flash flood and tornado events will be referred to as TORFF(s), short for **TOR**nado and **F**lash **F**lood, for the sake of simplicity. "Concurrent" in this study will refer to events where the period of each individual threat overlaps, and not necessarily to events that occurred at the exact same time. Furthermore, "collocated" will refer to a particular location experiencing both threats. A visual representation of a recent multi-threat tornado and flash flood scenario is presented in Fig. 1.1 and illustrates the complicated warning scenarios that can arise. The region encompassed by both the flash flood and tornado warnings, including the towns of Keene, Cleburne, and Grandview, Texas (Fig. 1.1), provide an example of the type of situation in which a TORFF event may occur.

[1]Part of this chapter has been published by the American Meteorological Society in *Weather and Forecasting*: Nielsen, E. R., G.R. Herman, R.C. Tournay, J.M. Peters and R.S. Schumacher, 2015: Double Impact: When Both Tornadoes and Flash Floods Threaten the Same Place at the Same Time. *Wea. Foecasting*, **30 (6)**, 1673–1693. doi: 10.1175/WAF-D-15-0084.1. ©2015 American Meteorological Society. Used with permission.

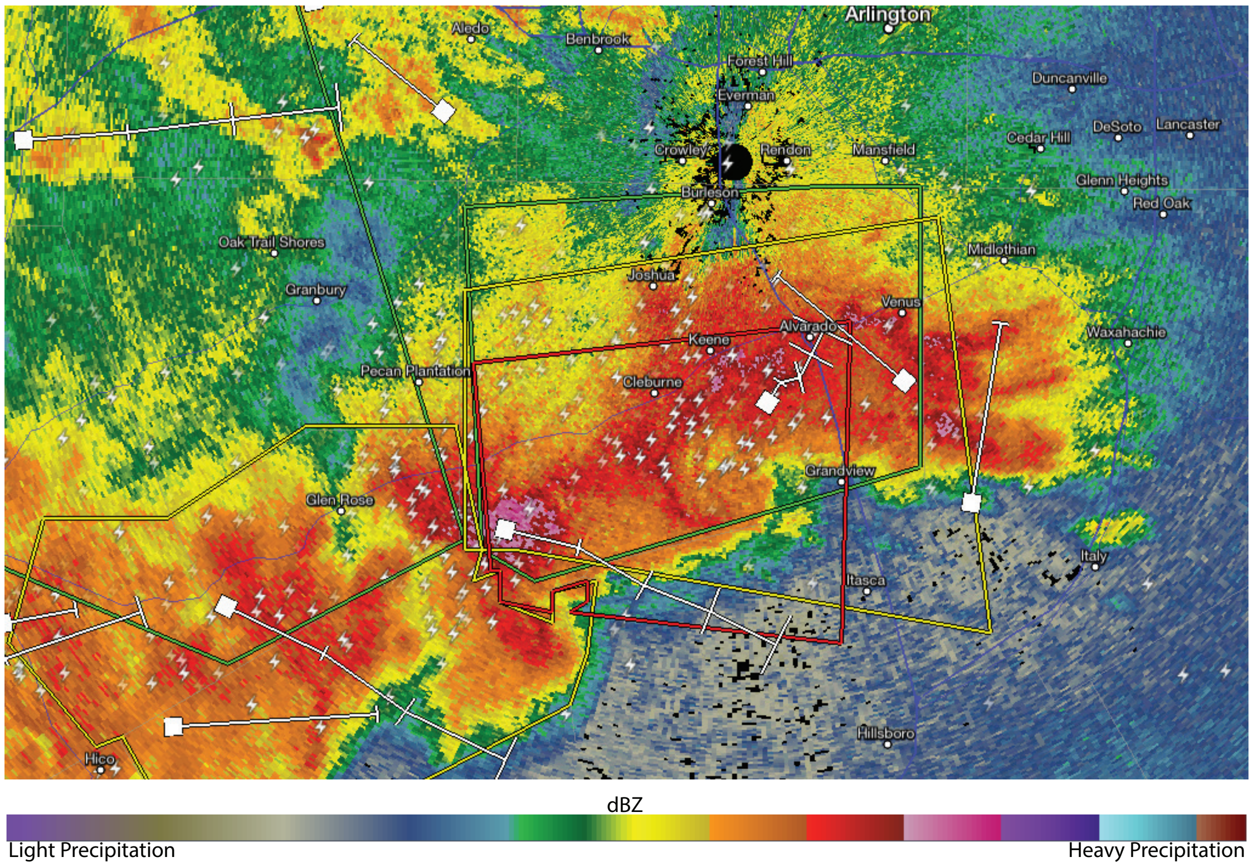

FIG. 1.1. Radar image from Dallas-Fort Worth NEXRAD radar (KFWS), obtained from RadarScope by Weather Decision Technologies, for recent observed overlapping tornado and flash flood warning scenario valid 0311 UTC 27 April 2015 in north central-Texas (just south of Dallas-Fort Worth area). Red polygon corresponds to tornado warning, green to flash flood warning, and yellow severe thunderstorm warning. Reproduced from Nielsen et al. (2015) Fig. 1.

There are numerous historical examples of the impacts that TORFF events can have on society. On 31 May 2013, a TORFF event in Oklahoma City, OK tragically illustrated an example of how the additional complexities in warning dissemination and risk perception in a multi-threat, collocated event could further magnified the danger beyond the meteorological hazard alone. Thirteen deaths were associated from the flash flooding whereas eight deaths were directly associated with the tornado. Perhaps most alarming, members of the public interviewed seemed to have no knowledge of the flash flooding threat despite warnings in place and social media dissemination (NWS 2014). More recently, a woman drowned in Oklahoma in May 2015 while seeking refuge from a tornado in a storm shelter (KWTV 2015). These events, and other similar events (e.g., Nashville Flood in 2010, NWS 2011), underscore the exceptionally life-threatening situation that TORFFs can produce. Compared to single hazard events, it moreover illustrates how such events can increase the public's vulnerability due to complications affecting their awareness, understanding, sensitivity, and adaptive capacity (e.g., Morss et al. 2011).

TORFF events also pose a particularly difficult challenge to operational forecasters (Rogash and Smith 2000), which further compounds the complexity and danger of these situations. Meteorological conditions that are favorable for tornado formation are often not conducive for flash flooding and vice versa (compare e.g., Maddox et al. 1979; Doswell et al. 1996; Doswell 2001; Markowski and Richardson 2010; Mercer et al. 2009; Smith et al. 2012; Thompson et al. 2012). For instance, tornadoes are associated with surface based convection (Nowotarski et al. 2011) and fast convective cell motions, while flash floods can be caused by both surface based and elevated convection and usually need slow cell motions or “echo-training" to cause large rainfall accumulations. Of course, there are exceptions to these generalizations (See: Bunkers and Doswell 2016; Nielsen et al. 2016a). Forecasters must be aware of and closely monitor complex situations that can provide the environmental ingredients necessary for both tornadoes and flash floods. Furthermore, the occurrence of one phenomenon – typically tornadoes – before the onset of another hazard can potentially take priority and hamper identification of subsequent weather hazards such as flash floods (e.g., Schwartz et al. 1990). The failure of forecasters to identify the flash flooding event in a timely manner can further increase the danger of TORFF events.

Compared to individual tornado and flash flood events, relatively few studies have examined the meteorology and climatology associated with TORFF events (Maddox and Deitrich 1982; Rogash and Smith 2000; Smith et al. 2001; Rogash and Racy 2002). Maddox and Deitrich (1982) examined the characteristics of 11 synoptic systems in the 1970s that produced tornadoes, hail, damaging wind, and flash flooding. The authors found that the primary difference between the synoptic systems that produced multiple hazards and those that produced just flash flooding was an increase in surface temperature and dewpoint in the prior cases. Additionally, it was seen that the lower atmosphere winds (i.e., surface to 850 hPa) were stronger and more southerly, hereby, increasing low-level warm air advection and low-level wind shear compared to flooding only events. Rogash and Racy (2002) discussed the meteorological characteristics associated with significant tornado events (at least two F2 or one F3 tornado) and flash flooding that occurs within 250 km and 3 hours of one another from 1992-1998, and found that the meteorological setup was largely indicative of typical tornadic environmental characteristics. However, Rogash and Racy (2002) identified three main meteorological setups (Fig. 1.2) that were conducive for the nearby concurrence of tornadoes and flash flooding.

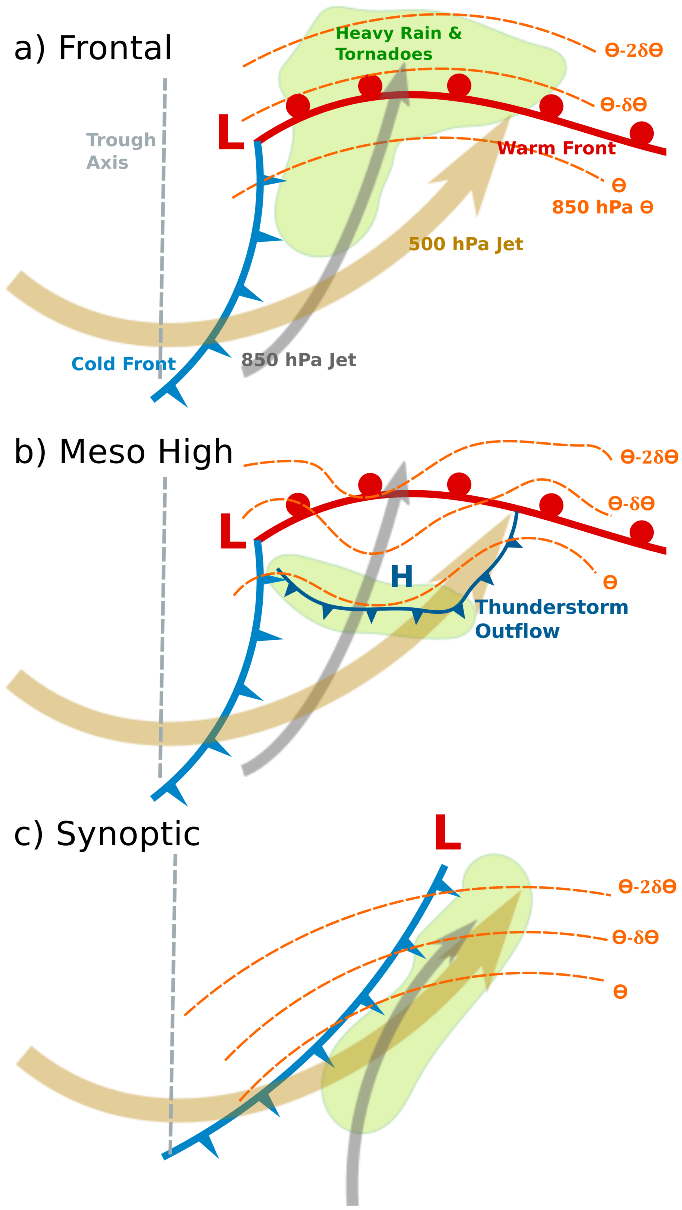

FIG. 1.2. Adapted from Figs. 2, 3, 4 of Rogash and Racy (2002) showing features associated with each synoptic pattern, identified within the paper, of near tornado and flash flood events. Frontal type pattern is presented in (a), mesohigh (outflow boundary) pattern in (b), and synoptic pattern in (c). Surface low and high centers are represented by L and H, respectively. Surface boundaries are denoted in normal mapping convention, with the exception of the outflow boundary which is denoted by the darker, thiner cold front convention. Dashed grey lines represent 500 hPa trough axis, brown arrows represent 500 hPa jet location, and grey arrows represent 850 hPa jet. Orange dashed lines represent 850 hPa potential temperature contours. Shaded green region marks area where the potential for tornadoes and heavy rainfall exists. Reproduced from Nielsen et al. (2015) Fig. 2.

Although differences do exist between the scenarios, one commonality is proximity to an approaching, distinct mid-tropospheric trough with event location in the divergent region of an upper-tropospheric jet streak. While Rogash and Racy (2002) and Maddox and Deitrich (1982) looked at patterns conducive to both tornadoes and flash flooding from the same synoptic system, these authors did not investigate the enhanced hazards of *directly* collocated, concurrent tornado and flash flood events, and the associated complicated decision-making aspects of these events.

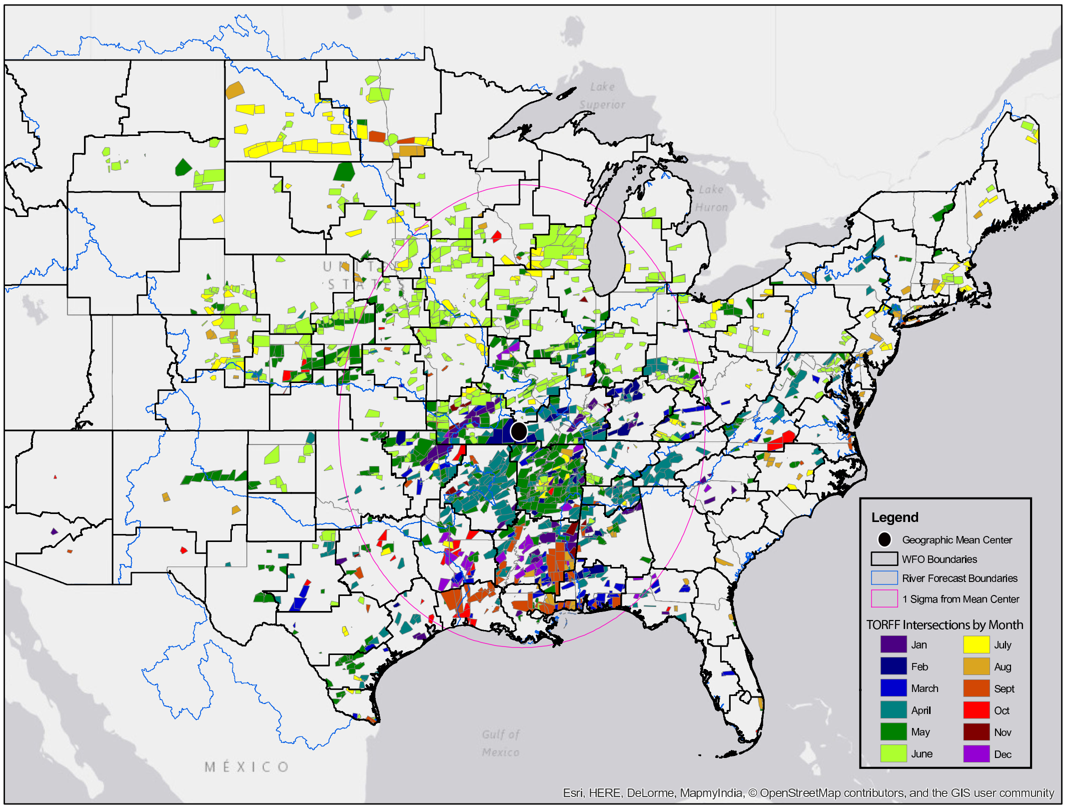

FIG. 1.3. Geographic distribution of concurrent, collocated tornado and flash flood warnings over the period from 2008-2014 (colored by month). Black dot represents geographic mean center, pink ellipse represents one spatial standard deviation away from mean center, and the black and blue lines represent NWS WFO and RFC boundaries, respectively. Reproduced from Nielsen et al. (2015) Fig. 6.

In an effort to expand upon this background knowledge, Nielsen et al. (2015) examined the frequency, from both a warning and an observational perspective, and meteorological characteristics of concurrent and directly collocated tornado and flash flood events in the United States between 2008 and 2013/14. Nielsen et al. (2015) found that TORFF intersections, defined as officially disseminated overlapping warnings issued within 30-minutes of one another, occurred, on average, 400 times per year between 2008 and 2014 (Fig. 1.3), which highlights the frequency that such threats are regularly

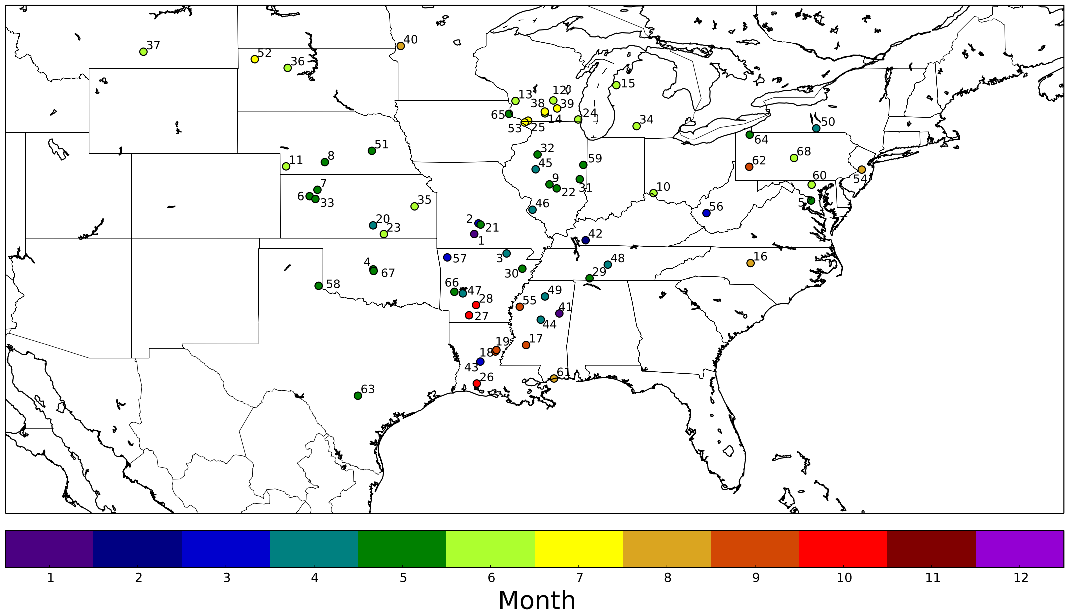

FIG. 1.4. Geographic distribution of identified concurrent, collocated tornado and flash flood events over the period from 2008-2013 (colored by month to match Fig. 1.3). Reproduced from Fig. 7 of Nielsen et al. (2015) with the number near each marker corresponds to event specifics listed in Appendix A of the same paper.

communicated to the public. They occurred with maximum frequency in the lower Mississippi River valley with relatively few occurrences west of the Continental Divide.

Additionally, 68 TORFF events were identified by the authors from 2008 to 2013 (Fig. 1.4), using only a temporal buffer between observations for TORFF verification (i.e., for events to have been identified the tornado and flash flood observations had to be at the exact same point). This event total more than doubles the 31 events identified, albeit with different but similar criteria, by Rogash and Racy (2002) from 1992 to 1998. A radar classification of the verified events by Nielsen et al. (2015) showed that TORFF events occurred in mesoscale convective systems (MCSs), discrete supercells, tropical cyclones, synoptically forced frontal regions, and periods of transition between discrete cells and organized convection with near equal frequency. The latter classification highlights the period of upscale growth from discrete convection to organized mesoscale systems as a particularly favorable situation for verified TORFF events to occur.

Meteorologically, Nielsen et al. (2015) found that the synoptic conditions associated with verified TORFF events were found to be similar to typical tornadic environments; however, the TORFF environment exhibited stronger large-scale forcing for ascent and tended to be moister through the atmospheric column. However, the authors discuss how these differences are relatively small making verified TORFF events difficult to distinguish from tornadic events that share these characteristics and do not produce a collocated flash flood. These results were expanded in a formal comment (Bunkers and Doswell 2016) and reply (Nielsen et al. 2016a) series on the matter specifically discussing TORFF event storm motion, as it is an important control on the total observed precipitation totals (e.g., Doswell et al. 1996). The results showed that mean winds speeds throughout the atmospheric column, for the 68 verified events, were anomalously high for TORFF events, and, further, TORFF events have anomalously higher mean wind speeds than tornadic only events. This potentially adds further ambiguity to the synoptic differences between TORFF and tornadic only events. Overall, the results of Nielsen et al. (2015) show that TORFF events occur in complex meteorological scenarios with substantial frequency and present challenges through the entire weather warning process from forecasting to public communication and action.

The ambiguity in the defining meteorological characteristics of TORFF events in Nielsen et al. (2015) combined with the identified event's ability to occur in multiple storm modes (i.e., MCSs, discrete cells, tropical cyclones, and transitioning modes) motivates further investigation into the storm scale dynamics of such events. In order to frame this research from a baseline level, it is worth noting that the only requirement that must be true across all the TORFF events discussed in Nielsen et al. (2015) is that rotation around the vertical axis capable of producing a tornado must be present at some point in a convective system with rainfall capable of producing flash flooding[2]. This motivates inquiry into any possible interactions that may or may not exist between rainfall production processes and meso-γ to meso-β-scale rotation around a vertical axis[3], since the presence of rotation introduces additional dynamics to a convective system in the form of rotationally induced pressure perturbation forces that traditionally have not been examined in precipitation research (e.g., Rotunno and Klemp 1982; Klemp 1987; Markowski and Richardson 2010).

In addition to Nielsen et al. (2015), several studies have shown the ability for rotating storms, especially suprercells, to produce extreme rainfall and flash flooding (e.g., Moller et al. 1994; Smith et al. 2001; Duda and Gallus 2010; Hitchens and Brooks 2013; Schumacher 2015a; Smith et al. 2018), despite the belief that the highly sheared environment in which they form and hail production limits this ability (e.g., Marwitz 1972; Foote and Fankhauser 1973; Browning 1977). The ability for rotating storms

[2]The author acknowledges the importance of static and non-static hydrologic characteristics, such as soil moisture, as constraints on the development of flash flooding. However, for the purposes of this manuscript the main focus will be on the rainfall portion of hydrometeorology as it relates to this problem.

[3]Hereafter, the use of the word "rotation" will refer to rotation around a vertical axis.

to produce intense rainfall, despite these conflicting results, has been theorized (e.g., Doswell et al. 1996) to be caused by intense non-buoyant accelerations associated with rotation that are a substantial source for positive vertical momentum in supercells (e.g., Rotunno and Klemp 1982; Weisman and Klemp 1984). The resulting dynamically enhanced updrafts could then serve to enhance rainfall production to first order by simply creating more robust updrafts, over similar convection that does not contain rotation. While the effect of these rotationally induced dynamic forces and the related intensity of 0–1km shear (e.g., Craven et al. 2004) has been extensively studied in regards to tornadogensis (e.g., Markowski et al. 2012; Markowski and Richardson 2014; Coffer and Parker 2015), their effect on precipitation processes has not been systematically examined.

The research presented in this manuscript serves to examine rotating, extreme rainfall producing storms from an observational and dynamical point of view to determine the frequency of collocation of extreme rain rates and rotation; the effects that rotation has on precipitation processes, in both idealized and non-idealized numerical simulations; and the prevalence of TORFF events in the United States, using a new verification method. The appropriate specific scientific background, motivation, hypothesized specifics, and methods for each set of scientific analyses are given in each research chapter within.

Chapter 2 serves to extend the research presented in Nielsen et al. (2015) by providing an improved, more realistic climatology of TORFF events in the United States by taking into account spatial variability between tornado and flash flood observations[4]. Additionally, two TORFF events samples as part of the VORTEX-SE field campaign will be examined. Chapter 3 examines the effect of rotation on extreme rainfall in an idealized modeling setup, specifically focusing on the dynamic impacts of rotation on the updraft strength and total vertical mass flux[5]. Chapter 4 identifies the propensity for rotation to be associated with extreme short-term rain rates (i.e., >75 mm hr^{-1}) in the United States, independent of whether a tornado was produced, providing climatological context to the potential impact of the results of Chapter 3[6]. An in depth observational and modeling case study of the Houston "Tax Day" flood of 2016 is presented in Chapter 5, which examines whether the results of Chapter 3 are seen in a

[4]The climatological results presented within Chapter 2 plan to be submitted as part of a larger study in *Weather and Forecasting* by the end of 2019.

[5]The research presented within Chapter 3 have already been published in the *Journal of the Atmospheric Science* as Nielsen and Schumacher (2018).

[6]The results presented in Chapter 4 are currently accepted pending major revisions in *Monthly Weather Review*.

real-time, horizontally homogenous simulation[7]. Chapter 6 will provide the overarching conclusions and discussion of future work.

[7] The results of Chapter 5 will be submitted by the end of 2019 to *Monthly Weather Review*.

CHAPTER 2

An Updated Climatology of Concurrent, Collocated Tornado and Flash Flood Events

2.1 Introduction

As discussed previously in Nielsen et al. (2015) and in the first chapter of this manuscript, the occurrence of tornadoes and flash floods in the same place at the same time, known as "TORFF" events, present a unique set of concerns that can pose an increased risk to public safety outside of each individual threat alone. Among these unique concerns for dual threat scenarios is a conflict between the recommended life-saving action for each individual hazard, which can increase confusion and lead to sub-optimal precautionary responses. Given these complexities, a proper understanding of TORFF frequency and the associated environmental characteristics is essential to prediction of such events and application of the proper warning communication practices.

Nielsen et al. (2015) looked at TORFF climatology in two different ways. The first, used overlapping tornado and flash flood warnings with various temporal offsets to examine how often the potential for a TORFF event existed in the U.S. over the study period. This informs the frequency of TORFF threat communication, which has important implications for warning messaging and risk personalization. Secondly, TORFF events were "verified" using storm observations to examine the frequency of meteorological occurrence. That is, how often both a flash flood and tornado threat were actually concurrent and collocated, which has implications on the meteorological conditions that are associated with TORFF events.

The initial climatology on "verified" TORFF events was performed by using tornado track data from the Storm Prediction Center's (SPC) Severe Geographic Information System (SVRGIS) database and flash flood reports associated with the Flooded Locations and Simulated Hydrographs project (FLASH Gourley et al. 2017) from 2008 through 2013. Using no spatial buffer and a 3 hour temporal buffer between the tornado and flash flood report issuance times, Nielsen et al. (2015) identified 68 "verified" events over the period. As discussed in the paper, issues with the reporting practices and the accuracy of the flash flood observations, likely led the previously used spatial offset (i.e., none) to be overly conservative in the verification of TORFF events. Further, the chosen flash flood dataset limited the analysis to only six years. While this served as an excellent starting point, these overlapping threats vary temporally as well as spatially. The latter aspect of this was not addressed originally in Nielsen et al. (2015) and warrants further investigation, especially, given recent results regarding the risk communication in other warning scenarios (e.g., Morss et al. 2017; Demuth et al. 2018).

The meteorological characteristics of TORFF events in Nielsen et al. (2015) were largely treated in a bulk sense. This yielded important information regarding the event characteristics relative to a localized, baseline climatology, which informed differences between TORFF event and tornado-only event environments (see Section 3c Nielsen et al. 2015). However, significant differences existed between the storm modes of the "verified" TORFF events in Nielsen et al. (2015). Examining the differences in the storm-scale dynamics of individual events offers important insights into a specific storm's potential to produce a TORFF event, since understanding the entire distribution of events is an important aspect of meteorology. The ongoing **V**erification of the **O**rigins of **R**otation in **T**ornadoes **EX**periment-**S**outh**E**ast (VORTEX-SE) allowed for the opportunity to use targeted, in-situ observations for the analysis of potential TORFF events in a region historically associated with many TORFF events and warning intersections (Fig. 2.1). The additional radar observations, soundings, and project-tailored numerical modeling served as a springboard to understand potential TORFF events that were sampled as part of the project on a storm-scale.

This chapter serves to expand the knowledge of TORFF events in the United States over the initial discussion presented in Nielsen et al. (2015), by examining new sources of meteorological data and gauging the spatial uncertainty of TORFF events. Additionally, observations and modeling conducted during the first two years of the VORTEX-SE experiment will be used to analyze the storm-scale interactions of a TORFF event that occurred in March of 2016 and an event with forecasted TORFF hazards that occurred along the Alabama-Georgia border in April of 2017. Connections will be made back to the research presented in Nielsen et al. (2015), and a discussion of each event's unique characteristics will be presented.

2.2 Methods

2.2.1 TORFF Climatology

Two different identification methods were used to examine the climatology of TORFF events in the United States. In the first, as done in Nielsen et al. (2015), tornado and flash flood warnings that overlap within 30-minutes of their respective issuance times were identified to determine the frequency that TORFF threats are communicated as imminent to the public. A 30-minute temporal buffer was chosen because it approximately corresponds to the average length of a tornado warning in the U.S. (e.g., Sutter and Erickson 2010). The archived tornado and flash flood warnings from 2008 through 2018 were obtained from the Iowa Environmental Mesonet (IEM) Geographic Information System (GIS) archive (IEM 2018b) and processed through tools in ArcGIS to arrive at a geographic distribution of warning intersections. These intersections of the tornado and flash flood warnings, provided they were issued within 30-minutes, will be referred to as "TORFF warning intersections" or , simply, "warning intersections," hereafter. The spatial mean center and spatial standard deviation associated with the warning intersections were then calculated, and the spatial and temporal patterns examined.

While tornado and flash flood warning intersections show where both threats are deemed imminent by the National Weather Service (NWS), they do not confirm whether a TORFF event occurred. In order to create a dataset of TORFF events that are "verified[1]" in terms of meteorological/hydrological occurrence, spatial intersections between confirmed tornado tracks and local storm reports (LSRs) of flash flooding were calculated from 2003 through 2017. Tornado tracks were obtained from the Storm Prediction Center's (SPC) Severe Geographic Information System (SVRGIS; Smith 2006), and flash flood LSRs from the IEM GIS archive (IEM 2018b). Spatial buffers with radii of 10, 20, 30, 40, and 50 km were placed around the flash flood LSRs to test the spatial sensitivity of TORFF events to distances between the tornado and flash flood observations. This also accounts for errors or uncertainties that potentially exist in the geolocation of the flash flood local storm reports. A temporal buffer of $\leq \pm 3$ hr between tornado track start time and flash flood LSR report was used, as in Nielsen et al. (2015). The spatial intersections between the tornado tracks and the flash flood LSRs were clustered into TORFF events using the density-based algorithm for spatial datasets with noise (DBScan; Ester et al. 1996) executed using the Scikit-learn (Pedregosa et al. 2011) Python programing library. This created 5 separate "verified" TORFF datasets, one for each spatial buffer over the period.

Lastly, information about the number of intersections in each event and the event occurrence relative to sunset/sunrise were retained. The start time, date, latitude, and longitude of each individual tornado in the above dataset was then used to calculate the local sunset and sunrise time for each tornado using the Python programming language PyEphem library (Rhodes 2011). Each individual tornado start time was then converted to a sunset and sunrise relative framework. This sunset/sunrise information for each tornado within a specific TORFF event was used to determine the TORFF event timeline relative to the nocturnal evening transition (ET; Defined in this study as the two hour period

[1]"Verified" is presented here in quotations, since the events are verified per the specific spatial proximities, temporal offsets, and observational datasets chosen in this study and may include inaccuracies associated with these options.

prior and following local sunset; Acevedo and Fitzjarrald 2001; Bonin et al. 2013; Anderson-Frey et al. 2016), which is characterized by continued relatively large MLCAPE, increasing 0–1km and 0–6km SRH, and lowering LCL heights, which leads to an overall increase in tornadic potential. The motivation for this is two fold and serves to relate TORFF event characteristics to known tornado only event characteristics. First, due to the previously established limitation in verification of TORFF events, little to no information is known about the distribution of TORFF events relative to the diurnal cycle and the associated storm mode. Research has shown that, in tornado-only events, tornadoes associated with right-moving supercells peak during the ET, with tornadoes from quasi-linear convective systems (QLCSs) increasing into the night (e.g., Anderson-Frey et al. 2016). Second, nocturnal tornadoes pose elevated threats over daytime tornadoes because additional factors (e.g., at night the potential environmental cues associated storms are difficult to visually identify and people tend to be asleep) limit the ability to take effective life-saving action and, in turn, enhance vulnerability (e.g., Ashley et al. 2008). Given that TORFF events are complicated multi-threat scenarios, it is important to understand the propensity for nocturnal TORFF events, which, similarly to nocturnal tornado-only events, add even further communication changes to daytime TORFF events. The "verified" TORFF events are discriminated into those that last from the afternoon past the end of the ET period (hereafter referred to as BOTH events), from tornado events that produce their final tornado during or before the ET period (hereafter referred to as EARLY events), and from tornado events that occur exclusively after the ET period (LATE events), as determined by the tornado track(s) responsible for each individual TORFF event.

2.2.2 Individual TORFF Event Analysis

As part of the VORTEX-SE field project, several sets of semi-permanent observations, targeted observations, and regional-specific modeling data were collected to meet the field project objectives. The field project domain was centered on Huntsville, Alabama and encompassed the northern third of the state of Alabama. The project had several objectives, but those of the Colorado State University researchers focused on examining the environmental characteristics, the official warning issuance process in multi-threat scenarios, and the public interpretation of TORFF events. The personalization of TORFF events by the public and forecasters, alike, was examined in 2016. The environmental characteristics of TORFF events were examined in 2016 by using the existing observational network across the region and again in 2017 with the addition of targeted mobile radiosonde observations taken by Colorado State University.

Observations from both the existing operational network and those taken as part of the VORTEX-SE field project will be used to examine the environmental characteristics that are associated with any "verified" TORFF events and any event with forecasted TORFF hazards that occurred during the 2016 and 2017 field phases of VORTEX-SE. A "verified" TORFF event is defined as a TORFF event identified as described in the above methods subsection on TORFF climatology. An event with forecasted TORFF hazards is defined as a predicted severe weather event that contains concurrent and overlapping tornado probabilities from the Storm Prediction Center (SPC) (for discussion of probabilities see; Hitchens and Brooks 2012, 2014, 2017; Herman et al. 2018) and excessive rainfall probabilities from the Weather Prediction Center (WPC) issued as part of the Excessive Rainfall Outlook product (e.g., Barthold et al. 2015). No minimum threshold was place on the probabilities from either center, in an effort to ensure any an all events were captured.

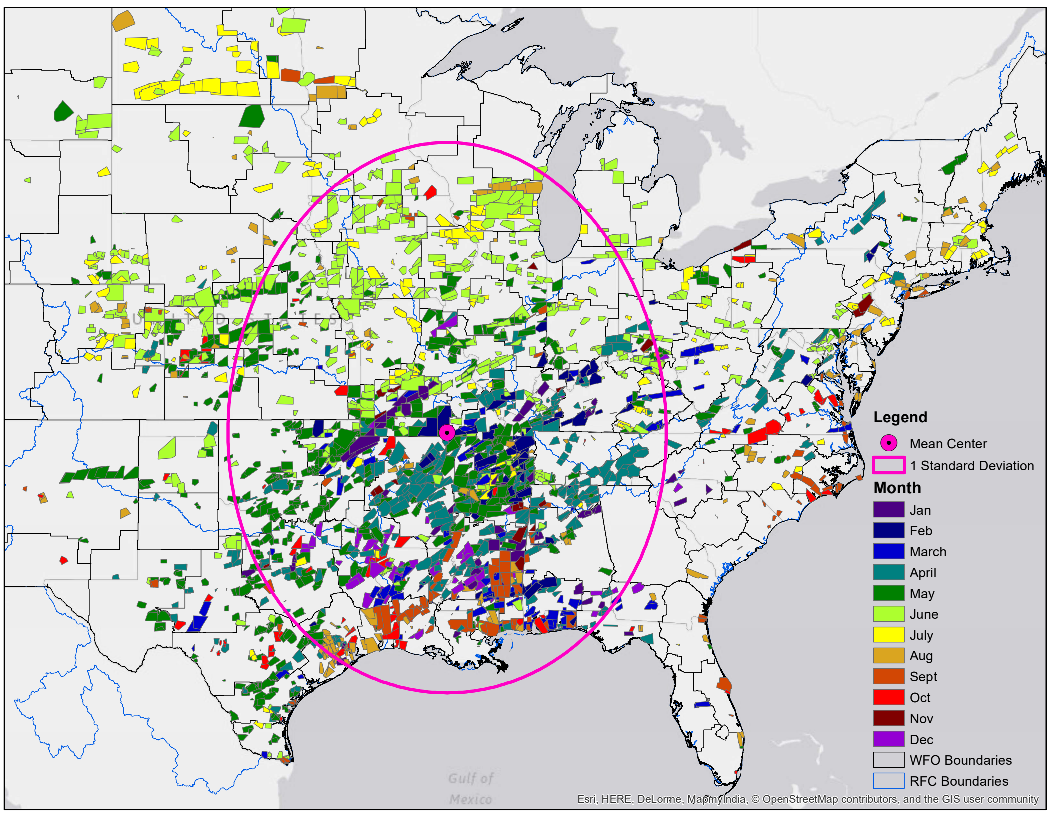

FIG. 2.1. Geographic distribution of concurrent, collocated flash flood and tornado warnings that were issued within 30-minutes of one another from 2008 through 2018 (colored by month). Area shaded on the map corresponds to the area common between both the flash flood and tornado warning. Pink marker represents the geographic mean center, pink ellipse represents one spatial standard deviation away from mean center, black line denote NWS WFO boundaries, and blue lines denote RFC boundaries.

Two events, one "verified" and one with forecasted TORFF hazards occurred during the field phases of VORTEX-SE and will be examined in detail in this chapter. The "verified" event occurred overnight into the early morning hours of 31 March 2016 in "Telmin[2]", while the second event examined was forecasted to occur during the afternoon hours of 05 April 2017 in the southeastern United States. Specific attention will be given to the synoptic and mesoscale characteristics of each event, especially as related to low-level wind shear.

2.3 Results

2.3.1 Climatology

Between 2008 and 2018, a total of 3843 TORFF warning intersections, or about 350 per year, occurred within 30-minutes of one another across the United States (Fig. 2.1). The yearly frequency of the TORFF warning intersections is slightly reduced compared to the numbers (i.e., ~400 per year) originally seen in Nielsen et al. (2015) for the period from 2008 to 2014. The geographic distribution of the warning intersections remains similar to the results presented in Nielsen et al. (2015) (cf. their Fig. 6 and Fig. 2.1) with the geographic center located in the central Mississippi Valley along the Arkansas-Missouri border, which is slightly south of the original geographic center in Nielsen et al. (2015) (their Fig. 6). The majority of the warning intersections, not surprisingly, are seen between the Rocky and Appalachian Mountains (Fig. 2.1), with intersections occurring across the contiguous U.S. and in Hawaii (not shown). However, a slight southwestward shift in the 1 sigma spatial standard deviation is seen from Nielsen et al. (2015) (cf. their Fig. 6 and Fig. 2.1). Seasonally, the TORFF warning intersections are seen farther north as the calendar year progresses, which is similar to the tornado climatology (e.g., Brooks et al. 2003, Fig. 2.1). Additionally, warning intersections caused by tropical cyclones are evident in the record along the Atlantic and Gulf of Mexico coastlines in August through October (Fig. 2.1). For instance, Hurricane Harvey in 2017 was responsible for 68 different warning intersections as the storm processed inland (Fig. 2.2) and presented many complicated communication scenarios associated with these warning intersections (NWS 2018a).

[2]"Telmin" is not the real name of the town affected by the particular TORFF event in question. The names and some information about the National Weather Service (NWS) weather forecast office (WFO) location, the warnings, and town affected have been changed to protect the identity of forecasters and the public, as interviews conducted during this event are utilized in another study. The approximate location of the event will be denoted by circles on corresponding spatial maps, where "Telmin" could be located at any point within the circle.

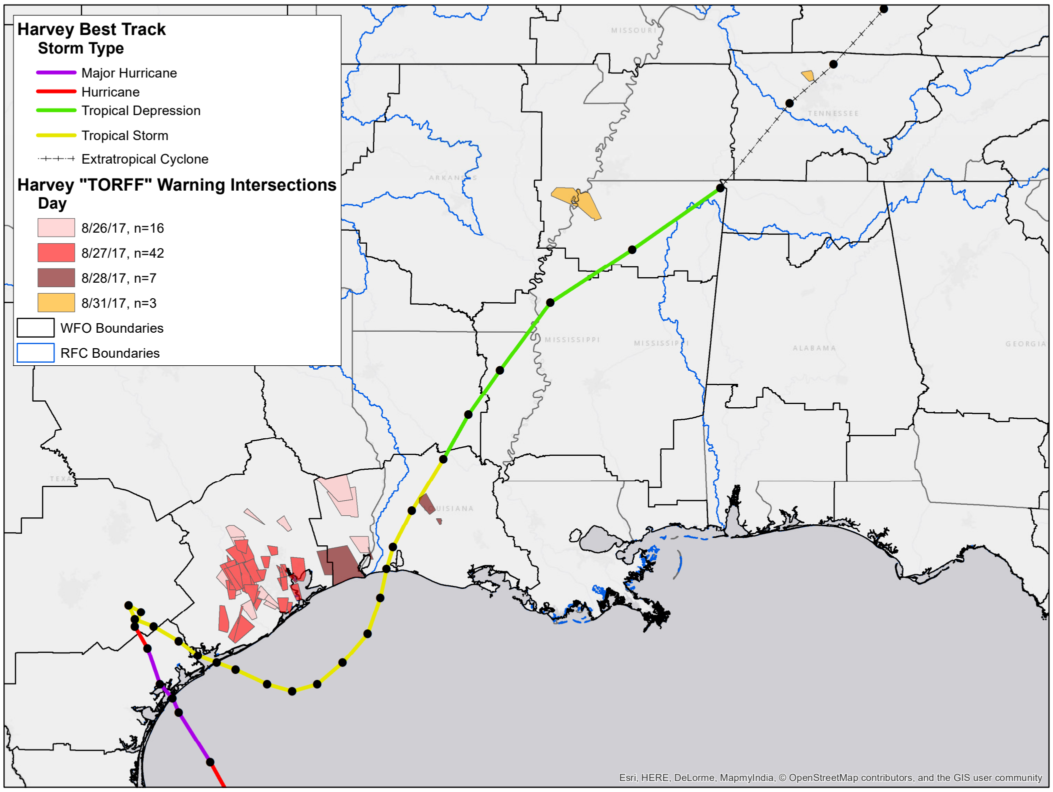

FIG. 2.2. Hurricane Harvey (2017) TORFF warning intersections color coded by day (fill polygons), storm best track color coded by storm classification (thick line), NWS WFO boundary (black lines), and NWS RFC boundary (blue lines).

As in Nielsen et al. (2015), sharp gradients exist in some locations across WFO and, to a lesser degree, across RFC borders (Fig. 2.1). Given the influence both the WFOs and RFCs have on the standard timeline of warning development, from both a severe weather and hydrologic perspective, this is not unexpected and might speak to specific WFO warning issuance tendencies. Furthermore, since flash flood guidance (FFG; Sweeney 1992) development and specifics vary between RFCs, forecaster guidance variance could also account for some of these differences.

TABLE 2.1. Number of "verified" TORFF events per specified spatial buffer from 2003 to 2017. All use a 3-hour temporal buffer as described in Section 2.2.1. Last column shows the precent increase of total events over next smallest spatial buffer.

Spatial Buffer Radius	Number of Events	Yearly Average	% Increase
10 km	414	27.6	n/a
20 km	559	37.3	35.0%
30 km	887	59.1	58.7%
40 km	1051	70.1	18.5%
50 km	1153	76.9	9.7%

The allowing of a spatial offset, in addition to a temporal offset used in Nielsen et al. (2015), and the use of the flash flood LSR dataset to "verify" TORFF events led to a rapid increase in the number of "verified" events over the 68 originally seen with no spatial offset in Nielsen et al. (2015). The total number of "verified" TORFF events from 2003 to 2017 increases from 414 to 1153 (see Table 2.1), as the spatial buffer allowed between the tornado track and flash flood LSR increases from 10 to 50 km (Fig. 2.3).

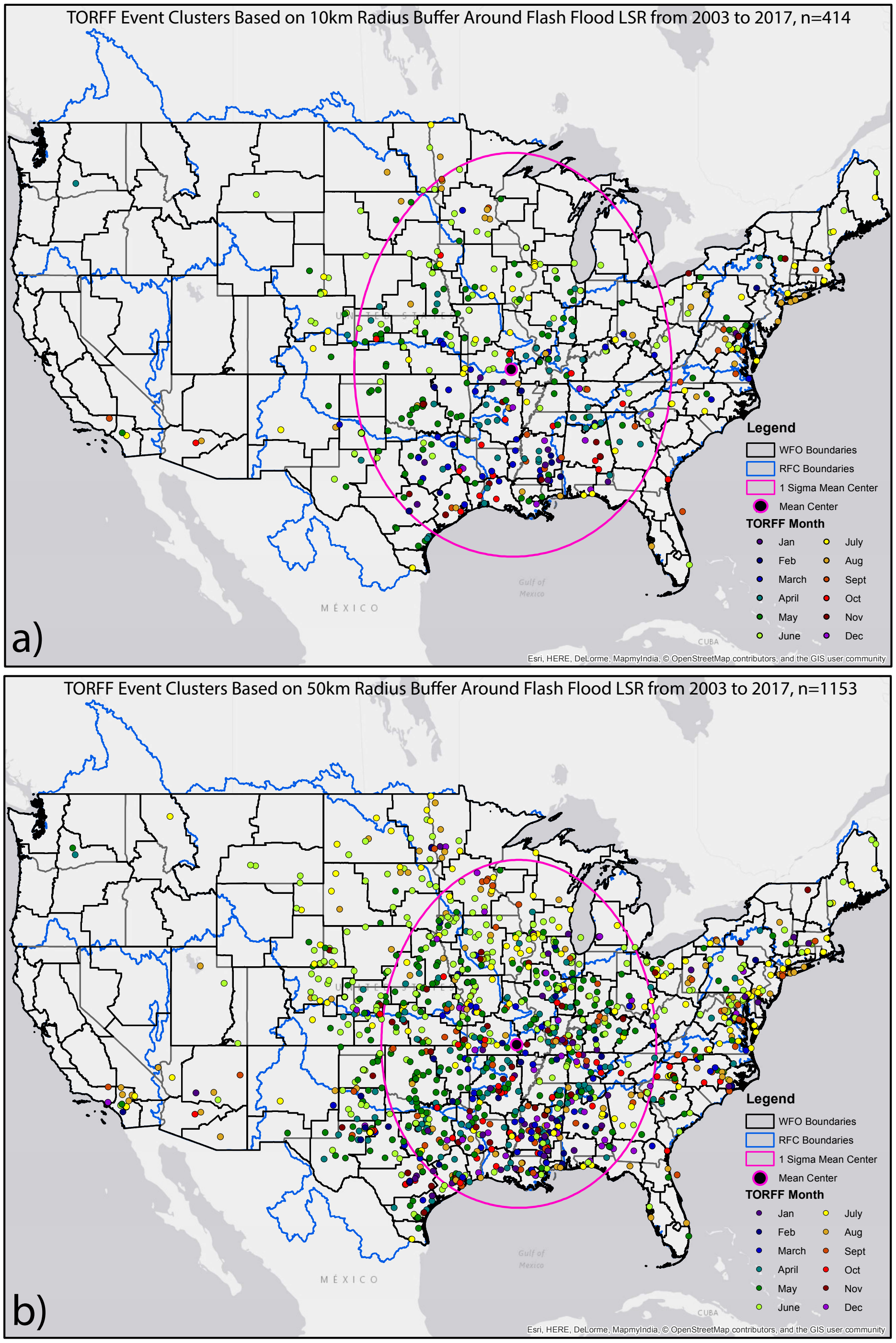

FIG. 2.3. TORFF event clusters, color coded by month, from 2008 through 2017 based upon a 10 km (a) and 50 km (b) radius around the flash flood local storm reports (LSRs), using a 3 hour temporal buffer between the tornado tracks and flash flood LSRs. Pink ellipse in each figure represents 1-sigma spatial standard deviation from geographic mean TORFF center, which is represented by black dot with pink outline. Weather forecast office (WFO) boundaries are shown in black, and river forecast center (RFC) boundaries are shown in blue.

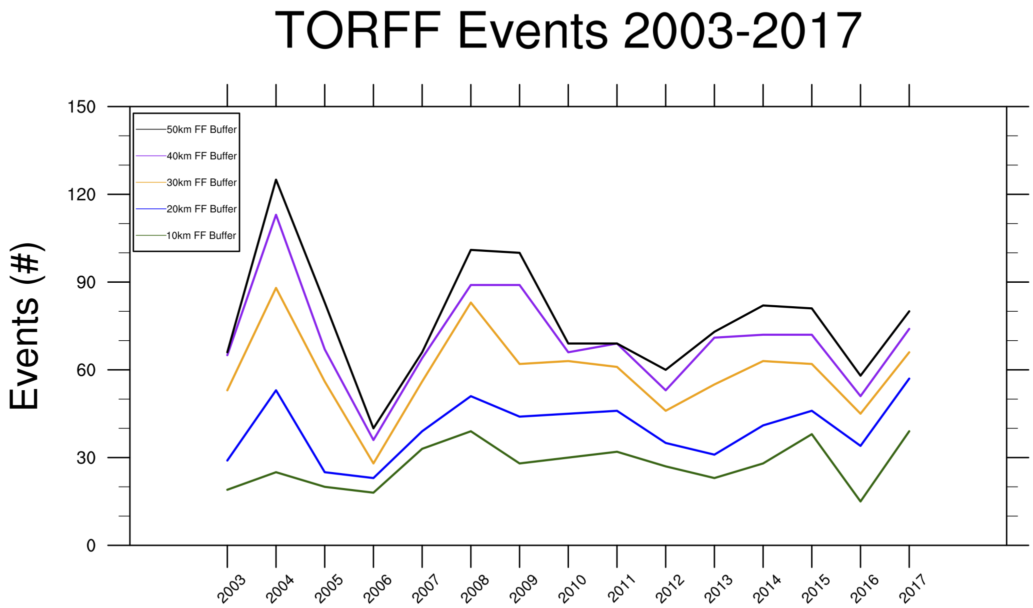

FIG. 2.4. Time series of the number of "verified" TORFF events per spatial buffer radius from 2003 to 2017.

As expected, the number of events increases as the spatial tolerance between the tornado path and flash flood LSR is increased. The greatest increase in events over the next lowest spatial buffer is seen at 30 km (Table 2.1), which might indicate a critical radius for TORFF identification in the framework established here. Regardless of the spatial buffer chosen, multiple "verified" TORFF events occur each year (Fig. 2.4), which points to TORFF events occurring with appreciable frequency outside of the most extreme events. This further adds weight to the conclusions of Nielsen et al. (2015) that TORFF events occur "with substantial frequency (p. 1690)" in the U.S.

The results show that the geographic distributions of the "verified" TORFF events are almost identical, regardless of the spatial buffer used (cf. Figs. 2.3 and 2.5). Furthermore, the geographic distribution of the "verified" events closely matches that associated with the warning intersections (cf. Fig. 2.1 and Figs. 2.3 and 2.5). Both of these methods of TORFF identification (i.e., the warning intersections and "verified" events) point to the Southeastern U.S. and the Mississippi Valley regions as the locations where the most TORFF events occur.

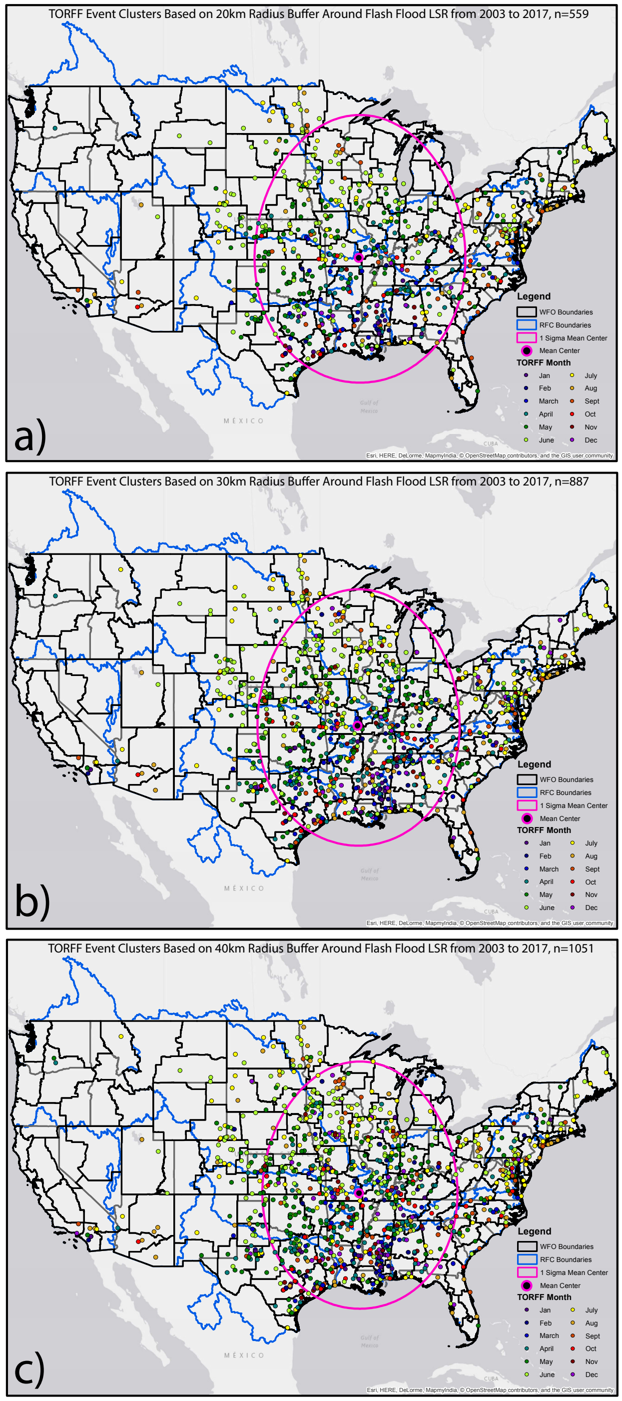

FIG. 2.5. As in Fig. 2.3 but for a (a) 20 km, (b) 30 km, and (c) 40 km spatial buffer around the flash flood LSRs.

It should be noted that the use of the flash flood LSRs in this study likely biases the TORFF events towards metropolitan areas (e.g., Dallas and Houston, Texas) or heavily trafficked roads (e.g., I-35 between Dallas, Texas and Oklahoma City, Oklahoma; Fig. 2.3b), which leads to an underreporting bias in rural areas, and causes large uncertainty in knowing the actual time flash flooding began, since the reports are conveyed by observers (e.g., Gourley et al. 2013). This problem does exist in tornado observations as well and

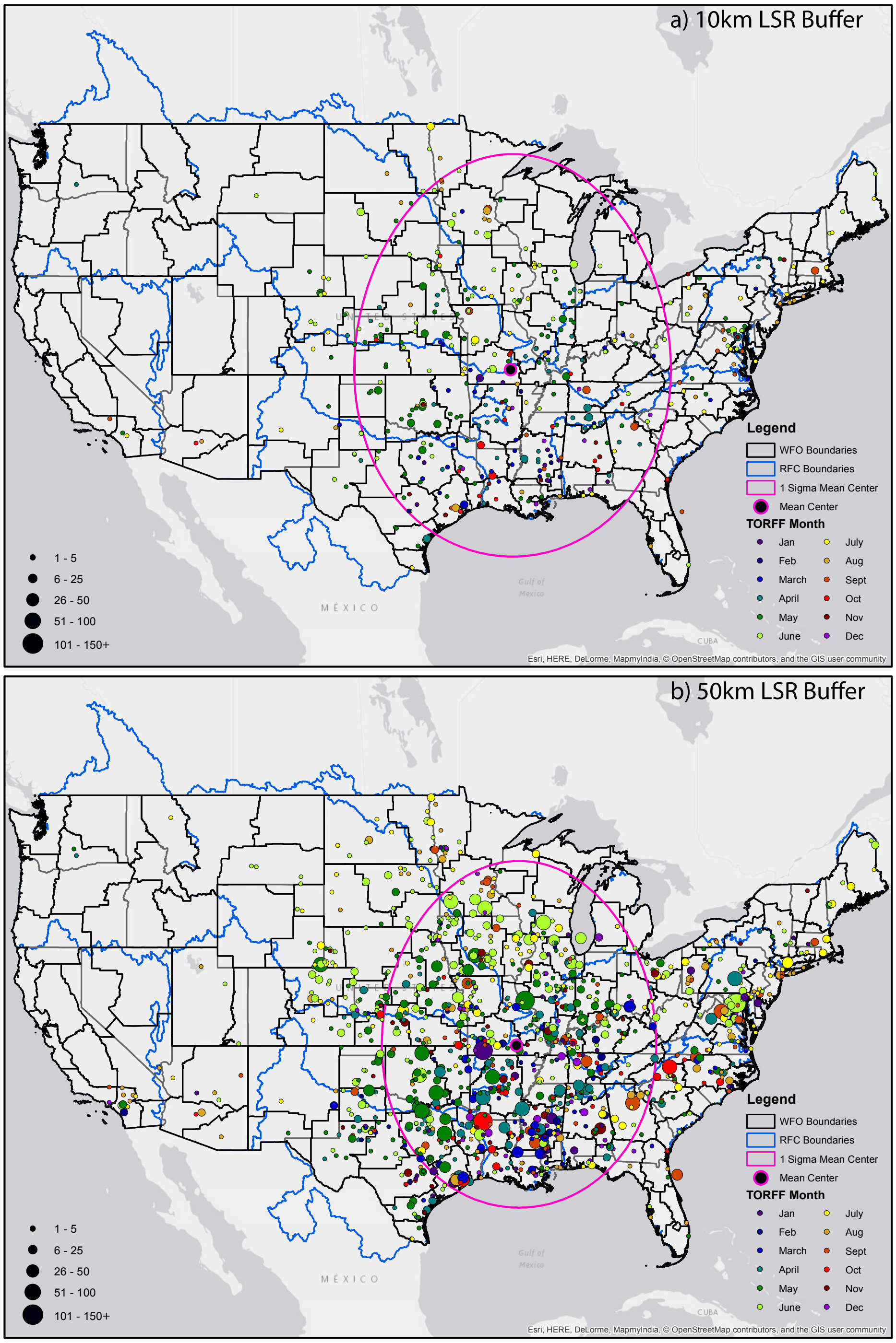

FIG. 2.6. As in Fig. 2.3 except marker size reflects the number tornado and flash flood intersections within the 3 hour temporal buffer and the respective flash flood LSR spatial buffer.

has been thought to lead to an increase in tornado reports, especially at the (E)F0 rating, in the official record, with similar issues of potential underreporting in rural areas (e.g., Verbout et al. 2006; Doswell 2007; Agee and Childs 2014; Potvin et al. 2019).

Seasonally, the "verified" TORFF events follow a similar pattern to the warning intersections and what is typically known for tornadoes (Figs. 2.3 and 2.5), with events occurring more frequently in the northern latitudes later in the calendar year. The influence of tropical cyclones can still be seen along the Atlantic and Gulf of Mexico coasts in August through November (Figs. 2.3 and 2.5). For instance, hurricanes Harvey and Irma in 2017 both produced "verified" TORFF events, but their footprints are more clearly seen in the warning intersection maps (cf. Fig. 2.1 and Figs. 2.3 and 2.5), since each "verified" event can be associated with many warning or observational intersections. The number of tornadoes and flash flood LSR intersections associated with each "verified" TORFF event increases with the spatial buffer radius (cf. Fig. 2.6a-b). While this result is expected due to the design of the verification methodology, it does highlight regions that can and have experienced TORFFs that produce multiple concurrent and collocated observations of tornadoes and flash flooding within a relatively small area. The TORFF events that occur in the Mississippi Valley tend to be associated with more spatial intersections between the tornado tracks and flash flood LSRs, compared to CONUS-wide events, with the largest number of intersections per event occurring in the southern Mississippi Valley, eastern Oklahoma, and eastern Texas (Fig. 2.6b). The number of intersections between the tornado and flash flood observations cannot likely be used directly to determine the intensity or spatial coverage of a particular TORFF event, due to the temporal uncertainty and geographic biases associated with the flash flood LSR dataset. However, it does likely speak well to the number of people affected by a particular TORFF event.

TABLE 2.2. Number of "verified" TORFF events per specified spatial buffer from 2003 to 2017 broken into EARLY, BOTH, and LATE classifications. Percentages given in parenthesis denote approximate percentage of each classification (i.e., EARLY, BOTH, or LATE) per spatial buffer radius.

Spatial Buffer Radius	**EARLY**	**BOTH**	**LATE**
10 km	296 (71.5%)	27 (6.5%)	91 (22.0%)
20 km	428 (76.7%)	77 (13.8%)	94 (16.8%)
30 km	603 (68.0%)	113 (12.7%)	171 (19.3%)
40 km	692 (65.8%)	147 (14.0%)	212 (20.2%)
50 km	763 (66.2%)	161 (14.0%)	229 (19.9%)

At the 50 km spatial buffer radius, 763 (∼66.2%) of the TORFFs were classified as EARLY events (i.e., occurring entirely between sunrise and sunset), 161 (∼14%) as BOTH events (i.e., beginning after sunrise and continuing after sunset), and 229 (∼19.9%) as LATE events (i.e., occurring between sunset and sunrise; Table 2.2). While fewer total TORFF events were identified at the 10 km spatial buffer radius, similar proportions were seen for the EARLY (∼71.5%), BOTH (∼6.5%), and LATE (∼22.2%) events, with the largest difference being seen for the BOTH events (Table 2.2). These results show that roughly 30% of TORFF events, regardless of the spatial buffer, are associated with nocturnal tornadoes. Geographically, EARLY TORFF events occur across the U.S. and make up the majority of the events that occur in the lee of the Rocky Mountains (Fig. 2.7), following generally what could be expected from the tornado climatology. BOTH events occur generally in the same region, but are more clustered in the Mississippi valley through southeastern U.S. and less frequently occur in the lee of the Rocky Mountains (Fig. 2.7). The proportion of BOTH events to total "verified" TORFF events also increases constantly (Table 2.2) as the flash flood LSR spatial buffer is increased, which suggests these events are more sensitive to the area considered and potentially more widespread events. LATE TORFF events follow a very similar geographic distribution as BOTH events at the 50 km spatial buffer radius (Fig. 2.7b), but are more concentrated along the Gulf of Mexico coast and southern Mississippi Valley at the 10 km threshold (Fig. 2.7a). Additionally, LATE events make up a roughly constant 20% (Table 2.2) of the TORFF event total regardless of spatial buffer considered. Tropical cyclone cases are included in this dataset as previously mentioned. While they are classified relative to sunset in this analysis similarly to every other TORFF event, the likely importance of the normal continental diurnal cycle on the event evolution is significantly lessened (e.g., Baker et al. 2009; Morin and Parker 2011; Edwards et al. 2012).

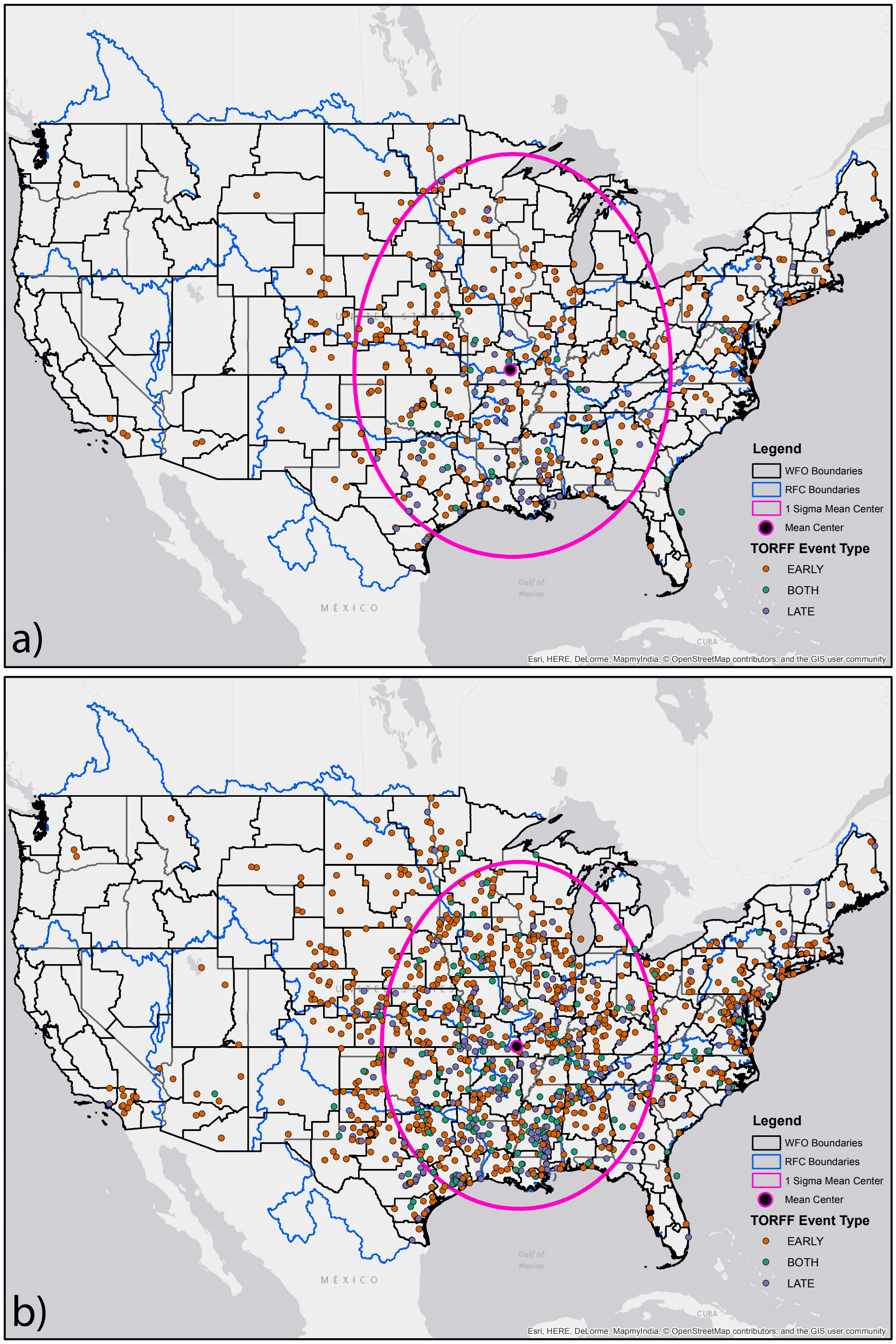

FIG. 2.7. As in Fig. 2.3 except marker color reflects whether the TORFF event is classified as EARLY (orange; i.e., starts and ends before sunset), BOTH (green; i.e., starts before sunset and ends after), or LATE (purple; starts and ends after sunset).

2.3.2 “Telmin” TORFF Event

Near 0400 UTC on 31 March 2016, a TORFF event associated with a quasi-linear convective system (QLCS) tornado occurred in the town of Telmin. Various bowing segments were present along the QLCS that stretched from northern Louisiana to southern Indiana (Fig. 2.8). Rotation embedded in the end of one of these segments was responsible for producing the tornado as it passed over Telmin near 0400 UTC (Fig. 2.9), during the observing period for VORTEX-SE in 2016.

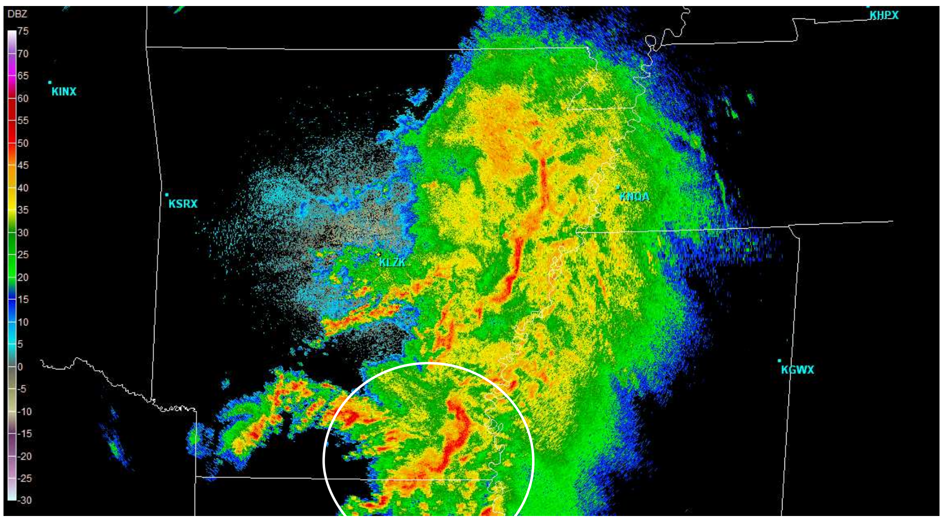

FIG. 2.8. A zoomed out, regional radar view of the system from the Little Rock, AR radar valid same time as Fig. 2.9. White circle represents the approximate location of the Telmin event.

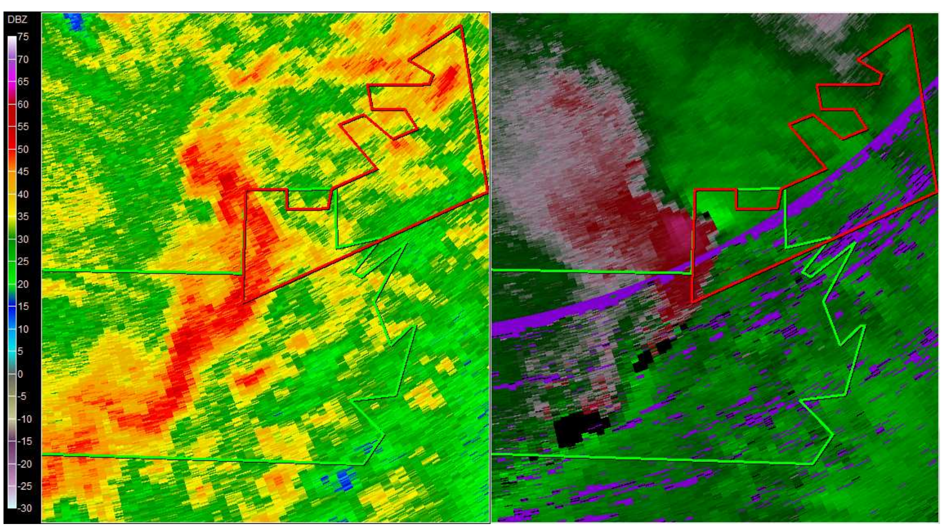

FIG. 2.9. Radar images of (left) reflectivity and (right) radial velocity from the closest radar to Telmin valid 31 Match 2016 showing the circulation responsible for the EF-1 tornado and flash flooding event. Red and green polygons represent valid tornado and flash flood warnings, respectively.

One injury was reported with many buildings in the town sustaining wind and water damage. The tornado was rated EF-1 and had a path length of 3.67 miles with a width of 150 yards (Fig. 2.10). The tornado path was within a mile of a previous tornado that occurred on March 13th and reached its strongest northeastern terminus of the track with maximum winds estimated at 110 mph. Flooding was reported both in the city and on major roads leading out of the city within 15-minutes after the tornado passed through the town, with feet of water reported over roads in some places. Antecedent rainfall had led to saturated soil conditions for most of the previous month and this event exacerbated ongoing river flooding in the area (NOAA 2016a).

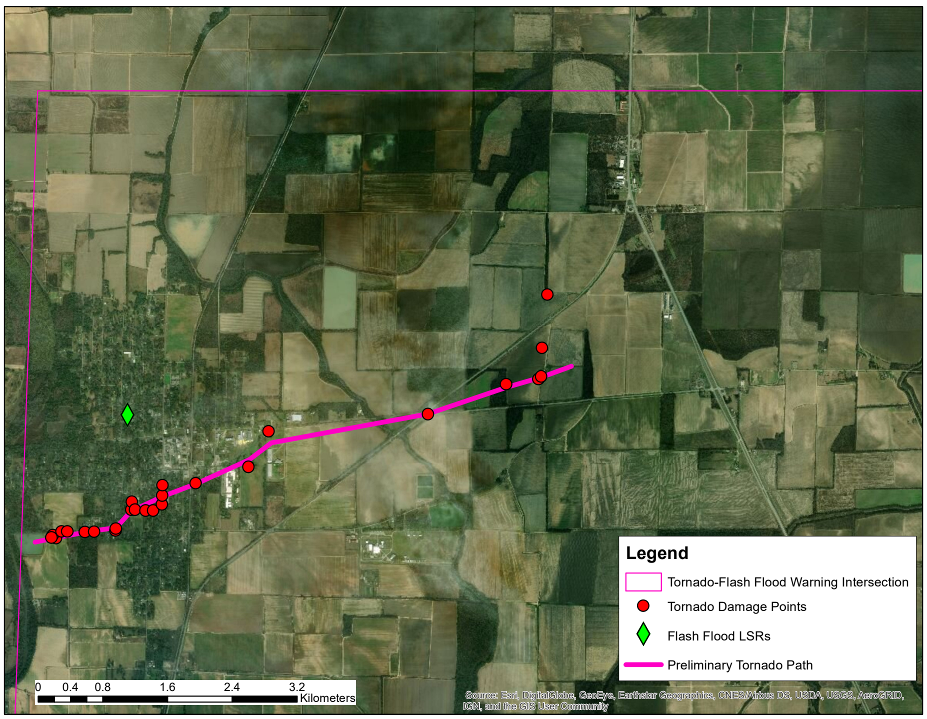

FIG. 2.10. Satellite map depicting tornado damage points (red markers), flash flood local storm reports (LSRs; green diamonds), preliminary tornado path (blue line), and intersection between the tornado and flash flood warning (pink polygon) for the TORFF event that occurred in Telmin 31 March 2016.

The closest ASOS rain gauges had 53.34 mm and 54.11 mm event totals, respectively (IEM 2018a), with the majority coming between 0200 and 0500 UTC on 31 March. Remote sensing based rainfall estimates range between 50 to just over 100 mm for the event total across the region (Fig. 2.11a) with the majority coming in the same three hour period (Fig. 2.12d-f). These event precipitation totals are not particularly intense or rare for the region, with the values falling at or below the average one year recurrence interval for 1-hr and 3-hr accumulations (e.g., Herman and Schumacher 2018b). While the precipitation was not historic, it did approach and, in some places, exceed the regional FFG (e.g., Sweeney 1992). This illustrates that the observed flash flooding was possible given the rainfall amounts and antecedent soil conditions (Fig. 2.12).

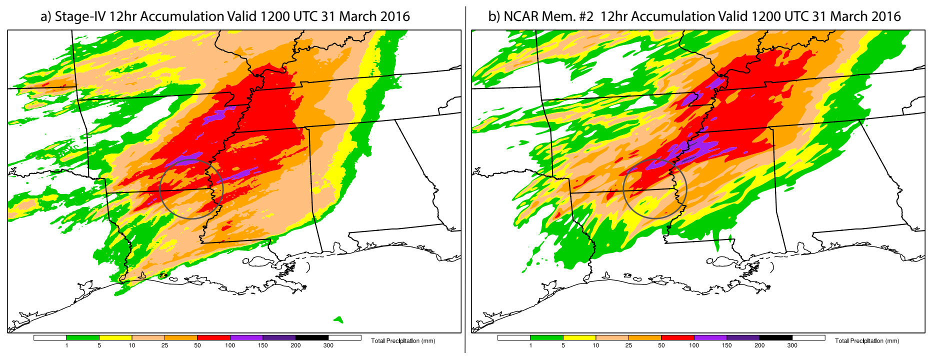

FIG. 2.11. 12-hr precipitation totals valid 1200 UTC 31 March 2016 for the Telmin TORFF event from the Stage-IV precipitation analysis (a) and (b) from Member 2 of the NCAR ensemble initialized 0000 UTC 31 March 2016.

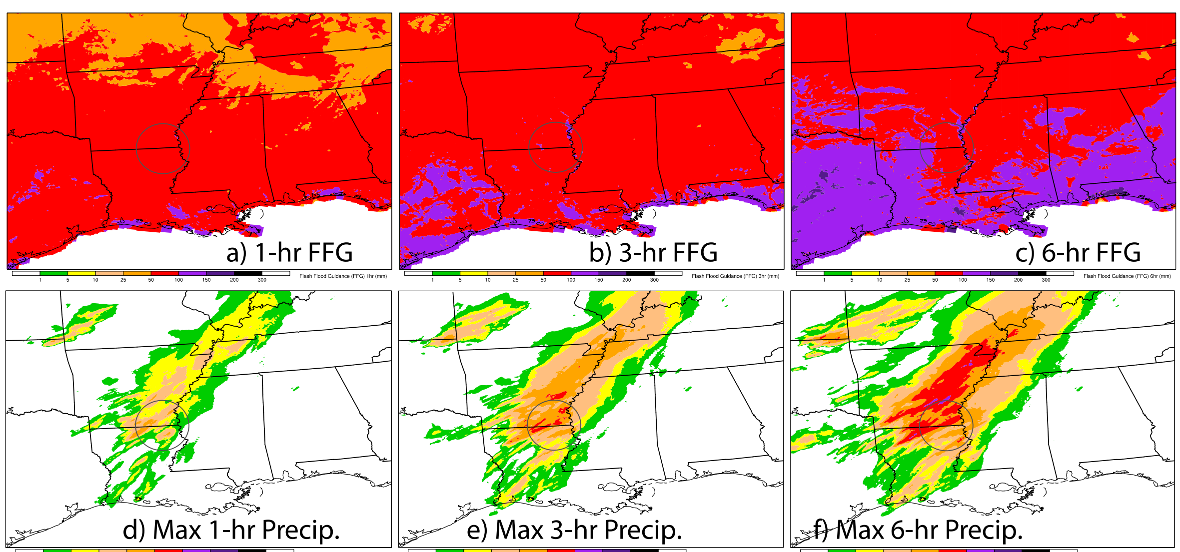

FIG. 2.12. 1-hr (a), 3-hr (b), and 6-hr (c) NWS River Forecast Center (RFC) flash flood guidance (FFG) valid 0000 UTC 31 March 2016 for the southeastern United States. Maximum (d) 1-hr, (e) 3-hr, and (f) 6-hr Stage-IV precipitation accumulation for the Telmin TORFF event valid for the 1-hr accumulation ending 0400 UTC, for the 3-hr accumulation ending 0500 UTC, and the 6-hr accumulation ending 0600 UTC 31 March 2016, respectively. Grey circle represents the approximate location of Telmin.

The event was associated with a surface cyclone (Fig. 2.13d) and slow-moving cold front that developed ahead of a digging upper-level trough centered over the Rocky Mountains (Fig. 2.13a,b). The presence of a robust subtropical jet over Texas and Mexico (Fig. 2.13a) further aided storm development by providing upper-level support for the convection. Warm, moist flow (Fig. 2.13c,d) off the Gulf of Mexico, after the passage of the warm front, provided moisture, instability, and continued warm air advection into the region. Further, due to the overall strength of the storm system, fairly strong winds were seen at all levels (Fig. 2.13a-c), especially at 850-hPa (Fig. 2.13c), which led to significant shear in the pre-storm environment. The synoptic forcing for ascent associated with the subtropical jet is clearly seen in the corresponding q-vector field (Fig. 2.14). The axis of main synoptic forcing coincides well with the location of convective initiation and storm systems' propagation for the event. Convection initiated along the Oklahoma-Arkansas-Texas border near 1500 UTC 30 March 2016 (Fig. 2.14a).

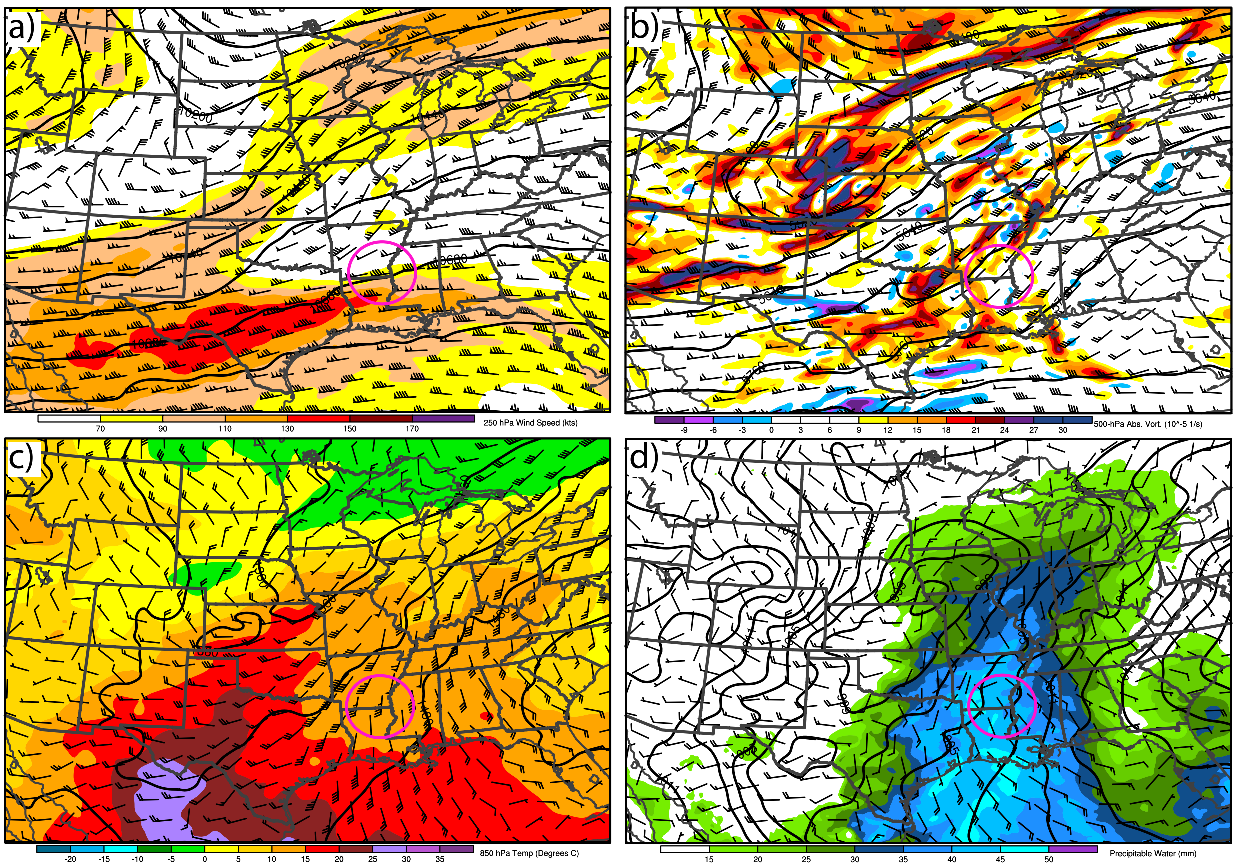

FIG. 2.13. (a)–(d) Rapid Refresh (RAP; Benjamin et al. 2016) analysis valid at 0000 UTC 31 March 2016. (a) 250-hPa isotachs (shaded every 20 kt over 70 kt, 1 kt = 0.5144 m s^{-1}), 250-hPa geopotential height (contoured every 120 m), and 250-hPa wind barbs (half barb = 5 kt, full barb = 10kt, pennant = 50 kt,). (b) Absolute vorticity at 500-hPa ($\times 10^{-5} s^{-1}$), shaded every $3\times 10^{-5} s^{-1}$ above $9\times 10^{-5} s^{-1}$; 500-hPa geopotential height (contoured every 60m); and 500-hPa wind barbs. (c) 850-hPa geopotential height (contoured every 25 m), 850-hPa wind barbs, and 850-hPa temperature (shaded every 5°C from -20°C to 35°C). (d) precipitable water (shaded contours every 5 mm for values from 10 mm to 50 mm), 10 m wind barbs, and mean sea level pressure (MSLP) (contoured every 3 hPa). Pink circle denotes area of interest around Telmin.

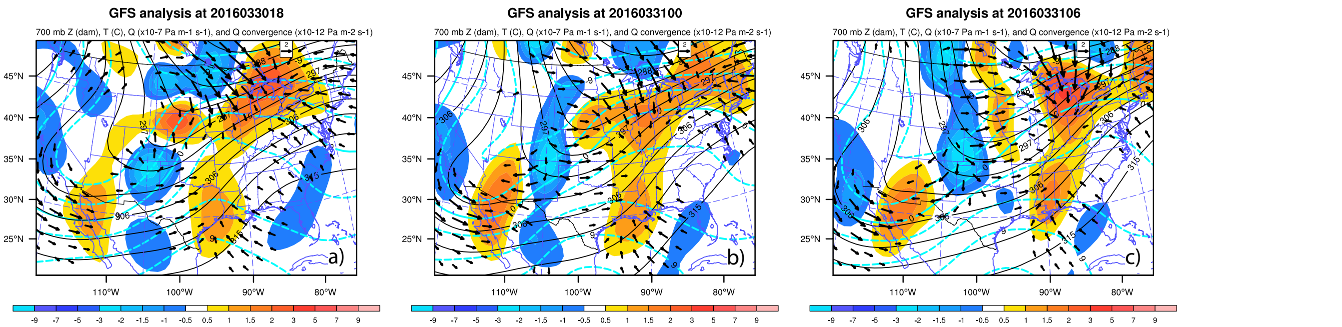

FIG. 2.14. 700-hPa height (dam; black contours), 700-hPa temperature (C; cyan dash contours), Q-vectors ($\times 10^{-7}$ Pa m^{-1} s^{-1}, black vectors with scale in top right corner of plot), and Q-vector convergence (filled contours, $\times 10^{-12}$ Pa m^{-2} s^{-1}) from the GFS analysis valid at (a) 1800 UTC 30 March 2016, (b) 0000 UTC, and (c) 0600 UTC on 31 March 2016.

The system continued to grow upscale and by 2300 UTC the same day began to resemble a typical QLCS (not shown), stretching from the Illinois-Missouri border to Central Louisiana (Fig. 2.14b). By 0700 UTC the bulk of the convection was located over central Mississippi, with the strongest convection being located along the latitude of the Arkansas-Louisiana border associated with the strongest synoptic forcing for ascent (Fig. 2.14c).

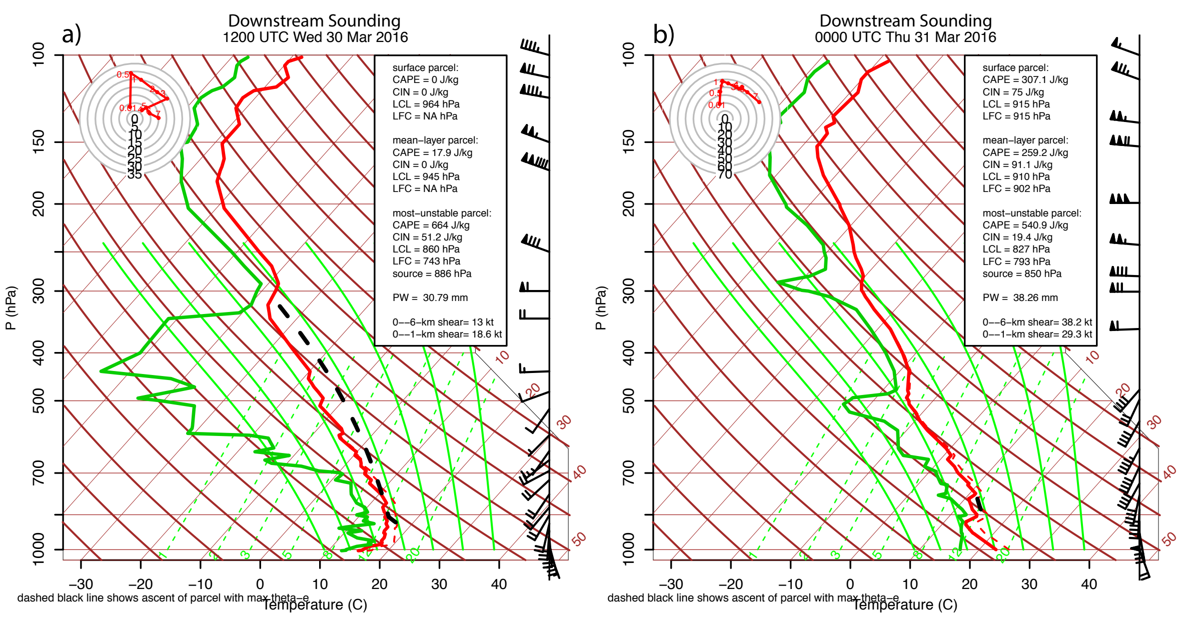

FIG. 2.15. Observed soundings downstream of Telmin valid (a) 1200 UTC 30 March 2016 and (b) 0000 UTC 31 March 2016. Red line in each panel represents the temperature profile, green line dewpoint profile, dashed red line temperature profile with virtual temperature correction, and dash black line shows ascent path of parcel with highest θ_e. Hodograph in upper left corner of each plot is in kt.

Observed downstream thermodynamic profiles leading up to the event, show the increase in mid-to-lower level moisture seen in the warm sector the 12-hours leading up to the event (Fig. 2.15). Additionally, the soundings show a corresponding increase in the depth and intensity of the southerly flow off the Gulf of Mexico over the same period (Fig. 2.15). Given sounding site's location downstream of Telmin, the instability profiles of the observed soundings are likely not as representative of points west because of differences in the event timing that leads to the soundings being more out of phase with the upper-level system (i.e., by 0000 UTC 31 March 2016 the synoptic forcing was just reaching the downstream sounding site Fig. 2.14b).

Given the issues surrounding the operational upper-air network for this event, a convection-allowing simulation of the event was examined to get a more thorough three-dimensional view of the event. Initial and boundary condition files from Member 2 of the NCAR Ensemble (Schwartz et al. 2015) initialized at 0000 UTC 31 March 2016 were obtained and used to re-created the simulation, as the operational run captured the timing, intensity, and the evolution of the convection. Additionally, the precipitation accumulation over the event was quite representative as well (cf. Figs. 2.11a and 2.11b).

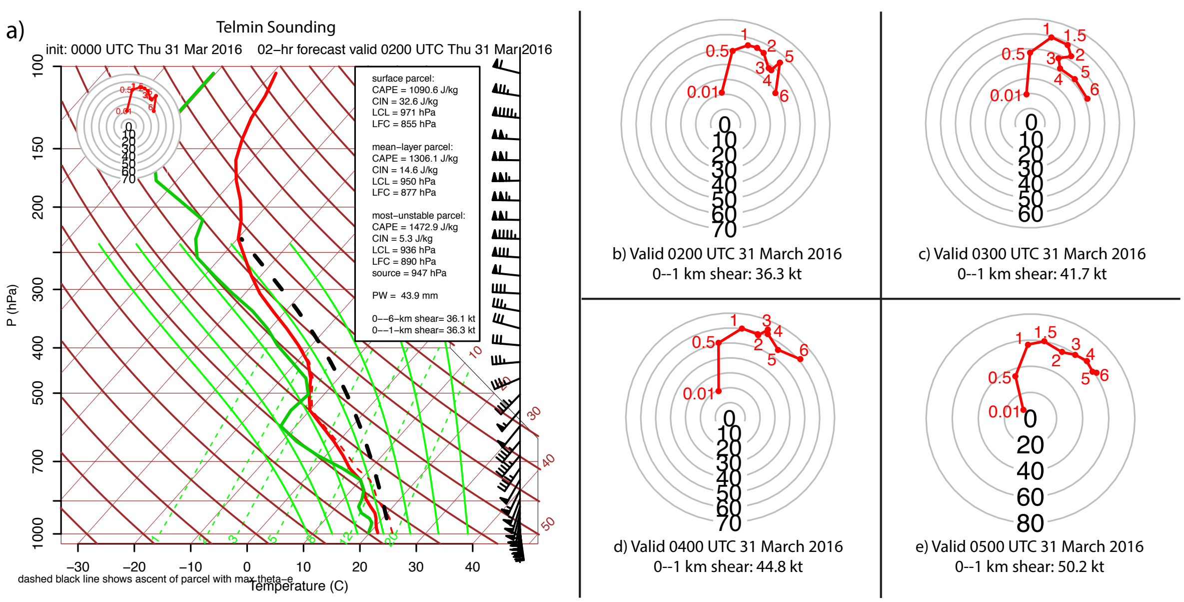

FIG. 2.16. (a) as in Fig 2.15 but for a model sounding for Telmin valid 0200 UTC 31 March 2016 from Member 2 of the NCAR Ensemble initialized at 0000 UTC 31 March 2016. (b)-(e) hodographs in kt valid at (b) 0200 UTC, (c) 0300 UTC, (d) 0400 UTC, and (e) 0500 UTC from the same location and model run as (a). Note that the hodographs in (b)-(e) are not on the same scale.

Thermodynamic profiles from Member 2 of the NCAR ensemble from Telmin, just prior to convection impinging upon the city, show moderate, elevated instability (1300 J kg^{-1}) in a flash flood type profile (Fig. 2.16a Davis 2001; Schumacher and Johnson 2009; Schroeder et al. 2016). While slight inhibition does exist for both the surface and most unstable parcels (Fig. 2.16a), it does not prohibit the formation of storms, given the intense upper-level forcing. Pre-convective soundings show significant 0–1 km shear (Fig. 2.16a) with values well over 30 kt. Additionally, the 0–1 km layer contains the majority of the shear in the 0–6 km layer as well (Fig. 2.16a). The 0–1km low-level shear greatly intensifies over the period increasing from 36.3 kt at 0200 UTC to 50.2 kt at 0500 UTC (Fig. 2.16b-e). Further, as the axis of the upper-level system approaches, a corresponding increase in wind speed is seen throughout the column. This, combined with the strengthening of the winds at lower-levels, yields increasingly favorable hodographs for rotation (Fig. 2.16b-e).

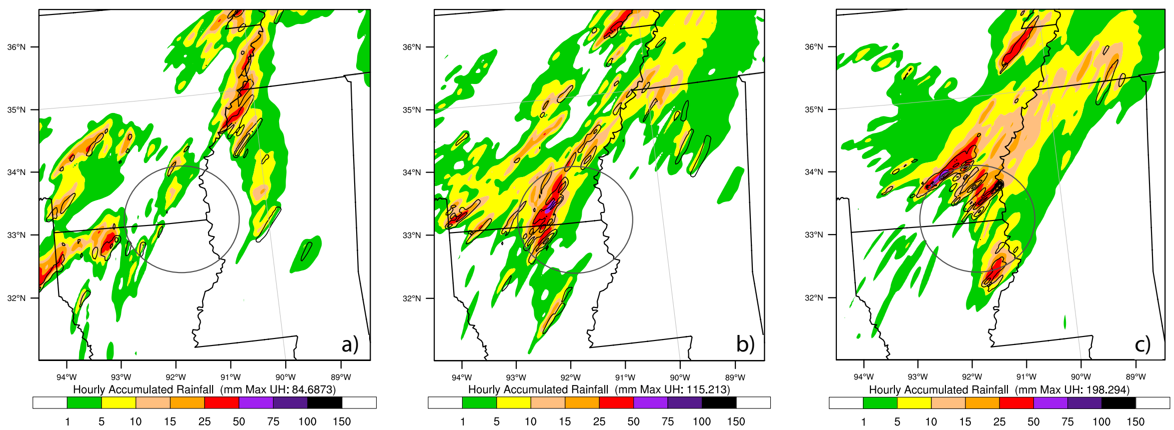

FIG. 2.17. Hourly precipitation accumulation (fill) and maximum updraft helicity (UH) contoured every 20 m^2 s^{-2} valid (a) 0200 UTC, (b) 0400 UTC, and (c) 0600 UTC 31 March 2016 from Member 2 of the NCAR ensemble. Grey circle represents the approximate location of Telmin.

While short-lived rotating elements were seen both in observations and the above model simulation in the hours before the TORFF event, the areal coverage, intensity, and longevity of the embedded rotating elements increased with the increasing 0–1 km shear values. This is well illustrated by Member 2 of the NCAR ensemble simulation where the increase in areal coverage of rotating elements and values of updraft helicity increase with increasing 0–1 km shear (Fig. 2.17). Additionally, hourly precipitation accumulations produced by the model increased to over 50 mm as the strength of the embedded rotation increased and were almost exactly collocated in space with the strongest rotating elements (Fig. 2.17b-c). Given this collocation of rotating convective elements with the most intense sustained hourly rain rates in Member 2 of the NCAR ensemble, the interaction between the rotation and the precipitation processes in such TORFF events can likely not be treated as independent.

2.3.3 05 April 2017 TORFF Event

A strong upper-level system moved through the VORTEX-SE domain on 5 April 2017 (Fig. 2.18a) leading to enhancement of total-column moisture (Fig. 2.18c), synoptic-scale forcing for ascent (Fig. 2.18a-b), environmental shear (Fig. 2.18a-c), and the development of a strong surface cyclone (Fig. 2.18c).

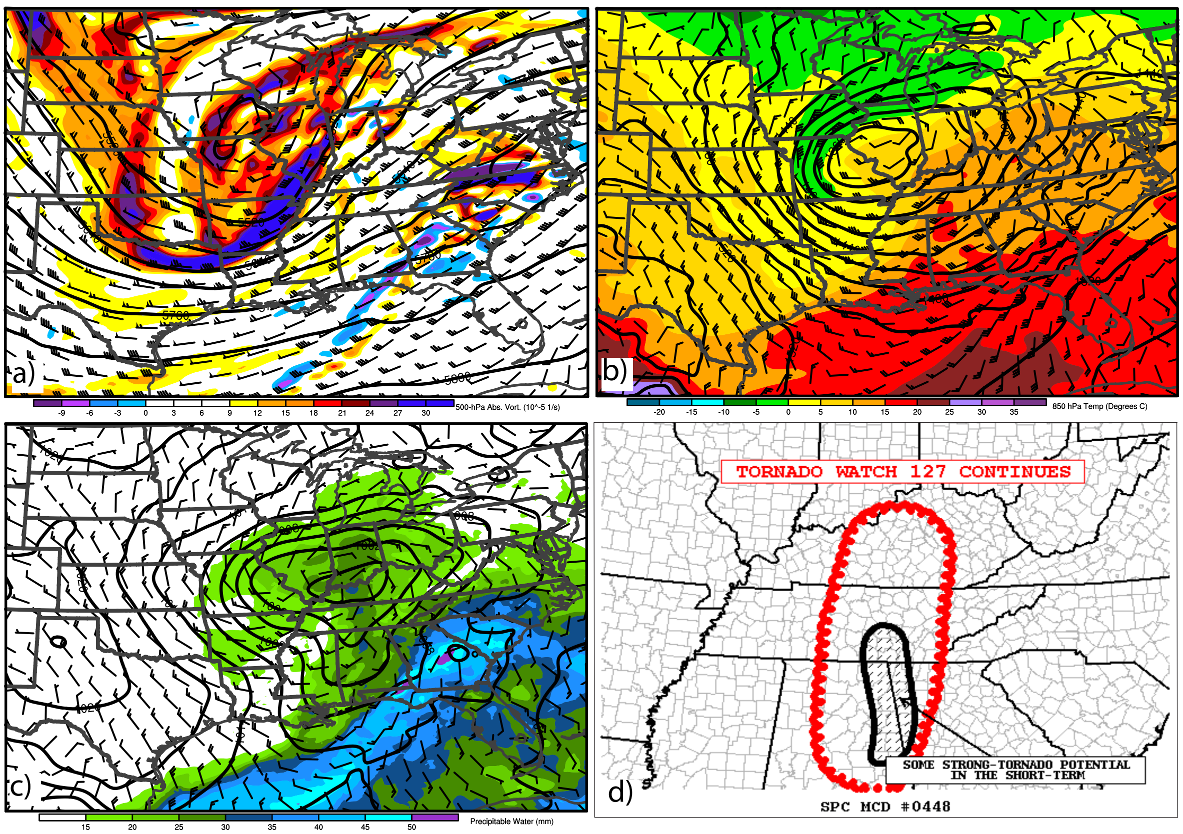

FIG. 2.18. (a)–(c) RAP analysis valid 2000 UTC 05 April 2017. (a) Absolute vorticity at 500-hPa ($\times 10^{-5}$s^{-1}), shaded every 3×10^{-5}s^{-1} above 9×10^{-5}s^{-1}; 500-hPa geopotential height (contoured every 60m); and 500-hPa wind barbs (half barb = 5 kt, full barb = 10kt, pennant = 50 kt,). (b) 850-hPa geopotential height (contoured every 25 m), 850-hPa wind barbs, and 850-hPa temperature (shaded every 5°C from -20°C to 35°C). (c) precipitable water (shaded contours every 5 mm for values from 10 mm to 50 mm), 10 m wind barbs, and mean sea level pressure (MSLP) (contoured every 3 hPa). (d) Graphic from SPC Mesoscale Discussion 448 valid 2051 UTC to 2215 UTC 5 April 2017.

Given the forecast timing and ingredients for convection, the Storm Prediction Center (SPC) issued a moderate risk in their 1630 UTC convective outlook (Fig. 2.19a) over the far eastern side of the VORTEX-SE domain that corresponded to a 15% significant probabilistic tornado forecast (Fig. 2.19b). The tornado threat, specifically, in the eastern portion of the VORTEX-SE domain was highlighted in several

SPC mesoscale discussions on that day (Fig. 2.18d). A SPC high risk was present farther east in central Georgia and South Carolina (Fig. 2.19a) that corresponded to a 30% contour in the tornado probabilities (Fig. 2.19b). Additionally, the region was highlighted as having a 5-10% of exceeding flash flood guidance in the Weather Prediction Center (WPC) excessive rainfall outlook (Fig. 2.19c). As the ingredients for flash flooding and tornadoes were forecast to exist in the same place at the same time, the event was of particular interest as it as it was forecasted to be associated with TORFF hazards.

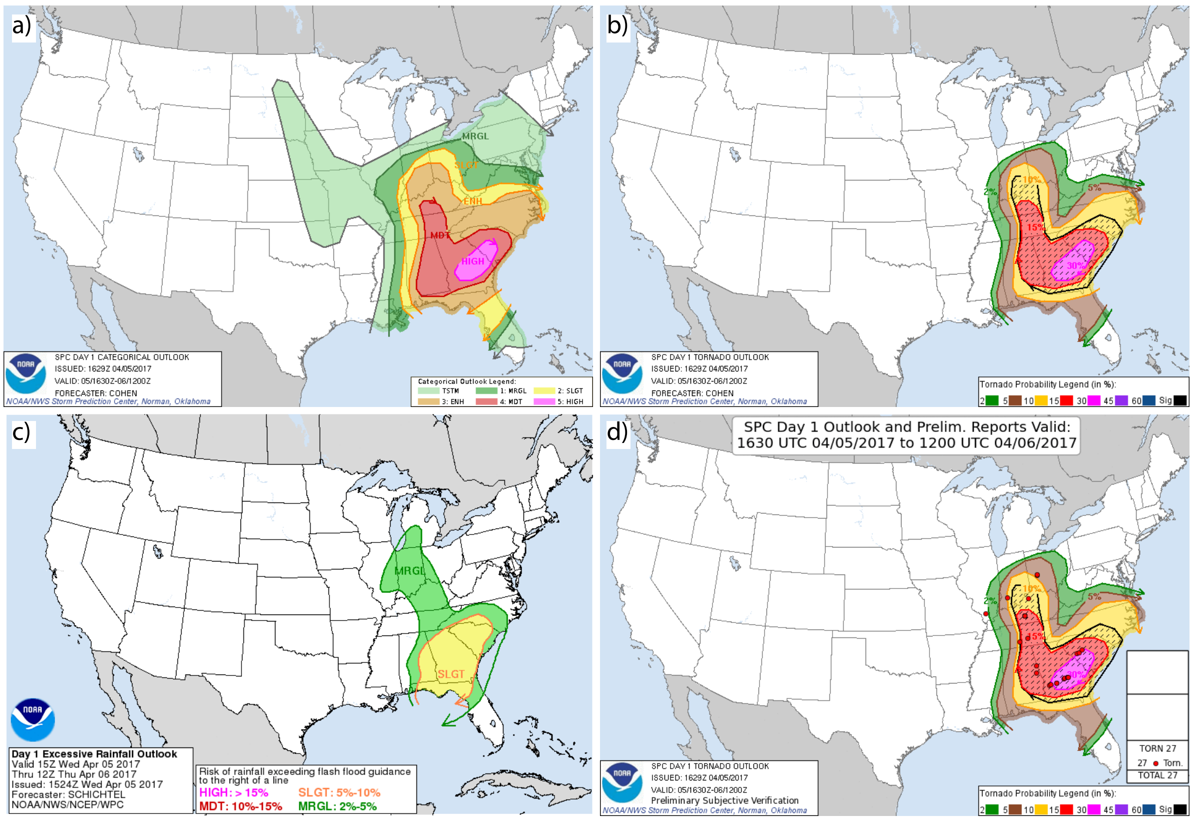

FIG. 2.19. (a) Storm Prediction Center (SPC) categorical Day 1 Convective Outlook valid 20170405 at 1630 UTC, (b) corresponding probabilistic tornado outlook, and (c) Weather Prediction Center (WPC) excessive rainfall outlook valid 1500 UTC the same day. (d) Preliminary verification of SPC probabilistic tornado outlook (i.e., (b)) where red dots represent tornado reports.

Given the potential for a high-impact tornado event, special operational soundings were ordered throughout the southeast during the mid-afternoon hours on 5 April 2017 (Fig. 2.20).

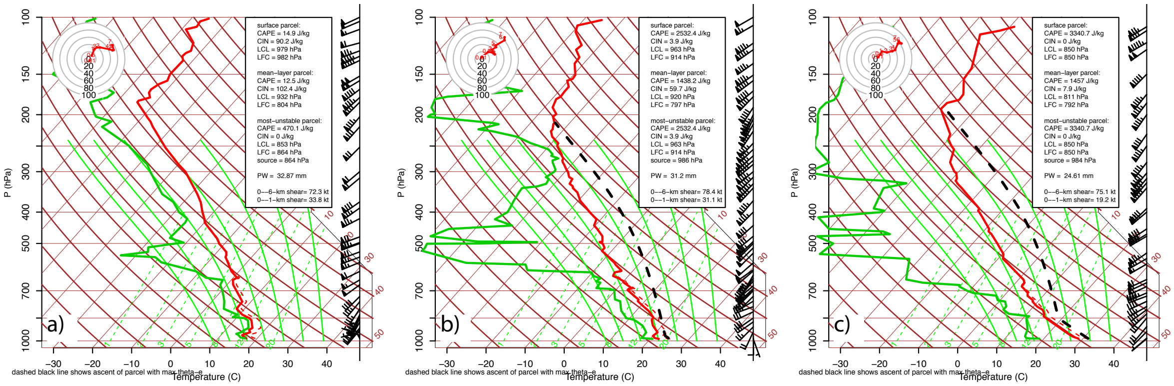

FIG. 2.20. Observed soundings from Birmingham, AL (BMX) valid (a) 1800 UTC and (b) 2100 UTC 5 April 2017. (c) observed sounding from Peachtree City, GA (FFC) valid 1800 UTC 5 April 2017.

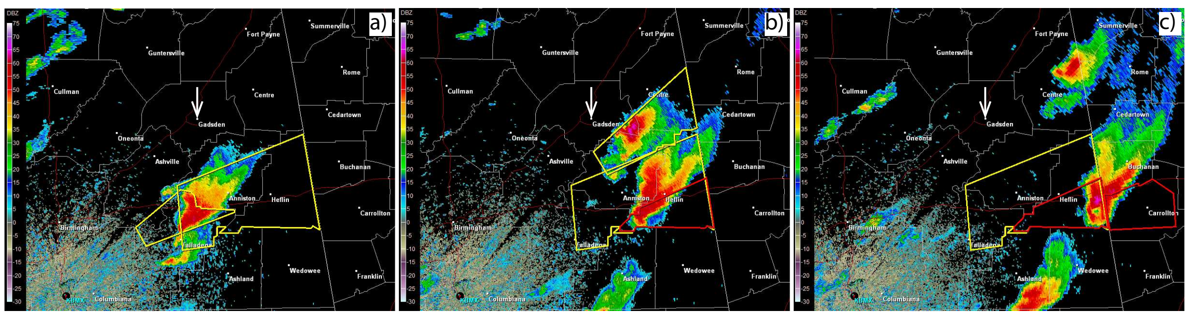

FIG. 2.21. Radar images of reflectivity and valid warnings (red and yellow for tornado and severe thunderstorm warnings, respectively) from the Birmingham, AL radar (KBMX) valid 2045 UTC (a), 2115 UTC (b), amd 2145 UTC (c) 5 April 2017 showing the location of the pre-storm environment and supercell storm samples by the CSU sounding team,who were located in Gadsden, AL (denoted by white arrow) from 1000 UTC to 2300 UTC that same day.

Additional soundings were taken throughout the morning and afternoon by Colorado State University (CSU) from Gadsden, Alabama (Fig. 2.21a) as part of the VORTEX-SE field project (Schumacher and Nielsen 2018). An early-morning MCS moved through northern Alabama and Georgia between 1000 and 1800 UTC, prior to the main frontal forcing. The post-convective environment was sampled by the 1800 UTC special sounding from Birmingham, Alabama (Fig. 2.20a) and the 1715 UTC CSU radiosonde from Gadsden, Alabama (Fig. 2.22a). The resulting profile in both soundings shows instability for elevated parcels and relatively moist low levels. Significant environmental shear both in the 0–1 km and 0–6 km layers was present in the region (Figs. 2.20a and 2.22a), with 0–6 km shear over 75 kt at 1800 UTC downstream in Georgia (Fig. 2.20c). As the afternoon progressed, the additional surface heating led to an rapid increase in surface-based CAPE in Alabama at both locations (Figs. 2.20b and 2.22b-c), where values increasing to above 3000 J kg^{-1} with little to no inhibition. Similar CAPE values were already present by 1800 UTC in Georgia (Fig. 2.20c). As the main upper-level system approached, the observed kinematic profiles continued to contain more low-level and mid-level shear. Shear values increased in the CSU soundings from 26 kt to 34 kt in the 0–1 km layer and from 70 kt to 91 kt in the 0–6 km layer between 1715 UTC and 2100 UTC (Fig. 2.22a-c).

Discrete supercells began to initiate ahead of the surface front in central Alabama at 2000 UTC 5 April 2017 and began to move into Georgia by 2100 UTC (not shown). Additionally, with the increase in shear, tornadic storms were observed in the southern portions of the still ongoing MCS from that morning over southern Georgia.

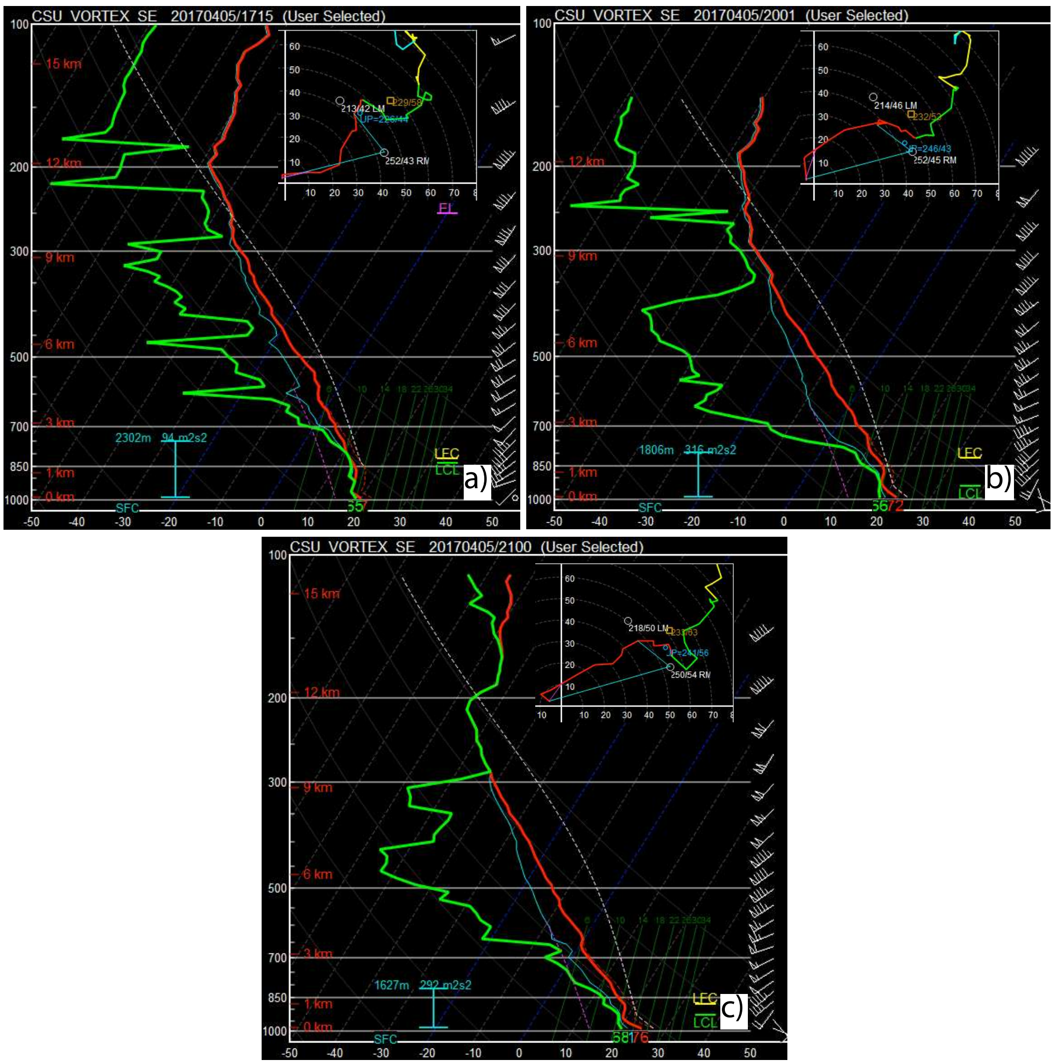

FIG. 2.22. Observed soundings launched by Colorado State University (Schumacher and Nielsen 2018) from Gadsden, AL valid at (a) 1715 UTC, (b) 2001 UTC, and (c) 2100 UTC on 5 April 2017.

By 0100 UTC 6 April 2017, convection had become linearly organized in a very narrow band along the front, which dramatically lessened the tornado potential by 0200 UTC.

Overall, the event produced 27 tornado reports (Fig. 2.19d), including a few longer track tornadoes (red lines in Fig. 2.23). Additionally, several flash flood reports throughout the region (IEM 2017), mostly clustered around major population centers (green dots in Fig. 2.23). This event was in fact verified as a TORFF event at all spatial buffer radii as part of the results presented in Section 2.3.1. This can be seen in Fig. 2.23a by the presence of a tornado track within the 10 km spatial buffer placed around a flash flood LSR near Peach Tree City, Georgia, with further intersections seen at the 50 km radius in Fig. 2.23b. While the SPC tornado probabilities successfully encompassed all but one tornado report (Fig. 2.19d), relatively few reports, compared to other high risk days, were seen in the region of maximum probabilities. This negative bias in the reliability of SPC tornado probabilities has been seen in previous verification research as well (e.g., Herman et al. 2018). Additionally, only two tornado reports were seen near the VORTEX-SE domain, in the region highlighted by SPC mesoscale discussion 448 (Fig. 2.18d), despite being encompassed by the 15% tornado probability contour. There was little to no storm development seen at the CSU sounding location, with weak radar returns and some towering cumulus observed. However, just to the south of Gadsden, AL, along the Alabama-Georgia border, splitting supercells (Fig. 2.21a-c) were observed, with the right mover producing several tornado reports (Fig. 2.19d).

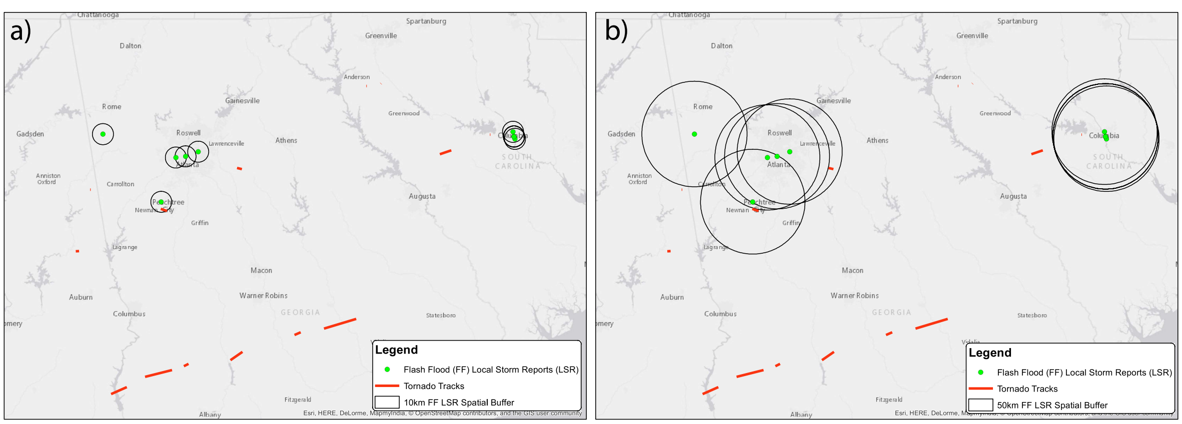

FIG. 2.23. Flash flood local storm reports (green dots), official tornado tracks from SPC (red lines), and spatial buffers (black circles) at 10 km (a) and 50 km (b) radii used in the TORFF verification presented in Section 2.3.1 for the 05 April 2017 TORFF event.

A time-height analysis based upon the observed CSU soundings shows rapid drying at midlevels as the afternoon progressed (Fig. 2.24a). This is illustrated well in both the extra operational soundings (Fig. 2.20) and the individual soundings taken from CSU that are used in the time-height analysis (Fig. 2.22). The mid-level drying also coincided with the aforementioned increase in shear throughout the column (cf. Fig. 2.24a-b). The lack of severe convection in the VORTEX-SE domain seems to have been associated with the increasing mid-level dryness and intense shear values that caused the developing updrafts to entrain dry, environmental air. The storms struggled during their development stages to overcome this entrainment, which in turn limited the storms ability to survive long enough to utilize the available instability in the region, despite the intensely rotating updrafts that were present at various points during the event. Local mesoscale differences in moisture and shear, resulting from the morning's MCS, likely enabled some storms to reach maturity and become tornadic despite the somewhat hostile environment.

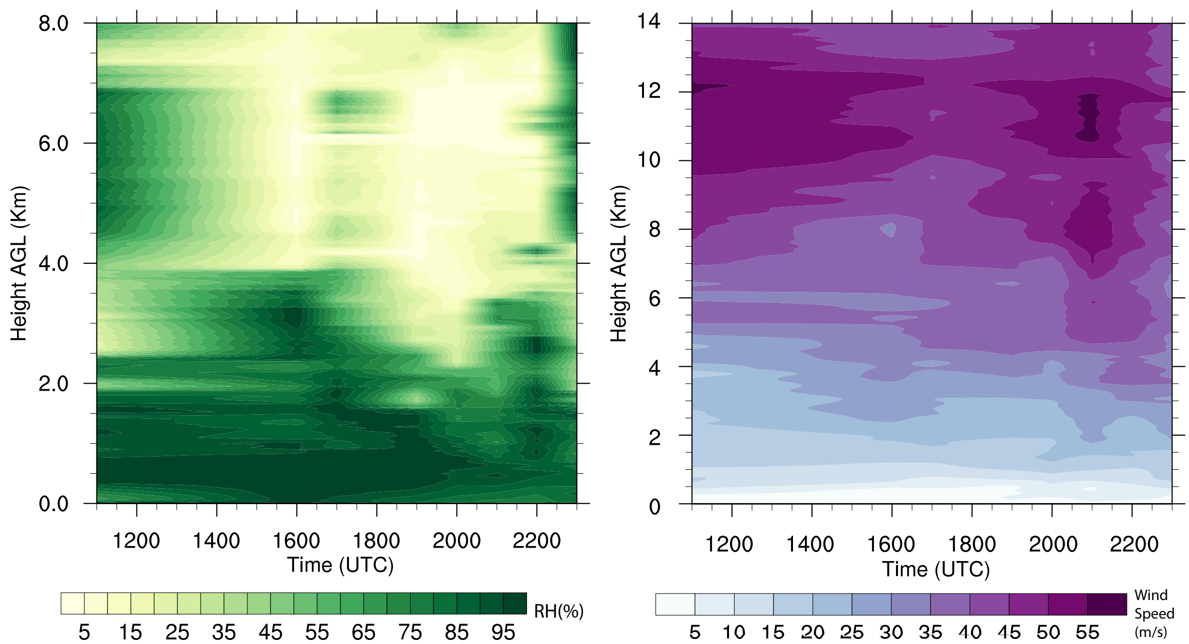

FIG. 2.24. Time vs. height plots of (a) relative humidity (RH) and (b) wind speed created from 8 soundings taken by Colorado State University (Schumacher and Nielsen 2018) in Gadsden, AL. Soundings used in the interpolation were taken at 1055 UTC, 1400 UTC, 1600 UTC, 1715 UTC, 1900 UTC, 2001 UTC, 2200 UTC, and 2302 UTC on 5 April 2017 in support of IOP-3B.

2.4 DISCUSSION AND CONCLUSIONS

The updated TORFF climatology Fig. 2.3 presents a similar geographic distribution of events to that already established in Nielsen et al. (2015) and further established TORFF events as relatively common meteorological events (Fig 2.4 and Table 2.1). The inclusion of a spatial buffer between the tornado and flash flood reports used to verify the events established a yearly frequency of TORFF events between approximately 25 and 75 per year (Table 2.1), depending on the buffer used. These numbers are a substantial increase over those presented originally in Nielsen et al. (2015). Furthermore, given that ~30% of "verified" TORFF events presented in this study were associated with at least some nocturnal tornadoes (i.e., BOTH or LATE events, Table 2.2), the already complex warning communication challenges normally associated with TORFF events (i.e., the contradicting life-saving action of the primary threats) are, in some cases, increased by the additional complexity of nocturnal tornadoes (e.g., Ashley et al. 2008). The known nuanced nature of threat communication and personalization in high-impact, multi-threat events (e.g., Demuth et al. 2018) combine with the multitude of aforementioned communication complexities in TORFF events continue to point for the need for further research to improve forecasting and communication practices in TORFF events and other multi-hazard events.

The geographic distribution of EARLY TORFF events is somewhat expected given what is know about the diurnal progression of upscale storm growth in the central (e.g., Carbone et al. 2002; Trier et al. 2010) and eastern (e.g., Parker and Ahijevych 2007) U.S., combine with the propensity for discrete cells to produce tornadoes (e.g., Smith et al. 2012) during the late afternoon to early evening time period. Interestingly, at all spatial buffer radii, LATE events are responsible for a larger percentage of total TORFF events than BOTH events (Table 2.2). The prevalence of LATE events over BOTH events was not expected *a priori* by the author, and could possibility have something to do with the classification criteria. However, the timing of the LATE events (i.e., entirely nocturnal) points to a scenario, in order to maintain tornado potential, where surface based convection is either initiated or maintained through the ET. Previous research (e.g., Nowotarski et al. 2011; Coffer and Parker 2015) has shown how surface based convection can be maintained and even enhanced in situations of nocturnal stabilization by the enhancement of dynamic pressure accelerations associated with increases in low-level rotation and low-level wind shear. These same dynamic effects have also been shown in Nielsen and Schumacher (2018) to increase precipitation by enhancing the low-level updrafts and lifting of otherwise negatively buoyant parcels that contain moisture and CAPE. Thus, the interaction and feedback between the low-level shear, resulting rotation, and induced dynamical accelerations with the environmental moisture profiles is important in the development and evolution of TORFF events, especially LATE (and to a point BOTH) events.

The Telmin TORFF event discussed in Section 2.3.2. serves as a potential real-time example of how the dynamic accelerations associated with the relationship between 0–1 km shear and rotation can also enhance the resulting precipitation. The increase in areal coverage and intensity of rotation in the Telmin TORFF with the increase in shear is not surprising given the known influence of 0–1 km shear/helicity on tornado potential in both discrete (e.g., Craven et al. 2004) and embedded (e.g., Weisman and Trapp 2003) storm modes. However, given the nocturnal nature of this event, the increase in 0–1 km shear and the associated increase in rotationally induced dynamic low-level forcing for ascent were likely essential in maintaining surface-based convection in a stabilizing nocturnal environment (e.g., Coffer and Parker 2015). This, in turn, can serve to lower the base of the updraft and increase the tornado potential for a particular convective element (e.g., Markowski and Richardson 2014). In the NCAR ensemble simulation for the Telmin case, the highest hourly rainfall rates were also associated with the regions of most intense rotation (Fig. 2.17). Additionally, the modeled hourly accumulations increased as the strength of the rotation increased, with hourly accumulations over 50 mm located coincident with the most intensely rotating features (Fig. 2.17b-c). This suggests that the rotating updrafts are able to produce more intense precipitation than other, non-rotating convective elements. The rotationally induced dynamic low-level forcing for ascent associated with the maintenance of surface based convection/tornado potential, provides an explanation for this precipitation enhancement, as it enhances low-level updrafts and allows storms to tap into inhibited parcels that still contain moisture and CAPE (e.g., Nielsen and Schumacher 2018). While the environment is clearly conducive for intense rainfall (e.g., sustained moisture source and strongly synoptically forced), Member 2 of the NCAR ensemble provides evidence that the rotation associated with the Telmin TORFF event, itself, could have enhanced the precipitation accumulations seen in the region.

In conclusion, the addition of a spatial buffer between the tornado tracks and flash flood LSRs in the TORFF verification produced a substantial increase in number of "verified" TORFFs across the United States. While the spatial distribution is similar to that seen in Nielsen et al. (2015), ∼30% of the events have a nocturnal component to them, which increases the communication challenges associated with the events. Two TORFF events sampled as part of the VORTEX-SE field experiment illustrate the importance and potential sensitivity of 0–1 km shear in the development and evolution of the TORFF events. Specifically, through complex interactions between the environmental moisture profile, shear, induced rotation, and resulting dynamical accelerations can serve to enhance both the tornado and precipitation potential of a particular event.

CHAPTER 3

Dynamical Insights into Extreme Short-Term Precipitation Associated with Supercells and Mesovortices[1]

3.1 Introduction

Throughout the United States, flash flooding continues to threaten life and property, despite increased awareness and forecasting advances (e.g., Ashley and Ashley 2008). Forecasting the extreme rainfall and often associated flash flooding presents many challenges because one must correctly predict both the occurrence and magnitude of extreme rainfall to correctly predict the occurrence and magnitude (i.e., potential impacts) of the flash flooding (e.g., Doswell et al. 1996). The accurate numerical prediction[2] and nowcasting[3] of rainfall accumulations remain a continued challenge in the meteorological community (e.g., Fritsch and Carbone 2004; Novak et al. 2011; Zhang et al. 2016; Herman and Schumacher 2018a).

At the most basic level, extreme precipitation accumulations over some area is required before flash flooding can occur. For large rainfall accumulations to occur, high rain rates must persist in a location for a long period of time (e.g., Chappell 1986; Doswell 1994; Doswell et al. 1996). From Doswell et al. (1996) the total precipitation at a location can be expressed simply as:

$$P = \bar{R}D \tag{3.1}$$

where $\bar{R}$ is the average rainfall rate and D is the rainfall duration. The average rainfall rate, $\bar{R}$, is often not particularly illustrative of the ingredients needed for extreme rainfall. However, the instantaneous rainfall rate, R, can be broken down into separate illustrative elements. R can be expressed as:

$$R = Ewq \tag{3.2}$$

where E is the precipitation efficiency, q is the water vapor mixing ratio of the rising air, and w is the ascent rate. The precipitation efficiency, E, is a proportionality constant relating rainfall rate to water vapor flux (see appendix of Doswell et al. 1996). As shown by Eqn. 1, high precipitation accumulations

[1]This chapter has been published by the American Meteorological Society in *Journal of the Atmospheric Sciences*: Nielsen, E. R. and R.S. Schumacher, 2018: Dynamical Insights into Extreme Short-Term Precipitation Associated with Supercells and Mesovortices. *J. Atmos. Sci.*, **75 (9)**, 2983–3009. doi: 10.1175/JAS-D-17-0385.1. ©2018 American Meteorological Society. Used with permission.

[2]Known as quantitative precipitation forecasting (QPF).

[3]Known as quantitative precipitation estimation (QPE), which is the real-time estimation of rainfall accumulations using rain gauge observations combined with remote sensing techniques (e.g., Zhang et al. 2016).

could also be the result of slow moving convective systems or "echo training" (i.e., maximizing the duration, D, in Eqn. 1). Quasi-stationary or back building mesoscale convective systems such as these can be especially prevalent flash flood producers (e.g., Bluestein and Jain 1985; Chappell 1986; Doswell et al. 1996; Schumacher and Johnson 2005); however, the foremost focus of this research will not be on storm motion or propagation, but rather dynamical accelerations, specifically related to the presence of rotation, within the storms that could lead to high rainfall rates. Doswell et al. (1996) theorized that intense nonbuoyant accelerations, which are a substantial source for positive vertical momentum in supercells (e.g., Rotunno and Klemp 1982; Weisman and Klemp 1984), and the resulting intense updrafts (i.e., w, in Eqn. 2) create an increased potential for intense rainfall rates that is otherwise lessened (all else being equal) without the presence of rotation.

Within the general classifications of extreme rainfall producing storms, it has often been observed that precipitation is associated with mesoscale vortices on various scales, including supercells (e.g., Moller et al. 1994; Smith et al. 2001; Hitchens and Brooks 2013; Schumacher 2015a) and larger mesoscale structures, such as mesoscale convective vortices (MCVs) (e.g., Bosart and Sanders 1981; Fritsch et al. 1994; Trier et al. 2000b; Schumacher and Johnson 2009; Morales et al. 2015; Nielsen et al. 2016b). Further, from a broader impacts point of view, the presence of tornadoes (i.e., from rotation) and flash flooding (i.e., from extreme rainfall) in the same place at the same time presents a dangerous situation where life saving actions are contradictory (TORFF events; Nielsen et al. 2015, 2016a; Bunkers and Doswell 2016). Additionally, tropical cyclones can possess environmental characteristics conducive for the development of mesoscale rotation and supercells, especially within attendant rainbands (i.e., high low-level shear; McCaul and Weisman 2001; Baker et al. 2009; Morin and Parker 2011; Edwards et al. 2012; Wang et al. 2015). The presence of rotation and flooding in these high impact weather events further motivates the need to investigate any possible relationship between the dynamics of rotation and extreme rainfall production.

Supercells were once thought not to produce extreme rainfall/rain rates, due to low precipitation efficiency, E in Eqn. 2, associated with large values of convective available potential energy (CAPE), shear, and hail production (e.g., Marwitz 1972; Foote and Fankhauser 1973; Browning 1977). However, recent studies (Smith et al. 2001; Duda and Gallus 2010; Hitchens and Brooks 2013) have shown that supercells have been responsible for extreme rainfall events, even noted world record accumulations (Dalrymple 1937), and might be underrepresented causes of flash floods. A specific subclass of supercells, known as high precipitation (HP) supercells (e.g., Moller et al. 1994), are known to produce more precipitation than other supercell storms. HP supercells produce the greatest threat of flash flooding, among all the supercell archetypes, with multiple flash flood events caused by such storms (e.g., Moller et al. 1994; Smith et al. 2001; Bunkers and Doswell 2016). The high rain rates in HP supercells has been attributed to the ability of an intense and/or spatially large updraft to ingest significant amounts of water vapor (e.g., Smith et al. 2001; Beatty et al. 2008), which fits into the rotational enhancement framework discussed in Doswell et al. (1996).

Specifically, the observed extreme rain rates seen in supercells, despite low precipitation efficiency, can possibly be explained by noting that supercells have an additional positive source of vertical momentum (i.e., w in Eqn. 2) from the non-linear dynamic vertical perturbation pressure gradient force associated with the mesocyclone (e.g., Weisman and Klemp 1984; Doswell et al. 1996). The illustration of the effects that rotation has on vertical pressure gradients can be found in the mathematical decomposition of the vertical perturbation pressure, $p^{'}$, gradient force (VPPGF) into buoyant (i.e., $p^{'}_{B}$), dynamic linear (i.e., $p^{'}_{DL}$), and dynamic non-linear (i.e., $p^{'}_{DNL}$) components (e.g., Rotunno and Klemp 1982; Klemp 1987; Markowski and Richardson 2010). For the sake of brevity, the full decomposition will not be undertaken here. However, the resulting expanded vertical momentum equation following this decomposition, excluding the Coriolis force, can be expressed as:

$$\frac{\partial w}{\partial t} = \underbrace{\vec{v}\cdot\nabla_h w}_{\text{Advection}} \underbrace{- \frac{1}{\rho_0}\frac{\partial p^{'}_{B}}{\partial z} \underbrace{-g\frac{\rho^{'}}{\rho_0}}_{\text{Buoyancy (B)}} - \underbrace{g q_h}_{\text{Drag}}}_{\text{Total Buoyant Acc. (ACCB)}} \underbrace{- \underbrace{\frac{1}{\rho_0}\frac{\partial p^{'}_{DL}}{\partial z}}_{\text{Linear Dynamic Acc.}} - \underbrace{\frac{1}{\rho_0}\frac{\partial p^{'}_{DNL}}{\partial z}}_{\text{Nonlinear Dynamic Acc. (NLD-VPPGF)}}}_{\text{Total Dynamic Acc. (ACCD)}} \tag{3.3}$$

where the total buoyant acceleration (hereafter ACCB) is the acceleration that results from the combined effects of thermodynamically driven buoyancy, hydrometeor drag (i.e., $g q_h$, where q_h is the total hydrometeor mixing ratio), and the vertical gradient in the buoyancy pressure field. The total dynamic acceleration (hereafter ACCD) is associated with the effects of both the linear and nonlinear dynamic (hereafter NLD-VPPGF) perturbation pressure induced accelerations. In order to conceptualize what physical processes affect the individual terms of the VPPGF (i.e., $p^{'}_{DL}$, $p^{'}_{DNL}$, and $p^{'}_{B}$) a simplified, approximate decomposition of the perturbation pressure, $p^{'}$, can be written, following Markowski and Richardson (2010), for well-behaved, incompressible, storm scale flows as:

$$p' \propto \underbrace{\underbrace{e'^{2}_{ij}}_{\text{splat}} - \underbrace{\frac{1}{2}|\vec{\omega}'|^2}_{\text{spin}}}_{\text{Nonlinear Dynamic } (p^{'}_{DNL})} + \underbrace{2\vec{S}\cdot\nabla_h w'}_{\text{Linear Dynamic } (p^{'}_{DL})} - \underbrace{\frac{\partial B}{\partial z}}_{\text{Buoyant } (p^{'}_{B})} \tag{3.4}$$

where e_{ij} is the deformation tensor, $\vec{\omega}$ is the total vorticity of the perturbation wind, B is buoyancy, w is vertical motion, and $\vec{S}$ is the mean environmental wind shear vector. The nonlinear dynamic pressure perturbation (i.e., $p^{\prime}_{DNL}$) is made up of the "splat" and "spin" terms, which produce opposite signed pressure perturbations (Eqn. 4). The "spin" term implies that strong rotation around any axis in any direction is associated with a negative pressure perturbation. However, rotation around a vertical axis will be the focus of the research presented here. This negative pressure perturbation can act to dynamically enhance or retard the strength of the updraft (i.e., w), depending on the vertical distribution of the rotation[4]. The influence of rotation and the induced pressure perturbation highlights the physical mechanism by which rotation could potentially enhance rain rates. Although the influence of the VPPGF has been investigated in regards to supercells and tornadogenesis, little attention has been devoted to its impact on precipitation processes when supercells or embedded mesovortices are present.

On the convective scale, cells that produce the most extreme rain rates have been shown to be associated with a positive potential vorticity (PV) monopole, compared to the expected PV dipole that is seen in other convective storms (i.e., the positive PV anomaly dominates over the negative anomaly; Chagnon and Gray 2009; Weijenborg et al. 2015, 2017), which can persist even after the storm decays. This implies that the convective cells that produce the most intense rain rates have supercellular like structure (i.e., a long lived, rotating updraft) in PV space (Weijenborg et al. 2017). The positive PV monopole structure described here is, similar to what is known about MCV [5] development (see Haynes and McIntyre 1987; Raymond and Jiang 1990; Hertenstein and Schubert 1991; Trier et al. 2000a), partially influenced by the latent heat release in a convective storm's updraft and further illustrates the pathway for positive feedbacks to exists between rotation and intense precipitation (e.g., Schumacher et al. 2013; Morales et al. 2015; Nielsen and Schumacher 2016).

The positive or negative effects on a storm's updraft associated with the NLD-VPPGF can alter the depth of the layer(s) that serve as the primary energy source for buoyant ascent in updrafts. In the United States, the majority of warm season heavy rainfall flash flood events are the result of MCSs (e.g., Fritsch et al. 1986; Schumacher and Johnson 2006) and tend to occur overnight (e.g., Stevenson and Schumacher 2014; Herman and Schumacher 2016). The latter point implies the presence of a

[4]For more discussion on this, especially the latter point, see work on mesovortices embedded in squall lines by Weisman and Trapp (2003) and Trapp and Weisman (2003)

[5]It should be noted that MCVs themselves do not often possess large rotation rates compared to mesovortices or supercell mesocyclones (e.g., James and Johnson 2010), and therefore have limited sources of vertical momentum from the VPPGF.

stable nocturnal planetary boundary layer (PBL), and the presence of a nocturnal low-level jet (e.g., Bonner 1968), which is an important synoptic-to-mesoscale feature common to warm season MCSs (e.g., Parker and Johnson 2000; Moore et al. 2003; Schumacher and Johnson 2005) that can serve to enhance 0–1km shear. Surface to 1 km shear, specifically, has been found to be particularly favorable for tornado (e.g., Craven et al. 2004) and mesovortex development (e.g., Weisman and Trapp 2003; Trapp and Weisman 2003; Atkins and St. Laurent 2009). The shear is associated with environmental horizontal vorticity confined to the low levels that, through its tilting and ingestion into a developing updraft, effectively lowers the base of and strengthens the mid-level mesocyclone, (e.g., Markowski et al. 2012; Markowski and Richardson 2014; Coffer and Parker 2015), due to the development of rotation around a vertical axis and the dynamical enhancement (i.e., from the NLD-VPPGF) of the updraft. This lowering, in turn, makes it easier for the rotationally induced NLD-VPPGF to lift negatively buoyant air, especially in the case of weak cold pools, in the PBL (e.g., Nowotarski et al. 2011; Davenport and Parker 2015) that can be an additional source of moisture and instability to the storm (Schumacher 2015b). Further, this process can also serve to create a positive feedback between horizontal environmental vorticity, rotation rate, updraft strength, and magnitude of the NLD-VPPGF (Coffer and Parker 2015).

With these potential interactions in mind, it is hypothesized that the presence of moist convective meso-γ to meso-β-scale vortices associated with intense 0–1 km shear have an increased propensity to produce extreme rain rates, all else being equal, compared to other storm types. This is accomplished by first, dynamically enhancing the updraft through the non-linear dynamic component of the vertical pressure perturbation gradient acceleration, and second, with this enhancement, dynamically lift otherwise inhibited parcels that still possess moisture and instability from an otherwise stable boundary layer. Furthermore, if the presence of mesoscale rotation can serve to enhance rain rates, it perhaps could serve as a compounding physical explanation, in addition to echo training, for the occurrence and frequency of TORFF events in the United States (Nielsen et al. 2015). In this study, numerical modeling experiments where the 0–1 km shear [6] is varied are used to explore the dynamical effects of rotation on precipitation processes. The resulting storm characteristics, precipitation accumulations, and induced mesoscale dynamic accelerations will be examined. Section 2 provides a description of the extreme rainfall event used as the basis for the model initial conditions; section 3 describes the methodology used in this study; section 4 presents the results of simulations with planetary rotation;

[6]From this point on in this manuscript, the "wind shear" verbiage will refer to the bulk wind difference over the specified layer and the units will reflect as such.

section 5 presents the results with planetary rotation included; and section 6 summarizes the results and presents a discussion about the conclusions.

3.2 Case of Interest

Although quantifying the proportion of extreme short-term rain events associated with low-level rotation is beyond the scope of this study and is a topic of ongoing research by the authors, one example that served as the initial motivation for this study is summarized here.

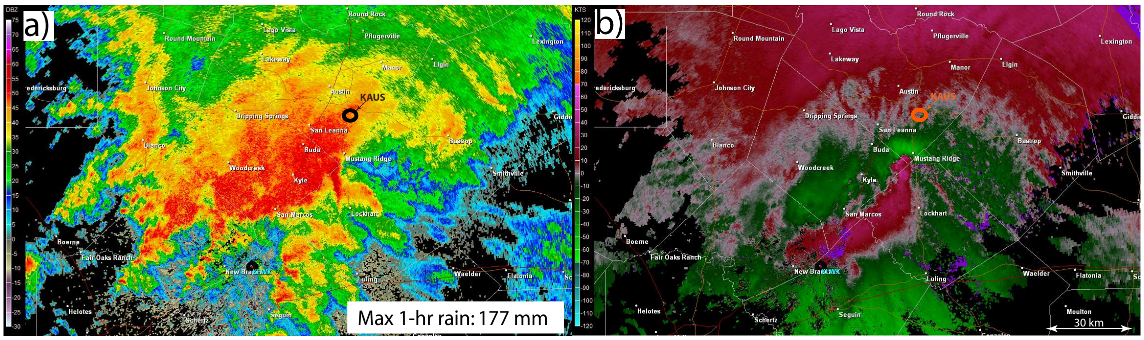

FIG. 3.1. Radar reflectivity (a) and base velocity (b) for the case of interest where intense rainfall accumulations were observed attendant with mesoscale rotation 1342 UTC 30 October 2015 from Austin/San Antonio, TX (KEWX) radar. The METAR station where rainfall accumulations were observed is labeled on the radar reflectivity plot. Maximum one hour rainfall observation from local METAR or mesonet networks are labeled for the case.

A TORFF event that occurred in south-central Texas on 30 October 2015 (Fig. 3.1a,b) will serve as the basis for the numerical modeling experiments presented in this study. A very strong, long lived mesoscale vortex developed northeast of San Antonio, Texas, within an already developed MCS near 1200 UTC that day. As the vortex moved north towards Austin, Texas, over the next three hours (Fig. 3.1b), hourly rainfall observations of 100 to 177 mm were observed by several Lower Colorado River Authority gauges along its path (not shown; LCRA 2017). Furthermore, an hourly accumulation of 146.3 mm was recorded at Austin-Bergstrom International Airport (KAUS) (Fig. 3.1a,b). A total of 11 flash flood and 11 tornado warnings were issued by NWS Austin/San Antonio during the event, with a total of four tornadoes, including 2 EF-2s, surveyed, and 5 fatalities were associated with the flash flooding (NCEI 2017).

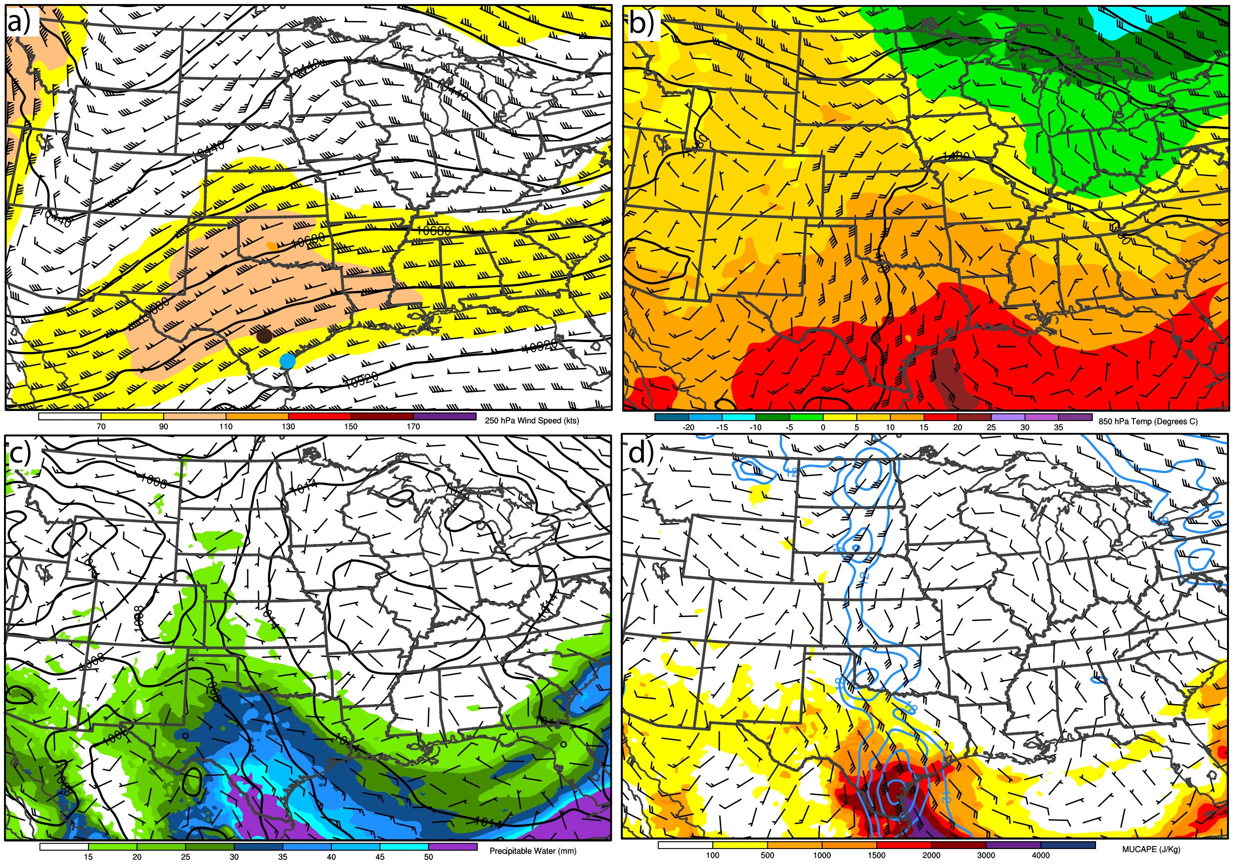

FIG. 3.2. (a)–(d) Rapid Refresh (RAP; Benjamin et al. 2016) analyses valid at 0900 UTC 30 October 2015. (a) 250-hPa isotachs (shaded every 20 kt over 70 kt, 1 kt = 0.5144 m s^{-1}), 250-hPa geopotential height (contoured every 120 m), 250-hPa wind barbs(half barb = 5 kt, full barb = 10kt, pennant = 50 kt,), and cyan dot represents the approximate location of the Corpus Christi, TX sounding in Fig. 3.3a, and black dot represents the location of San Antonio, TX. (b) 850-hPa geopotential height (contoured every 25 m), 850-hPa wind barbs, and 850-hPa temperature (shaded every 5°C from -20°C to 35°C). (c) precipitable water (shaded contours every 5 mm for values from 10 mm to 50 mm), 10 m wind barbs, and mean sea level pressure (MSLP) (contoured every 3 hPa). (d) Most Unstable CAPE (MUCAPE; shaded at 100 J kg^{-1} then every 500 J kg^{-1} above 500 J kg^{-1}), 900-hPa wind barbs, and 900-hPa isotachs (contoured every 3 m s^{-1} above 12 m^{-1}).

South-central Texas was positioned in the southern portion of a subtropical jet streak (Fig. 3.2a) downstream of an approaching long-wave trough by 0900 UTC on 30 October 2015 (Fig. 3.2a). The convection that eventually formed into the MCS in question initiated over the Mexican Plateau and Texas-Mexico border near 0600 UTC that day, as the upper-level forcing moved into the area. Significant southeasterly flow off the Gulf of Mexico ahead of the upper-level trough provided a reservoir of moisture and buoyancy into the region (Fig. 3.2c,d), as well as, continued warm air advection (Fig. 3.2b). The intense low level flow (i.e., approaching 50 kt at 850 hPa and 900 hPa; Fig. 3.2b,d) also created a strongly sheared low-level environment. The upstream 0000 UTC sounding from Corpus Christi, Texas, (KCRP) contained 16.8 m s^{-1} 0–1 km shear and 52.4 mm of precipitable water (PWAT) with the surface parcel being slightly inhibited (Fig. 3.3a). A sounding taken from the 0000 UTC initialization of the Colorado State University (CSU) Advanced Research Weather Research and Forecasting (WRF-ARW; Klemp et al. 2007; Skamarock et al. 2008; Skamarock and Klemp 2008) numerical model[7] shows at 1500 UTC a similar low-level kinematic picture with 17.2 m s^{-1} 0–1 km shear, strong veering in the low-level hodograph, and similar amounts of PWAT (cf. Figs. 3.3a,b).

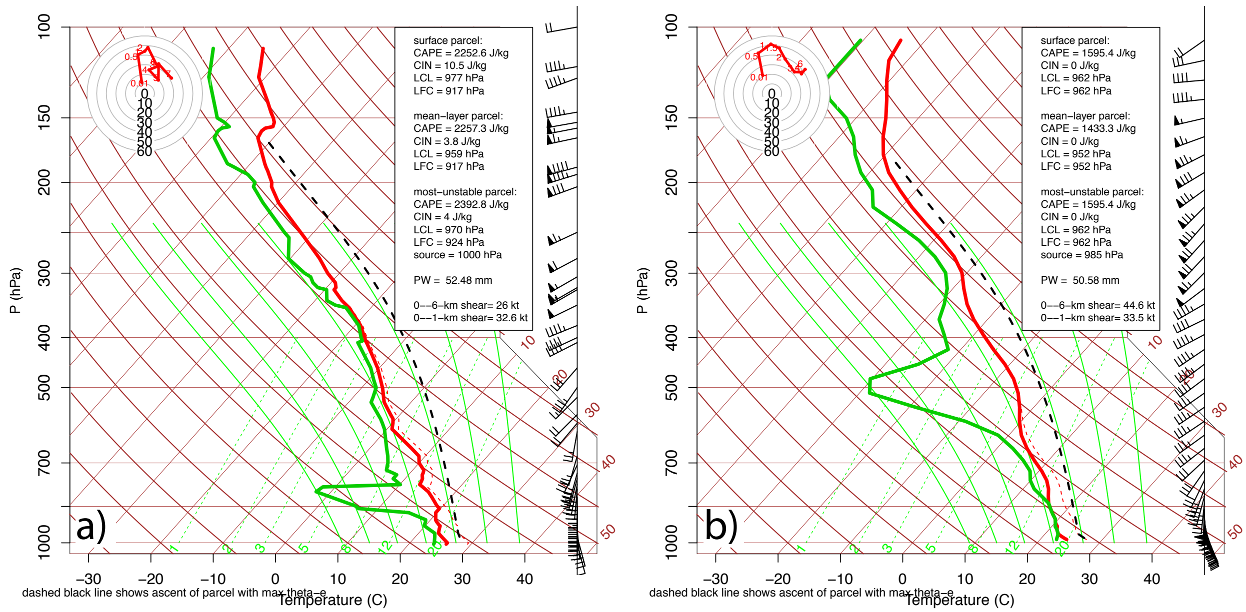

FIG. 3.3. (a) Observed sounding valid 1200 UTC 30 October 2015 from Corpus Christi, TX (KCRP). (b) Model sounding from the Colorado State University WRF-ARW (see Schumacher 2015a; Peters et al. 2017, for model setup information) for San Antonio, TX (location denoted by black dot in Fig. 3.2) valid 1500 UTC 30 October 2015. Black dashed line in both soundings represents the temperature of a lifted parcel with the maximum equivalent potential temperature (i.e., θ_e), using the virtual temperature correction. Red dotted line in both soundings represents the virtual temperature correction to the temperature profile.

A kinematic profile partially based upon this CSU-WRF model sounding (Fig. 3.3b) was used to set up the initial conditions for the experiments described below, due to the sounding's close proximity (both temporally and spatially) to the modeled mesoscale vortex and the low-level kinematic similarities to the observed upstream sounding from Corpus Christi, Texas.

3.3 METHODS

Three dimensional numerical model simulations were conducted in Cloud Model 1 version 1.18 (CM1; Bryan and Fritsch 2002) in a similar configuration as that described in Schumacher (2009, 2015b).

[7]See Schumacher (2015a) and Peters et al. (2017) for model setup information.

Some of the more pertinent model specifics include 500 m horizontal grid spacing on a 1200 × 1200 grid point domain (i.e., 600 × 600 km), a stretched vertical grid with 61 levels, 100 m vertical resolution near the surface, 500 m vertical resolution aloft, free slip upper and lower boundaries, and open-radiative boundary conditions (Durran and Klemp 1983) that are restricted so the outward mass flux does not exceed the inward. Additionally, radiative processes were excluded, and the Morrison two-moment microphysics scheme with graupel prescribed as the large ice category was used (Morrison et al. 2009). The model domain was translated at a speed of $u = 6.5$ m s^{-1} and $v = 8.0$ m s^{-1}. As in Schumacher (2009, 2015b), the convection was initiated using a momentum forcing that develops a three-dimensional circular convergence field, which imitates the gradual mesoscale ascent that is typically associated with an MCV, following the methods developed by Loftus et al. (2008). The forcing was horizontally centered at grid point 460 × 460 (i.e., 230 km into the domain in both the x and y direction), vertically centered at 1.4 km, had a vertical radius of 1 km, and a horizontal radius of 140 km. The maximum divergence prescribed was -1×10^{-5} s^{-1} and increased incrementally over the first 2-3 hours, where it levels off at approximately the chosen maximum divergence (convergence).

The initial environmental horizontally homogenous thermodynamic base state profile for the simulations undertaken in this study was taken from the composite sounding (Fig. 3.4a) created by Schumacher and Johnson (2009) over six extreme rainfall events where the lowest kilometer reflects the effects of nocturnal stabilization. The profile is characterized by moist low levels, 50 mm (∼2 in.) of PWAT, moderate convective available potential energy (CAPE), and no convective inhibition (CIN) for the most unstable parcel sourced at 875 hPa. However, non-negligible CIN (61 J kg^{-1}) is present for surface-based parcels. This initial thermodynamic profile was chosen for these simulations because it is smooth relative to the individual cases and excludes the possible influence of noisy case-dependent variations in temperature and moisture from unique cases (i.e., see construction of profile in Schumacher and Johnson 2009). Further, passive tracers were placed in the PBL, throughout the entire layer below 750 m, to test whether parcels were ingested from the stable boundary layer present in the initial conditions (Fig. 3.4a).

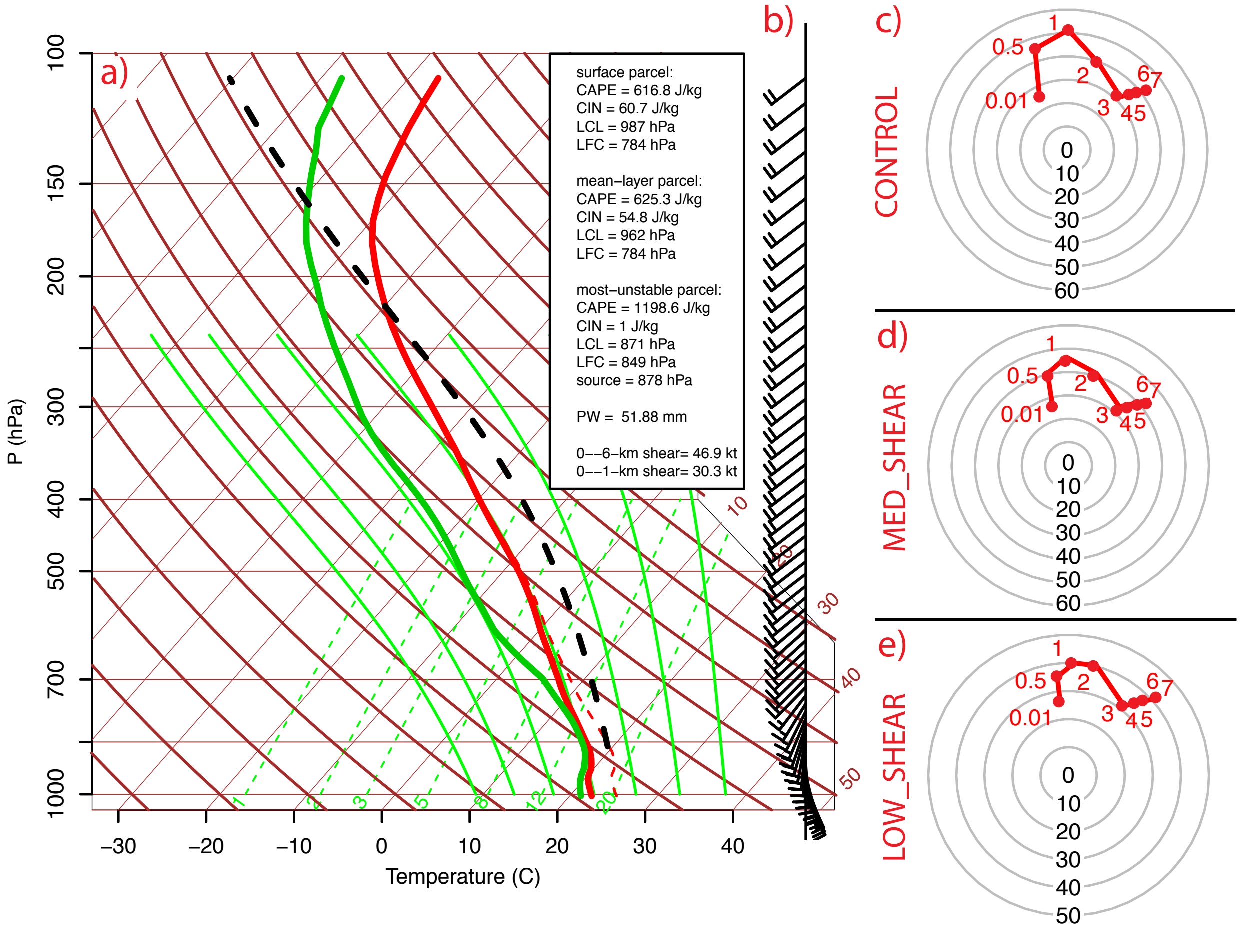

FIG. 3.4. (a) Composite thermodynamic profile and parcel characteristics for extreme rainfall events from Schumacher and Johnson (2009), red dashed line in (a) shows the environmental virtual temperature curve, and black dashed line (a) shows the virtual temperature of a lifted parcel that contains the highest θ_e. Hodographs (kt) of wind profile used for wind 0–1km shear sensitivity experiments for CONTROL (c), MED_SHEAR (d), and LOW_SHEAR (e) cases derived from CSU-WRF model sounding valid 1500 UTC 30 October 2015 near San Antonio, TX (e.g., Fig. 3.3b), where each numeric value along hodograph trace represent wind vector height (km) at corresponding marker (note LOW_SHEAR hodograph ring maximum is 50 kt compared to 60 kt for other two cases). (b) wind profile corresponding to control hodograph (c).

The initial wind profile was taken from the aforementioned CSU-WRF model sounding (i.e., Fig. 3.3b) valid at 1500 UTC 30 October 2015 near San Antonio, Texas. To focus the experiments on the role of low-level wind shear, the shear above 6 km was removed from the CSU-WRF sounding (Fig. 3.4b). The resultant wind profile (Fig. 3.4b) and hodograph (Fig. 3.4c) represent the kinematic profile that was used as the control for the quasi-idealized experiments presented in this study. The influence of the rotation on precipitation processes was examined by producing a set of simulations in which the the low-level wind shear was modified. The primary purpose of these experiments is to explore how changes in the magnitude of the low-level wind shear affects storm dynamics and precipitation production. Thus, we developed two additional wind profiles with weaker low-level shear, but a similar hodograph shape. Furthermore, these wind profiles were modified slightly so that the predicted motion of a right-moving supercell (using the method of Bunkers et al. 2000) would be the same for all of the simulations. The wind profile in the first run, referred to hereafter as CONTROL, was the slightly modified wind profile described above that contains the highest 0–1 km shear of the simulations with a value over 15 m s^{-1} (Fig. 3.4c and Table 3.1). The 0–1 km shear was then reduced to approximately 10 m s^{-1} and 7.5 m s^{-1} for the medium shear (Fig. 3.4d and Table 3.1; hereafter referred to as MED_SHEAR) and low shear (Fig. 3.4e and Table 3.1; hereafter referred to as LOW_SHEAR) runs, respectively. Additionally, two more simulations were performed using the CONTROL and LOW_SHEAR kinematic profiles where Coriolis force was applied to the model perturbations (hereafter referred to as CONTROL_COR and LOW_SHEAR_COR, respectively) assuming an f-plane value of 8.882×10^{-5} s^{-1}, which corresponds to the latitude of Springfield, Missouri (37.25°N).

TABLE 3.1. Characteristics of the three wind profiles used in the CONTROL, MED_SHEAR, and LOW_SHEAR experiments. The storm relative helicity (SRH) is calculated for the Bunkers predicted right mover storm motion (e.g., Bunkers et al. 2000) of $u = 7.3$ m s^{-1} and $v = 8.3$ m s^{-1} (or 220° at 11m s^{-1}) that is approximately equal for each wind profile.

	CONTROL	**MED_SHEAR**	**LOW_SHEAR**
0–1km Bulk Wind Difference (m s^{-1})	15.2	10.7	7.6
0–6 km Bulk Wind Difference (m s^{-1})	24.1	21.1	18.0
0–1km SRH (m^2s^{-2})	286	161	96
0–3km SRH (m^2s^{-2})	406	281	184

Buoyant and dynamic components (i.e., all terms in Eqn. 3) of VPPGF were numerically solved for each run following the methods of Parker and Johnson (2004) and Coffer and Parker (2015) to investigate the wind shear induced differences in the VPPGF. Briefly (see Eqn. 3), in this method, the buoyant pressure perturbation, $p_B^{'}$, dynamic pressure perturbation, $p_D^{'}$, and the dynamic linear pressure perturbation, $p_{DL}^{'}$, were numerically solved following the diagnostic equations presented in Wilhelmson and Ogura (1972) and Rotunno and Klemp (1982). Since the retrieval of the individual pressure perturbation terms required the inversion of a Laplacian (e.g., Rotunno and Klemp 1982, among others) the following boundary conditions were assumed (e.g., as in Coffer and Parker 2015): (a) the buoyant pressure perturbation, $p_B^{'}$, satisfied the hydrostatic balance at the model boundaries; (b) the dynamic pressure perturbation, $p_D^{'}$, satisfied $p_D^{'} = p^{'} - p_B^{'}$ at the lateral boundaries, where $p^{'}$ is the pressure perturbation known from the model output; (c) the dynamic linear pressure perturbation, $p_{DL}^{'}$, satisfied $p_{DL}^{'} = 0$ at the model boundaries; and (d) the dynamic non-linear portion of the perturbation pressure, $p_{DNL}^{'}$, was then treated as the residual of the dynamic pressure perturbation, $p_D^{'}$, minus the dynamic linear pressure perturbation, $p_{DL}^{'}$ (i.e., $p_{DNL}^{'} = p_D^{'} - p_{DL}^{'}$). The resulting pressure perturbations were used to calculate the vertical accelerations associated with the various terms of the standard decomposition (e.g., those generalized in Eqn. 4 and shown in Eqn. 3). This analysis helps isolate the influence of the rotation on the overall strength of the updrafts and storm inflow through the calculation of the accelerations associated with VPPGF (i.e., terms in Eq. 3), including those caused by $p_{DNL}^{'}$ (i.e., the “spin" term in Eq. 4), the non-linear dynamic vertical pressure perturbation force (hereafter NLD-VPPGF will refer to the accelerations induced by this term).

3.4 Results: Non-Coriolis Simulations

The three simulations without Coriolis described above go on to produce convective systems that are similar in size, shape, and speed. Convection initiates from the forced convergence 2–3 hours into the simulations, and all three simulations produce similar convective systems by 6 hours into the simulations. Similar storms, from a simulated reflectivity point of view, develop in all three runs by t=9 h (Fig. 3.5a,c,e and simulation animations in online supplement) and are maintained through the end of the simulations (see discussion below). All three runs produce the most intense convection in a fairly localized area on the south and western flank of the storm, where low-to-mid level rotation is present in varying degrees of strength and maintenance depending on the specific simulation. A broad downshear stratiform region is present in all simulations, but slight variations in spatial extent are noticeable. The simulations produce similar radar depictions as the observed case described in section 2 (cf. Fig. 3.5a,c,e and Fig. 3.1a).

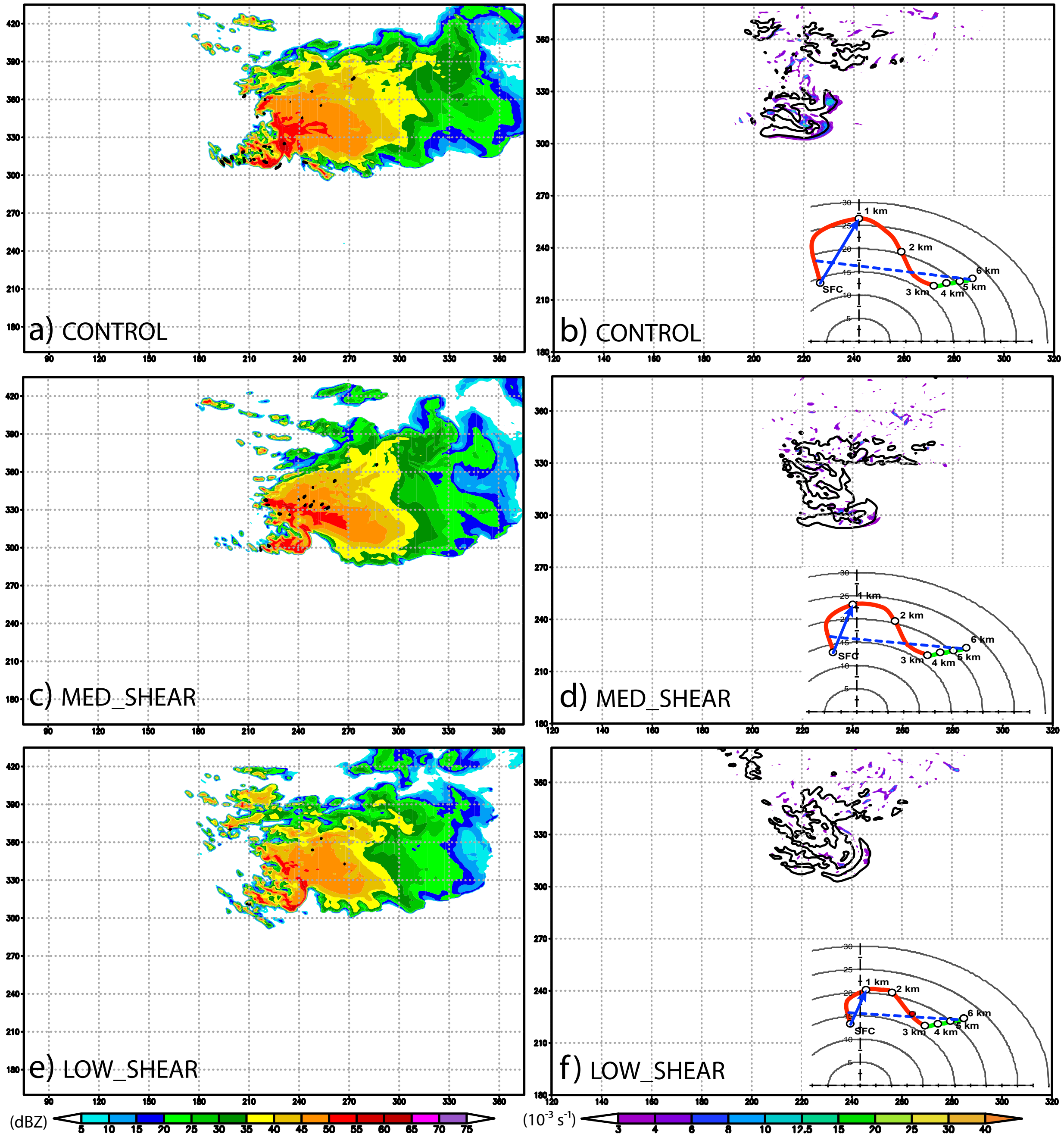

FIG. 3.5. (a,c,e) Simulated 1 km radar reflectivity (shaded; every 5 dBZ from 5dBZ to 70 dBZ) and contoured 1 km vertical vorticity (black contours; starting at 10.0×10^{-3} s^{-1} every 5.0×10^{-3} s^{-1}) valid t=9 h into the simulations for the (a) CONTROL, (b) MED_SHEAR, (c) LOW_SHEAR simulations. (b,d,f) Corresponding 500 m vertical vorticity ($\times 10^{-3}$ s^{-1}) and 500 m perturbation potential temperature ($\theta^{'}$; -1.0 K contoured in black), for the (b) CONTROL, (d) MED_SHEAR, (f) LOW_SHEAR simulations. Grid tick marks are in km. Hodographs for each simulation are embedded in the right column where the solid blue arrow represents 0–1 km bulk wind difference, and dashed blue line represents boundary layer to 6 km bulk wind difference.

The convective systems produced in the simulations have spatial scales smaller than the MCS[8] (∼ 80-100 km in spatial extent is seen for the CONTROL simulation) discussed in section 2 (cf. Fig. 3.1a-b and Fig. 3.5a,c,e).

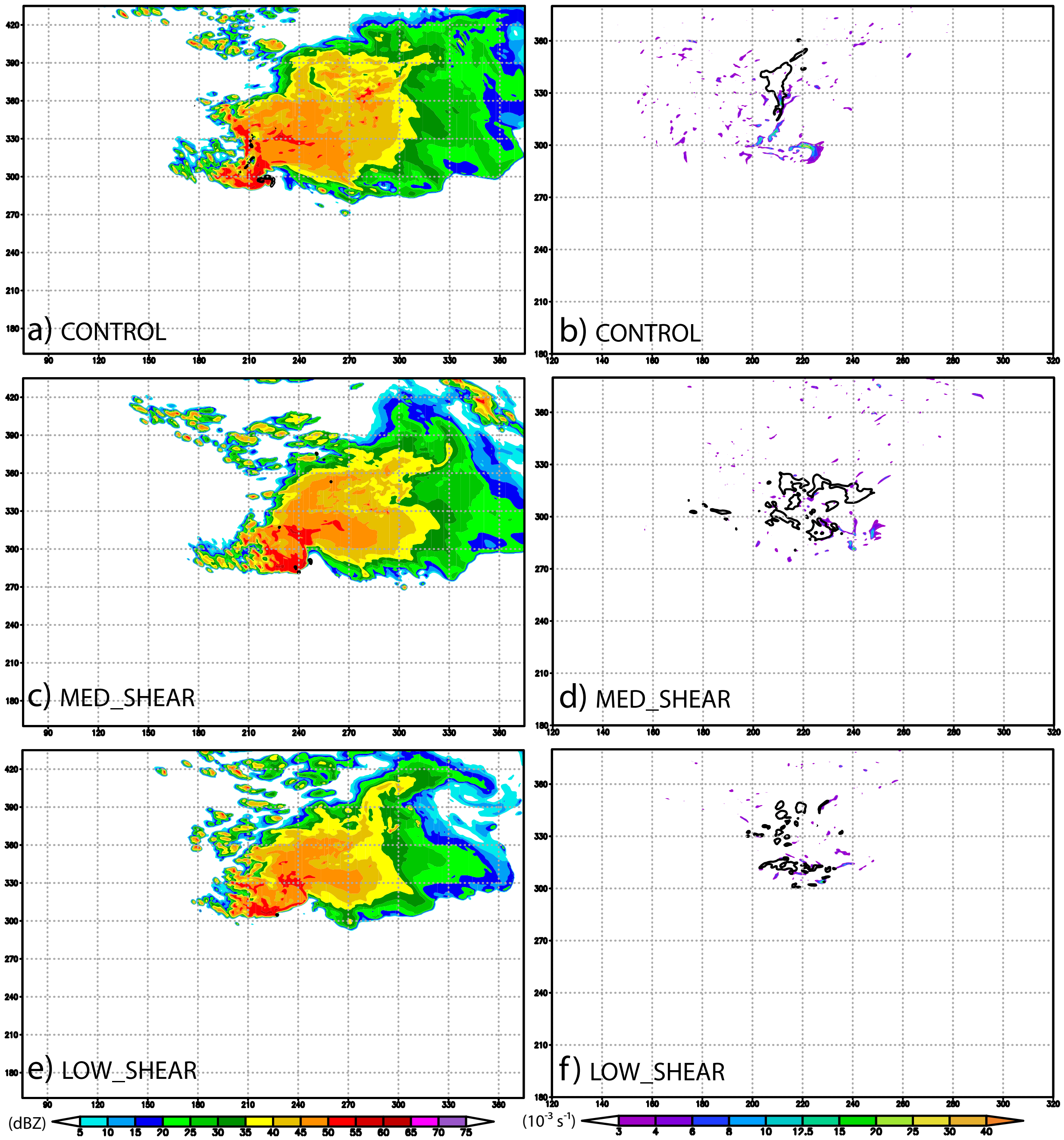

FIG. 3.6. Same as Fig. 3.5 except valid t=11 h into the simulations.

[8]The resulting convective systems simulated in the numerical runs do not all meet the strict length requirements often used for a MCS (e.g., > 35 dBz for > 100 km, Parker and Johnson 2000)

However, the simulations do contain embedded supercells, similar to the observed case (Fig. 3.1a-b). Due to the system longevity, nature of the initial forcing (i.e., elevated forced convergence), and the initially thermodynamically stable boundary layer, one could categorize the simulated systems as an MCS with embedded supercells.

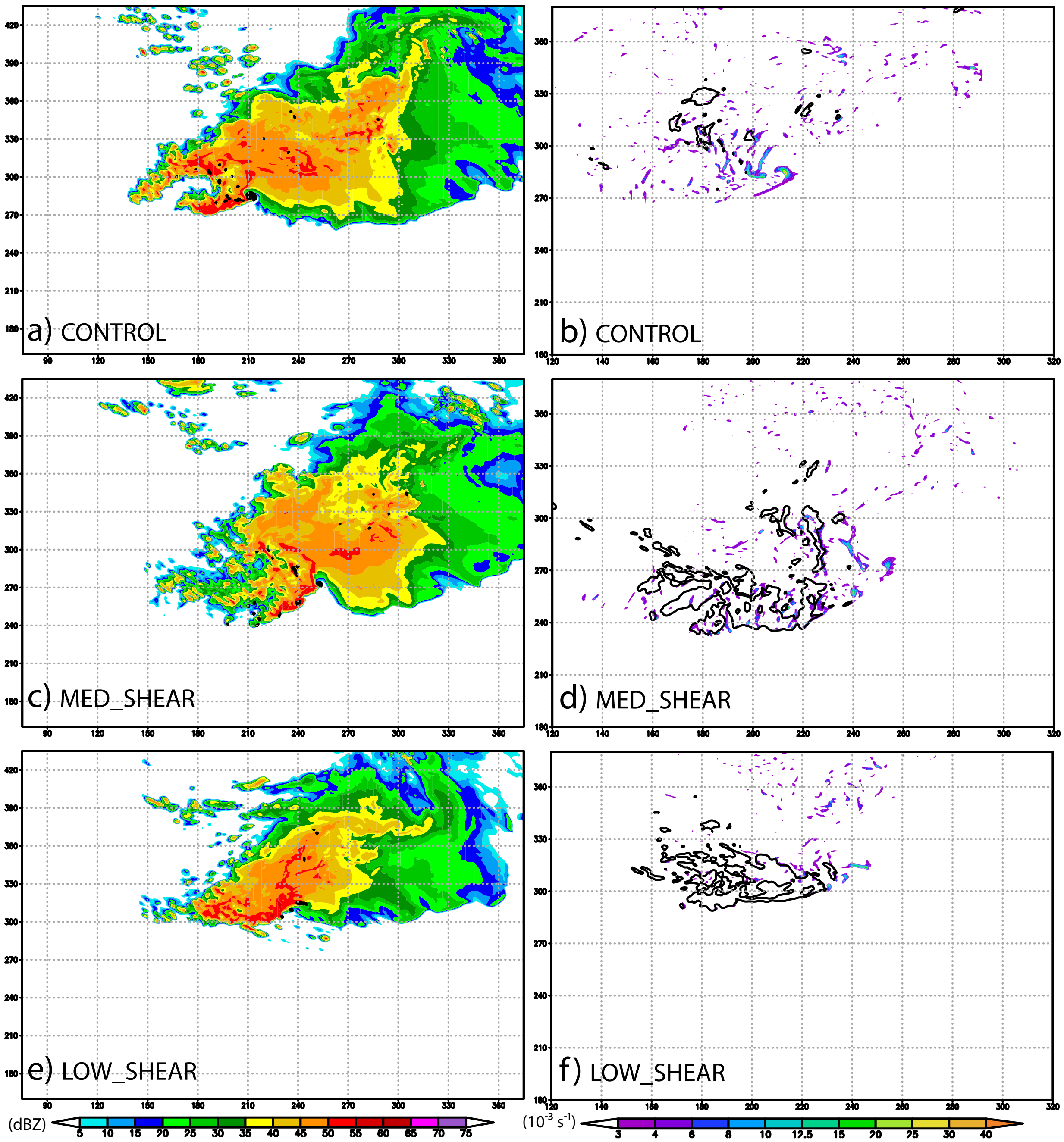

FIG. 3.7. Same as Fig. 3.5 except valid t=13 h into the simulations.

By t=11 h into each simulation, all three convective systems are continually back building (e.g., Schumacher and Johnson 2005) with the stratiform region still located downshear of the main convective region (Fig. 3.6a,c,e).

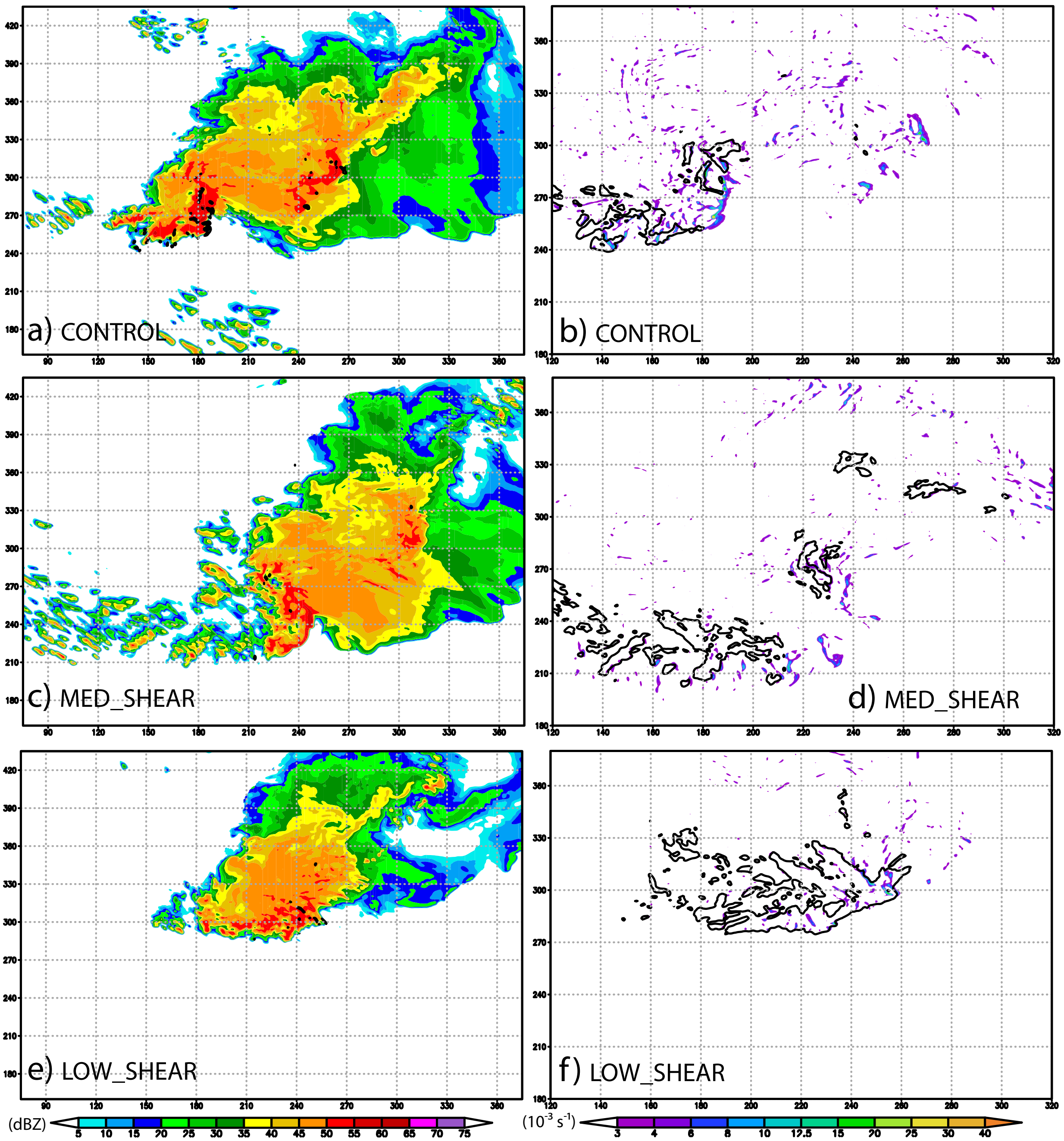

FIG. 3.8. Same as Fig. 3.5 except valid t=15 h into the simulations (i.e., the end).

Low and mid-level rotation is present in all three cases, but with varying strengths and longevity. Strong, sustained rotation and repeated mesocyclone development is seen in the CONTROL run (Fig. 3.6-

3.8b), while comparatively weak, scattered, shallow, and short-lived rotations is seen in the LOW_SHEAR simulation (Fig. 3.6- 3.8f). The MED_SHEAR run produces low-level rotation characteristics somewhere between CONTROL and LOW_SHEAR runs, in terms of strength and vortex longevity (Fig. 3.6-3.8d), which is not surprising given its 0–1 km shear value lies between the other two runs. A small cold pool develops in each simulation after t=9 h that is anchored to the region of most intense convection (Fig. 3.5b,d,f and even shrinks by t=11 h). One hour later, a total of t=13 h into the simulations, each simulation has a similar radar depiction (Fig. 3.7a,c,e); however, stronger, more persistent rotation is still maintained in the runs with higher 0–1 km shear (Fig. 3.7b,d,f). A rather robust cold pool has developed in the MED_SHEAR run (Fig. 3.7d) and is beginning to develop in the LOW_SHEAR run (Fig. 3.7f) but not in the CONTROL simulation (Fig. 3.7b). At the end of the simulations (i.e., after t=15 h of integration), the cold pools in the MED_SHEAR and LOW_SHEAR case have outrun the convection (Fig. 3.8d,f), which has resulted in limited low-level rotation (Fig. 3.8d,f) and weakened convection on the western flank of the storms. The CONTROL run shows signs of continued, but slow, cold pool development and maintains low-level rotation throughout the simulations (Fig. 3.8a,b). The stratiform regions of the CONTROL and MED_SHEAR simulations are larger in spatial coverage and intensity compared to the LOW_SHEAR run, through the last two hours of both simulations (cf. Fig. 3.7a,c,e and Fig. 3.8a,c,e).

Substantially more precipitation occurred in terms of point maximum, areal mean, and areal coverage of large accumulations (e.g., 25 mm, 50 mm, 100 mm, etc, Table 3.2) for the CONTROL run compared to the MED_SHEAR and LOW_SHEAR simulations (Fig. 3.9, Table 3.2). The largest differences in accumulated precipitation between the runs appear in the areal coverage at the upper accumulation thresholds. The CONTROL run produces accumulation over 200 mm at multiple points, while the MED_SHEAR and LOW_SHEAR only have point maxima of 167 mm and 142 mm, respectively (Fig. 3.9, Table 3.2). Furthermore, the amount of total accumulated precipitation and domain coverage at specific thresholds appears to increase with the magnitude of the low-level shear in the initial wind profile (Table 3.2). In other words, the accumulated precipitation for the three runs without Coriolis is larger in the simulations with more intense and prolonged low-level rotation, which is associated with the magnitude of the low-level shear. The increase in 0–1km shear between the simulations does lead to an increase in storm relative inflow, since the approximate storm motion for each simulation is equal. Although this likely contributes to the increased precipitation, it does not explain the magnitude of the precipitation increases, likely because the stable boundary-layer air would not reach its level of free convection by this process alone (see additional discussion on this matter in section 6).

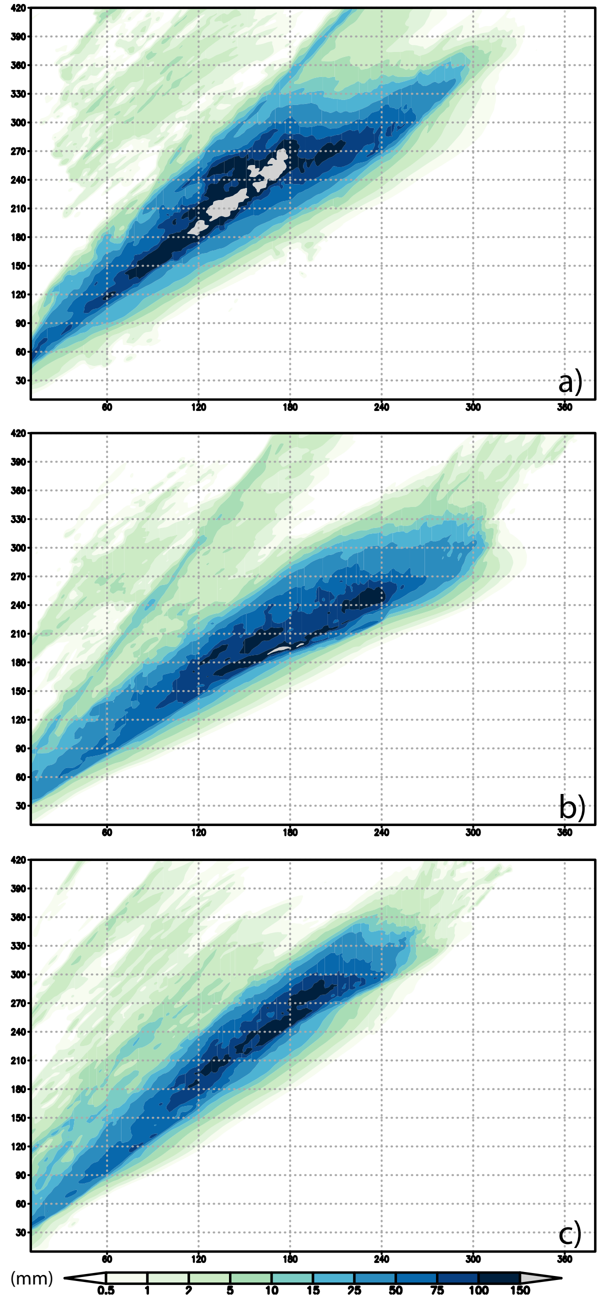

FIG. 3.9. Total accumulated precipitation (mm), accounting for the translation of the numerical model domain, in (a) CONTROL (b) MED_SHEAR, and (c) LOW_SHEAR simulations. Run specific statistics are presented in Table 3.2. Axis tick marks are in kilometers.

TABLE 3.2. Modeled rainfall accumulation statistics for simulations performed in this study.

Statistic	**Control**	**Med_Shear**	**Low_Shear**	**Control_cor**	**Low_Shear_cor**
Mean Areal (mm km^{-2})	3.10	2.43	1.95	2.03	1.75
Max (mm)	220	167	142	222	132
Coverage ≥ 25 mm	5.66%	5.05%	3.88%	4.17%	3.77%
Coverage ≥ 50 mm	3.75%	2.90%	2.36%	1.83%	2.30 %
Coverage ≥ 100 mm	1.19%	0.42%	0.36%	0.60%	0.33%
Coverage ≥ 150 mm	0.27%	0.02%	N/A	0.20%	N/A
Coverage ≥ 200 mm	0.009%	N/A	N/A	0.02%	N/A

Substantial differences in both mean (Fig. 3.10a-c) and maximum (Fig. 3.11a,c,e) vertical velocity were seen among the three simulations without Coriolis at the low-levels. The average low-level vertical motion is larger and sustained for a longer period of time in the CONTROL simulation compared to the MED_SHEAR and LOW_SHEAR runs. The largest enhancements in the CONTROL run areal mean vertical velocity over the other two simulations are seen at and above 1 km in height (cf. Fig. 3.10a-c). However, enhancements over the weaker shear simulations are still seen in mean vertical velocity in the lowest levels (i.e., 300 and 500 m) of the CONTROL run (cf. Fig. 3.10a-c). The CONTROL run continues to produce areal mean positive low-level updrafts for an hour over the LOW_SHEAR simulation and for thirty minutes over the MED_SHEAR run (cf. Fig. 3.10a-c). Furthermore, the CONTROL regularly produces stronger maximum updrafts (cf. Fig. 3.11a,c,e) than the other simulations with values approaching 20 m s^{-1} at 500 m and up to 40 m s^{-1} at 1.5 km (Fig. 3.11a). Similarly, the CONTROL simulation produces higher maximum vertical vorticity values throughout the low levels both at individual times and in a mean-maximum sense (i.e., the mean of the maximum values) compared to the MED_SHEAR and LOW_SHEAR runs (cf. Fig. 3.11b,d,f). The MED_SHEAR simulation, while showing relatively little difference in the areal mean vertical velocity compared to LOW_SHEAR (cf. Fig. 3.11d,f), consistently produces higher maximum vertical motions throughout the low levels throughout the length of the simulation. All three runs show temporally sporadic, but intense peaks in the maximum low-level vertical velocity (cf. Fig. 3.11a,c,e); however, the frequency and magnitude of these peaks are reduced from the CONTROL, to the MED_SHEAR, and to the LOW_SHEAR runs (i.e., as you reduce the amount of 0–1km wind shear in the base state profiles).

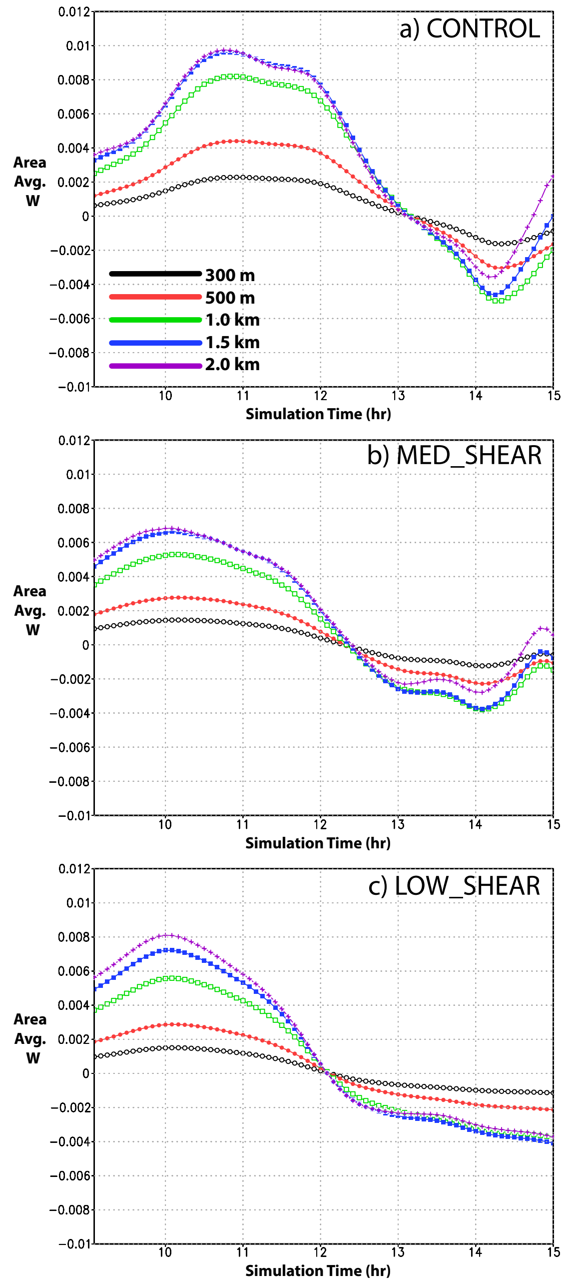

FIG. 3.10. Time series of area averaged vertical motion (m s^{-1} m^{-2}) for the (a) CONTROL, (b) MED_SHEAR, and (c) LOW_SHEAR simulations at model height levels of 300 m (black), 500 m (red), 1 km (green), 1.5 km (blue), and 2.0 km (purple). The areal averaging was performed over the spatial extent of the model domain depicted in Fig. 3.5-3.8.

The timing of the low-level maximum vertical velocities in all three runs is temporally correlated to periods of higher maximum vertical vorticity of similar duration (cf. Fig. 3.11a,c,e and Fig. 3.11b,d,f), where the more intense low-level vertical vorticity is associated with more intense vertical velocity. The temporal correlation and pulsing nature of the maximum low-level vertical velocity and vorticity is likely a manifestation of the pulsing nature of the low-level vortices that develop in each run, where the longevity and magnitude of the vortices are reduced with the amount of 0–1km shear (cf. Fig.3.6-3.8b,d,f; Fig. 3.11b,d,f; and simulation animations in online supplement).

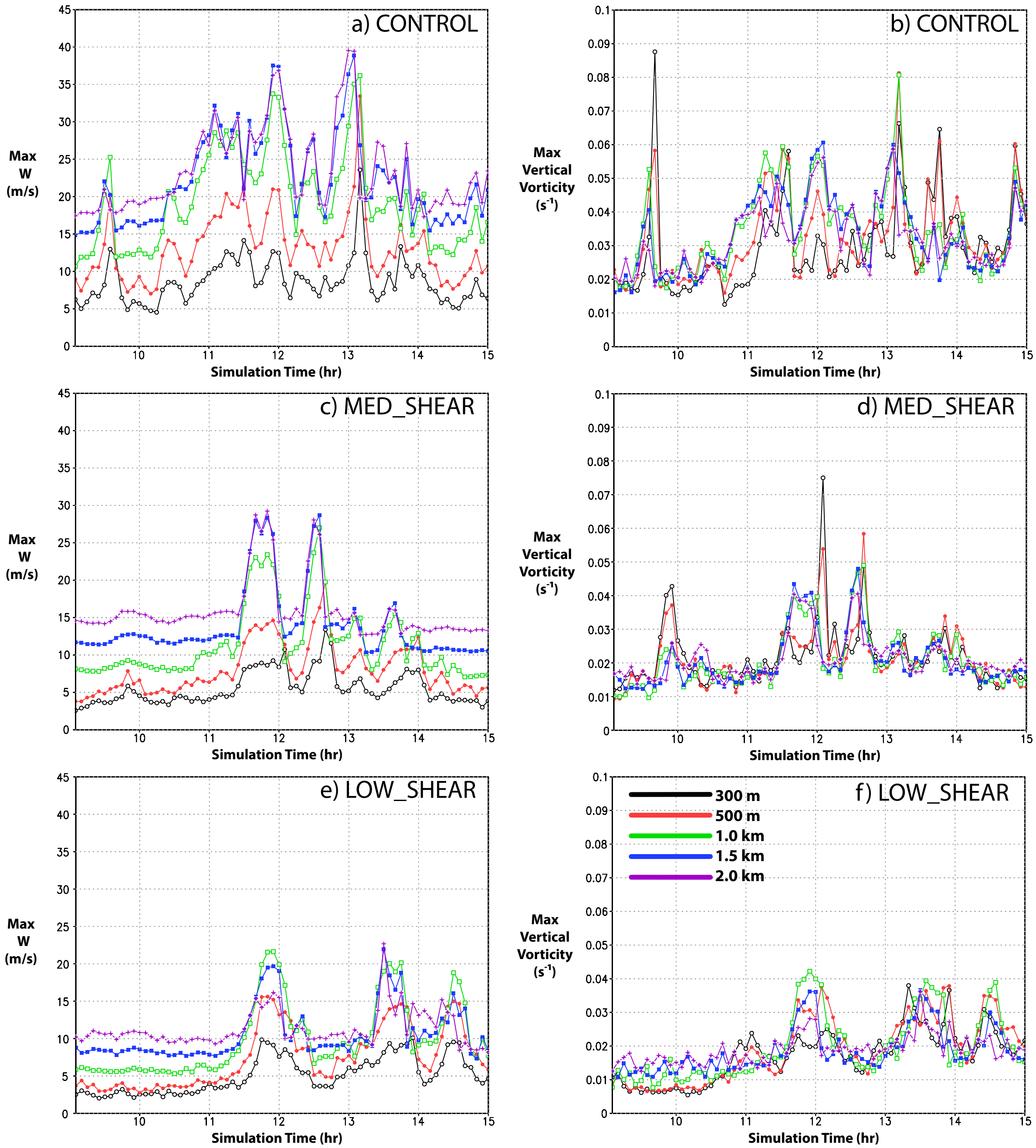

FIG. 3.11. Time series of maximum updraft velocity, w (m s^{-1}), for the (a) CONTROL, (c) MED_SHEAR, and (e) LOW_SHEAR runs at model height levels of 300 m (black), 500 m (red), 1 km (green), 1.5 km (blue), and 2.0 km (purple). Time series of maximum vertical vorticity (s^{-1}) for the (b) CONTROL, (d)MED_SHEAR, and (f) LOW_SHEAR runs at the same model height as (a,c,e).

The presence of such sustained and large vertical motions in the low-levels of the simulation is worth noting, since there is substantial inhibition in the sounding for the surface-based parcel (i.e., Fig. 3.4a). However, all three simulated MCSs with embedded supercells are able to ingest parcels that originate below 750 m (hereafter low-level tracers), which contain moisture and CAPE, into the various updrafts (not shown).

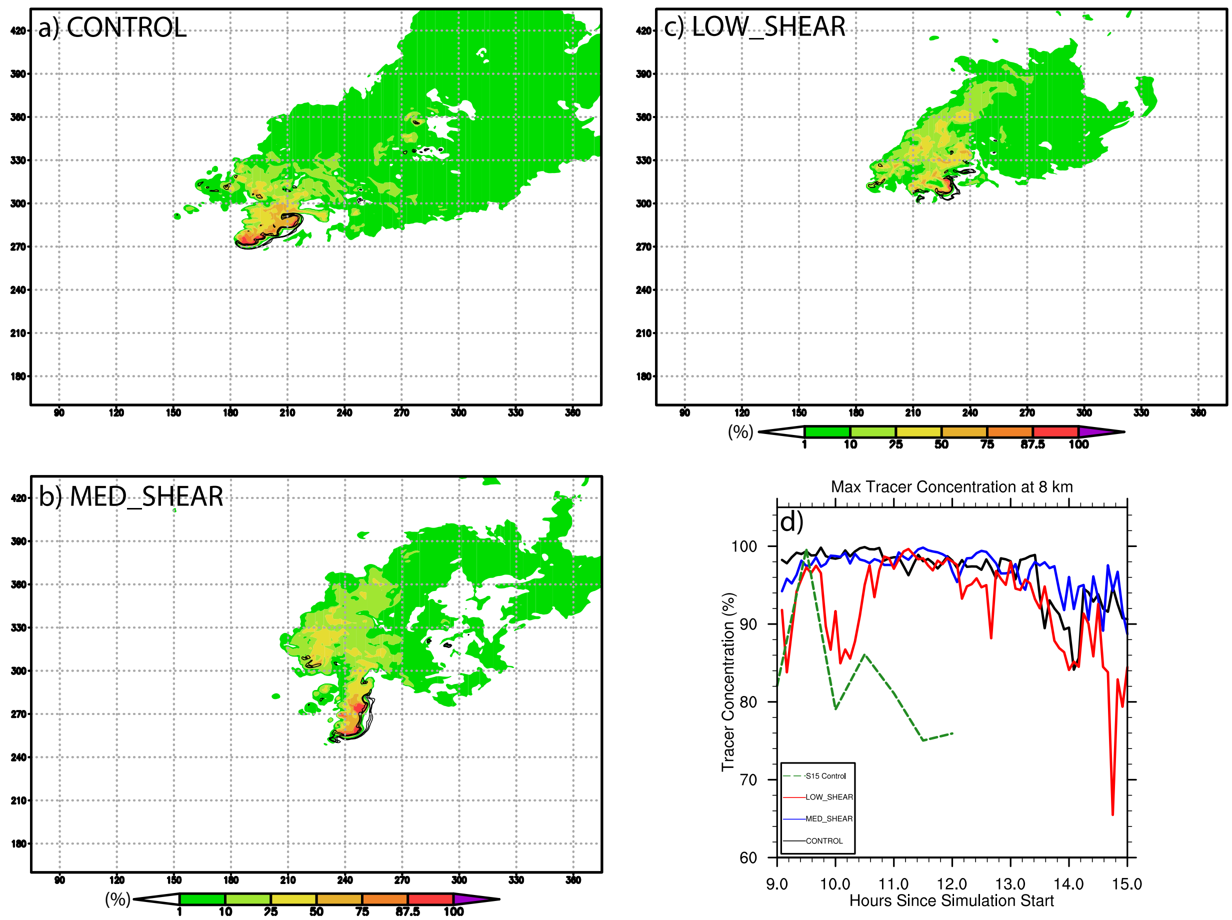

FIG. 3.12. Concentration of tracers released at or below 750 m (fill contours; %) at 8 km height valid 13 hr into the simulation for the (a) CONTROL, (b) MED_SHEAR, and (c) LOW_SHEAR model runs. Corresponding 1 km vertical velocity, w (m s^{-2}; black contours drawn at 15, 20, and 15 m s^{-1}), for the same simulations. (d) Time series of maximum concentration of tracers released at or below 750 m at 8 km in height for the CONTROL (black line), MED_SHEAR (blue line), LOW_SHEAR (red line), and control run from Schumacher (2015b) (green dashed line) when data was available.

The concentrations of low-level tracers that reach 8 km do not differ substantially between the three runs, but the mean concentration is ordered to the amount of low-level shear in each simulation (not shown). All three simulations presented here are able to bring some parcels, almost undiluted, from the low levels (Fig. 3.12d) throughout the simulation.

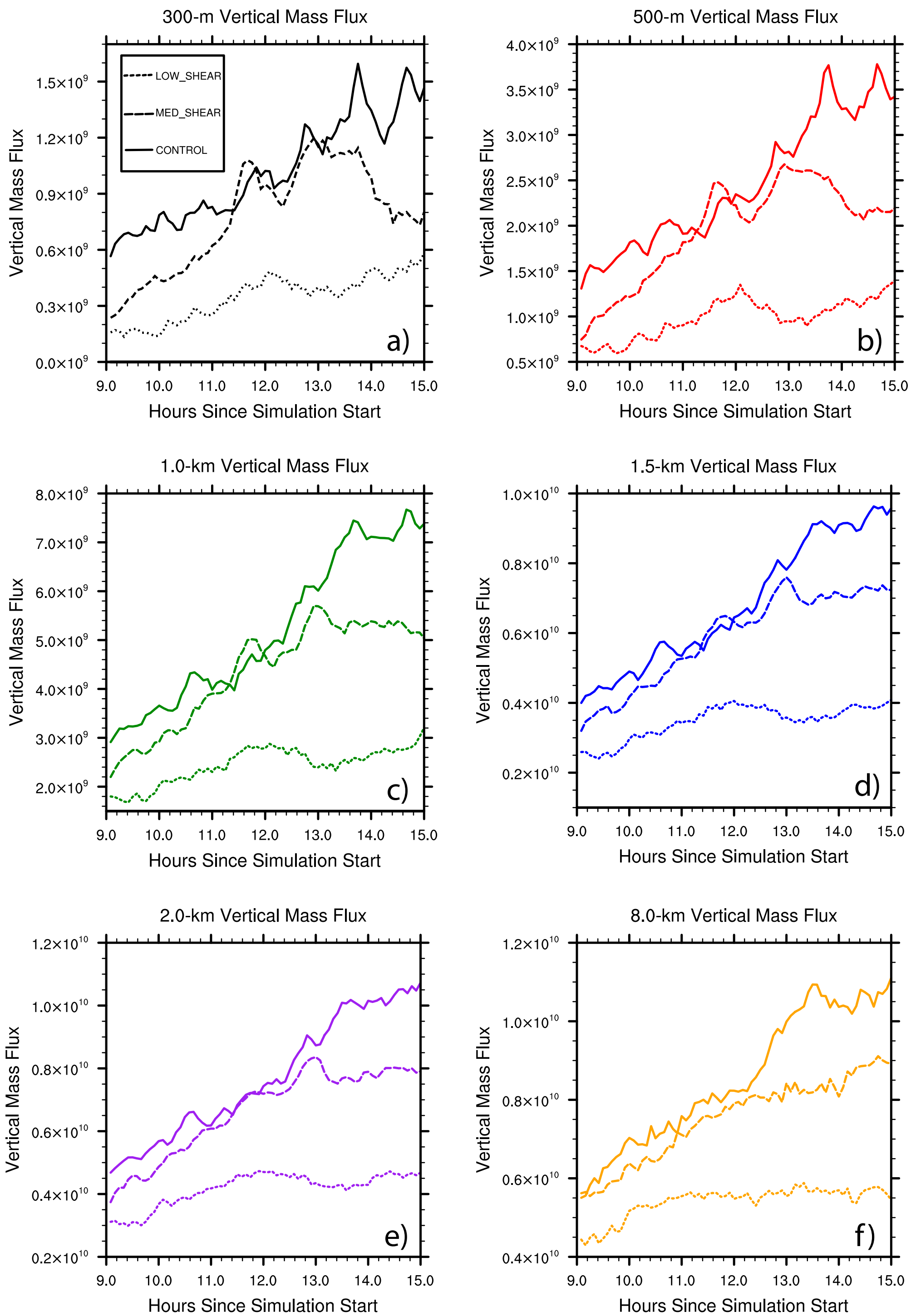

FIG. 3.13. Total vertical mass flux (g s^{-1}) of updrafts with magnitude over 1 m s^{-1} over the portion of the domain containing the modeled MCS at z = (a) 300 m, (b) 500 m, (c) 1.0 km, (d) 1.5 km, (e) 2.0 km, and (e) 8.0 km for the CONTROL (solid line), MED_SHEAR (long dashed line), and LOW_SHEAR (short dashed line) runs. The scale of the ordinate is different in each panel. The areal averaging was performed over the spatial extent of the model domain depicted in Fig. 3.5-3.8.

This is not seen in the control simulation from Schumacher (2015b) (Fig. 3.12d), which used a wind profile with weak deep-layer shear and featured an MCS with little low-level rotation.

Large differences are seen in the low-level total positive vertical mass flux from updrafts (Fig. 3.13). A substantial and noteworthy increase in low-level positive vertical mass flux is seen for the CONTROL simulation versus the MED_SHEAR and LOW_SHEAR runs (Fig. 3.13) by the end of the simulations. These differences, especially between the CONTROL and LOW_SHEAR runs, are maintained through all levels (Fig. 3.13b-d) with the vertical mass flux at each vertical level ordered to the amount of low-level shear (and the amount of low-level vertical rotation, Fig. 3.10) in each simulation (i.e., higher 0–1 km shear has higher vertical mass flux, Fig. 3.13). These vertical mass flux differences illustrate the net effect of the large low-level vertical velocity differences seen between each simulation (cf. Fig. 3.10 and Fig. 3.13). The differences in vertical mass flux are greatest between the CONTROL and LOW_SHEAR simulations. The MED_SHEAR run maintains vertical mass flux values that are much closer in magnitude to the CONTROL simulation above the lowest levels (Fig. 3.13), but both simulations maintain substantially larger vertical mass flux values when compared to the LOW_SHEAR run. The large reduction in vertical mass flux near t=13 h at low levels in the MED_SHEAR (Fig. 3.13a,b) run is likely due to the cold pool undercutting the most intense, rotation-containing convection on the southern flank of the storm (Fig. 3.7c). The MED_SHEAR and LOW_SHEAR runs develop cold pools with horizontal scales matching that of the storm itself and maximum θ' depressions at 500 m of $\theta' \sim -2.5$K, while the cold pool in the CONTROL simulation is weaker, maximum θ' depressions at 500 m of $\theta' \sim -1.5$ to -2.0K, and has less spatial extent (see Figs. 3.6-3.8). Considering the greater rainfall in CONTROL (and thus larger quantity of hydrometeors), it is unclear why the cold pool remains weak compared to the lower-shear runs.

Given that intense updrafts are present at and below 500 m in the CONTROL, MED_SHEAR, and LOW_SHEAR runs and that these updrafts are ingesting high concentrations of passive tracers from within an inhibited boundary layer, the horizontal characteristics of the VPPGF at or near 500 m were a focus of the pressure retrieval diagnostics. While VPPGF accelerations are present at other vertical levels in the simulations, the nature of the rotation (i.e., largest in lower levels) leads to the largest VPPGF being found in low levels.

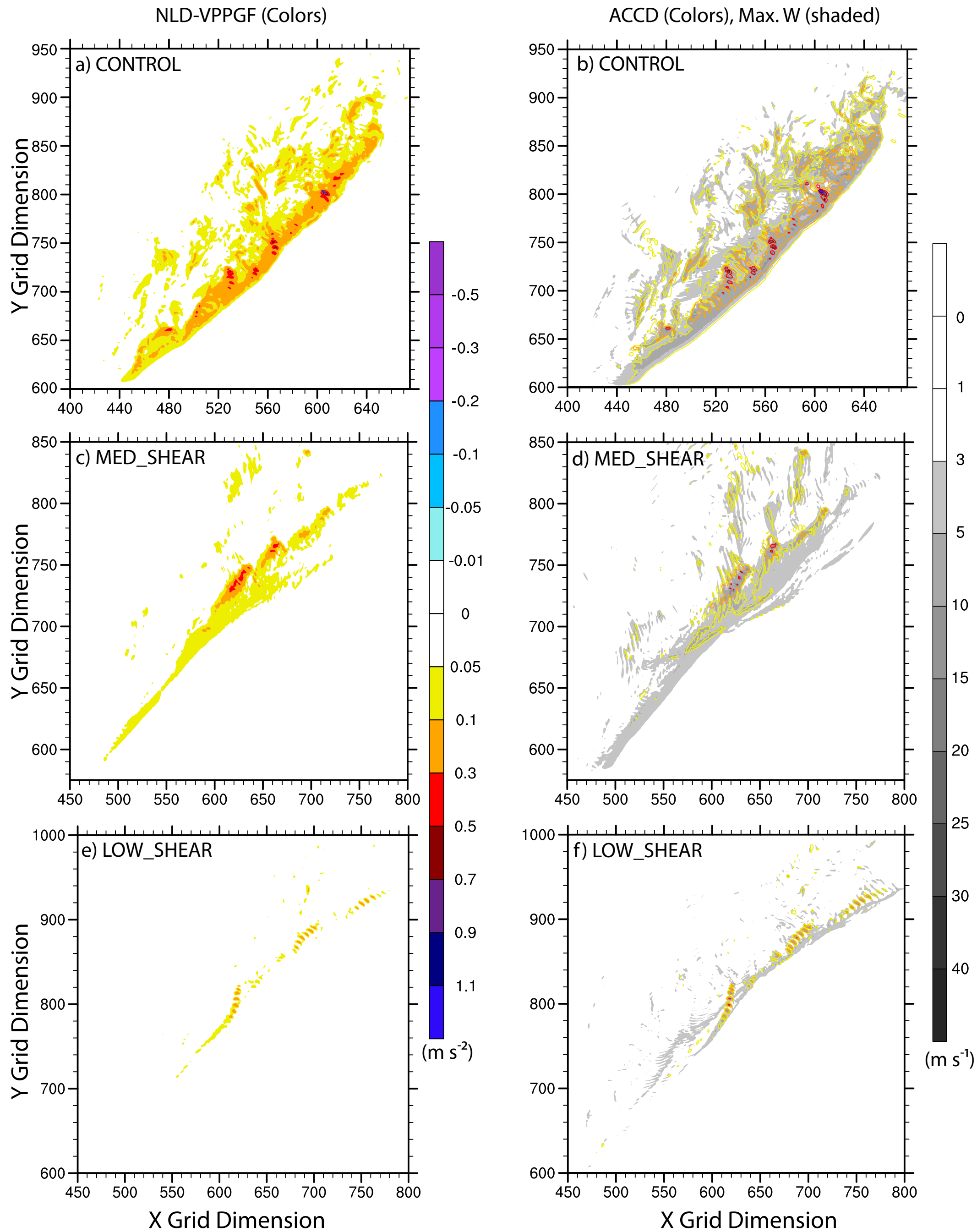

FIG. 3.14. Translated swaths of maximum 500 m dynamic nonlinear vertical perturbation pressure gradient acceleration (NLD-VPPGF; shaded m s^{-2}) valid from t=9 to t=15 h into the (a) CONTROL, (c) MED_SHEAR, and (e) LOW_SHEAR simulations. (b,d,f) translated swaths of maximum 500 m vertical velocity (shaded; m s^{-1}), with maximum 500 m total dynamic acceleration (ACCD; contoured; colors match fill contour values in (a,c,e)) overlaid for the (b) CONTROL, (d) MED_SHEAR, and (f) LOW_SHEAR run valid from t=9 to t=15 h into the simulations. Axes depict model grid points where grid spacing between points is 500 m.

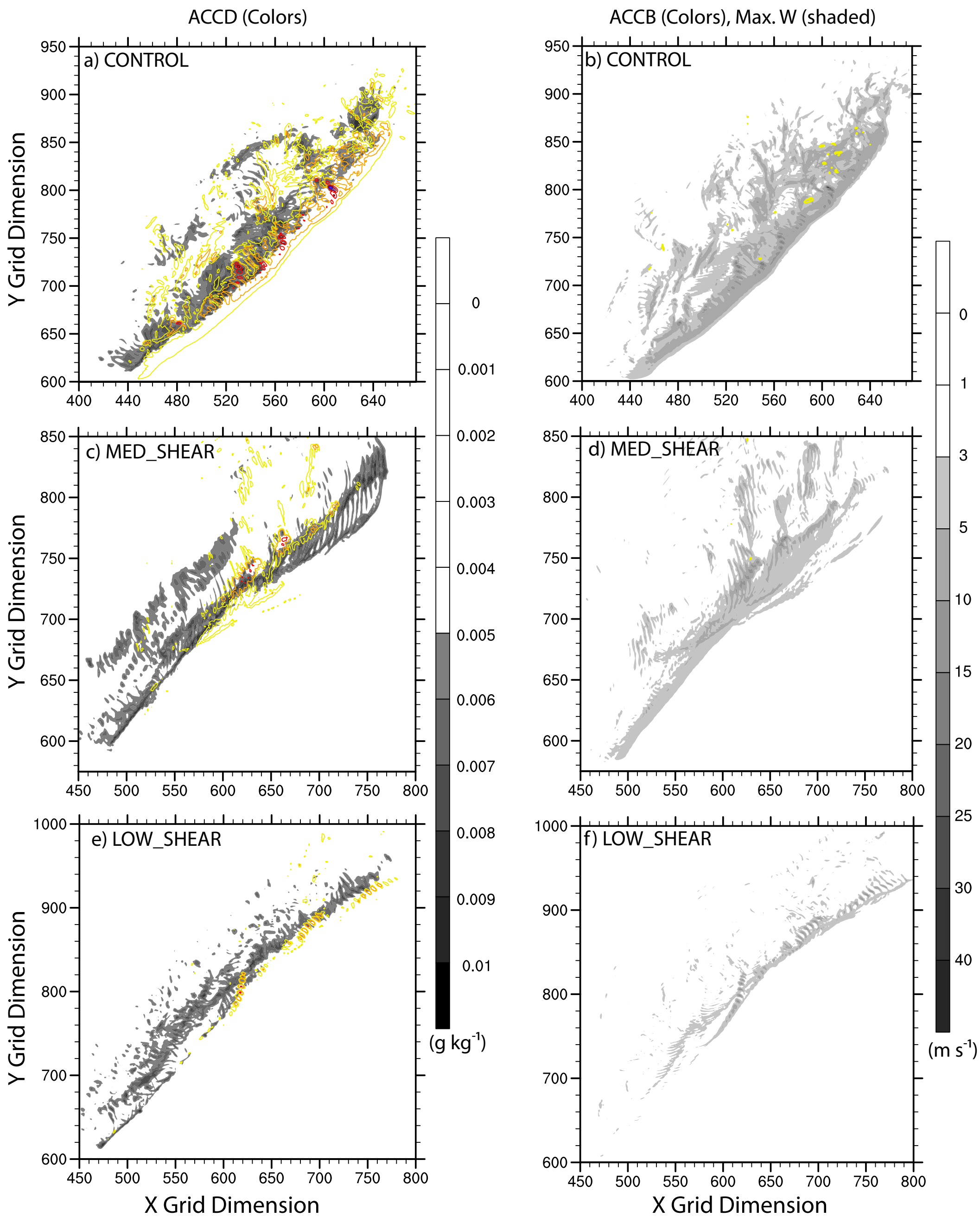

FIG. 3.15. (a,c,e) translated swaths of maximum 500 m maximum total condensate mixing ratio (left column, shaded; g kg^{-1}), with maximum 500 m ACCD (contoured; colors match fill contour values in Fig. 3.14a,c,e) overlaid for the (a) CONTROL, (c) MED_SHEAR, and (e) LOW_SHEAR run valid from t=9 to t=15 h into the simulations. (b,d,f) translated swaths of maximum 500 m vertical velocity (right column), w (shaded; m s^{-1}), with maximum 500 m total buoyant acceleration (contoured; colors match fill contour values in Fig. 3.14a,c,e) overlaid for the (b) CONTROL, (d) MED_SHEAR, and (f) LOW_SHEAR run valid from t=9 to t=15 h into the simulations. Axes depict model grid points where grid spacing between points is 500 m.

The analysis was mainly accomplished by creating translated swaths (i.e., map views from t=9-15 h where the plotting accounts for the numerical model domain translation speed) of maximum dynamic forcing terms at 500 m at any grid point, which can be interpreted similar to maximum updraft helicity swaths (e.g., Clark et al. 2013) used in severe storms forecasting (e.g., Fig. 3.14a,c,e). The resulting analysis shows that intense, persistent low-level acceleration associated with the NLD-VPPGF is present in the CONTROL run, but is continually less persistent and intense in the MED_SHEAR and LOW_SHEAR simulations (cf. Fig. 3.14a,c,e). The signature of individual rotating updrafts and cyclic mesocyclogenesis (e.g., Adlerman et al. 1999) can be seen in all simulations, but is especially noticeable for a couple instances the LOW_SHEAR run (Fig. 3.14e). This reinforces the notion that the CONTROL run (and to some extent the MED_SHEAR simulation) maintains persistent rotation and the associated low-level acceleration, which is comparatively intense (cf. Fig. 3.14a,c,e), over a large portion of the domain, as opposed to the few brief isolated spin ups seen in the LOW_SHEAR run. When both acceleration from the NLD-VPPGF and the linear dynamic VPPGF (see Eqn. 3) is taken into account to create the total dynamic acceleration (ACCD), a very similar low level acceleration to that associated with the NLD-VPPGF is seen (cf. fill contours in Fig. 3.14a,c,e to contours in Fig. 3.14b,d,f). This implies that the NLD-VPPGF dominates the total low-level dynamic acceleration in these simulations.

The influence of the low-level ACCD on the low-level vertical velocity field is quite apparent in the non-Coriolis simulations (Fig. 3.14b,d,f). A clear correlation, especially in the CONTROL run, exists between the most intense low-level updrafts and the location of the greatest ACCD. This shows the importance of the ACCD in getting intense, in some cases up to 20 m s^{-1}, updrafts near the surface (i.e., 500 m) when the parcels themselves are conditionally stable. This is further reinforced by relative lack of total positive buoyant acceleration (ACCB, see Eqn. 3) of a similar magnitude in any of the simulations near the surface (e.g., lack of color contours in Fig. 3.15b,d,f). The extent and magnitude of the 500-m updrafts between the CONTROL, MED_SHEAR, and LOW_SHEAR runs increases with the extent and magnitude of the NLD-VPPGF at that same level, which also intensifies with the amount of 0–1km shear in the base state kinematic profile of each simulation. The highest low-level total condensate mixing ratios (e.g., Fig. 3.15a,c,e) are offset from the region of largest ACCD (and corresponding updrafts) with the breadth and maximum of the condensate values increasing with 0–1km shear values.

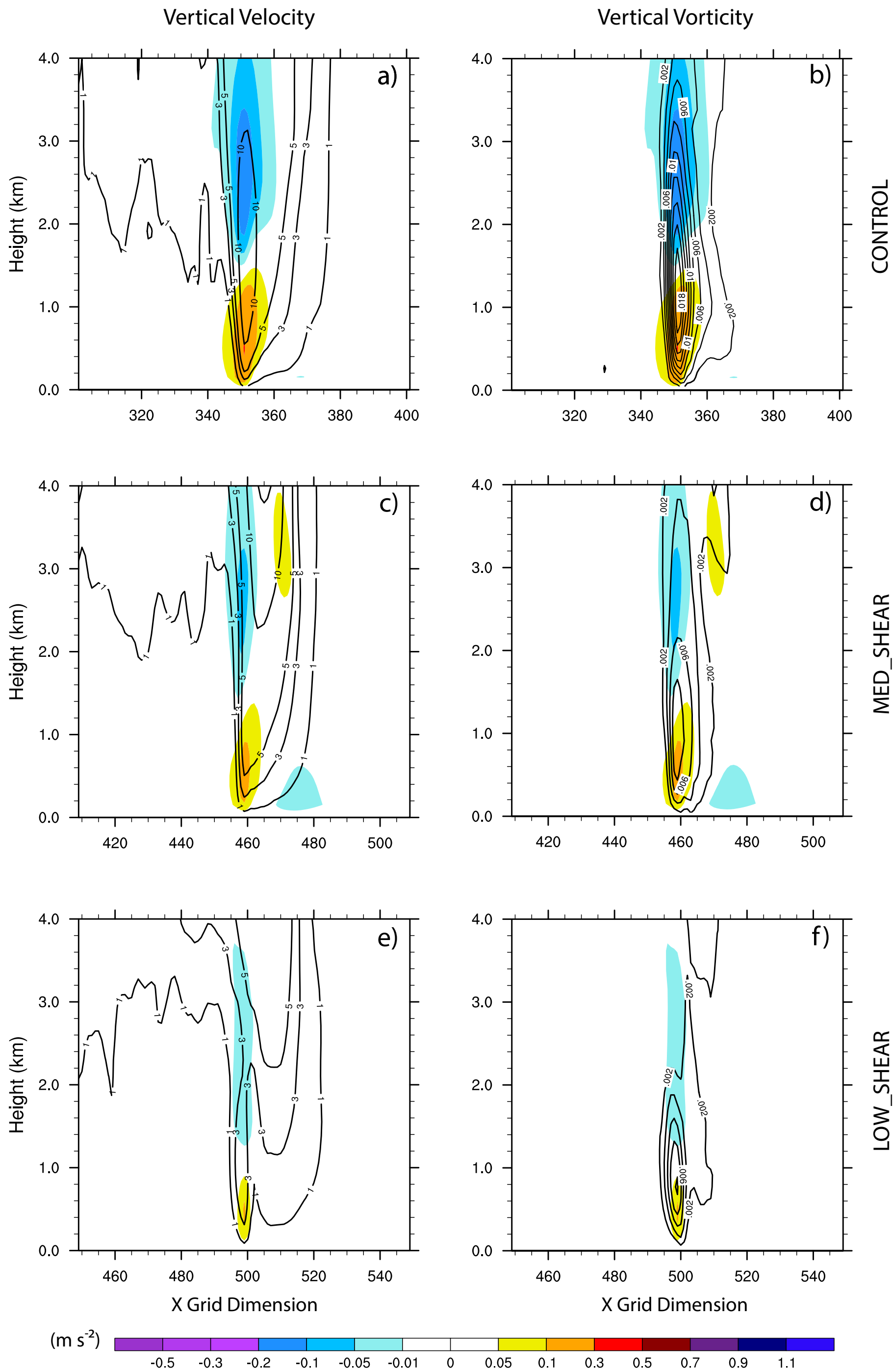

FIG. 3.16. Time mean east-west cross sections through the point of maximum 500 m NLD-VPPGF acceleration (fill contour; m s^{-2}) overlaid with the corresponding mean vertical velocity (left column; contoured at 1 m s^{-1}, 3 m s^{-1}, then every 5 m s^{-1} above 5 m s^{-1}), and vertical vorticity (right column; contoured every 5×10^{-3} s^{-1} above 5×10^{-3} s^{-1}) for the CONTROL (top row), MED_SHEAR (middle row), and LOW_SHEAR (bottom row) simulations. x-axis depicts model grid points where grid spacing between points is 500 m.

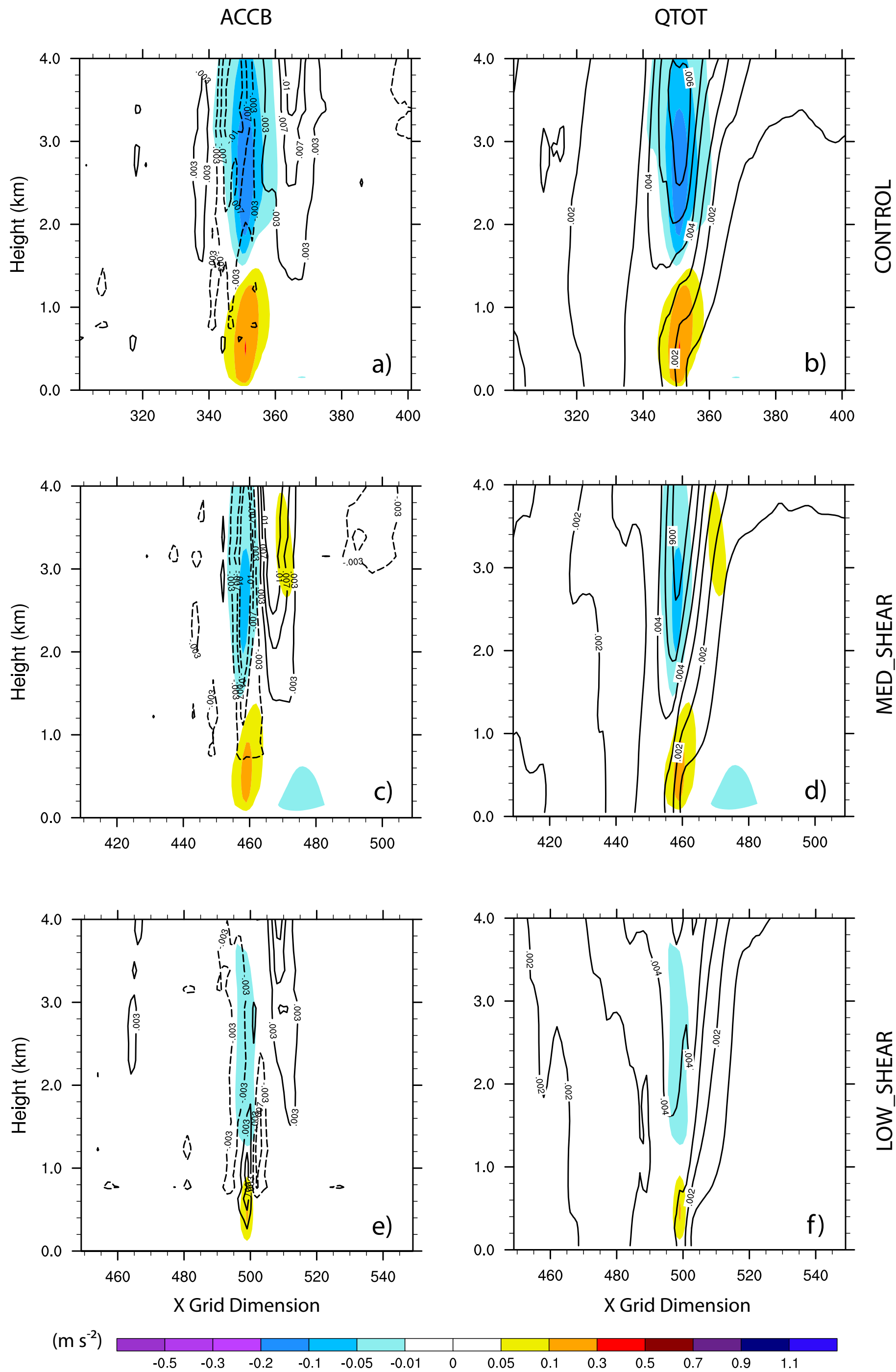

FIG. 3.17. Time mean east-west cross sections through the point of maximum 500 m NLD-VPPGF acceleration (fill contour; m s^{-2}) overlaid with the corresponding total condensate mixing ratio (QTOT, left column; contoured every 0.01 g kg^{-1}), and ACCB (right column; solid contours (dashed) positive (negative) values at ± 0.003, ± 0.007, and ± 0.01 m s^{-2}) for the CONTROL (top row), MED_SHEAR (middle row), and LOW_SHEAR (bottom row) simulations. x-axis depicts model grid points where grid spacing between points is 500 m.

The vertical extent and magnitude of the NLD-VPPGF is maximized in the CONTROL simulation (cf. Fig. 3.16a,c,e) with diminishing values in both depth and intensity when moving sequentially to the lower shear runs (i.e., to MED_SHEAR and LOW_SHEAR, respectively). This in turn leads to more intense updrafts closer to ground level as the low-level shear increases (and with that the low-level rotation) with time mean 10 m s^{-1}, 5 m s^{-1}, and 3 m s^{-1} updrafts sustained below 1 km for the CONTROL, MED_SHEAR, and LOW_SHEAR runs, respectively (Fig. 3.16a,c,e). The cross sections show that ACCB is present in the low-levels of each simulation, but the largest values are maximized above 2 km in height (Fig. 3.17a,c,e) with little to no positive (in most cases negative) ACCB present in the lowest levels. Additionally, the ACCB that is present is an order of magnitude less than the acceleration associated with the NLD-VPPGF, which is not necessarily surprising given the nature of the forcing and the initial thermodynamic profile. Mean low-level total condensate mixing ratios also increase with increasing mean low-level updraft strength (Fig. 3.17b,d,f), which intensifies with the amount of low-level acceleration form the NLD-VPPGF and 0–1 km vertical wind shear. The more intense lower updrafts lead to increased volume of higher mean total condensate values (i.e., the breadth of higher magnitude mean total condensate contours is larger at a given level) lower in the atmospheric column in the higher shear runs (Fig. 3.17b,d,f). This seems to show the enhancement of precipitation formation processes by the NLD-VPPGF forced low-level updrafts in the runs with higher low-level vertical wind shear.

While the pressure decomposition undertaken here does not explicitly separate NLD-VPPGF term into the accelerations associated with spin and those associated with deformation (i.e., the “splat” term in Eqn. 4), the terms do produce oppositely signed pressure perturbations. Thus, if negative pressure perturbation from the dynamic non-linear term exists (which we have quantitatively and numerically explicitly solved for), it is because the “spin” term is dominating over the “splat” term. The vertical low-level accelerations presented in this manuscript are largely associated with negative non-linear dynamic pressure perturbations (Fig. 3.18), which implies that the “spin” term is dominating over the deformation term in these dynamically forced updrafts. Persistent low-to-mid-level vertical rotation is present at the location of maximum NLD-VPPGF acceleration in all three simulations (Fig. 3.16b,d,f). The vertical depth and mean magnitude of the vertical rotation increases with the increase in low-level shear through the simulations (cf. Fig. 3.16b,d,f). Correspondingly, the magnitude and depth of the positive acceleration associated with the NLD-VPPGF increases with increasing vertical vorticity (fill colors in Fig. 3.16b,d,f). These spatial relationships hold in the mean sense (i.e., Fig. 3.16b,d,f), but also are seen in the regular temporal and spatial collocation of vertical vorticity and NLD-VPPGF associated acceleration at individual times throughout all three of the simulations (see supplemental material for animations).

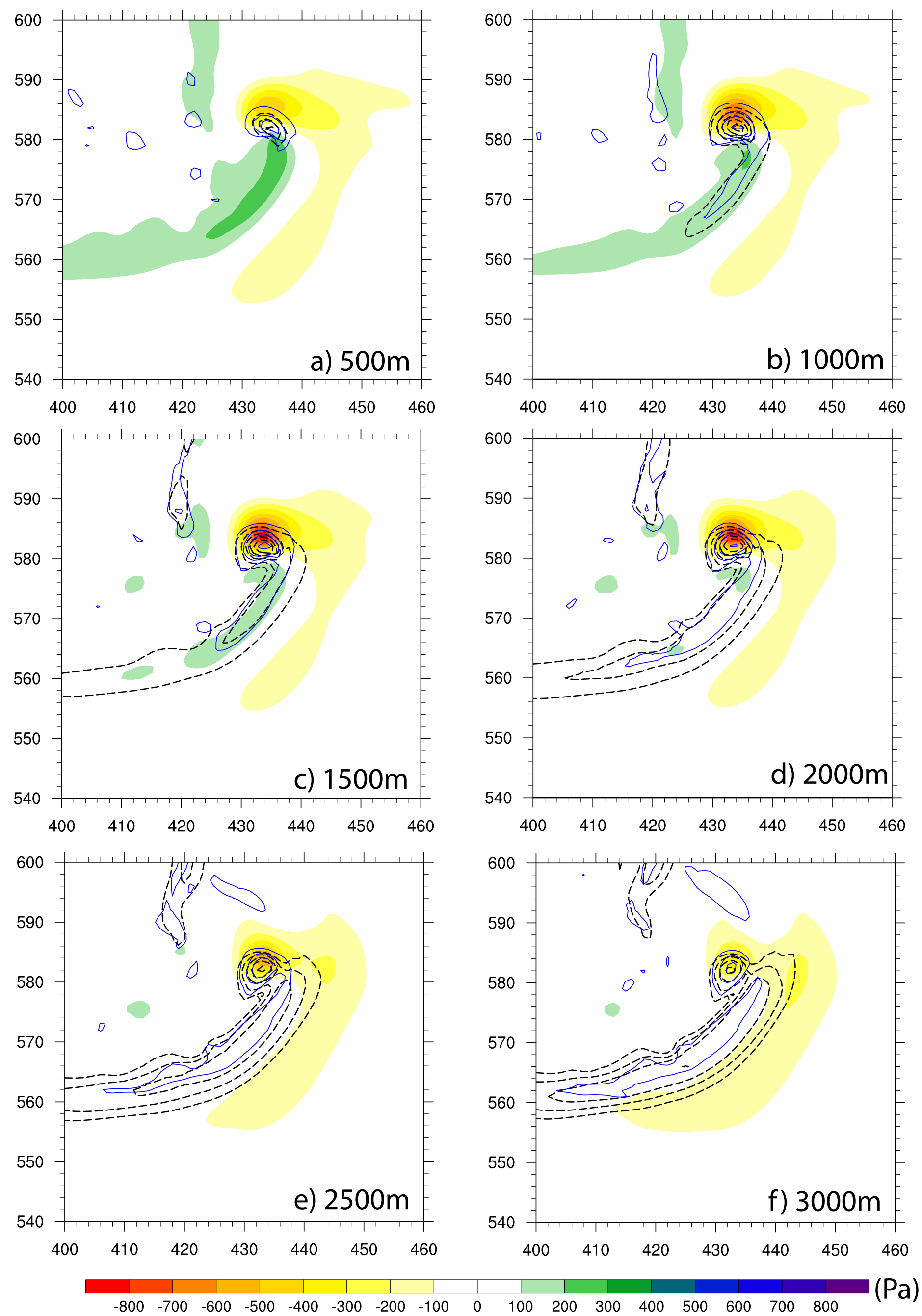

FIG. 3.18. Dynamic non-linear perturbation pressure (shaded, Pa), vertical velocity (black dashed lines contoured every 5 m s^{-1} started at 10 m s^{-1}), and vertical vorticity (blue contours at 0.01, 0.02, 0.03, and 0.05 s^{-1}) for the CONTROL simulation 11 hr and 55 minutes into the run at (a) 500 m, (b) 1000 m, (c) 1500 m, (d) 2000 m, (e) 2500 m, and (f) 3000 m above the ground.

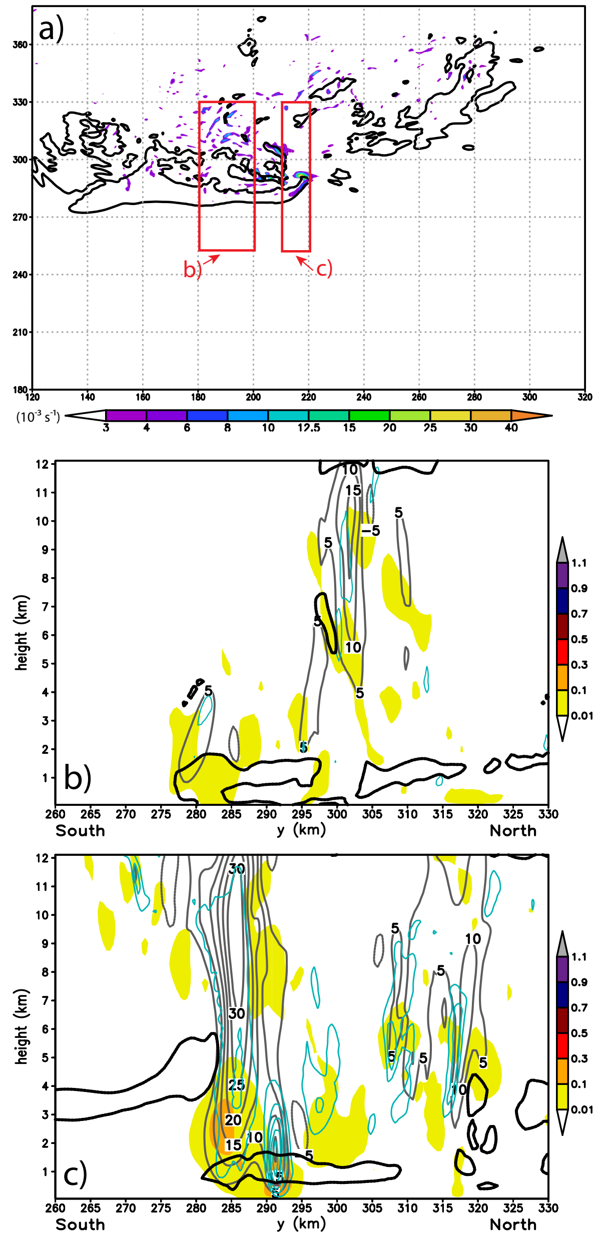

FIG. 3.19. (a) 500 m vertical vorticity ($\times10^{-3}$ s^{-1}) and surface perturbation potential temperature ($\theta^{'}$; -0.5 K contoured in black), for the CONTROL simulation 11 hr and 55 min into the model run. Red boxes in (a) indicate the east-west extend over which the north-south vertical cross sections in (b) and (c) were averaged. (b) average north-south vertical cross section of dynamic nonlinear vertical perturbation pressure gradient acceleration (NLD-VPPGF; shaded m s^{-2}), perturbation potential temperature ($\theta^{'}$; -0.5 K contoured in black), vertical velocity (w; grey contours; contoured every 5 m s^{-1}), and vertical vorticity (cyan contours, contoured every 5$\times10^{-3}$ s^{-1} above 5$\times10^{-3}$ s^{-1}) for red box labeled (b) in panel (a). (c) same as (b), but valid over the red box labeled (c) in (a).

The continued collocated of the NLD-VPPGF acceleration and vertical vorticity, in the bulk sense (i.e., described by the mean cross sections), support the idea that the “spin" portion of the NLD-VPPGF is playing the primary role in enhancing the low-level acceleration and, thus, updrafts. Specifically examining the CONTROL simulation during the mature phase of the storm (i.e., Fig. 3.19 at t= 11 h 55 m), the main storm-scale region of surface based vertical motion is collocated with the region of significant vertical vorticity and NLD-VPPGF acceleration (Fig. 3.19a,c), where, as the pressure perturbation theory suggests, the NLD-VPPGF accelerations are maximized below the levels of maximum rotation. In this region where the embedded supercells are present, w exceeds 15 m s^{-1} within the originally stable boundary layer, just above the regions of most intense NLD-VPPGF accelerations, which is collocated with regions of intense rotation around the vertical axis (Fig. 3.19a,c). The mid-to-upper level updrafts are also maximized above the low-level regions of NLD-VPPGF associated acceleration (Fig. 3.19c). Lifting along the cold pool at this time in the CONTROL run is much shallower and weaker (Fig. 3.19a,b). While very weak acceleration, compared to the regions where rotation is present, associated with the NLD-VPPGF is seen, the resulting combination of this lift and traditional cold pool lifting results in a shallow updraft that does not extend through the mid-levels (Fig. 3.19b). While this lifting along the cold pool edge is more persistent in other simulations (not shown), it is regularly weaker and more elevated than that associated with rotating updrafts, due to the enhancement of the NLD-VPPGF. Additionally, the theta perturbations (Fig. 3.19b,c) appear to be elevated off the surface, centered largely near 1 km, which is likely a results of the stability in the low-levels of the initial thermodynamic profile. This hints that gravity wave processes might be acting along with the cold pool to lift parcels along the flanks of the system (as in Schumacher 2009).

3.5 RESULTS: CORIOLIS SIMULATIONS

When the Coriolis force is taken into account for kinematic profiles with the highest (i.e., CONTROL_COR) and lowest (i.e., LOW_SHEAR_COR) 0–1 km shear, very little change is seen in the MCS's evolution compared to the runs without the inclusion of the Coriolis force. The CONTROL_COR and LOW_SHEAR_COR both produce a back building type MCS (Fig. 3.20a,b) similar in both spatial appearance and the low-level vortex characteristics to the non-Coriolis simulations (cf. Fig. 3.20c-d to Fig. 3.7). However, the runs that include Coriolis produce less mean areal precipitation, but similar maximum values when compared to the runs without Coriolis (Table 3.2). This seems to be most likely associated with the CONTROL_COR and LOW_SHEAR_COR runs producing smaller convective systems (cf. Fig. 3.20a-b to Fig. 3.7a,e). The differing system sizes can likely be exampled by the Coriolis simulations having a finite Rossby radius, compared to an infinite Rossby radius in the simulations without Coriolis.

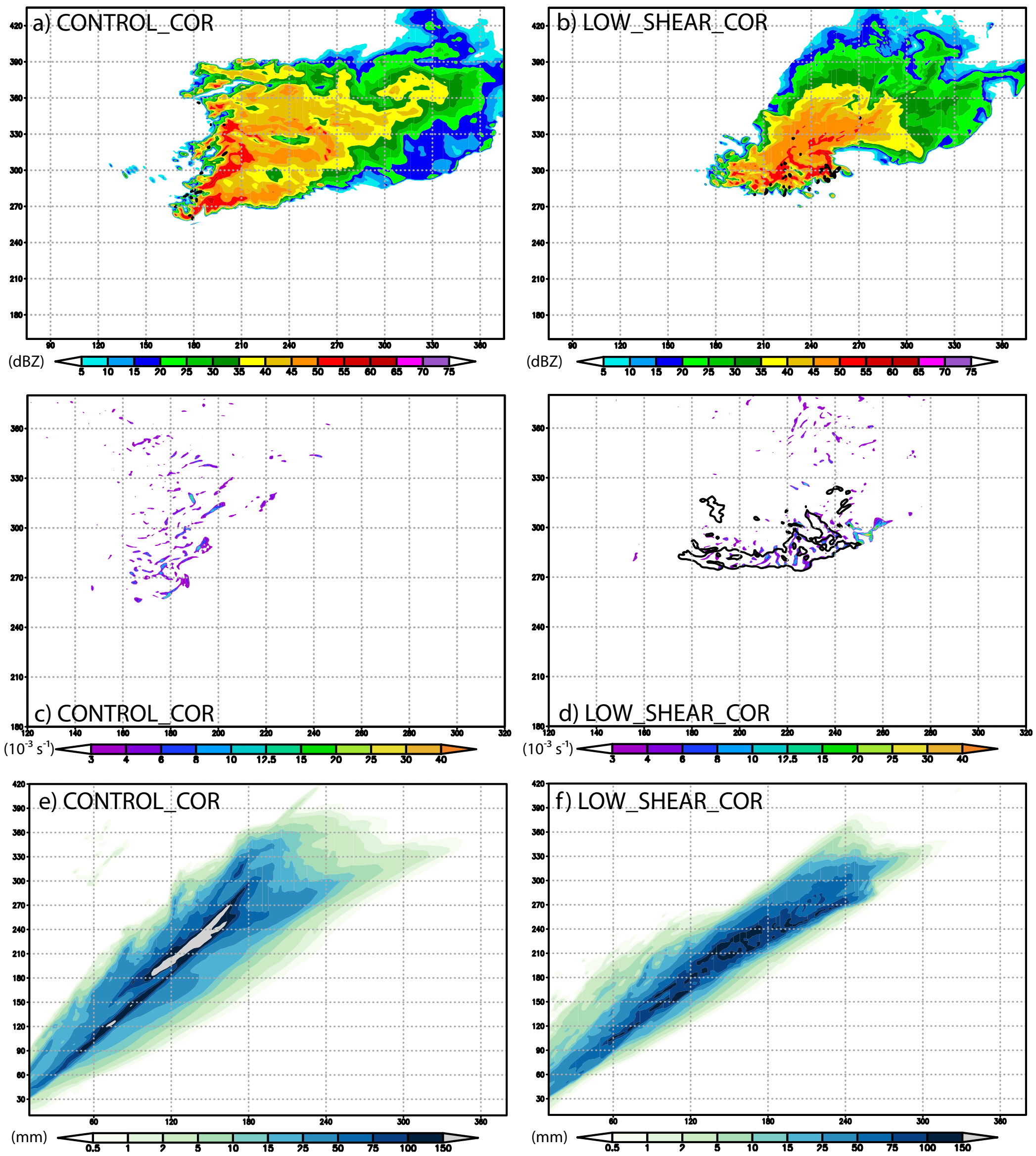

FIG. 3.20. (a-b) Simulated 1 km radar reflectivity (shaded; every 5 dBZ from 5dBZ to 70 dBZ), surface perturbation potential temperature (θ'; contoured at -1.5 and -2.5 K in dark purple and magenta, respectively), and contoured 1 km vertical vorticity (black contours; starting at 10.0×10^{-3} s^{-1} every 5.0×10^{-3} s^{-1}) valid 13 hours into the simulation for the (a) CONTROL_COR and (b) LOW_SHEAR_COR simulations. (c-d) 1 km vertical vorticity ($\times 10^{-3}$ s^{-1}) for the (c) CONTROL_COR and (d) LOW_SHEAR_COR simulations valid at the same time as (a-b). Translated total accumulated precipitation (mm) in (e) CONTROL_COR and (f) LOW_SHEAR_COR simulations. Run specific statistics are presented in Table 3.2.

Stronger, more sustained rotation is seen in the CONTROL_COR run (brief snapshot presented in Fig. 3.20c,d), compared to the LOW_SHEAR_COR simulation. As in the CONTROL and LOW_SHEAR runs, the CONTROL_COR and LOW_SHEAR_COR simulations produce a very weak but quite extensive cold pool, respectively, by t=13 h into the model integration (Fig. 3.20a,b). Further, the CONTROL_COR run produces more run accumulated total precipitation, areal average precipitation, and domain coverage of largest accumulation amounts (Fig. 3.20e,f, Table 3.2). Higher mean and maximum low-level updrafts are seen in the CONTROL_COR run compared to the LOW_SHEAR_COR (not shown), again following a similar pattern to the non-Coriolis simulations. While an in-depth analysis of perturbation pressure fields for the CONTROL_COR and LOW_SHEAR_COR is not presented in this manuscript, the similarities in the MCS morphology, vortex development, updraft strengths, the accumulated precipitation, and how these characteristics scale with the 0–1km shear between the runs with and without Coriolis suggest that the mechanisms discussed above are not strongly sensitive to planetary rotation.

3.6 Summary, Discussion, and Conclusions

In summary, high intensity, short term extreme rainfall accumulations have been observed with concurrent and near collocated mesoscale rotation. One such event that occurred in south-central Texas on 30 October 2015 served as motivation for several numerical simulations to determine the effects of intense 0–1 km low-level shear and the resulting rotation on the accumulated precipitation. Various storm-scale aspects of the simulations were analyzed with a focus given to those related to precipitation intensity. Further, accelerations associated with the buoyant and dynamic components (i.e., linear and non-linear) of the vertical perturbation pressure gradient force were calculated for each simulation to examine potential sources of vertical momentum not associated with thermodynamic buoyancy.

The resulting simulations produced similar MCSs with embedded supercells that all produced low-level vertical rotation, albeit at various strengths. The simulations with more intense 0–1 km shear produced higher precipitation accumulations in the mean, point maximum, and domain coverage of the highest accumulations. Further, the strength and longevity of the low-level rotation increased with 0–1 km shear magnitude. Similarly, the areal mean and maximum low-level updrafts increased with increasing 0–1km shear, as did the resulting low-level mass flux. Parcels in all of the simulations were regularly lifted out of the thermodynamically stable boundary layer, where cold pool development is limited in the CONTROL simulation compared to the other lower shear runs. Accelerations from the

NLD-VPPGF were found to dominate in the low-levels over both linear dynamic and total buoyancy accelerations. These accelerations were found to increase in spatial extent, magnitude, and longevity as the 0–1 km shear increased (i.e., from the CONTROL to the MED_SHEAR to the LOW_SHEAR runs), consistent with other studies. This is not surprising given that horizontal rotation can contribute to the NLD-VPPGF (i.e., Eqn. 4), which in turn is highly correlated with large values of 0–1 km shear. The higher NLD-VPPGF accelerations, which are an order of magnitude higher than the total buoyancy accelerations (ACCB) at low-levels, lead to lower, more intense updrafts in the simulations with stronger low-level shear.

The results of these simulations highlight the potential for mesocyclones or other meso-γ-scale vortices associated with intense 0–1 km shear to enhance precipitation processes by enhancing low-level updrafts and, depending on the environmental thermodynamic profile, tapping into sources of moisture and instability that are otherwise difficult to ingest into the storm. The collocations of NLD-VPPGF associated acceleration with rotation (Figs. 3.16b,d,f and 3.19c), presence of low-level tracers at upper levels, the persistent increase in low-level mass flux (Fig. 3.13), updraft strength (Fig. 3.10), and the total accumulated precipitation (Fig. 3.9) in the CONTROL run versus the lower shear simulations (i.e., MED_SHEAR and LOW_SHEAR) illustrates these points well. Previous literature has established that 0–1 km shear is conducive for tornado development because it effectively lowers the base of the mid-level mesocyclone (e.g., Markowski et al. 2012; Markowski and Richardson 2014; Coffer and Parker 2015), which, in turn, makes it easier for the NLD-VPPGF associated with the rotation to lift negatively buoyant air (e.g., Nowotarski et al. 2011; Davenport and Parker 2015) from both the boundary layer and the cold pool. While the focus in this previous work was on the ability of the NLD-VPPGF to interact with baroclinically generated horizontal vorticity to lead to tornadogenesis, the experiments conducted in this study show that the same physical processes can simultaneously act to increase the ingredients needed for extreme rain rates. The enhancement of low-level updrafts, w in Eqn. 2, and the potential associated increase in the availability of moisture and CAPE, q in Eqn. 2, that otherwise would not be available to the system (e.g., Schumacher 2015b) leads to an increase in the instantaneous rain rate, R in Eqn. 2. Further, as suggested in the tornado literature, it is plausible that a positive feedback can occur between the initial rotation, enhancement of the updraft with the NLD-VPPGF, and increased rotation (e.g., Coffer and Parker 2015). Additionally, the longevity of MCSs and supercells, such as those simulated above, would also allow for potential feedbacks between precipitation process and rotation to occur, due to diabatic heating (e.g., Raymond and Jiang 1990; Weijenborg et al. 2017).

Note that the increase in 0–1 km shear from the LOW_SHEAR to CONTROL run increases the strength of the storm-relative inflow and resultant moisture flux into the storm, which affects q and E in Eqn. 2. The approximate increase in storm-relative inflow between each simulation is mainly related to the increase in wind speed through the 0–1 km layer, since the layer moisture content and approximate storm motions are the same for each simulation. This increase in storm-relative moisture flux is quite substantial, near 30 %, between the LOW_SHEAR and CONTROL simulations at 500 m, and is a compounding factor, along with the increase in low-level vertical motion, in the modeled increase in accumulated precipitation as 0–1 km shear increases. However, a ∼60% increase in mean precipitation is seen from the LOW_SHEAR run to the CONTROL simulation, which cannot be explained by the increase in inflow alone. Further, the thermodynamically stable, moisture laden air in the storm inflow still needs to be lifted out of the boundary layer, which is accomplished more effectively, compared to the lower-shear simulations, by the rotationally induced NLD-VPPGF in the CONTROL run that is also related to the magnitude of the 0–1 km shear. In other words, the increase in low-level storm relative inflow as the 0–1 km shear increases is likely working in addition to the NLD-VPPGF to enhance precipitation accumulations in instances of intense 0–1 km shear, though the influences of each individual process are difficult to isolate. Additionally, since only one thermodynamic profile was tested, thermodynamic sensitivities assuredly exist for the processes discussed in this manuscript.

The presence of intense 0–1 km shear (e.g., for various storm modes, Tuttle and Davis 2006; Morin and Parker 2011; Markowski and Richardson 2014) and the development of isolated rotation or embedded rotation in MCSs/MCVs (e.g., Morales et al. 2015), tropical cyclone rainbands (e.g. Edwards et al. 2012; Wang et al. 2015), and supercells, in theory, means that precipitation enhancement, as described in the manuscript, could be seen in many different storm morphologies. This mechanism can serve to explain why supercells are often associated with intense rain rates, despite low precipitation efficiency (e.g., Smith et al. 2001; Duda and Gallus 2010; Hitchens and Brooks 2013). The enhancement of vertical momentum and, thus, precipitation by these mechanisms does not, in principle, preclude the formation of a tornado, since the same mechanisms (i.e., intense, dynamically induced updrafts near the surface) are favorable for tornadogenesis (e.g., Markowski and Richardson 2014). Additionally, the potential for simultaneous enhancement of both rainfall intensity and tornado potential provides a potential explanation for the observed frequency, around 80 events per year between 2003-2015 (Nielsen et al. 2017), of concurrent, collocated tornado and flash flood events, TORFFs, that occur in isolated supercells, organized MCSs, and tropical cyclones (Nielsen et al. 2015) without any clear dependence on storm motion (Bunkers and Doswell 2016; Nielsen et al. 2016a).

In conclusion, precipitation systems in intense 0–1 km shear that develop mesoscale rotation can aid in producing extreme precipitation by enhancing the magnitude of low-level updrafts through accelerations associated with rotationally induced non-linear dynamic vertical perturbation pressure gradient forces. The resulting increase in low-level vertical motion can further serve to enhance precipitation, depending on the environmental conditions, by ingesting otherwise negatively buoyant parcels that still contain moisture and CAPE. These precipitation enhancements could be more pronounced in situations where thermodynamic buoyancy is limited and moisture is abundant. Ongoing work is examining rain gauge and gridded precipitation data to determine the propensity for extreme, short term rainfall accumulations (i.e., greater than 75 mm hr^{-1}) to be associated with near concurrent, collocated mesoscale rotation outside of the motivating case presented in this research.

CHAPTER 4

Observations of Extreme Short-term Precipitation Associated with Supercells and Mesovortices

4.1 Introduction

Flash flooding continues to pose a substantial threat to life, property, and infrastructure throughout the United States. Even with increased societal awareness and civil mitigation, there has been no appreciable decrease in the number of flash flood fatalities in recent years (Ashley and Ashley 2008; Špitalar et al. 2014; Terti et al. 2017). Since 2003, flash flooding has been responsible for 10% of all weather-related fatalities and 20% of all weather-related property and crop-related damages in the United States, with 2015-2017 being the three most deadly of the last 15 years (NWS 2018b). Flash flooding differs from slow-rise flooding, such as riverine flooding, in that the rise of water is, by definition[1], rapid and presents a particular danger to people in cars (e.g., Ashley and Ashley 2008; Maples and Tiefenbacher 2009; Sharif et al. 2015; Terti et al. 2017) or in situations with inadequate structural protection and notification methods (e.g., Špitalar et al. 2014; Terti et al. 2017).

While the rapid rise in water is related to many static and non-static hydrologic characteristics including topography, soil moisture, and catchment specific runoff dynamics (e.g., Costa 1987; Hapuarachchi et al. 2011; Saharia et al. 2017), the accurate prediction of the location, amount, and rate of rainfall is essential to correctly infer the hydrologic impacts and inform the decision making process, especially when catchment dynamics and human decision making processes have similar response times (e.g., Creutin et al. 2009). While the numerical forecasting and real time estimation of extreme rainfall remains a challenge within the weather community (e.g., Fritsch and Carbone 2004; Novak et al. 2011; Zhang et al. 2016), forecasting advances are continually being made to improve the identification of flash flooding potential on multi-day (e.g., Herman and Schumacher 2018a,c) and nowcasting timescales (e.g., Gourley et al. 2017).

Not surprisingly, the longer and harder it rains, the higher the rainfall accumulation a location experiences. Events have occurred where either the average short-term rainfall rate (e.g., Smith et al. 2001; Hitchens and Brooks 2013), the duration/quasi-stationarity of the storms (e.g., Schumacher and Johnson 2005, 2009; Nielsen et al. 2016b), or long-term combination of the two (e.g., NWS 1999, 2011;

[1]Defined by the National Weather Service (NWS 2017) as "a damaging and life-threatening, rapid rise of water into a normally dry area beginning within minutes to multiple hours of the causative event (e.g., intense rainfall, dam failure, ice jam)."

Gochis et al. 2015) led to the extreme accumulation and attendant flash flooding. The ingredients for extreme rainfall are, broadly, well known (e.g., Doswell et al. 1996) and allow for the isolation of the synoptic-to-mesoscale ingredients that are conducive for flash flooding. Within the framework established by Doswell et al. (1996), the instantaneous rain rate, R, can be thought of as the product of the ascent rate, w; water vapor mixing ratio of the rising air, q; and the precipitation efficiency, E, a term that relates water vapor inflow to rainfall rate (i.e., $R = Ewq$). The rain rate seen by a specific location is known to be an important factor for runoff, soil erosion, and the resulting flood impacts, with the detrimental effects increasing for the more intense rainfall rates (e.g., Kandel et al. 2004; Mohamadi and Kavian 2015), which, in turn, can accelerate the resulting flash flood response (e.g., Kelsch et al. 2001; Kelsch 2001). For these reasons, it is important to investigate how often extreme rain rates are maintained and the meteorological conditions that support such convective systems.

Nielsen and Schumacher (2018) showed that the development of rotation around a vertical axis[2] in convective systems associated with intense 0–1 km shear can dynamically enhance the storm's low-level updrafts and aid in lifting convectively inhibited parcels that still contain moisture and convective available potential energy (CAPE). Examining these two dynamically included effects within the framework established by Doswell et al. (1996), it becomes clear that the presence of dynamic accelerations associated with rotation can potentially enhance the observed rain rates, since both the strength of the ascent rate (i.e., w) and water vapor mixing ratio (i.e., q) of the air ingested by the storm are potentially increased, all else being equal. This rain rate enhancement was demonstrated in Nielsen and Schumacher (2018) with three numerical simulations where the simulations with higher 0–1 km shear and corresponding increased rotation produced significantly larger rainfall totals. As discussed in Nielsen and Schumacher (2018), the presence of strong, dynamically forced updrafts at low-levels is also a favorable condition for tornadogenesis (e.g., Markowski and Richardson 2014). The ability for rotation to enhance precipitation and the associated parallel threat for a tornado serves as a dynamic explanation for the frequency of concurrent, collocated tornado and flash flood events (TORFF events, Nielsen et al. 2015) in various storm modes, both single-cell and multi-cell, without a clear reliance on storm duration or motion (Bunkers and Doswell 2016; Nielsen et al. 2016a). Such concurrent, collocated scenarios elevate the threat to life and property, since the recommended life saving actions for a tornado and flash flood scenario are contradictory[3].

[2]Throughout the rest of this manuscript, the word "rotation" will be used to denote rotation only around a vertical axis.

[3]During tornado threats, it is recommended that you retreat to the lowest, central room of a sturdy building. However, for flash flooding scenarios, it is recommended that you retreat to higher ground.

The numerical simulations performed in Nielsen and Schumacher (2018) were based upon a single extreme rainfall producing event in south-central Texas on 30-31 October 2015. While many other such events have been anecdotally noted by the authors and analyzed in a limited fashion by Smith et al. (2001) and Hitchens and Brooks (2013), a more complete examination of the distribution of extreme, short-term rainfall accumulations events has not been undertaken recently for the United States. This, combined with the recent results of Nielsen and Schumacher (2018), provide the motivation to examine such extreme rainfall events for the presence of rotation. The ultimate goal is to provide some idea of the frequency of extreme short-term rain rates and mesovortex collocation relative to other storm types using radar observations, and to create a case list of such collocations that can be used to examine the observed environmental characteristics associated with the events. This research tests the observational based tenants of the hypothesis presented in Nielsen and Schumacher (2018). That is, it is hypothesized that extreme, hourly rainfall accumulations are associated with rotation and elevated values of 0–1 km shear a non-negligible amount of the time (See Nielsen and Schumacher (2018) for more background discussion on this matter). Section 2 will present a few notable event examples, section 3 will present the methodology used, section 4 will present the results of the analysis, section 5 will present a discussion of the results, and section 6 the summary of the conclusions.

4.2 Notable Event Examples

Outside of the event discussed in detail in Nielsen and Schumacher (2018), a few prominent events associated with intense one hour precipitation accumulations over 75 mm and attendant rotation on various scales are briefly discussed in this section. Additionally, an example of a case without the presence of rotation is presented.

On 21 June 2013, a storm with supercellular characteristics moved through southeastern North Dakota (Fig. 4.1a,b) and was responsible for producing two tornado and flash flood local storm reports (LSRs; IEM 2017) near Valley City, North Dakota. No flash flood warnings were issued for this storm; however, the temporal and spatial offsets between the tornado and flash flood LSRs still qualify this as a TORFF event (Nielsen et al. 2015), as do the next two events mentioned in this section. The 0055 UTC METAR observation at the Barnes County Municipal Airport (KBAC, denoted by black and orange markers in Fig. 4.1a,b, respectively) reported a one hour rainfall accumulation of 141.2 mm, while the maximum Stage-IV observation over that same period was 52.5 mm. The report location was nearly collocated with the rotation associated with the storm's mesocyclone (Fig. 4.1b) during this period of intense precipitation. The Bismarck, North Dakota sounding valid 0000 UTC 21 June 2013, the closest observed sounding to the event location, contained ∼10 m s^{-1} of 0–1 km shear[4] (not shown).

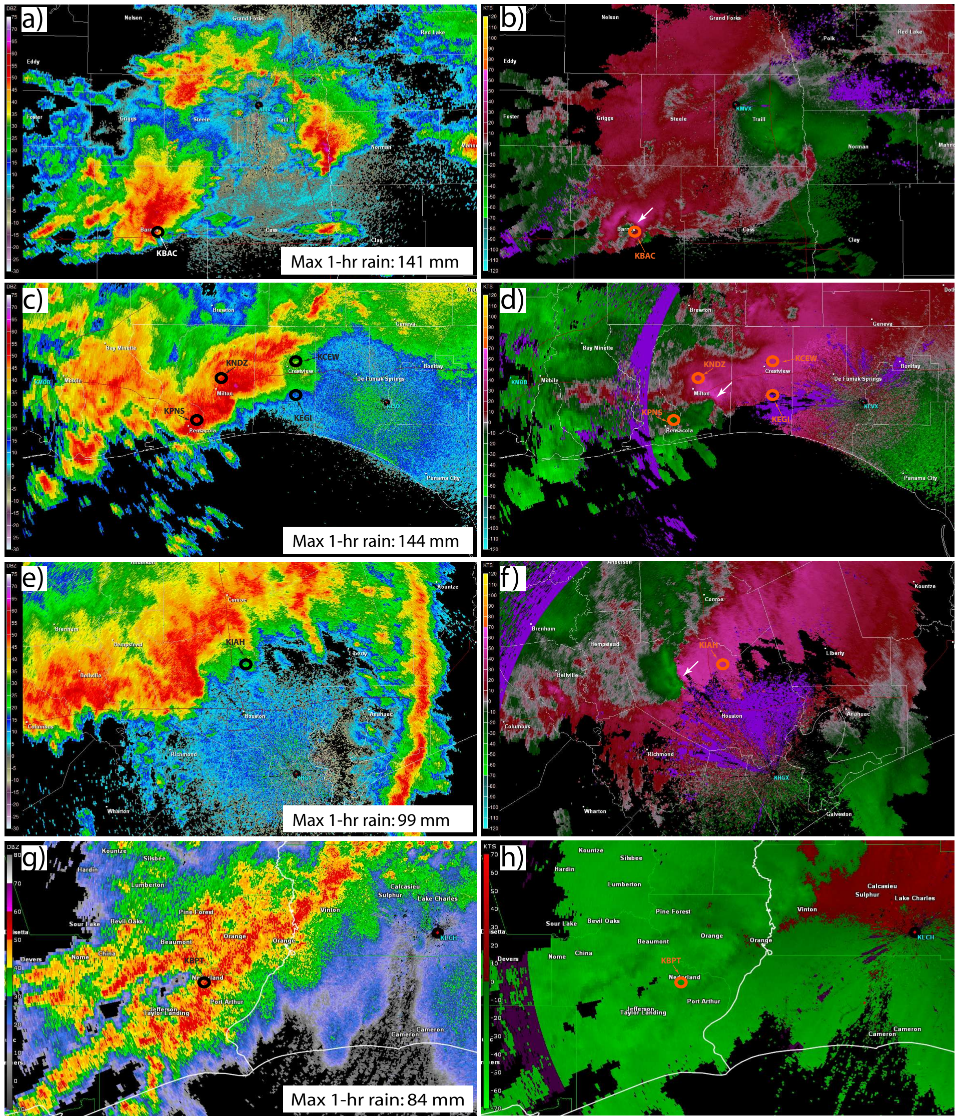

FIG. 4.1. Radar reflectivity (left column) and base velocity (right column) for three cases of 75 mm METAR rainfall accumulations with attendant mesoscale rotation. Black (left column) and orange dots (right column) represent location of METAR rainfall observations during the events. White arrows denote the locations of the attendant rotation. Images valid at (a,b) 0021 UTC 21 June 2013 from Grand Forks, ND (KMVX) radar, (c,d) 0222 UTC 30 April 2014 from Pensacola, FL (KEVX) radar, (e.f) 0817 UTC 18 April 2016 from Houston/Galveston, TX (KHGX) radar, and (g,h) 1210 UTC 18 July 2014 from the Lake Charles, LA (KLCH) radar. Individual METAR stations are labeled on the radar reflectivity plots for each case. Maximum one hour rainfall observations from local METAR or mesonet networks are labeled for each case (left column).

[4]Throughout this section and the rest of the paper, the 0–1 km shear nomenclature will refer to the 0–1 km bulk wind difference, and the units will reflect such.

Another instance of extreme rainfall with attendant rotation was observed near Pensacola, Florida, and points northeast from ∼0130 to 0500 UTC on 30 April 2014 (Fig. 4.1c,d). An MCS with strong embedded rotation (Fig. 4.1d) moved northeast during this period with its path tracing the approximate locations of the METAR observations (i.e., region bracketed by the four stations marked in Fig. 4.1c,d). One hour accumulations of 144.3 mm, 84.8 mm, 77.9 mm, and 78.9 mm were observed at Pensacola International Airport (KPNS), Naval Air Station Whiting Field-South (KNDZ), Bob Sikes Airport (KCEW), and Duke Field (KEGI), Florida, respectively. The Stage-IV analysis recorded one hour estimates of 165 mm and 140.1 mm concurrent with the above METAR observations of the event. Further, throughout the day on 30 April, the National Weather Service (NWS) forecast offices in Mobile, Alabama, and Tallahassee, Florida, issued twenty flash flood and thirteen tornado warnings (with many LSRs archived for both hazards; IEM 2017). Similar to the previous case, the Tallahassee, Florida, sounding valid 0000 UTC 30 April 2014 contained ∼12 m s^{-1} of 0–1km shear.

A third event occurred on 18 April 2016 in Houston, Texas. A mesoscale vortex embedded in a squall line moved through the area throughout the day (Fig. 4.1g,h) and produced significant flash flooding throughout the area. George Bush Intercontinental Airport (KIAH) recorded hourly accumulations of 98.6 and 81.0 mm during this event as the mesoscale vortex passed just to its north (Fig. 4.1g,h), while the maximum hourly Stage-IV accumulation during the same period was 113.8 mm. The Houston/Galveston NWS office issued 21 flash flood and 5 tornado warnings during this event (IEM 2017). Houston, Texas is in an operational upper-air observation void; however, the Storm Prediction Center's (SPC) mesoanalysis valid 0300 UTC 18 April 2016 had ∼15 m s^{-1} of 0–1km shear present over the region (SPC 2018). In summary, these three events all had intense hourly rainfall rates observed in association with near collocated, mesoscale rotation in environments of strong (i.e., 10+ m s^{-1}, Craven et al. 2004) of 0–1km shear.

A fourth event that did not have collocated rotation occurred in the morning hours of 18 July 2014 near Beaumont and Port Arthur, Texas (Fig. 4.1g,h). A developing surface low-pressure system associated with a late summer long wave trough and fairly robust upper-level forcing for ascent led to the development of an MCS that initiated north of Houston, Texas near 0300 UTC that same day (not shown). This, combined with precipitable water values over 2.3 inches, led to the development of intense, back building convection by 1000 UTC 18 July in the Beaumont/Port Arthur area (Fig. 4.1g,h). The 0000 UTC pre-convective sounding from Lake Charles, Louisiana contained ∼8 m s^{-1} of 0–1 km shear. The 1253 UTC METAR observation from Jack Brooks Regional Airport (KBPT) recorded an hourly accumulation of 83.6 mm, compared to a maximum Stage-IV accumulation over the same period of 81.4 mm. Flash flood warnings were issued for the region by the Lake Charles NWS office beginning at 1223 UTC, and reports of flooding continued in the area until approximately 1400 UTC (IEM 2017). Unlike the previous three cases present in this section, the extreme hourly rainfall was not associated with attendant rotation, but rather a narrow region of intense back building convection (Fig. 4.1g,h; Schumacher and Johnson 2005).

4.3 Methods

In order to provide an idea of the frequency of extreme rain rate and mesovortex collocation using radar observations, hourly precipitation accumulation data was obtained spanning 2013-2017 for rain gauges and 2013-2015 for gridded multi-sensor precipitation products.[5] The rain gauge dataset comprises METAR observations from across the U.S. acquired from the Iowa Environmental Mesonet (IEM 2018a) and filtered to retain hourly accumulations greater than or equal to 75 mm. Additionally, hourly accumulations greater than or equal to 100 mm were also obtained from the National Center for Atmospheric Research of the NCEP Stage-IV gridded precipitation analysis (Lin and Mitchell 2005) between 2013 and 2015, which is a multi-sensor approach using both rain gauge and radar based QPE. The specific rainfall accumulation thresholds mentioned above (i.e., hourly accumulations of 75 and 100 mm for the METAR data and Stage-IV data, respectively) were chosen to represent events that could be considered in the realm of 25 to 50 year average recurrence intervals (ARI) at the one hour accumulation threshold for the majority of CONUS (Fig. 4.2a-g, Stevenson and Schumacher 2014; Herman and Schumacher 2018b). While these hourly accumulations are not as extreme along the U.S. Gulf coast and the southeastern part of the country (i.e., between 10 and 25-yr ARIs for hourly accumulations), these thresholds were still chosen to ensure an adequate case list for analysis. Additionally, a rainfall rate of 75 to 100 mm hr^{-1} sustained over an hour would likely lead to significant flooding, especially in urban areas (e.g., Smith et al. 2001, 2013), since surface runoff is largely controlled by rain rate (e.g., Woolhiser and Goodrich 1988; Beven 2011) and has been shown to increase proportionally to the amount of built environment in the affected area (e.g., Gill et al. 2007). The increased filtering threshold in the Stage-IV dataset (i.e., 100 mm hr^{-1}), compared to the METAR dataset (i.e., 75 mm hr^{-1}), was chosen to maintain a similar relative exceedance frequency between the products, given increased spatial sampling associated with the remote sensing based Stage-IV product.

[5]The period over which the Stage-IV data was examined is shorter, compared to the METAR dataset, due to the significant increase in data points per year in the spatially continuous Stage-IV product.

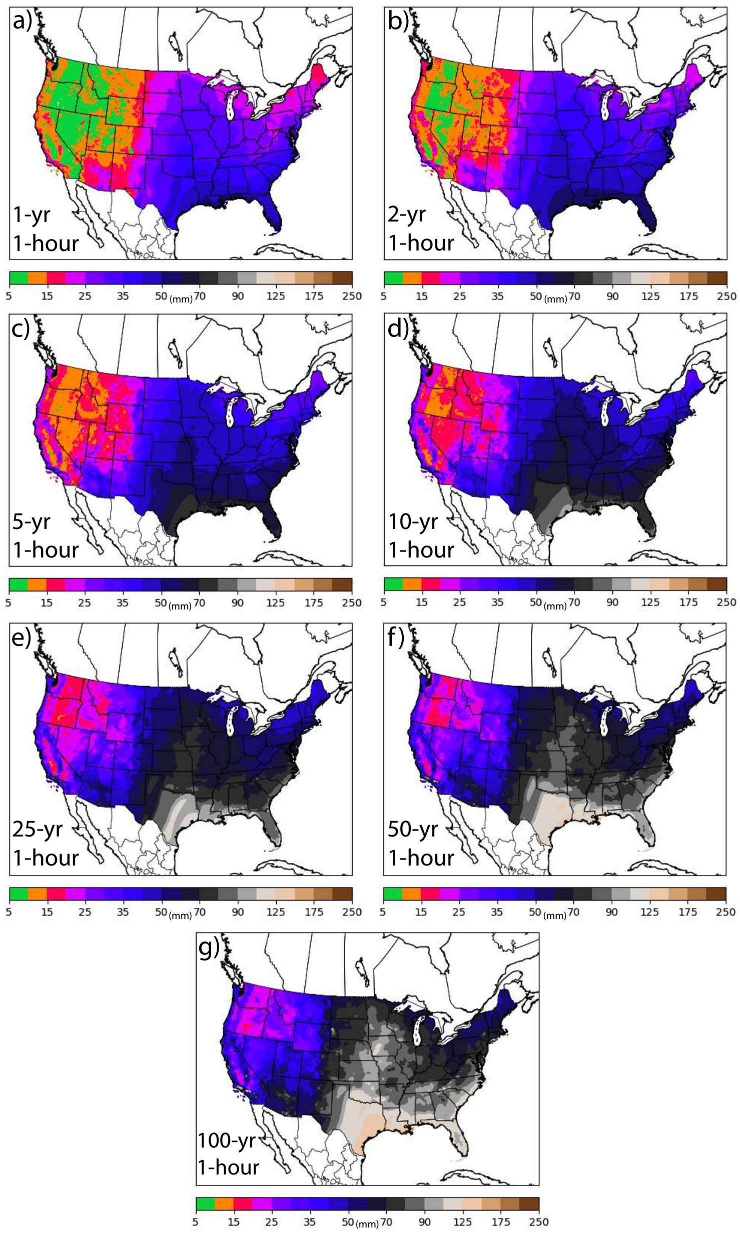

FIG. 4.2. One hour rainfall accumulation for the (a) 1-yr, (b) 2-yr, (c) 5-yr, (d) 10-yr, (e) 25-yr, (f) 50-yr, and (g) 100-yr average recurrence intervals (ARI) for the contiguous United States (CONUS) reproduced form Fig. 1 of Herman and Schumacher (2018b).

It should be noted that the list created by this method is by no means comprehensive nor are the measured values from the METAR observations (e.g., Legates and Deliberty 1993; Yang et al. 1998) or Stage-IV (e.g., Nelson et al. 2016) completely accurate. For instance, Stage-IV data tends to underestimate accumulations as the rain rate increases (Nelson et al. 2016). However, given the available data, these datasets provide a starting point for this analysis.

The gauge and gridded rainfall observations were then manually culled by regional radar analysis to filter out snowfall events, spurious accumulations/data in the Stage-IV analysis (e.g., Nelson et al. 2016; Herman and Schumacher 2016), and to remove rain gauge observations that were potentially reporting false data (e.g., no precipitation was visible on radar). Care was also taken to remove entries in the METAR data if the precipitation had ended and the gauge was still reporting continued rainfall. Multiple observations from the same event were not removed, initially, to evaluate the timing of the observation relative to any possible rotation. Local radar data including equivalent reflectivity, differential reflectivity, and radial velocity, was obtained for the remaining points for the hour preceding the observation time from the Unidata AWS Level II Radar Archive (Unidata 2018). This local radar data was then used to subjectively identify whether meso-β to meso-γ rotation was collocated with the identified points of extreme hourly rainfall accumulations. A subjective method was used, as part of this analysis, since the focus is on rotation of various scales and strengths and that detection algorithms still remain subjective as to the exact parameters chosen (e.g., Jones et al. 2004). If the points were not associated with rotation or it was not clear for any reason, the observation was classified as not being associated with rotation.

In addition to the subjective method, a limited objective method for rotation identification was used based upon Multi-Radar Multi-Sensor (MRMS; Smith et al. 2016; Zhang et al. 2016) hourly mid and low-level rotation tracks. MRMS rotation tracks are produced by recording the highest azimuthal shear value, over a specified time interval and vertical column depth, observed from the multi-radar synthesis that is produced as part of the MRMS data suite. In this research, the mid (3–6 km above ground level (AGL)) and low-level (0–2 km AGL) rotation tracks are used as summed over a 60 minute time interval updated every 2 minutes in real time (Smith et al. 2016) to objectively identify rotation in cases of extreme rainfall identified by the METAR dataset. The number of points in the MRMS rotation tracks dataset that exceeded 0.005 s^{-1}, 0.01 s^{-1}, and 0.015 s^{-1} rotation thresholds within radii of $\frac{1}{8}^{\circ}$ and $\frac{1}{16}^{\circ}$ degrees of the METAR events between September 2016 and the end of 2017 were recorded from the mid and low-level MRMS rotation track data. If an event had at least one point in low-level rotation tracks exceeding 0.005 s^{-1} within $\frac{1}{8}^{\circ}$ over the hour(s), it was deemed to have been associated with rotation. It should be noted that this objective method is performed on a limited portion of the dataset because, to the authors' knowledge, no publicly accessible archive of the MRMS rotation track data is available and the data presented here was self-archived by the authors in real time.

The resulting list of points of extreme hourly rainfall accumulations from each dataset (i.e., METAR and Stage-IV) were clustered into events using a density-based algorithm for spatial datasets with noise (DBScan; Ester et al. 1996) as implemented using the Scikit-learn (Pedregosa et al. 2011) Python programming library. The resulting event clusters were used to create event centered composites and parameter distributions from the Rapid Refresh (RAP; Benjamin et al. 2016) analysis to evaluate the environmental characteristics of extreme rainfall events with collocated rotation compared to those that did not. Select native RAP model variables and calculated derived variables were calculated and saved for the 260 km (i.e., 20 RAP grid points) surrounding each individual event center. The resulting data for each event was then equally weighted to create event centered composites. The composites were made from the event clusters with all the south Florida, tropical cyclone (TC), and those west of the U.S. continental divide removed from both the rotation and non-rotation datasets. The weakly forced Florida cases were removed to avoid diluting the composites with weak synoptic signals from convective spin ups that are dominated by sea breeze interactions that are likely not resolved well in the RAP. The cases located in the western U.S. were removed to exclude events that could be heavily influenced by orographic effects (e.g., Doswell et al. 1998). Similarly, the tropical cyclone cases were removed since the system wide kinematics and dynamics are quite different compared to continental convection (e.g., Baker et al. 2009; Morin and Parker 2011; Edwards et al. 2012). However, this does not lessen the importance of TCs in producing extreme short-term rainfall accumulations. Furthermore, 19 cases where radar data did not allow a conclusive subjective interpretation of whether rotation was present were not included in the composite analysis. However, these cases are still included in the general statistics as non-rotation cases. Lastly, the diurnal, seasonal, and maximum accumulation distributions of the rotation and non-rotation events will be examined for the cases that are included in the composite analysis.

4.4 Results

A total of 136 METAR and 732 Stage-IV points of accumulation over 75 mm and 100 mm per hour, respectively, were collected between 2013 and 2017 (Fig. 4.3a,b). A total of 66 (48.5%) of the METAR and 337 (46.0%) of the Stage-IV observations were associated with rotation on the meso-β to meso-γ-scale (Fig. 4.3c,d, Table 4.1). The spatial distribution of the points associated with these extreme rain rates follow the Gulf and Atlantic coastlines and extend into the central plains (Fig. 4.3a,b), which follows what one would expect *a priori* based upon the 10-50 year one hour ARIs for the United States (Herman and Schumacher 2018b).

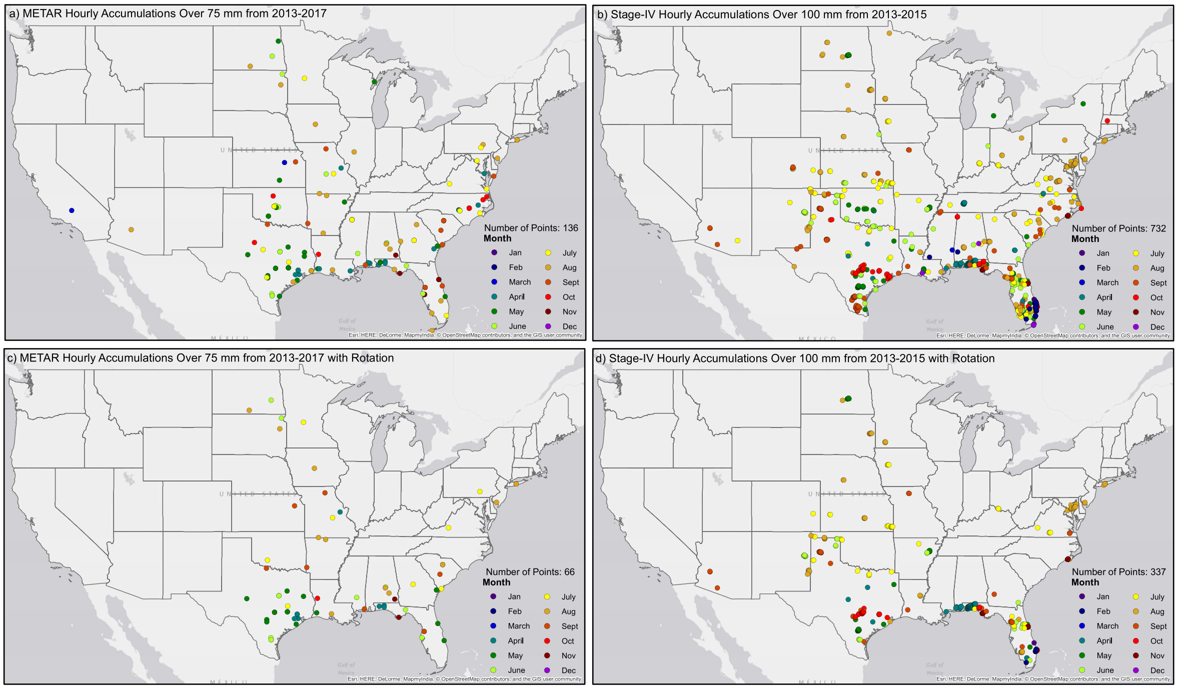

FIG. 4.3. Geographic distribution of METAR (a,c) and Stage-IV (b,d) hourly accumulations over 75 mm and 100 mm, respectively, not filtering for rotation (a,b) and those observations only associated with rotation (b,c). A total of 66/136 points in the METAR and 337/732 of the Stage-IV dataset are associated with rotation.

TABLE 4.1. Statistical breakdown and number of points associated with rotation for the extreme rainfall observations from the METAR and Stage-IV datasets utilized in this study. Last two columns show the number of points associated with rotation as subjectively and objectively identified, respectively.

Dataset	Points	Subjectively Identified Rotation	Objectively Identified Rotation
METAR from 2013-2017 > 75 mm hr^{-1}	136	66 (48.5%)	N/A
Stage-IV from 2013-2015 > 100 mm hr^{-1}	732	337 (46.0%)	N/A
METAR with MRMS Rotation Tracks Available	29	13 (44.8%)	27 (93.1%)

The points associated with collocated rotation follow a similar pattern (Fig. 4.3c,d), but are more focused on the coastlines and in the southeastern United States, compared to those without attendant rotation (Fig. 4.4b,c).

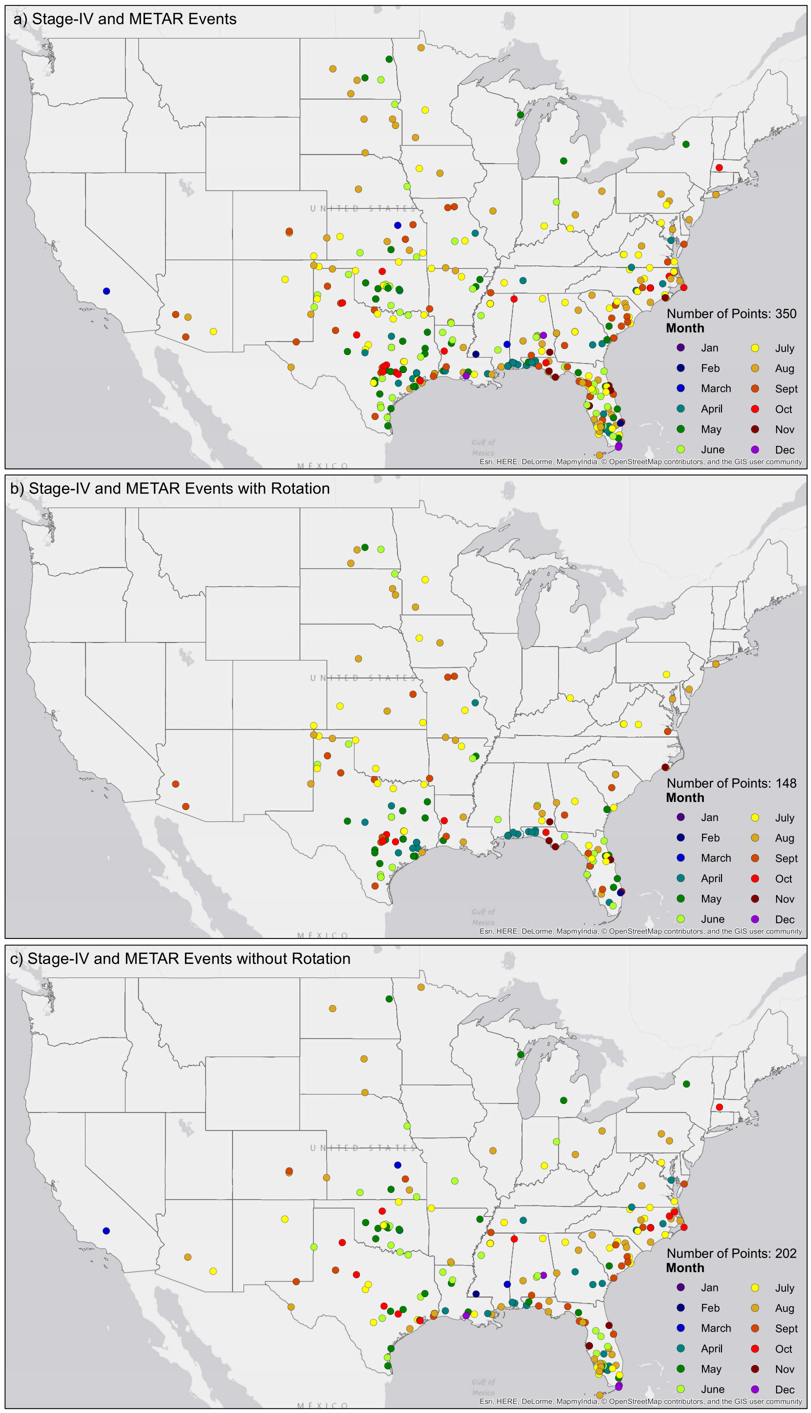

FIG. 4.4. (a) geographic depiction of all extreme rainfall event clusters created from both the METAR and Stage-IV datasets, (b) events that were subjectively identified with rotation, and (c) events not associated with rotation.

Once the clustering analysis on both the METAR and Stage-IV data was undertaken, a total of 350 extreme rainfall events result in the dataset (Fig. 4.4a). The geographic distribution of the events, by design, is similar to the individual observations of extreme rainfall seen in Fig. 4.3a,b. Of the 350 events in the combined dataset, 148 (42.3%) were associated with mesoscale rotation (Fig. 4.4b). Geographically, the events with (Fig. 4.4b) and without (Fig. 4.4c) rotation follow similar geographic patterns, with the importance of a moisture reservoir (e.g., the Gulf of Mexico) having clear importance in both subsets. The Stage-IV data, specifically, was clustered into 214 events, of which 82 (38.3%) of the events were associated with rotation. However, the 82 events associated with rotation accounted for 468 of the 732 Stage-IV grid cells that exceeded 100 mm hr^{-1}, which implies that the rotation events might be, from an areal sense, more prevalent producers of extreme rainfall.

As previously mentioned, an objective identification method for rotation was performed using the MRMS low and mid-level rotation track data when available for a subset of the METAR dataset. MRMS data was available for a total of 29 METAR events from late September 2016 through 2017, including for the accumulations seen in Hurricane Harvey's (2017) rainbands (Blake and Zelinsky 2018, Fig. 4.5b). In total 27 (93.1%) of the total cases examined had rotation present in the low-levels over the hour that the extreme rainfall observations occurred (Table 4.2), per the 0.005 s^{-1} within $\frac{1}{8}^{\circ}$ threshold described in the methods.

TABLE 4.2. Second row depicts the number of of METAR observation with > 75 mm hr^{-1} of precipitation accumulation where hourly MRMS low-level rotation track data is available (i.e., 29 possible points) with points over various thresholds (e.g., > 0.005 s^{-1}) within a specified radius (e.g., 1/16°). Criteria used to objectively identify low-level rotation is denoted by *. Third row lists the average number of points exceeding the specific rotation threshold that an event with rotation has for each rotation threshold and spatial offset.

	> .005 s^{-1} 1/16°	> .010 s^{-1} 1/16°	> .015 s^{-1} 1/16°	> .005 s^{-1} 1/8°*	> .010 s^{-1} 1/8°	> .015 s^{-1} 1/8°
METAR Points Satisfying Criteria	26 (89.7%)	8 (27.6%)	0	27 (93.1%)	12 (41.4%)	4 (13.8%)
Avg. Number of MRMS Points Per METAR	108.4	17.9	0	311.8	37.4	8.8

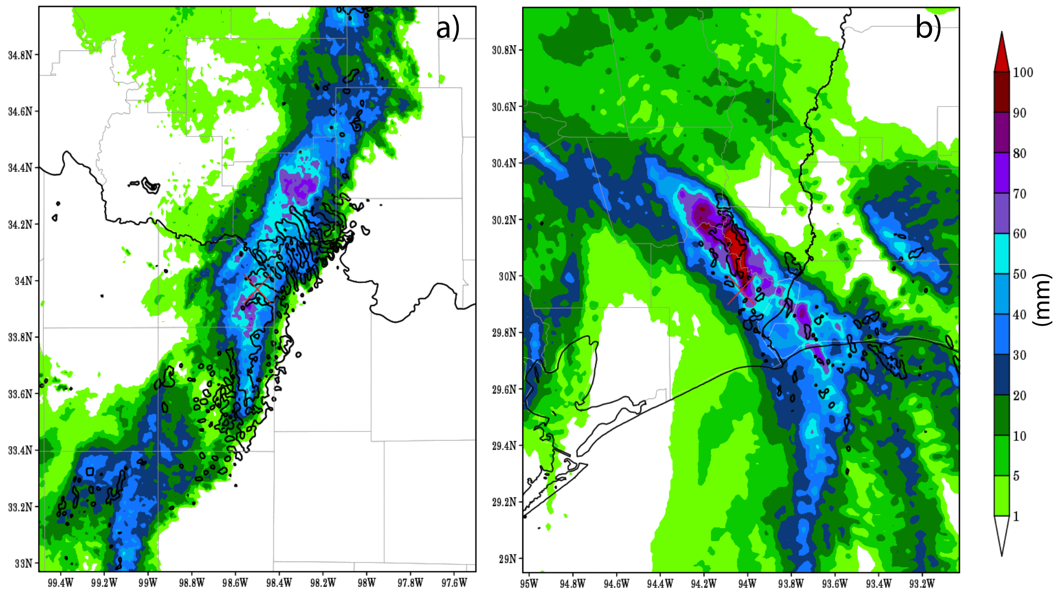

FIG. 4.5. MRMS gauge corrected quantitative precipitation estimated accumulated rainfall (shaded; mm), MRMS low-level hourly rotation tracks (black contours starting at 0.005 s^{-1}), and location of METAR observation over 75 mm hr^{-1} (red cross) valid (a) 0300 UTC 26 September 2016 and (b) 1500 UTC 27 August 2017.

Using this same threshold for the mid-level rotation, 25 (86.2%) events were associated with rotation (Table 4.3). Comparing Tables 4.2 and 4.3, the average number of points that satisfy all presented thresholds and radii is larger in the low-levels, which, in a bulk sense, implies that the rotation is more intense and/or more persistent in the lowest levels of the storms. While rotation is often present in the mid-levels, it is not seen as prevalently at the highest thresholds (e.g., 0.015 s^{-1}) compared to the low-level values (cf. Table 4.2 and Table 4.3). Further comparing the low and mid-level results, the number of cases classified with rotation is less dependent on the spatial offset and more on the magnitude of the rotation considered (cf. Table 4.2 and Table 4.3). Lastly, of the 29 events that are objectively analyzed using the MRMS data, only 13 were subjectively identified to present rotation. While this trend is difficult to extend to the full subjective analysis, it hints that the subjective results might be a conservative estimate for the number of cases with attendant rotation. It should also be noted that MRMS rotation track algorithm tendencies or event proximity to the nearest radar could influence the above results and are not accounted for in this analysis.

TABLE 4.3. Same as in Table 4.2, but for the mid-level MRMS rotation tracks.

	$> .005\ s^{-1}$ 1/16°	$> .010\ s^{-1}$ 1/16°	$> .015\ s^{-1}$ 1/16°	$> .005\ s^{-1}$ 1/8°*	$> .010\ s^{-1}$ 1/8°	$> .015\ s^{-1}$ 1/8°
METAR Points Satisfying Criteria	25 (86.2%)	1 (3.5%)	0	25 (86.2%)	4 (13.8%)	0
Avg. Number of MRMS Points Per METAR	77.9	11.0	0	209.3	12.5	0

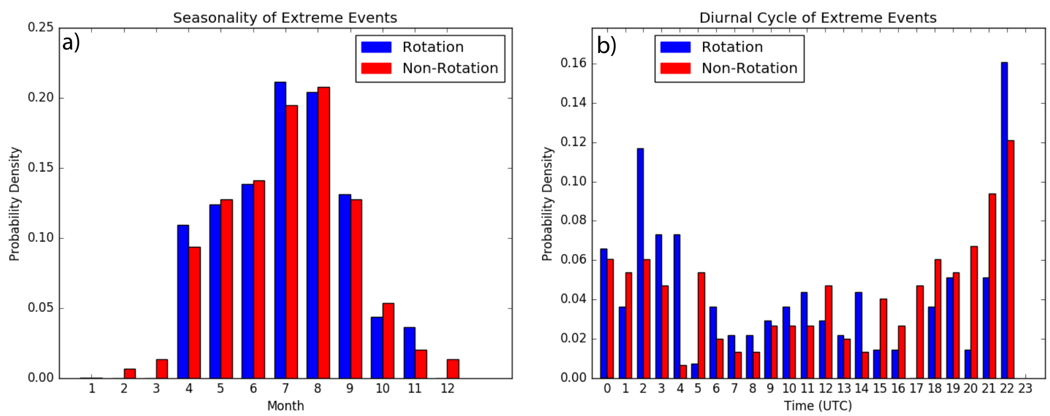

FIG. 4.6. Seasonal (a) and diurnal (b) distributions of the rotation (blue bars) and non-rotation (red bars) for the cases that were used to create the event centered composites in Figs. 4.9 and 4.10. Histograms are binned every month (a) and every hour of local UTC time (b) on the x-axis versus, while probability density is on the y-axis.

Seasonally, the events associated with rotation are more likely to occur in the late summer and are more confined to the warm season, compared to those without rotation (Fig. 4.6a). While the non-rotation events have a similar seasonal distribution to those with rotation, they occur more frequently in the winter months and early shoulder seasons (Fig. 4.6a). Further, the seasonal maximum of rotation events seems to appear slightly later in the year than the seasonal tornado maximum (e.g., Brooks et al. 2003). From a diurnal standpoint, the non-rotation event frequency peaked with diurnal heating (Fig. 4.6b), while the events associated with rotation tended to occur more during the late evening and nocturnal hours (Fig. 4.6b). Cases associated with coincident rotation tended to produce higher hourly accumulations than those without any rotation present[6] (Fig. 4.7). This is true for both the mean and median of the cases where rotation is present, compared to the cases where rotation is not present (see caption of Fig. 4.7 for specific values).

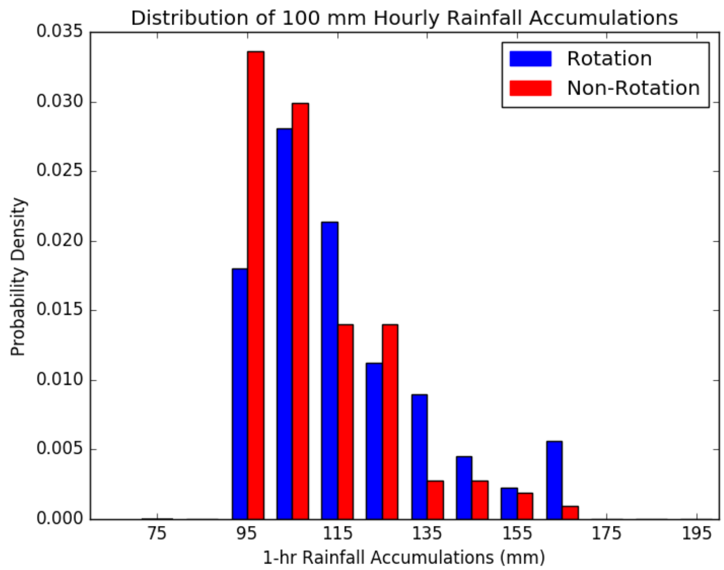

FIG. 4.7. As in Fig. 4.6 but for the distribution of 1 hr rainfall accumulations (mm, x-axis) for the rotation (blue bars) and non-rotation (red bars) binned every 10 mm. Mean and median of rotation cases are 121.5 mm and 116.5 mm, respectively. Mean and median of non-rotation cases are 114.5 and 110.0, respectively.

The RAP composites characterizing the mean environment at the start of the extreme rainfall for all of cases identified in this study are consistent with the ingredients that have been previously identified as needed for extreme precipitation (e.g., Doswell et al. 1996). The events tended to occur ahead of an upper-level trough (Fig. 4.8a,c,e) in the warm sector of an extratropical cyclone (Fig. 4.8b,d,e). The center of the events was located along a surface warm front/stationary boundary (Fig. 4.8b) near the nose of the lower-level jet (LLJ; Fig. 4.8d). The hint of a weak 500-hPa shortwave (Fig. 4.8), widespread 850-hPa warm air advection (Fig. 4.8g), and moderate levels of instability (~1500 J kg^{-1}; Fig. 4.8d) are also seen just upstream of the event center. A broad region of precipitable water (PWAT) values over 45 mm (~1.75 in; Fig. 4.8b) surrounds the event center, providing an ample supply of moisture.

[6]This is true for the distribution of events where the maximum hourly accumulation is over 100 mm. This upper threshold was chosen to make the most clean comparison between the METAR and Stage-IV based events, since the 75 mm hr^{-1} minimum was used originally for the METAR events and skews the distribution of both rotation and non-rotation events.

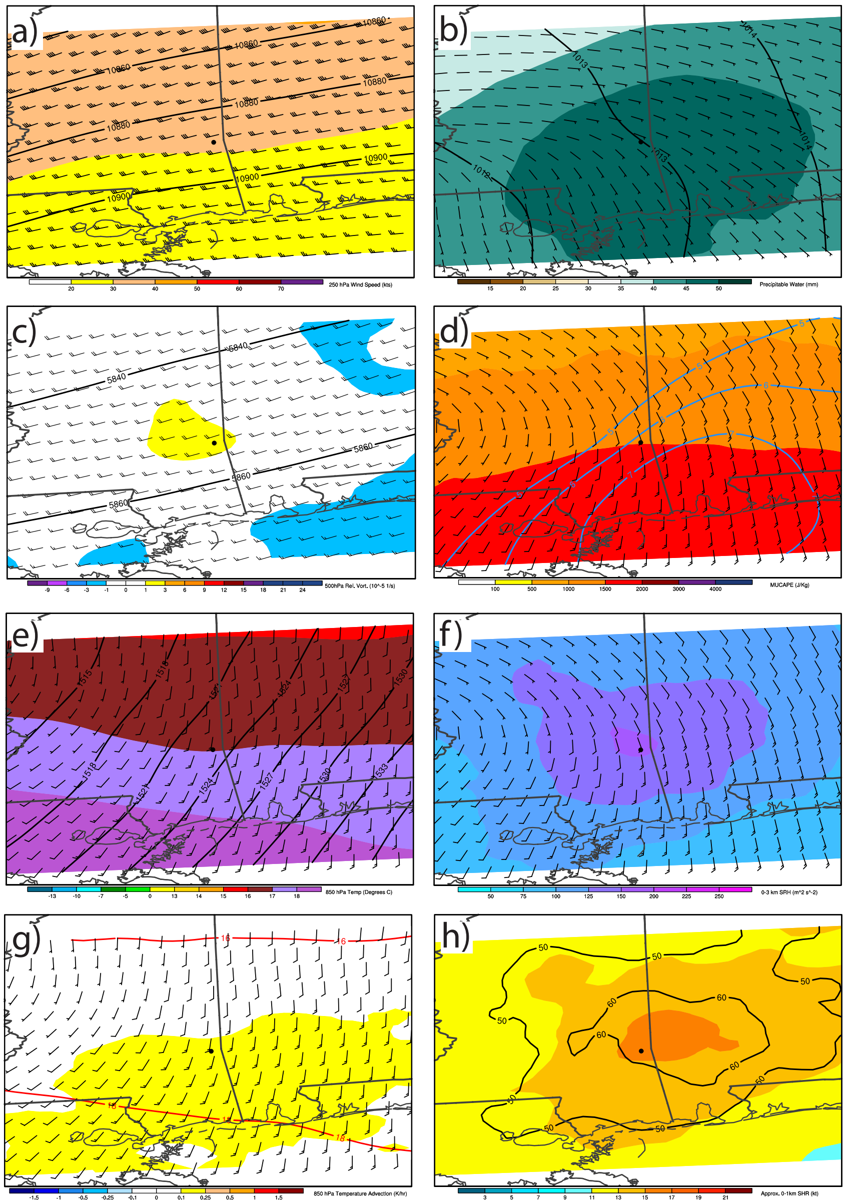

FIG. 4.8. Event centered composites for all the extreme precipitation events in this study. (a) 250 hPa heights (black contours, m), wind barbs (half barb = 5, full barb = 10, pennant = 50 kt, 1 kt = $0.5144 ms^{-1}$), and 250 hPa isotachs (shaded, kt). (b) mean sea-level pressure (black contours, hPa), 10-m wind barbs, and precipitable water (shaded, mm). (c) 500 hPa heights (black contours, m), 500 hPa wind barbs, and 500 hPa relative vorticity (shaded, X 10^{-5} s^{-1}. (d) 900 hPa isotachs (blue contours, m s^{-1}), 900 hPa wind barbs, and MUCAPE (shaded, J kg^{-1}). (e) 850 hPa heights (black contours, m), 850 hPa wind barbs, and 850 hPa temperature (shaded, °C). (f) 900 hPa wind barbs and 0–3 km storm relative helicity (shaded, m^2 s^{-2}). (g) 850 hPa temperature (red contours, °C), 850 hPa wind barbs, and 850 hPa temperature advection (shaded, K hr^{-1}). (h) 0–1 km storm relative helicity (black contours, m^2 s^{-2}) and approximate 0–1 km bulk wind difference (shaded, kt).

While the general flow aloft is weak, which generally points to slower storm motions, there is a non-negligible amount of approximate 0–1 km shear[7] and RAP estimated 0–3 km storm relative helicity (SRH; Fig. 4.8f,g).

The composites for the both the rotation and non-rotation events show synoptic and mesoscale differences; however, the synoptic-scale differences are generally less obvious than those seen at the mesoscale. The non-rotation cases are associated with slightly slower flow aloft (Fig. 4.9a-b) and slightly lower heights at the mid-to-upper levels (Fig. 4.9a-d), but both composite subsets show a signal of a shortwave embedded in the flow (Fig. 4.9c-d). However, the shortwave is slightly north of the event center in the non-rotation cases, compared to being at or upstream of the event in the cases with rotation (Fig. 4.9c-d). At lower levels (i.e., 850 hPa) the heights are lower and the winds more southerly for the cases with rotation (Fig. 4.9e-f). A tighter 850 hPa temperature gradient, slightly higher 850 hPa temperature, and more gradient perpendicular 850 hPa flow also lead to increase warm air advection in the rotation cases compared to the cases without rotation (Fig. 4.9e-h).

On the meso-to-convective scale, more differences between the rotation and non-rotation cases appear in the composites. The rotation cases are located more in the warm-sector at the surface (Fig. 4.10a,c), while the non-rotation cases are located along what appears to be a warm front/stationary boundary and closer to the surface low-pressure center (Fig. 4.10b). An expected northwestern shift is seen in the circulation at 900 hPa, given the surface circulation, in the cases without rotation with the flow remaining relatively week (Fig. 4.10b,d). Conversely, there appears to be the presence of a low-level jet at 900-hPa in the cases associated with rotation (Fig. 4.10c), which makes sense given the diurnal distribution of cases (Fig. 4.6b). Both non-rotation and rotation case composites contain similar values of mixed-layer convective available potential energy (MLCAPE; Fig. 4.10c,d), despite non-negligible differences in the mean positions of the surface low-pressure systems. Precipitable water values are higher at event center in the warm sector in the rotation cases compared to the non-rotation cases (Fig. Fig. 4.10a,b). The rotation cases were associated with increased values of 0–3km helicity, 0–1km helicity, and approximate 0–1km shear (Fig. 4.10e-h). Given the environmental conditions that are known to be conducive to rotation, this is not necessarily surprising.

[7]Since the RAP does not have native variables to calculate the 0–1 km wind shear, it was approximated as the bulk wind difference between the 10 m wind and mean 90-120 mb layer above ground wind.

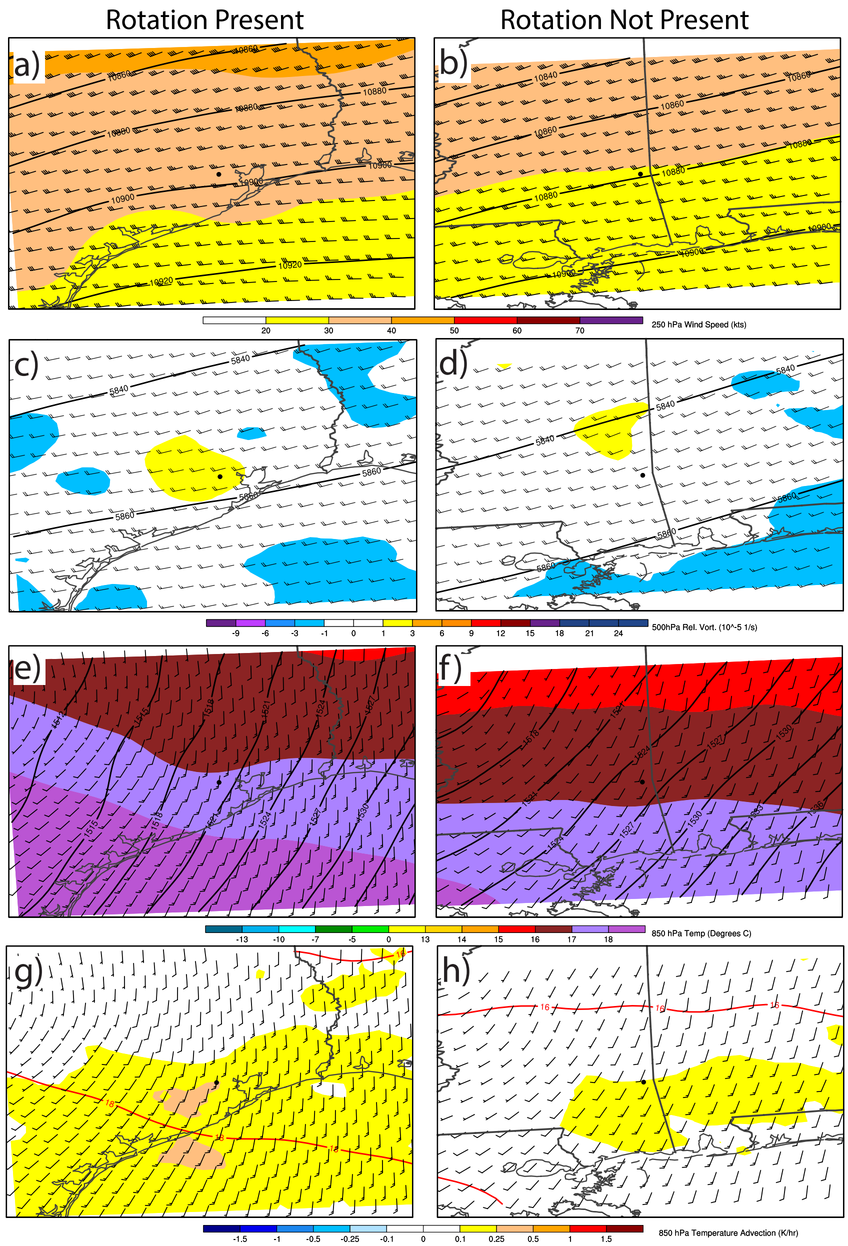

FIG. 4.9. Event centered composites for the rotation (left column) and non-rotation (right column) extreme precipitation events. (a,b) 250 hPa heights (black contours, m), wind barbs (half barb = 5, full barb = 10, pennant = 50 kt, 1 kt = 0.5144ms^{-1}), and 250 hPa isotachs (shaded, kt). (c,d) 500 hPa heights (black contours, m), 500 hPa wind barbs, and 500 hPa relative vorticity (shaded, X 10^{-5} s^{-1}. (e,f) 850 hPa heights (black contours, m), 850 hPa wind barbs, and 850 hPa temperature (shaded, °C). (g,h) 850 hPa temperature (red contours, °C), 850 hPa wind barbs, and 850 hPa temperature advection (shaded, K hr^{-1}).

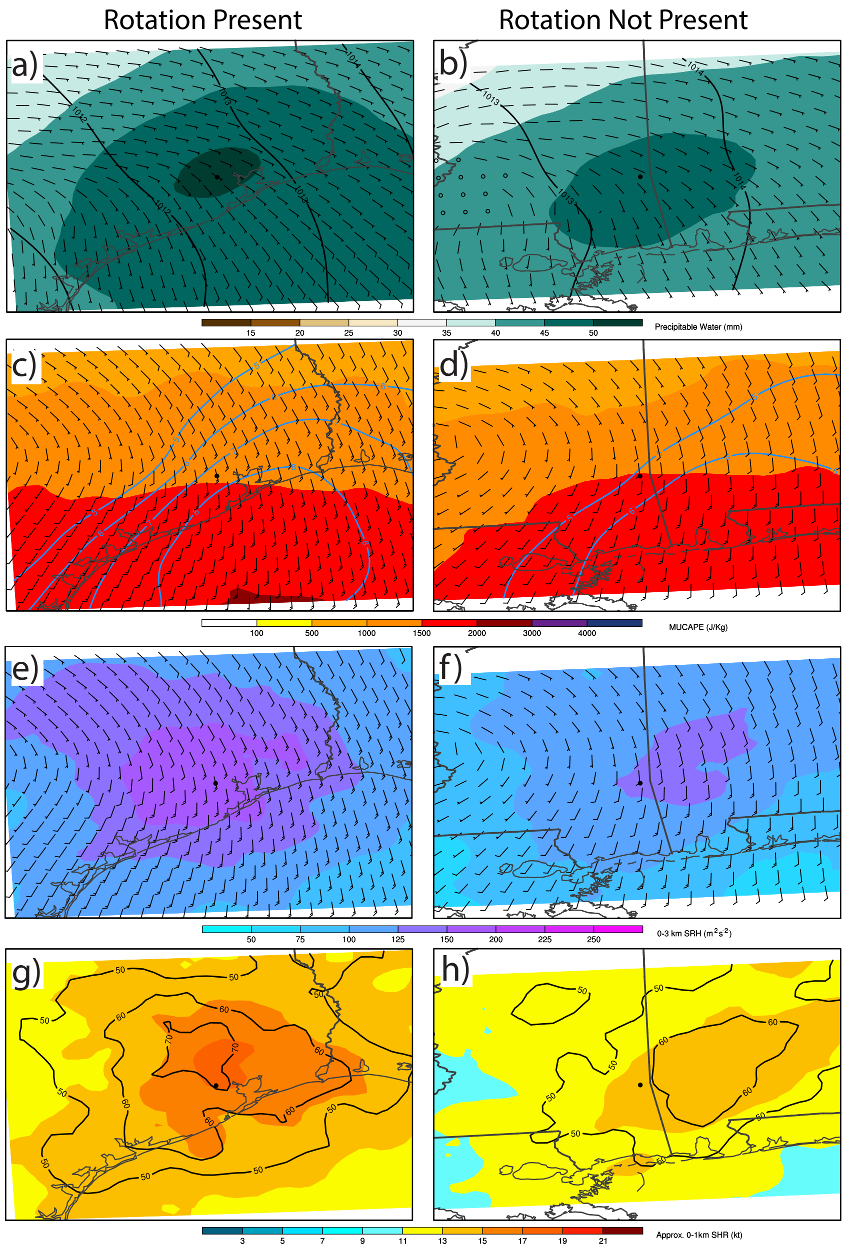

FIG. 4.10. Event centered composites for the rotation (left column) and non-rotation (right column) extreme precipitation events. (a,b) mean sea-level pressure (black contours, hPa), 10-m wind barbs, and precipitable water (shaded, mm). (c,d) 900 hPa isotachs (blue contours, m s^{-1}), 900 hPa wind barbs, and MUCAPE (shaded, J kg^{-1}). (e,f) 900 hPa wind barbs and 0–3 km storm relative helicity (shaded, m^2 s^{-2}). (g,h) 0–1 km storm relative helicity (black contours, m^2 s^{-2}) and approximate 0–1 km bulk wind difference (shaded, kt).

Given the wide range of cases examined and the relatively small differences in the event center composites, the distributions of select fields were calculated as in Potvin et al. (2010) in the presumed storm inflow region to better determine the nature of the differences. Generally, the distributions between the rotation and non-rotation cases are similar for the thermodynamic, moisture, and low-level kinematic variables (Fig. 4.11); however, the rotation cases tend to show more power in the upper half of the distribution of these parameters.

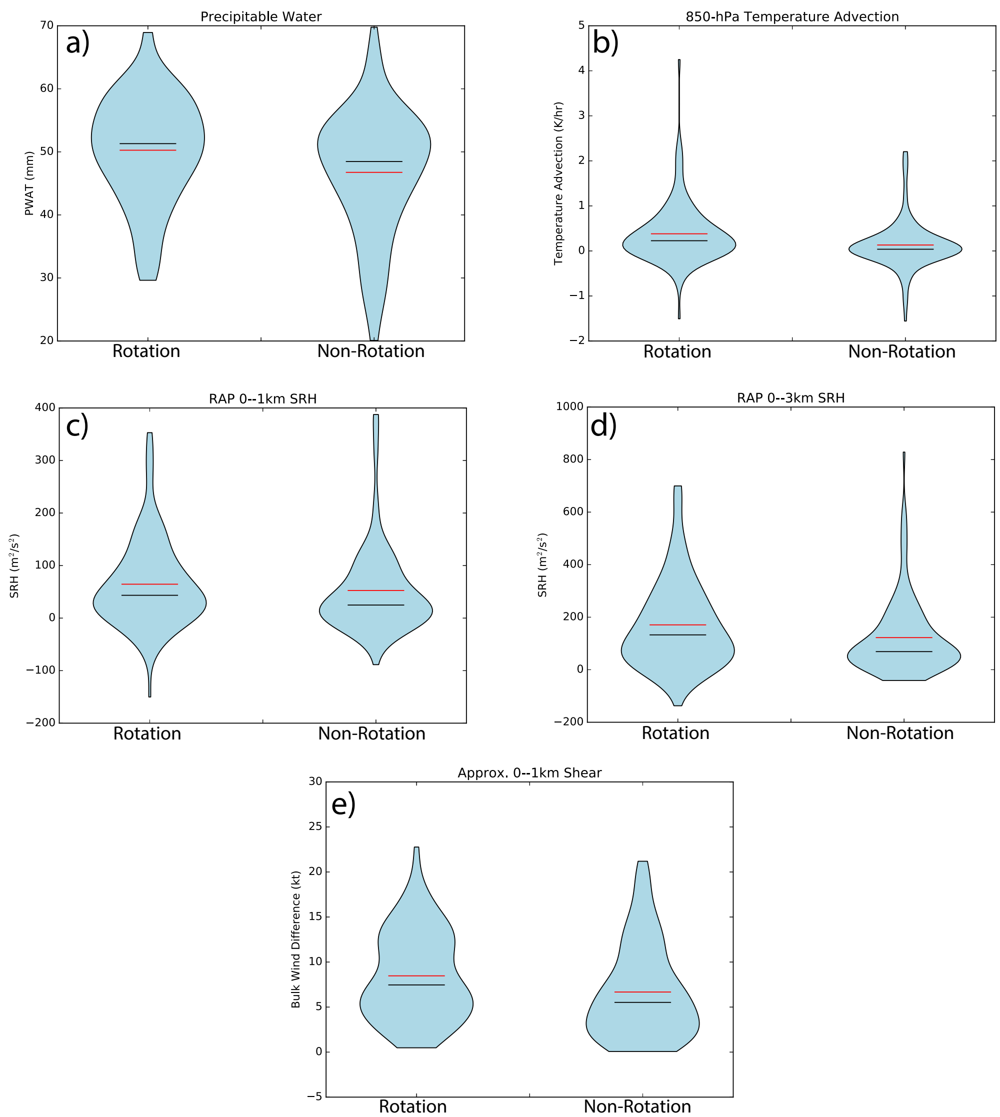

FIG. 4.11. Violin plots of (a) precipitable water (mm), (b) 850-hPa temperature advection (K hr^{-1}), (c) RAP 0–1 km storm relative helicity (SRH, m^2 s^{-2}), (d) RAP 0–3 km storm relative helicity (SRH, m^2 s^{-2}), and (e) approximate 0–1 km shear/bulk wind difference in the presumed inflow region for the rotation and non-rotation events. Black lines denote the median and red lines the mean.

The broadening of the higher end of the distribution in the rotation events is most prominent in the PWAT (Fig. 4.11a) and approximate 0–1 km shear (Fig. 4.11e) distributions. In addition to the broadening in the upper half of the PWAT distribution in the rotation events, the non-rotation event distribution has values regularly occurring below the minimum in the rotation cases (i.e., below ∼30 mm; Fig. 4.11a). While the increase in the upper portion of the approximate 0–1 km shear distribution in the rotation cases is the largest among the low-level shear variables (Fig. 4.11e), similar smaller increases in power are seen in the upper half of the RAP estimated 0–1 km and 0–3 km storm relative helicity distributions as well (Fig. 4.11c,d). The distribution of 850-hPa temperature advection is very similar between the rotation and non-rotation cases, with the exception of a few outliers in the rotation cases (Fig. 4.11b). In general, the distributions of the low-level kinematic values between the rotation and non-rotation events are similar; however, the low-level shear is more intense in the rotation cases.

4.5 Discussion

The surface and synoptic pattern for the non-rotation cases of extreme short-term rainfall is fairly consistent with the "frontal" archetype presented in Maddox et al. (1979). The ability of the surface boundary to repeatedly develop storms in the same area and the atmospheric mean flow to create a slow, boundary parallel storm motion leads to intense rainfall accumulations. On longer time scales, "training" events such these are well known flash flood and extreme rainfall producers (e.g., Doswell et al. 1996; Schumacher and Johnson 2005). However, on timescales examined in this study (i.e., hourly rainfall accumulations), the effects of storm motion/propagation are likely not as explicitly important, since it presumably needs to be raining the entire hour to yield the observations described here, but still play a role.

The presence of attendant rotation nearly half of the time when extreme hourly rainfall accumulations are observed supports recent studies that have identified storms that possess rotation on the meso-β to meso-γ scale, most often supercells, as prevalent producers of extreme rainfall (e.g., Smith et al. 2001; Duda and Gallus 2010; Hitchens and Brooks 2013; Weijenborg et al. 2017; Smith et al. 2018). The distribution of maximum event accumulations (Fig. 4.7) reinforces the idea that rotation events tend to produce higher hourly accumulations/rain rates then non-rotation events; however, known uncertainties exist surrounding the overall accuracy of both the datasets used in this analysis. It should be noted that, when the distribution of hourly accumulations is examined within the Stage-IV sample of events only, a similar increase with the presence of rotation is seen (not shown). Additionally, the

82 (38.3%) rotation events in the Stage-IV dataset that are associated with rotation produce 64% of the hourly gridded precipitation accumulations over 100 mm, which implies that the rotation events are more prevalent areal and/or persistent producers of extreme short term rainfall. These results not only support the general premise that rotational induced dynamical forcing on extreme rainfall cannot be ignored and is, at the very least, not necessarily prohibitive in producing extreme short term rain rates, but also suggest that the presence of rotation can lead to the enhancement of the short term rain rates, as discussed in Nielsen and Schumacher (2018).

Examining the results of the MRMS rotation track data and the event-centered composites, further evidence exists that the meteorological conditions in which the rotation events occur are suitable to support the enhancement mechanisms presented in Nielsen and Schumacher (2018) (i.e., that the presence of rotation can dynamically enhance the low-level updrafts and this enhancement can serve to ingest sources of moisture and CAPE that are negatively buoyant). The nocturnal nature of the rotation events (Fig. 4.6b) points to two important processes that are related to the impact that rotation can have on the storm system: nocturnal boundary layer stabilization and the enhancement of the low-level shear by the nocturnal low-level jet (LLJ). The increase in shear associated with the development of the LLJ has shown to increase values of vertical vorticity in existing supercells at low-levels and, through the increased dynamic lifting, more easily lift non-buoyant parcels (Coffer and Parker 2015). Similar results have been shown for increasing low-level shear not necessarily associated with the nocturnal transition as well (e.g., Markowski and Richardson 2014). The overall increased low-level shear of the rotation cases (cf. Fig. 4.10e,g and Fig. 4.10f,h), the signal of the LLJ in the rotation composites (Fig. 4.10c), and the maximum rotation in the MRMS data being located in the lower portions of the storms (i.e., 0–2 km, cf. Tables 4.2 and 4.3), follow with the idea that any rotationally induced dynamical enhancement of the updrafts would occur in the lower-levels of the storms. This agrees with the results of Nielsen and Schumacher (2018) where the dynamic rotational enhancement of the updrafts occurred in the same layer (see Nielsen and Schumacher (2018)'s Fig. 15), which in turn enhanced the rainfall accumulations in the model simulations. In Nielsen and Schumacher (2018) it was also shown that rotationally induced dynamic lifting can regularly lift thermodynamically stable parcels, that still contain moisture and CAPE, out of the nocturnal boundary layer and to their levels of free convection. Given that rotation events occur frequently in the nocturnal hours (Fig. 4.6b), it is not unreasonable to suspect that such an otherwise less available source of moisture and instability is accessible to the updrafts in the extreme rainfall cases with attendant rotation.

While the effect of rotation on precipitation efficiency is not discussed in this manuscript and is very difficult to accomplish from a bulk sense, it remains an important question that the authors plan to look at in specific cases moving forward. Second, the MRMS rotation tracks are based upon azimuthal shear zones in the low and mid-levels, which can highlight both regions of rotation and intense straight line wind signatures (Smith et al. 2016). Thus, some of points in the hourly accumulated low and mid-level rotation tracks used in this study might not be explicitly associated with rotation but other shear zones (e.g., the gradients associated with bowing convective segments). However, in an attempt to reduce the influence of azimuthal shear zones not associated with rotation on the analysis, the MRMS data was conditioned on a minimum rotation threshold of 0.005 s^{-1} at both low and mid-levels. Lastly, the subjective radar analysis is only as good as the radar data that was examined. Data quality issues surely exist based upon distance from the radar, beam blockage, and attenuation, which all could effect the subjective identification of rotation. These issues, which are known to the authors, informed the decision to be as conservative as possible in the subjective rotation versus non-rotation sorting as discussed in the methods.

The presence of rotation in nearly half of the cases of extreme hourly precipitation examined in this manuscript provides observational support for the importance of rotation in cases of extreme hourly rainfall accumulations. These results, combined with the modeling results of Nielsen and Schumacher (2018), support the theory that rotation can aid in enhancing precipitation by providing an additional source of positive momentum through dynamically induced pressure perturbations. The stronger meso-to-synoptic scale forcing (e.g., stronger 850 hPa warm-air advection) seen in the rotation composites is not unexpected, given the increase in low-level environmental shear (Fig. 4.10g,h) and the generally balanced nature of the atmosphere. However, the more pronounced ingredients for extreme rainfall do add a compounding factor into the quantitative attribution of the exact environmental processes leading to these extreme short-term rain rates. However, all else being equal, the addition of more lift will lead to a higher rain rate (e.g., Doswell et al. 1996). The increase in precipitation seen in systems with increasing 0–1 km shear in Nielsen and Schumacher (2018) supports the robustness of the rotational enhancement mechanism as it will occur independently of the background environmental gradients that are associated with any one particular event, although the exact impact of the enhancement on the storm system will change. The overarching conclusion is the same in that intense 0–1 km shear can lead to the production of extreme precipitation by aiding in the development of additional low-level dynamic lift through the presence of mesoscale rotation.

4.6 Summary and Conclusions

In this study, the frequency and environmental characteristics of extreme hourly rainfall accumulation events with attendant rotation was examined across the contiguous United States. METAR rain gauge observations and the Stage-IV gridded precipitation analysis from 2013-2017 and 2013-2015, respectively, were examined to produce a list of valid convectively driven extreme hourly rainfall accumulations. These points were then subjectively and objectively analyzed for the presence of collocated rotation during the hour the observation was valid. The resulting points were clustered into events and event center composites created from the RAP to investigate meteorological characteristics of both events with attendant rotation and those events without.

The results show that just under half of the subjectively identified points associated with extreme hourly rainfall accumulations in the METAR and Stage-IV were associated with collocated rotation (see Section 4 and Table 4.1). The events with collocated rotation, similar to those without rotation, occurred along the Atlantic and Gulf coasts with points extending north into the Great Plans and lower Mississippi valley, but are more focused in the coastal regions than non-rotation events (Figs. 4.3 and 4.4). Of the 29 cases objectively identified with rotation using the MRMS low and mid-level rotation tracks, the vast majority, ~93% and ~86% for the low and mid-level rotation, respectively, were associated with rotation (Tables 4.2 and 4.3). Both the subjective and objective rotation identification methods yield the same conclusion that rotation is often attendant with extreme short-term rainfall accumulations.

Seasonally, rotation events occurred more frequently in the warm season and are more likely in the mid-to-late summer. While non-rotation events share a similar distribution, they can occur into the late winter months, unlike the rotation events (Fig. 4.6a). Non-rotation extreme precipitation events tend to peak with diurnal heating, while rotation events are more common in the late evening and overnight hours (Fig. 4.6b). Further, rotation events tend to produce higher maximum hourly rainfall accumulations above 100 mm (Fig. 4.7). Slight, but important, differences are also seen in between the meteorological characteristics of each event subclass. Rotation events occurred more clearly in the warm sector and were associated with higher low-level shear, PWAT, 850 hPa warm air advection, and slightly weaker winds aloft (cf. left and right columns Figs. 4.9 and 4.10). Non-rotation events tended to occur along a surface boundary, such as a warm or stationary front, closer to the surface low pressure center with similar amounts of MUCAPE as rotation events (cf. left and right columns Figs. 4.9 and 4.10).

The results of this study agree with previous studies that highlight rotation storms as potentially underrepresented producers of extreme rainfall (e.g., Smith et al. 2001; Duda and Gallus 2010; Hitchens and Brooks 2013; Weijenborg et al. 2017) and that dynamically induced accelerations, especially those associated with rotation, should not be ignored when it comes to extreme precipitation. It also provides observational support for the mechanism for rotational enhancement of rain rates presented in Nielsen and Schumacher (2018) and continues the discussion of a potentially common physical mechanism behind the occurrence of concurrent, collocated tornado flash flood events (Nielsen et al. 2015). Ongoing work will attempt to examine individual cases of extreme hourly rainfall accumulations with attendant rotation from a non-idealized, 3-D modeling framework to examine more precisely how the presence of rotation directly or indirectly affects the development of precipitation from a microphysical standpoint.

CHAPTER 5

The Influence of Mesovortices on Precipitation Accumulations in the Houston "Tax Day" 2016 Flood

5.1 Introduction

Extreme rainfall and attendant flash flooding continue to pose significant threats to life and property in the United States. Per annum flash flood fatalities have shown no significant decrease in recent years, despite increased effort, through education and civil mitigation, to curb these statistics (e.g., Ashley and Ashley 2008; Špitalar et al. 2014; Terti et al. 2017). Billion-dollar losses due to flash flooding occurred every year from 2014 to 2017, and flash flooding was responsible for just under ~20% of the total weather related fatalities over that period, which is second only to the combined fatalities due to heat and cold (NWS 2018b) in that same time.

The ability to correctly predict the occurrence and magnitude of a flash flood event requires the proper representation of both the meteorological and hydrological processes at play. What happens once the rainfall hits the ground is dependent on many static and non-static hydrologic features (e.g., topography, soil moisture levels, and catchment scale dynamical characteristics). However, the correct prediction of the location, timing, amount, and rate of rainfall is essential to modeling these processes correctly (e.g., Costa 1987; Hapuarachchi et al. 2011; Saharia et al. 2017). While improvements have been made at nowcasting timescales (e.g., Gourley et al. 2017), advanced prediction of this information is needed, since catchment dynamics can operate on similar timescales (e.g., Creutin et al. 2009). Meteorological predictive systems still struggle to accurately predict extreme rainfall accumulations (e.g., Fritsch and Carbone 2004; Novak et al. 2011; Zhang et al. 2016), partially because the predictability characteristics of such events can very across the U.S. even on the same day (e.g., Nielsen and Schumacher 2016; Nielsen 2016). The utilization of new post processing techniques has proved successful in advancing the multi-day predictive horizons of extreme rainfall (e.g., Herman and Schumacher 2018a,c); however, the prediction of catchment scale and hourly-to-sub-hourly rainfall accumulations still remains a significant challenge (e.g., Schumacher 2017).

The challenge of extreme precipitation forecasting is compounded, compared to other phenomena, by the fact that the occurrence and the magnitude (i.e., both the event total and the rate of accumulation) at a sub-hourly temporal scale is needed. Generally, the environmental conditions conducive to extreme rainfall are well known (e.g., Maddox et al. 1979; Doswell et al. 1996; Schumacher 2017).

Similarly, it is known that extreme rainfall accumulations occur, not surprisingly, where high rain rates are maintained for a long period of time (e.g., Chappell 1986; Doswell et al. 1996). Thus, the resulting duration and rain rate of a particular event are critical constraints on the ability to produce extreme rainfall accumulations. High duration events, often associated with back-building or quasi-stationary convective systems, have been been the subject of a large body of research (e.g., Bluestein and Jain 1985; Chappell 1986; Doswell et al. 1996; Schumacher and Johnson 2005; Schumacher 2009; Nielsen et al. 2016b) and, generally, are driven by strong system scale and environmental interactions as the convective system organizes and matures (e.g., cold pool interactions, MCV development, or how an MCS orients to a synoptic scale boundary).

Comparatively, the processes that determine the rain rate of the system operate at the system scale and the scales of the individual convective elements. The controlling processes include updraft strength, the precipitation efficiency (related to the ongoing microphysical processes, among others; Sui et al. 2007), and the water vapor mixing ratio of the rising air (Equation 3.2; Doswell et al. 1996), which, given the chaotic nature of moist convection (e.g., Lorenz 1969; Zhang et al. 2006; Melhauser and Zhang 2012; Nielsen and Schumacher 2016), are difficult to constrain at the needed lead times. From a flash flooding perspective, the rainfall rate is known to be a important factor in determining the resulting flash flood potential, with harmful impacts increasing with the rain rate (e.g., Kelsch et al. 2001; Kelsch 2001; Kandel et al. 2004; Mohamadi and Kavian 2015). The predictive challenges and hydrologic importance motivate the need to examine the processes that allow for the most intense rainfall rates to be maintained.

Recent observational studies (Smith et al. 2001; Duda and Gallus 2010; Hitchens and Brooks 2013), including Chapter 4 of this dissertation, have shown that extreme rainfall rates can be produced and maintained by supercell thunderstorms and other meso-γ-scale rotation, despite the notion that such storms could not produce such rain rates because of low precipitation efficiency (e.g., Marwitz 1972; Foote and Fankhauser 1973; Browning 1977). Supercells and hail producing storms have even been responsible for world record accumulations (Dalrymple 1937) and some of the most intense flash floods in U.S. history (Smith et al. 2018). Additionally, concurrent, collocated tornado and flash flood events, known as “TORFF” events (Nielsen et al. 2015, 2016a; Bunkers and Doswell 2016), occur frequently in the U.S. (See Chapter 2 for more details). These studies point to the importance of rotating storms in producing extreme rainfall accumulations and rates.

Nielsen and Schumacher (2018) showed, using idealized simulations, that rotation associated with intense 0–1 km shear, can enhance rain rates through dynamic lifting from induced vertical perturbation pressure gradient forces (see Section 2.5.3 of Markowski and Richardson 2010) associated with rotation that are not present in non-rotating storms. The resulting rotationally induced dynamic lifting can aide in maximizing rain rates, first, by dynamically enhancing the updraft and, second, lifting otherwise negatively buoyant parcels that still contain moisture and instability to their level of free convection. These rotational precipitation enhancement mechanisms serve as a dynamical explanation for the ability for storms with meso-γ-scale rotation, including supercells, to produce extreme rainfall accumulations and intense rain rates. Furthermore, it offers a physical explanation for the frequency of TORFF events in the U.S.

Many high profile flash flooding events with concurrent and collocated tornado threats (i.e., TORFFs) have occurred in and around Houston, Texas in recent years. This includes floods in April 2009, the Memorial Day Flood of 2015, the "Tax Day" Flood in 2016 (Linder and Fitzgerald 2016), and Hurricane Harvey in 2017 (NWS 2018a). Specifically, these events have been associated with historically intense flooding and rainfall rates with embedded rotation on various scales throughout each event. The overall prevalence of such events in this region, combine with a dense network of operational radars and rain gauges (HCFWS; HCFCD 2019) from civil authorities, provides an excellent opportunity to examine the meteorological characteristics of these events and determine if the results of Nielsen and Schumacher (2018) are applicable outside an idealized framework.

This research serves to extend the idealized simulations of Nielsen and Schumacher (2018) by examining a full spatially heterogeneous simulation and performing a detailed modeling and observational analysis of the 18 April 2016 Houston "Tax Day" Flood, which led to 8 fatalities and damage to thousands of homes and automobiles. It is hypothesized, following Nielsen and Schumacher (2018), that the most intense rain rates are associated with embedded rotating features and possess more intense low-level updraft structures associated with the dynamical effects of rotation. Furthermore, it is hypothesized that the rainfall production associated with these rotating features is maximized following the development of the rotation. Section 5.3 describes the "Tax Day[1]" Flood event in detail, section 5.2 presents the methods, section 5.4 the results of the event analysis, section 5.5 the results of the model analysis, and section 5.6 a discussion and summary of the manuscript.

[1]The quotations will be dropped from this point forward.

5.2 Methods

Observational and modeling analyses of the Houston Tax Day flood are carried out in the manuscript, in an effort to test the hypotheses proposed in the previous section. The data sources and methodology are outline below.

5.2.1 Observational Analysis

The observational analysis examines the convective structure and evolution of the MCS using dual-pol radar observations from the Houston/Galveston NEXRAD (KHGX) radar system, where specific attention is given to any rotating features. This analysis was accomplished using Level II reflectivity and velocity data, as well as Level III specific differential phase (K_{dp}) data. The Gibson Ridge GRLevel2 Analysts software package (http://www.grlevelx.com/gr2analyst/) is used to analyze the data and calculate the K_{dp} for the event. Additionally, the Normalized Rotation (NROT) product, as derived in the GRLevel2 Analysts software package, is also used as an objective method to quantify the strength of any present rotation and more importantly, provide a level comparison between various analysis times. NROT is a fairly complex derived product that can be, at its most basic level, viewed as the azimuthal shear that is normalized to take into account the effects of beam spreading (More infromation can be found from Gibson Ridge). Any normalized values of NROT above 1 are considered significant, while values above 2.5 are considered extreme. However, as previously mentioned, the NROT field are used mainly to compare the strength of the rotation at different times within this event, as opposed to quantifying the strength of the rotating features compared to other events.

High spatial and temporal rain gauge data is used to evaluate the precipitation produced by varying convective features within the MCS, where the features are identified and characterized by the aforementioned radar data. The rainfall data is obtained from the Harris County Flood Control District's (HCFCD) Harris County Flood Warning System (HCFWS; HCFCD 2019). This network contains 163 rain gauges spread over the Houston Metropolitan Area, which provide 5-minute rainfall accumulation observations with a minimum detection threshold of ~1 mm (0.04 inches). The high temporal nature allows for near real-time interrogation of the rainfall being produced by an individual convective element embedded within the MCS.

Mesoscale and synoptic data is obtained from the Rapid Refresh Model (RAP; Benjamin et al. 2016) analysis at various times throughout the event. This data is supplemented by wind shear information obtained from the Storm Prediction Center's Mesoscale Analysis (SPC 2018). Additionally, Stage-IV gridded precipitation data (Lin and Mitchell 2005) is used to regionally evaluate any model precipitation forecasts.

5.2.2 Model Analysis

Operational numerical models did not forecast the severity, spatial coverage, or general location of this event well (not shown). Similar problems were seen in the operational High Resolution Rapid Refresh (HRRR; Smith et al. 2008, https://rapidrefresh.noaa.gov/hrrr/), despite 1-hour data assimilation updates. However, the 0000 UTC 18 April 2016 initialization of experimental version of the HRRR (HRRRx) at the time, captured the overall evolution and severity of the event quite well (cf. Fig. 5.1a,b). For this reason, the Weather Research and Forecasting Model Advanced Research Core (WRF-ARW, Klemp et al. 2007; Skamarock et al. 2008; Skamarock and Klemp 2008) initial and boundary conditions for the 0000 UTC 18 April 2016 initialization of the HRRRx were obtained from the Earth Systems Research Laboratory (ESRL). These files were then used to reproduce the HRRRx 3-km horizontal grid-spacing forecast using WRF-ARW version 3.6 and the same physics and model specifics as used in the original HRRRx run. An additional high-resolution nest with horizontal grid-spacing of 600 m was placed within the original HRRRx covering southeastern Texas (extent shown in Fig. 5.1c). The most pertinent model specifics include 1800 x 1060 3-km grid-spacing outer domain, 1001 x 901 600-m inner domain, stretched vertical grid with 51 levels in both domains, no cumulus parameterization in either domain, no feedback between domains, Thompson aerosol-aware microphysics on both domains (Thompson and Eidhammer 2014), RRTMG longwave and shortwave radiation on both domains (Mlawer et al. 1997), Rapid Update Cycle (RUC) land surface model on both domains (Smirnova et al. 1997, 2000, 2016), and Mellor-Yamada-Nakanishi-Niino planetary boundary layer scheme on both domains (MYNN; Mellor and Yamada 1982; Nakanish 2001; Nakanishi and Niino 2004). The simulation was run for 22-hours, ending 2200 UTC 18 April 2016. Model output was archived at 5-minute intervals on the inner domain and 30-min intervals on the outer domain. The inner domain serves as the analysis domain for this research. Specific focus is given to the relationships between updrafts, rotation, and precipitation formation processes.

5.3 Event Overview

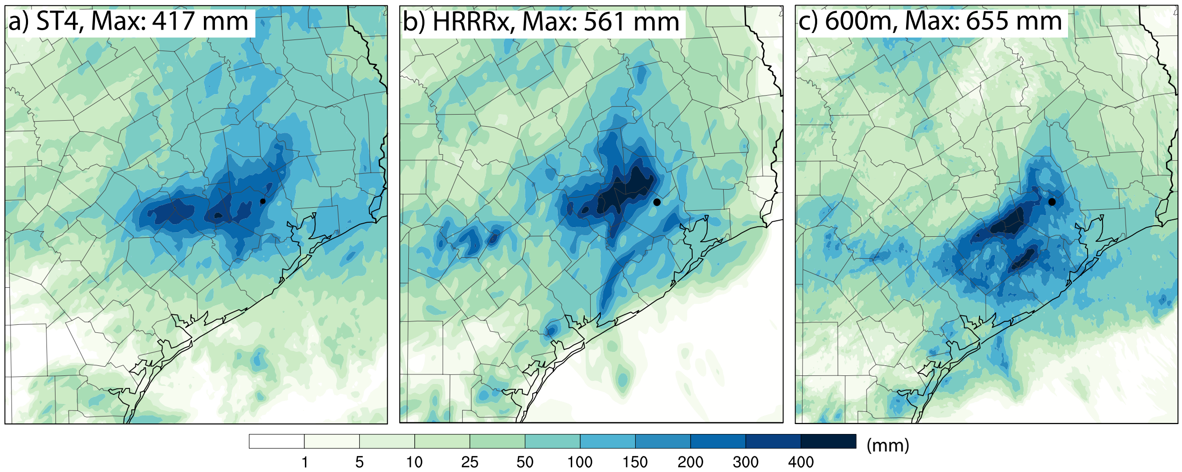

FIG. 5.1. 22-hr precipitation accumulation valid 2200 UTC 18 April 2016 from (a) the Stage-IV precipitation analysis (ST4; Lin and Mitchell 2005), (b) the 0000 UTC 18 April 2018 initialization of the experimental High-Resolution Rapid Refresh (HRRRx) model, and (c) the 500 m grid spacing inner domain initialized within the HRRRx. Geographic extent in figures corresponds to that of the high resolution inner domain.

The "Tax Day" flood of 18 April 2016 in Houston, Texas was responsible for significant rainfall (Fig. 5.2a-b) and flooding across the metropolitan area (Fig. 5.2c). Broad areas of 150 to 300 mm (~6 to 12 inches) of rainfall were seen over a large portion of southeastern Texas (Fig. 5.1a) throughout the event. Some portions of western Harris county received over 400 mm (~16 inches) of rain over a 12-hr period, as observed by the Harris County Flood Control District (HCFCD) rain gauge network, with values over 550 mm (~22 inches) seen in far western Waller County. An event maximum of ~600 mm (23.5 inches) was observed over 14.5-hr period in Pattison, Texas (Waller County) from a local observer (Linder and Fitzgerald 2016). The highest rainfall totals corresponded to extrapolated exceedance probabilities less than 0.1% (i.e., >1,000 year event; Fig. 5.2a), with the event maximum rainfall accumulation corresponding to a 0.01% exceedance chance (i.e., 10,000 year event; Linder and Fitzgerald 2016). The rainfall led to significant flooding along the creeks and bayous in eastern and northern Harris County, with exceedance probabilities less than 0.2% (i.e., 500 year event) observed (Fig. 5.2c). A total of eight fatalities were directly associated with flash flooding from the event, all from drownings in vehicles. Additionally, approximately 40,000 vehicles and 10,000 homes were damaged (Linder and Fitzgerald 2016; NOAA 2016b). While the flash flooding served to be the main hazard associated with the Tax Day flood, tornado warnings were issued by the Houston/Galveston WFO, and post event surveys identified that three EF-0 tornadoes occurred within the storm system. This led to the Tax Day flood being identified as a "verified" TORFF event in the results presented above in Chapter 2.

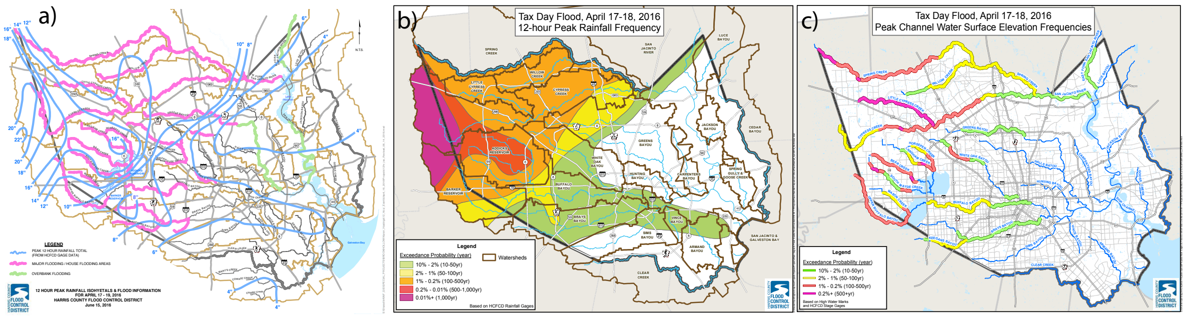

FIG. 5.2. (a) Harris County Flood Control District rain gauge analysis (blue lines) and noted channel flooding (pink lines) for the 18 April 2016 Tax Day Flood. (b) and (c) return period frequency analysis of rainfall and streamflow, respectively, from the same source. Plots are reproduced from Linder and Fitzgerald (2016).

The rainfall in and around the Houston area on 18 April 2016 was the result of a deep, slow moving upper-level system that was anchored over the Great Basin, due to the presence of an "omega" blocking ridge in the eastern United States (Fig. 5.3a,b). The counter-clockwise flow around the stationary upper-level system advected significant amounts of moisture off the Gulf of Mexico into the central United States (Fig. 5.3a-b,d). Warm-air advection at mid-levels was maximized in the southern portions of the U.S., specifically along the Texas Gulf Coast (Fig. 5.3c). Shortwaves embedded around the closed upper-level low (Fig. 5.3b) continued to initiate convection throughout the central and eastern U.S., until the upper-level system into the Atlantic Ocean by 24 April 2016 (not shown). The position of the cut-off upper-level trough and the blocking ridge led to relatively weak winds throughout the column in the Houston, Texas area (Fig. 5.3a), with the maximum wind speeds located below 850-hPa (Fig. 5.3c).

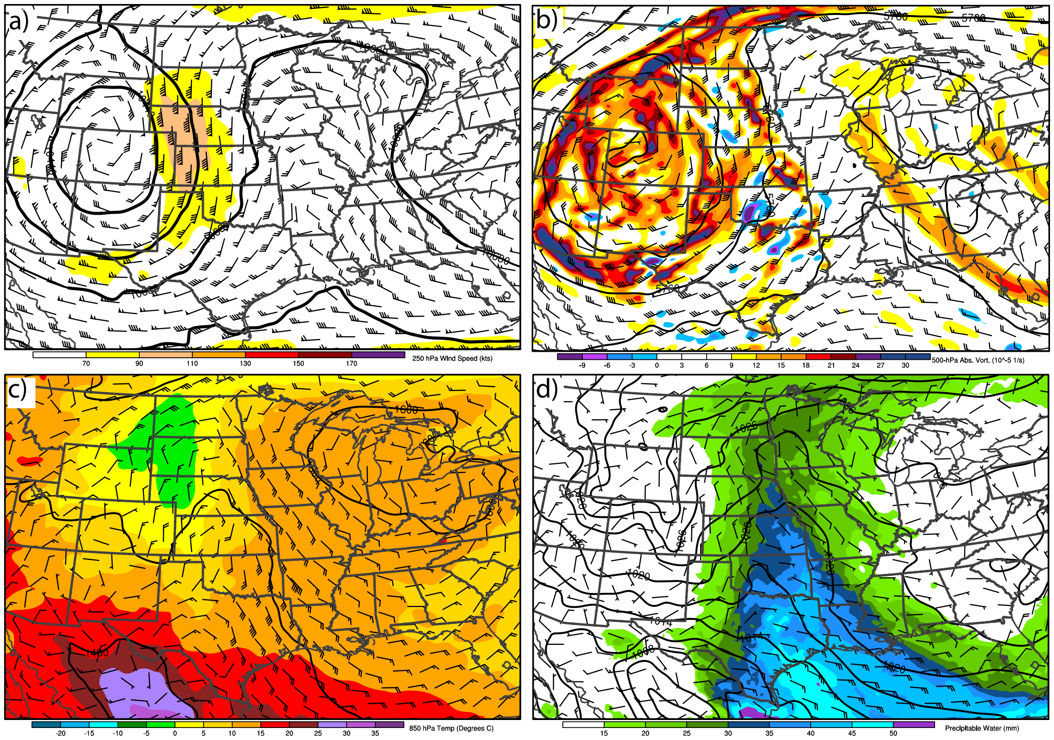

FIG. 5.3. (a)–(d) Rapid Refresh (RAP; Benjamin et al. 2016) analyses valid at 0000 UTC 18 April 2016. (a) 250-hPa isotachs (shaded every 20 kt over 70 kt, 1 kt = 0.5144 m s^{-1}), 250-hPa geopotential height (contoured every 120 m), 250-hPa wind barbs(half barb = 5 kt, full barb = 10kt, pennant = 50 kt,). (b) Absolute vorticity at 500-hPa ($\times 10^{-5} s^{-1}$), shaded every $3 \times 10^{-5} s^{-1}$ above $-9 \times 10^{-5} s^{-1}$), 500-hPa geopotential height (contoured every 60 m), and 500-hPa wind barbs. (c) 850-hPa geopotential height (contoured every 25 m), 850-hPa wind barbs, and 850-hPa temperature (shaded every 5°C from -20°C to 35°C). (d) precipitable water (shaded contours every 5 mm for values from 10 mm to 50 mm), 10 m wind barbs, and mean sea level pressure (MSLP) (contoured every 3 hPa).

Convection initiated in the Houston area associated with an upper-level shortwave near 2300 UTC 17 April 2016 (not shown). Over the next four hours the convection continued to intensify into the overnight hours associated with an increase in total column moisture (Fig. 5.4a) and instability (Fig. 5.4b) off the Gulf of Mexico, with PWAT exceeding 50 mm and MUCAPE exceeding 1500 J Kg^{-1}. The increase in moisture and instability coincided with the development of a robust nocturnal lower-level jet (LLJ) that approached 24 m s^{-1} at 900-hPa by 0300 UTC 18 April 2018 (Fig. 5.4b). No representative operational upper-air observations were available, since this portion of the upper Texas coast is located in an upper air observation hole (Benoit et al. 2018). However, SPC mesoanalysis (SPC 2018) shows 0–1 km shear values over 15 m s^{-1} (Fig. 5.4c) with the majority of the atmospheric shear being located in the low levels (cf. Figs. 5.4c and d), associated with the strength of the LLJ.

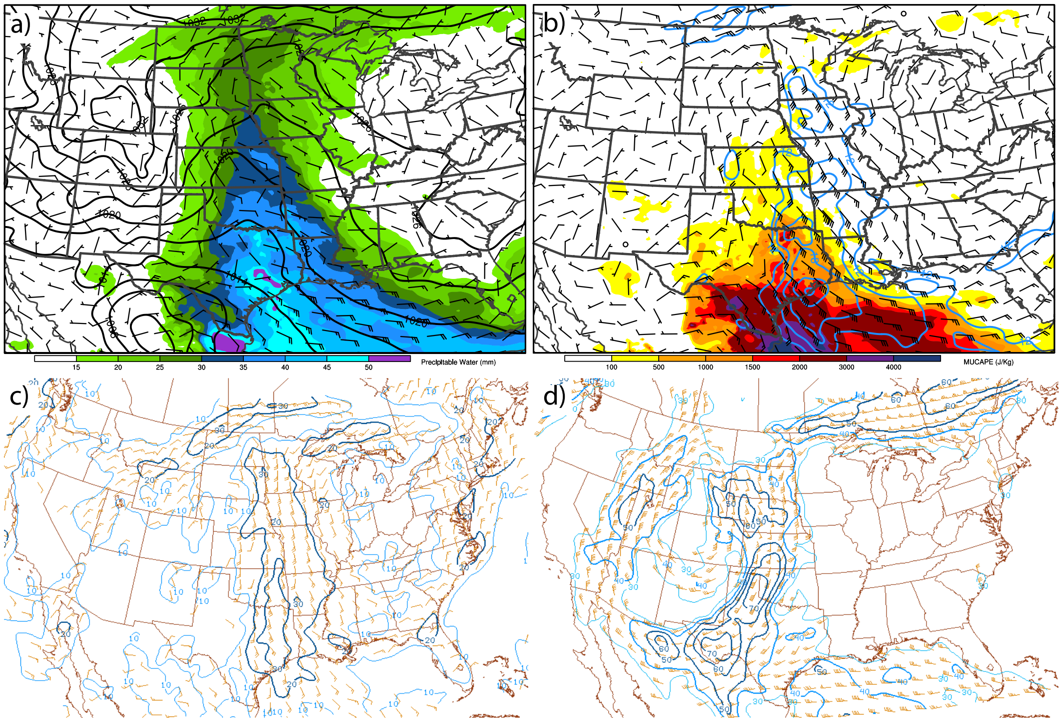

FIG. 5.4. (a)–(b) Rapid Refresh (RAP; Benjamin et al. 2016) analyses valid at 0300 UTC 18 April 2016. (a) precipitable water (shaded contours every 5 mm for values from 10 mm to 50 mm), 10 m wind barbs, and mean sea level pressure (MSLP) (contoured every 3 hPa). (b) Most Unstable CAPE (MUCAPE; shaded at 100 J kg^{-1} then every 500 J kg^{-1} above 500 J kg^{-1}), 900-hPa wind barbs, and 900-hPa isotachs (contoured every 3 m s^{-1} above 12 m^{-1}). 0–1 km (c) and 0–6 km (d) environmental shear from the Storm Prediction Center mesoscale analysis (SPC 2018).

The previously isolated convection began to congeal beginning about 0230 UTC 18 April 2016 (not shown). The cell mergers continued and the intensity of the convection increased, with a broad area of 50 dBz cores present by 0430 UTC that same day (Fig. 5.5a). Furthermore, a developing mesoscale convective vortex (MCV) and smaller rotating features were also visible in the radar imagery at this time Fig. 5.5d). The intense rainfall and the MCV led to reinforcement of a low-level cold pool boundary perpendicular to the onshore low-level jet. This created a somewhat stationary arc of rainfall along the edges of the boundary (Fig. 5.5b) that contained many rotating features on varying scales (Fig. 5.5e), some of which were tornado warned. As intense rainfall continued, the resulting cold pool strengthen and the MCS was able to move east, against the intense low-level jet (Fig. 5.5c,f). The now outflow dominate MCS moved into the Gulf of Mexico by 1700 UTC 18 April 2016, and light stratiform precipitation continued in the Houston area until approximately 1900 UTC.

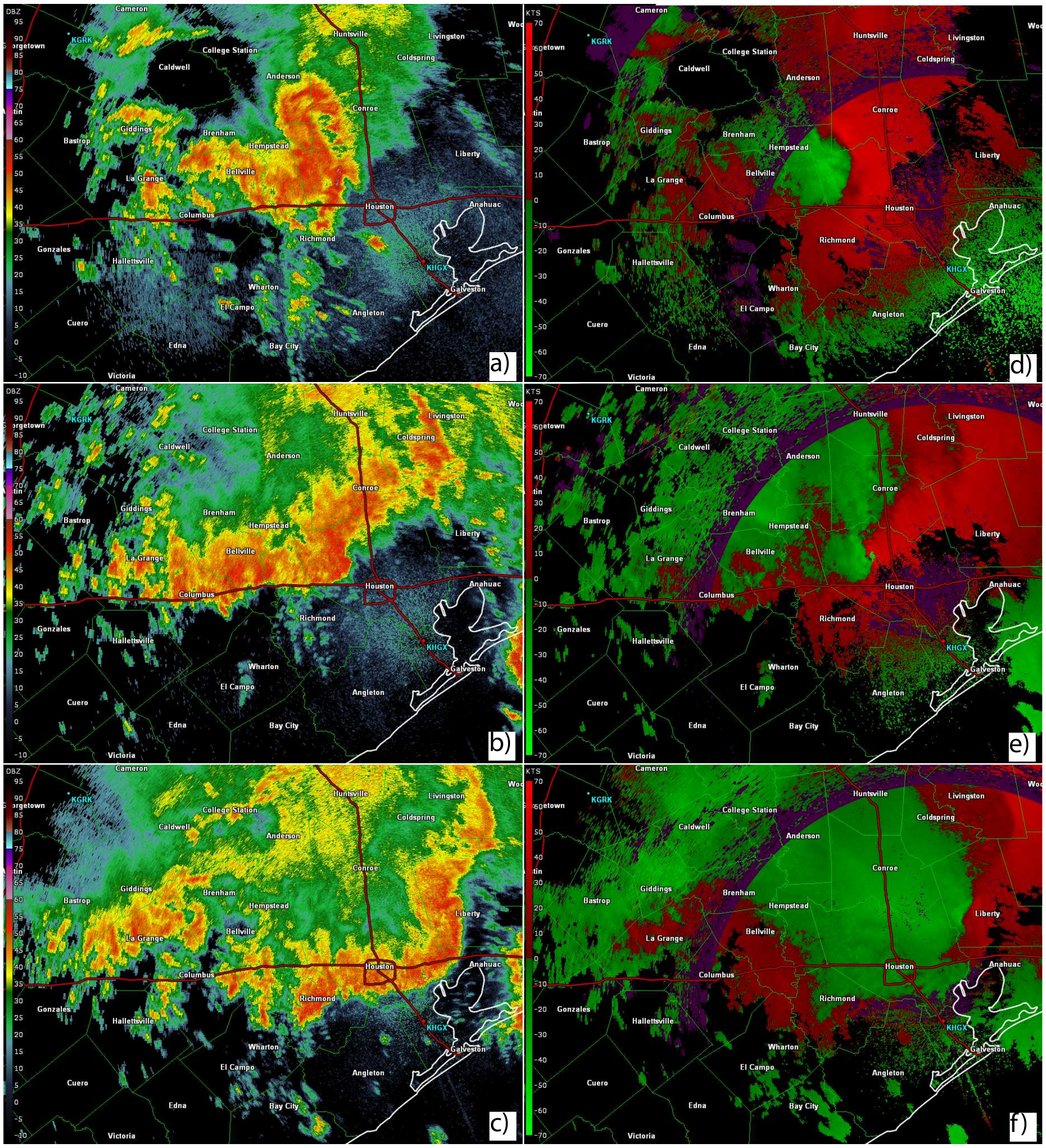

FIG. 5.5. Radar reflectivity (a-c) and velocity (d-f) from the Houston/Galveston (KHGX) radar valid (a,d) 0432 UTC, (b,e) 0822 UTC, and (c,f) 1059 UTC 18 April 2016.

5.4 RESULTS: OBSERVATIONAL ANALYSIS

While heavy rainfall was recorded throughout the event by many HCFCD rain gauges, two main periods of especially intense rainfall were observed by gauges on the north side of the Houston Metro area. The first period, between 0430 and 630 UTC and, the second period between 0700 and 0900 UTC (Fig. 5.6). Each period was associated with observed intense 5-minute rain rates, which in some cases were over 20 mm (~0.80 inches), that were sustained for close to an hour at each rain gauge location (Fig. 5.6). The 5-minute rain rates were maximized at the beginning of each period, but the storms still produced large short-term rainfall accumulations (i.e., 5-10 mm (~0.20-0.40 inches) in 5-minutes) in the following time periods.

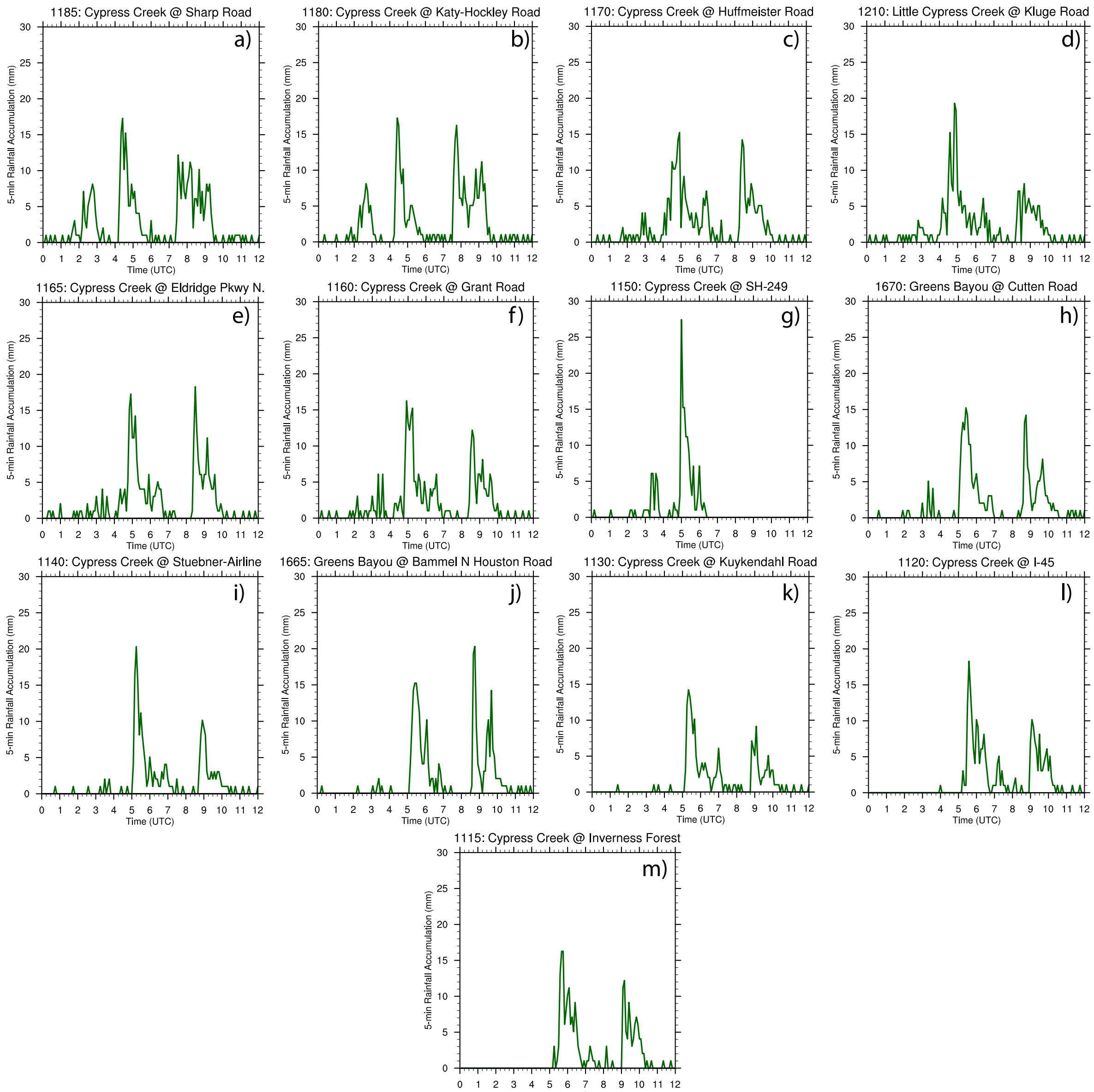

FIG. 5.6. Timeseries of 5-minuteute rainfall accumulations from 13 HCFWS gauges valid 0000 UTC to 1200UTC 18 April 2016. Gauge locations are noted in Figs. 5.7, 5.8, 5.9, and 5.10 by large white markers with letters corresponding to the panel labels in this figure. (d) is missing data between 0725 and 810 UTC. (g) is missing data after 0620 UTC.

The first period, between 0430 and 0630 UTC 18 April 2016, was associated with the development and maintenance of an embedded, rotating, and tornado-warned feature that moved across the northern Houston metro area. Radar imagery from this period (Fig. 5.7) shows robust convection sustained along and behind the leading edge of this feature for the majority of the period (Fig. 5.7a,e,i,m). The broad elongated rotation along the leading edge (Fig. 5.7b,f,j,n and Fig. 5.7d,h,l,p) is persistent through the period as well. The maximum rotation, per the NROT algorithm, is seen near 0500 UTC (Fig. 5.7f,h), just before the tornado warning is issued. Throughout the period the locations of rotation (Fig. 5.7d,h,l,p) are located just upstream from from the locations of broadly higher K_{dp} values (cf. Fig. 5.7d,h,l,p and Fig. 5.7c,g,k,o), with local maximums in the broad high K_{dp} region corresponding to local maximums in the upstream rotation. This can be seen south of gauge E in Fig. 5.7c,d; north of gauge F and G in Fig. 5.7g,h; and west of two regions of locally most intense-rotation in Fig. 5.7o,p.

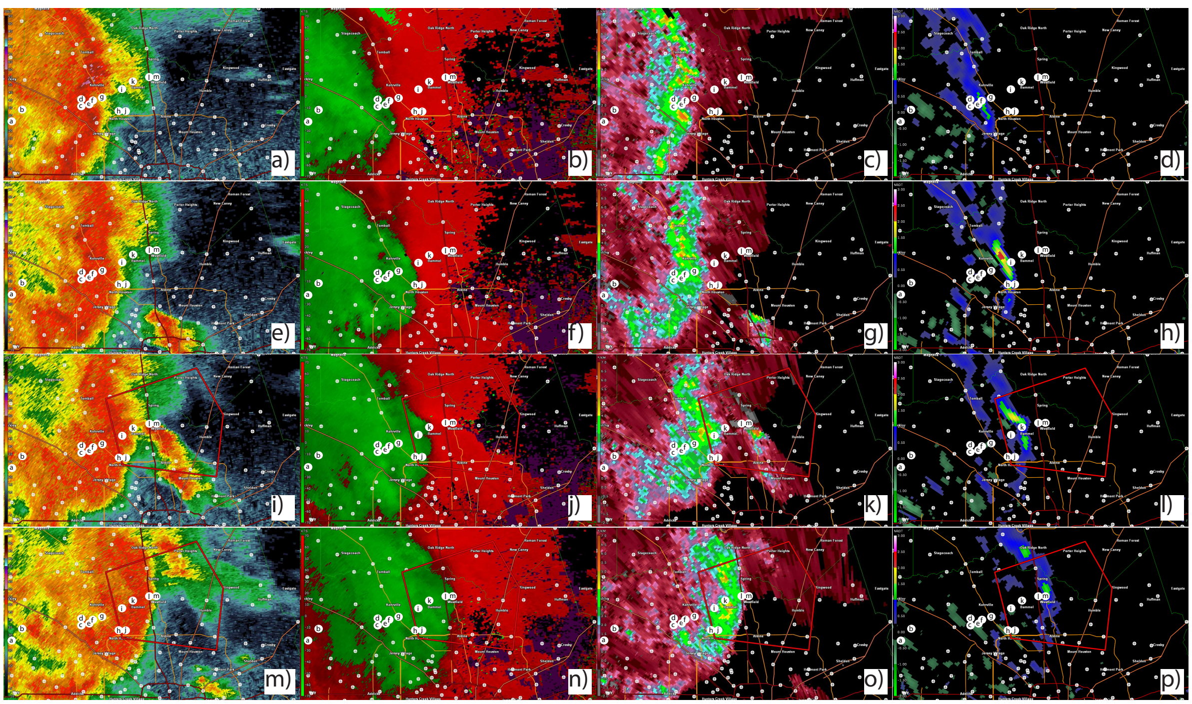

FIG. 5.7. Base radar reflectivity (first column), radial velocity (second column), specific differential phase (K_{dp}; third column), and normalized rotation (NROT; fourth column) as calculated by the Gibson Ridge GRLevel2 Analyst software (http://www.grlevelx.com/gr2analyst/) from the Houston/Galveston NEXRAD radar (KGHX) valid at (a-d) 0445 UTC, (e-h) 0459 UTC, (i-l) 0510 UTC, and (m-p) 0528 UTC 18 April 2016. Small white markers correspond to locations of rain gauges as part of the Harris County Flood Warning System (HCFWS). Red polygons correspond to valid tornado warnings. Large white markers indicate the locations of the gauges presented in Fig. 5.6, where the letter on the marker corresponds to the panel label in Fig. 5.6 showing each respective gauges timeseries.

The relationship is important to note, since K_{dp} is proportionate to liquid water content and has a nearly linear relationship to rain rate (e.g., Kumjian 2013a,b). Thus, the rotating updrafts are spatially correlated with the regions of most intense liquid water content as diagnosed by the radar on a broad and local scale.

The rain gauge data illustrates that the highest rain rates are, indeed, associated with the most intense K_{dp} values. Gauges C (Fig. 5.6c) and D (Fig. 5.6d) both show a rapid increase in observed rainfall accumulations beginning at 0440 UTC, right as the most intense K_{dp} values reached the gauges (5-minute before Fig. 5.7a-d). In the 15-minute period between 0440 and 0455 UTC (5-minute before Fig. 5.7e-h), gauges C and D recorded 40.64 mm (1.6 inches) and 44.70 mm (1.76 inches) of rain, respectively (Fig. 5.6c-d). This period corresponded to the passing of the locally intense K_{dp} structure associated with local maximum of rotation in the leading edge of the convection. Furthermore, once the locally intense K_{dp} feature passes gauge locations, intense rainfall is still measured (Fig. 5.6c-d), given that intense convection is still ongoing in the region (Fig. 5.7a,c,e,g). However, the rainfall rates are not to the magnitude of that seen with the rotating portion of the line.

The same pattern can be seen across the rest of the gauges presented in Fig. 5.6 extrapolating out in time as the rotating feature moves off to the east-northeast. For instance, gauge G (Fig. 5.6g) shows a rapid increase in rain rate at 0455 UTC, right as a locally high K_{dp} feature (orange region south gauge E in Fig. 5.7c) reaches its location (between time shown in Fig. 5.7a-d and Fig. 5.7e-h). By the time the high K_{dp} structure moves away from the gauge at 0510 UTC (Fig. 5.7i-l), ~58 mm (2.28 inches in 15-minute) of rain accumulated (Fig. 5.6g), including a 5-minute accumulation of 27.43 mm (1.08 inches). However, 5-10 mm (~0.2-0.4 inches) 5-minute accumulations are observed in the intense convection behind the high K_{dp} structure, until the rain gauge stops reporting. During the first period of intense rainfall, the gauges presented in Fig. 5.6 show that extreme 5-minute accumulations are observed associated with a locally intense K_{dp} structure that is spatially correlated with regions of most-intense rotation. The 5-minute rainfall observations behind this K_{dp} structure are still quite impressive, but not as extreme.

The second period between 0700 and 0900 UTC 18 April 2016, similar to the first, was associated with high 5-minute rain rates (Fig. 5.6) and the development/maintenance of another embedded rotating feature. The rotating feature in question was embedded in the MCS at the southeastern corner of the convective line (for regional view Fig. 5.5b,e) and moved east over the period. The rotation initially became evident in the radar data shortly after 0700 UTC (not shown). The main convective portion associated with the rotation reaches the outskirts of the Houston metro by about 0730 UTC (Fig. 5.8a). The convection with the embedded rotation continues to strengthen, and broaden, as it moves eastward until approximately 840 UTC (Figs. 5.8-5.10), at which point the rotation begins to weaken as the convection crosses Interstate 45. Multiple tornado warnings were issued during the period (Figs. 5.9-5.10) on the north and northwest side of the Houston metro.

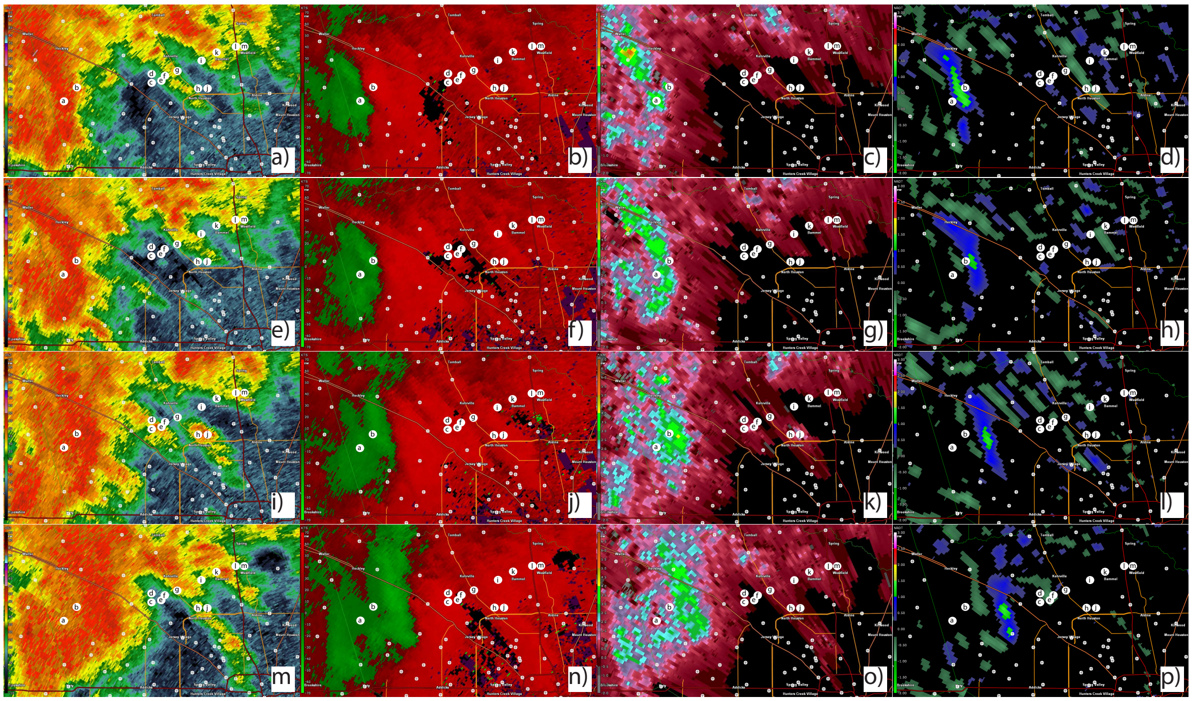

FIG. 5.8. As in Fig. 5.7, except valid at (a-d) 0726 UTC, (e-h) 0732 UTC, (i-l) 0739 UTC, and (m-p) 0749 UTC 18 April 2016.

As aforementioned in the first period of intense rainfall, there is a persistent region of high K_{dp} along the leading edge of the convection near just upstream from the rotating portions of the convection (cf. Figs 5.8-5.10c,g,k,o and Figs. 5.8-5.10d,h,i,p). Higher values of K_{dp} are present within this broad K_{dp} structure and are spatially correlated with the downstream regions of most intense rotation (cf. Figs. 5.8-5.10c,g,k,o and Figs. 5.8-5.10d,h,i,p), as in the first period of extreme rainfall. The spatial coverage of the high K_{dp} values on the leading convective edge appear to increase as the rotation broadens and intensifies over the period (cf. Figs. 5.8-5.9c,g,k,o and Figs. 5.8-5.9d,h,i,p). Furthermore, the most intense values of K_{dp} within the broader K_{dp} structure appear to intensify/are maintained as the spatially correlated upstream regions of most intense rotation also intensify/are maintained (cf. Figs. 5.8-5.9c,g,k,o and Figs. 5.8-5.9d,h,i,p). Both of these tendencies are illustrated well in 0808 to 0836 UTC time frame (Fig. 5.9c-d, g-h, k-l, o-p), as the rotation reaches its maximum.

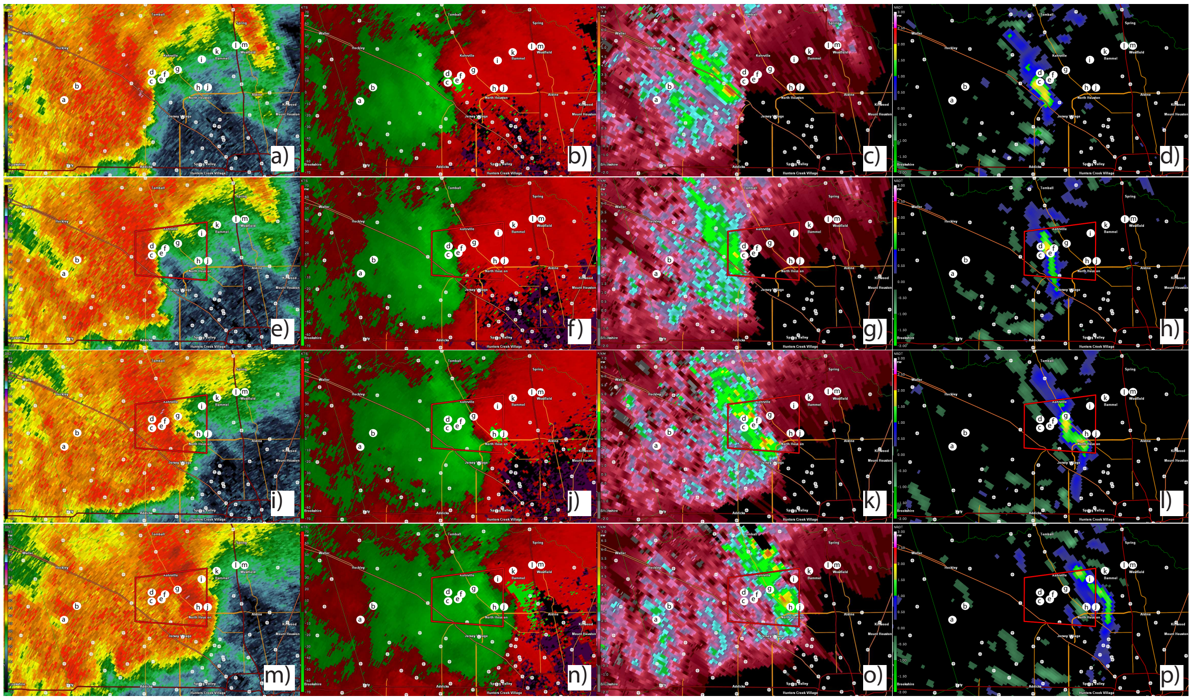

FIG. 5.9. As in Fig. 5.7, except valid at (a-d) 0808 UTC, (e-h) 0814 UTC, (i-l) 0825 UTC, and (m-p) 0836 UTC 18 April 2016.

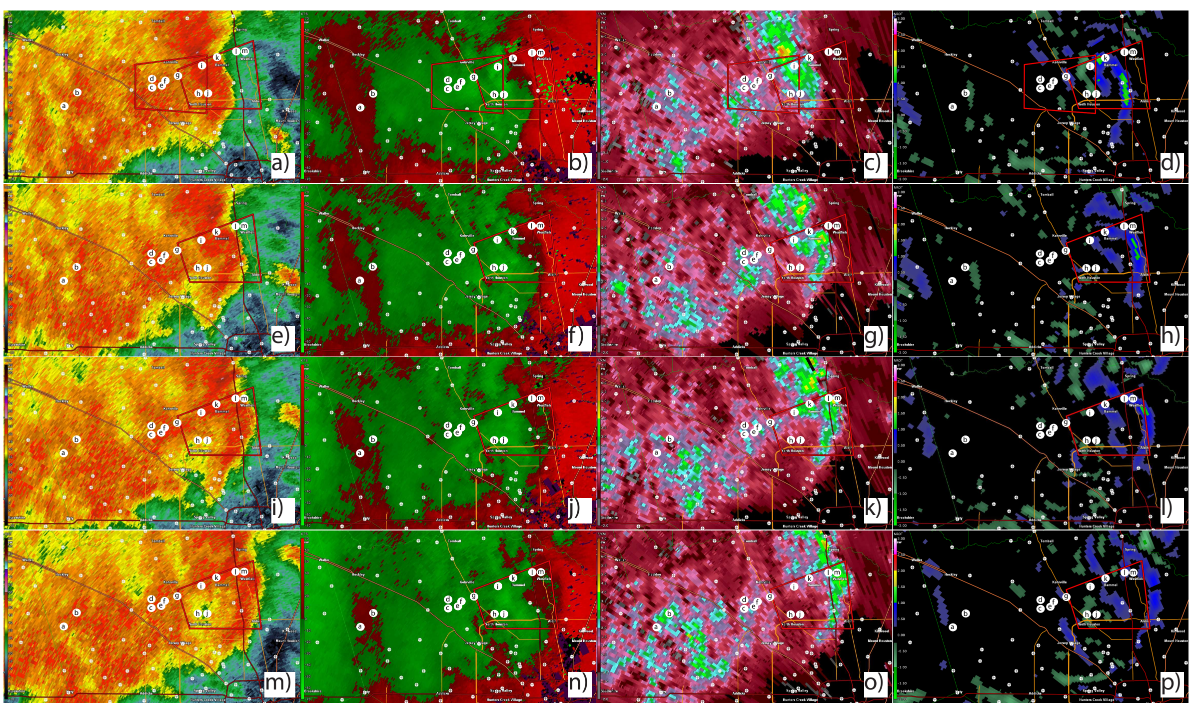

FIG. 5.10. As in Fig. 5.7, except valid at (a-d) 0844 UTC, (e-h) 0850 UTC, (i-l) 0855 UTC, and (m-p) 0900 UTC 18 April 2016.

The local maxima and overall breadth of the K_{dp} structure weakens as the rotation weakens as well (Fig. 5.10c-d, g-h, k-l, o-p). However, there appears to be a slight lag in the in the K_{dp} weakening, when referenced to the timing of rotational weakening (Fig. 5.10c-d, g-h, k-l, o-p). This make sense given that the rotation is a representation of the updraft strength, and the K_{dp} values are a representation of the hydrometeors.

The rain gauge data in this second period of intense rainfall shows, as the radar data, a very similar pattern to the first period. The rainfall produced in high K_{dp} values associated with the leading edge of the convection and rotation produce extreme 5-minute rainfall accumulations, followed by smaller, but still substantial, 5-minute accumulations after the highest K_{dp} structures pass (Fig. 5.6). Examples can be seen in gauges across the 0700 to 0900 UTC time frame as the convection moves off to the east (Fig. 5.6). For instance, gauge B (Fig. 5.6b) in the early part of the period received 42.7 mm (1.68 inches) in the 15-minute period beginning at 0735 UTC, which corresponds well to the period over which the high K_{dp} values were over the gauge location (Fig. 5.8g,k,o). However, 5-10 mm (~0.2-0.4 inches) 5-minute accumulations are still observed following the passage of the high K_{dp} region. As the rotating feature continues to move east over the period, similar patterns are seen at the remaining gauges with 15-minute accumulations associated with the K_{dp} ranging from ~22.4 to ~48.8 mm (0.88 to 1.92 inches). Gauges that experienced enhanced K_{dp} near more intense rotating elements received more intense accumulations over the same period. For example, gauges J (Fig. 5.6j) and H (Fig. 5.6h) received ~34.5 mm (1.36 inches) and ~48.8 mm (1.92 inches), respectively, in the 0835 to 0850 UTC period (from Fig. 5.9o to Fig. 5.10c and g). While gauge I (Fig. 5.6I), which experience smaller K_{dp} values between 0845 and 0900 (Fig. 5.10), received ~27.4 mm (1.08 inches). Lastly, as the rotation and K_{dp} values weakened as the convective line moved east, the 5-minute rainfall accumulation maximums also weakened (cf. Fig. 5.10 and Fig. 5.6i,k-m). These results, combine with those in the first period of intense rainfall, appear to show the importance of rotation in enhancing the short-term rainfall rates observed by the high-density rain gauge network in the Houston metro area.

5.5 Results: Model Analysis

The high-resolution, 600 m nest initiated within the HRRRx (referred hereafter as "analysis simulation") produced a convective system similar to that observed during the Tax Day flood (Fig. 5.11). As in the observed system, the initial isolated convection congealed into a linear MCS that moved eastward through the Houston metro area (cf. Fig. 5.5 and Fig. 5.11) on 18 April 2016. The convection in the analysis simulation produced regional rainfall accumulations on a similar order to those observed by the Stage-IV analysis (i.e., broad regions of over 300 mm, Fig. 5.1a,c), but also included an event maxima that was on the order of that observed by the HCFWS gauges (i.e., ~600 mm, Fig. 5.1c).

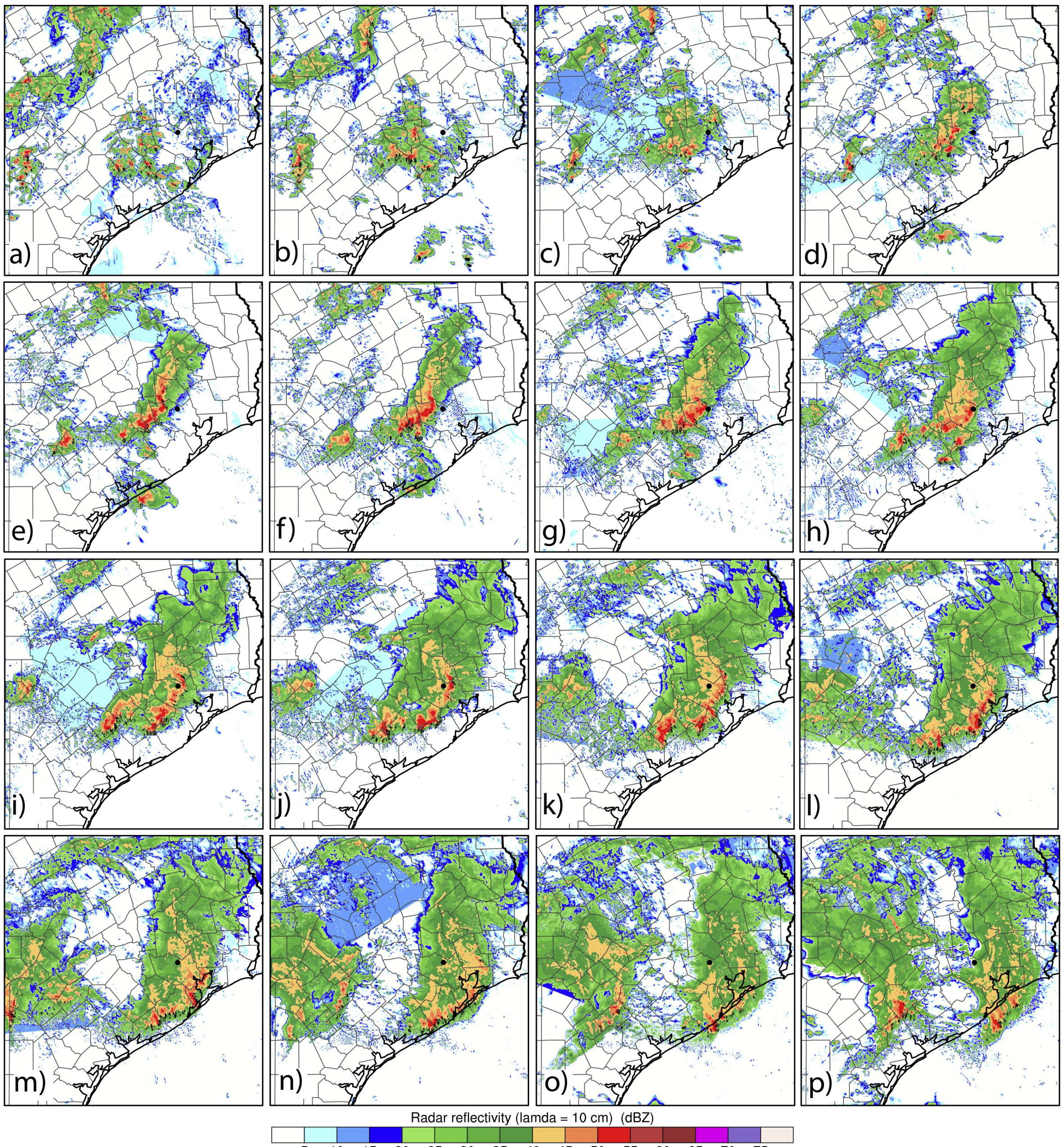

FIG. 5.11. Simulated 1 km radar reflectivity (fill; dBz) and maximum updraft helicity (black contours; every 100 m^2 s^{-2} starting at 150 m^2 s^{-2}) for the analysis domain valid (a) 30-min, (b) 1-hr 30-min, (c) 2-hr 30-min, (d) 3-hr 30-min, (e) 4-hr 30-min, (f) 5-hr 30-min, (g) 6-hr 30-min, (h) 7-hr 30-min, (i) 8-hr 30-min, (j) 9-hr 30-min, (k) 10-hr 30-min, (l) 11-hr 30-min, (m) 12-hr 30-min, (n) 13-hr 30-min, (o) 14-hr 30-min, and (p) 15-hr 30-min into the simulation initialized at 0000 UTC 18 April 2016. Black dot denotes the location of George H.W. Bush Intercontinental Airport (KIAH).

Additionally, the analysis simulation produced significant rotation on various scales throughout the lifecycle of the MCS (Fig. 5.11), including the development of supercells ahead of the convective line that eventually merge with the main body of convection(Fig. 5.11h-j). The presence of such features allow for further investigation of the rotational effects on this event.

Differences between the analysis simulation, observations, and, even, the HRRRx simulation that the analysis simulation was based on, do exist. The initial representation of the scattered convection at the start of the analysis simulation (Fig. 5.11a) was quite representative of observations (not shown). The convection in the simulation begins to congeal about the same time as seen in observations (between 0100 and 0200 UTC). However, the convection in the analysis simulation becomes more progressive and produces a larger north-south line of convection, compared to the observations, after the convection organizes into the convective line near 0430 UTC (cf. Fig. 5.5a and Fig. 5.11e). The increase in speed is seen by ∼0830 UTC, as the main portion of the convective line in the analysis simulation is through downtown Houston (Fig. 5.11i), but not in the observations (Fig. 5.5b). This trend continues throughout the simulation. Lastly, the back-building that is seen in observations along the stationary outflow boundary edge towards San Antonio/Austin (Fig. 5.5b-c) is significantly too far south in the analysis simulation (Fig. 5.11i-l).

The resulting differences in convective structure and speed between the observations and the analysis simulation, yield a precipitation swath that is more concentrated on the west side of Harris County in the analysis simulation compared to observations (Fig. 5.1a,c). There is also a lack of representation in the rainfall accumulations of the linear westward extension of convection towards San Antonio/Austin that was seen in observations (Fig. 5.1a,c) at the later times (Fig. 5.5c). These differences, combined with the increase in storm translation speed to the east in the analysis simulation, compared to both the observations and the HRRRx, leads to the bulk of heaviest rainfall amounts being seen south and east of where they were observed (Fig. 5.1a,c). While these differences are important, the presence of meso-γ-scale rotation, the ability for the analysis simulation to resolve the magnitude of the observed rainfall, and the two aspects of the event that are being investigated, allow the simulation to be used for analysis described above.

Soundings taken from the inflow region of the MCS in southern Fort Bend County, Texas show kinematic and thermodynamic values (Fig. 5.12) similar to those discussed earlier based upon the RAP analysis (Figs. 5.3 and 5.4). MUCAPE vales near 1500 J kg^{-1} with a vertical structure similar to a flash flood profile (e.g., Davis 2001; Schumacher and Johnson 2009; Schroeder et al. 2016) were maintained throughout the simulation (Fig. 5.12a-b). Further, the soundings show the presence of intense 0–1 km shear that intensified through the event to near ∼20 m s^{-1} (Fig. 5.12b). This was associated with 25+ m s^{-1} southeasterlies in the 500 m to 1 km layer (Fig. 5.12a-b), and weak winds aloft associated with upper-level Omega blocking pattern. This created hodographs that were quite favorable for the development of rotating storms. The modeled 0–6 km shear does increase with time and is larger than what is originally represented in the SPC mesoscale analysis, which could be explained by the influence of thunderstorm environmental modification on this metric. The surface parcel, despite the significant moisture in the low-levels, is still slightly stable. The most unstable parcel is uninhibited and has an origin near 950 hPa (Fig. 5.12a-b). Additionally, PWAT in the model, as in the RAP analysis (Fig. 5.4a), lies between 45 and 50 mm (∼2 inches) throughout the analysis simulation.

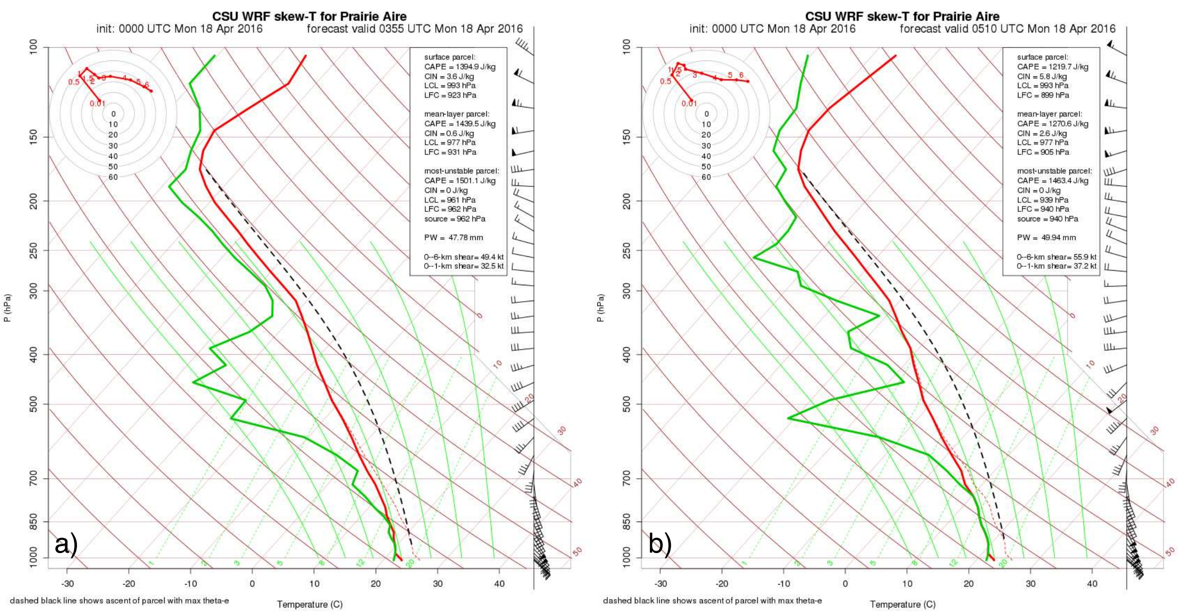

FIG. 5.12. Model soundings from the analysis domain valid at (a) 3-hr 55-minute and (b) 5-hr 10-min into the 0000 UTC 18 April 2016 initialization from Prairie Aire Airfield (K4TAO) in southern Fort Bend County, Texas. Location denoted by blue x enclosed by a circle in Figs. 5.15 and 5.16.

Given the ability for rotating features to create extreme short-term rain rates in the radar analysis presented in the previous section, hourly precipitation accumulations and maximum updraft helicity (UH) were examined for a few select periods of the simulation. The first, between 0300 and 0600 UTC (approximately Fig. 5.11d-g), was associated with the development of the main convective line and the formation/maintenance of several rotating features along the leading edge, similar to the two observed intense period of rainfall discussed in the previous section. The second, between 0700 and 1000 UTC (approximately Fig. 5.11h-k), was associated with the development ahead of and merger of supercells with the main convective line. Intense hourly accumulations were seen during both of these periods, with widespread regions of over 50 mm rainfall produced in the model (Fig. 5.13). Further, more localized, but still on the county spatial scale, regions of hourly accumulations between 100 and ~150 mm (4 to ~6 inches) were also seen in the model (Fig. 5.13). In the later period, the hourly maximum accumulations were over 200 mm (~8 inches; Fig. 5.13e-f). The maximum hourly accumulation observed by the HCFWS in the event was 120 mm (4.7 inches), which would imply that the upper threshold of the model simulation hourly accumulations might be unrealistic for this case. However, the analysis simulation rainfall values are still useful to compare between regions in the model.

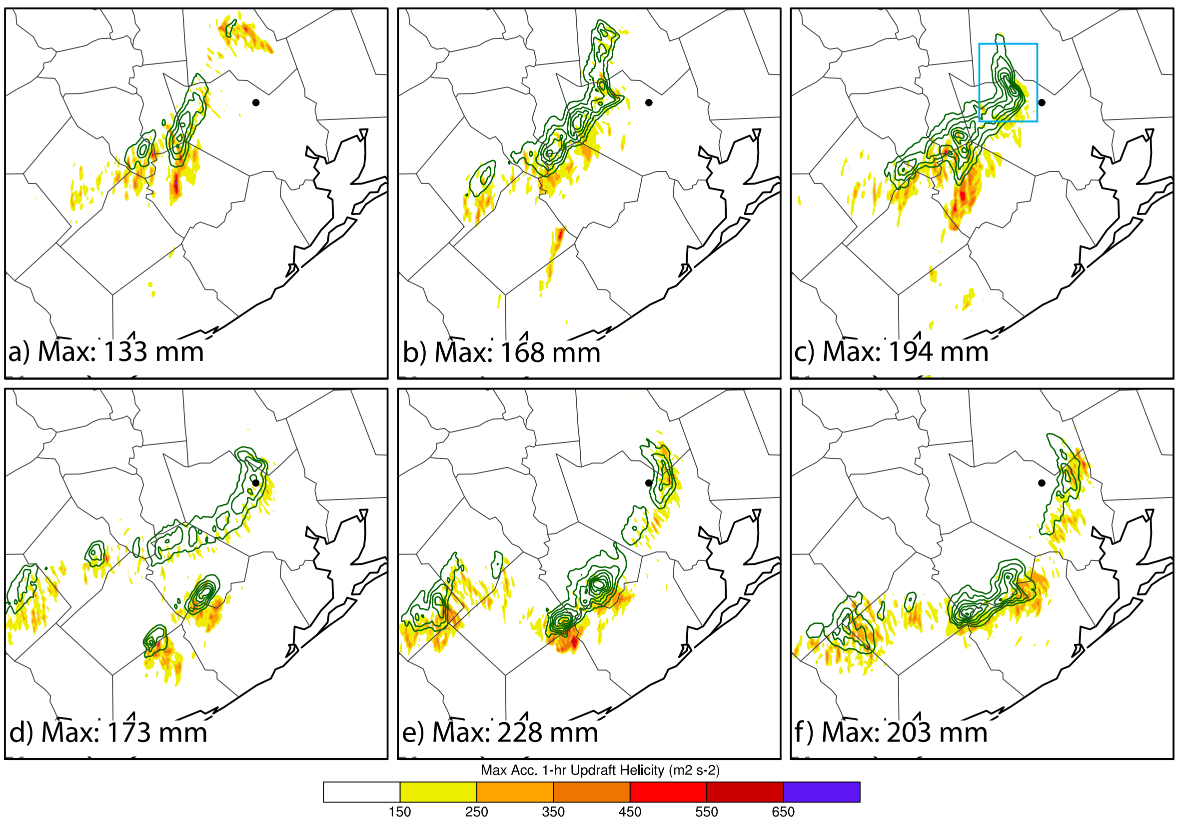

FIG. 5.13. 1-hr maximum updraft helicity swaths (fill, m^2 s^{-2}) and 1-hr precipitation accumulations (green contours; every 25 mm between 50 and 200 mm) valid (a) 4-hr, (b) 5-hr, (c) 6-hr, (d) 8-hr, (e) 9-hr, and (f) 10-hr into the 0000 UTC 18 April 2016 initialization for the analysis domain. Black dot denotes the location of George H.W. Bush Intercontinental Airport (KIAH). Maximum 1-hr rainfall accumulations are marked on each panel.

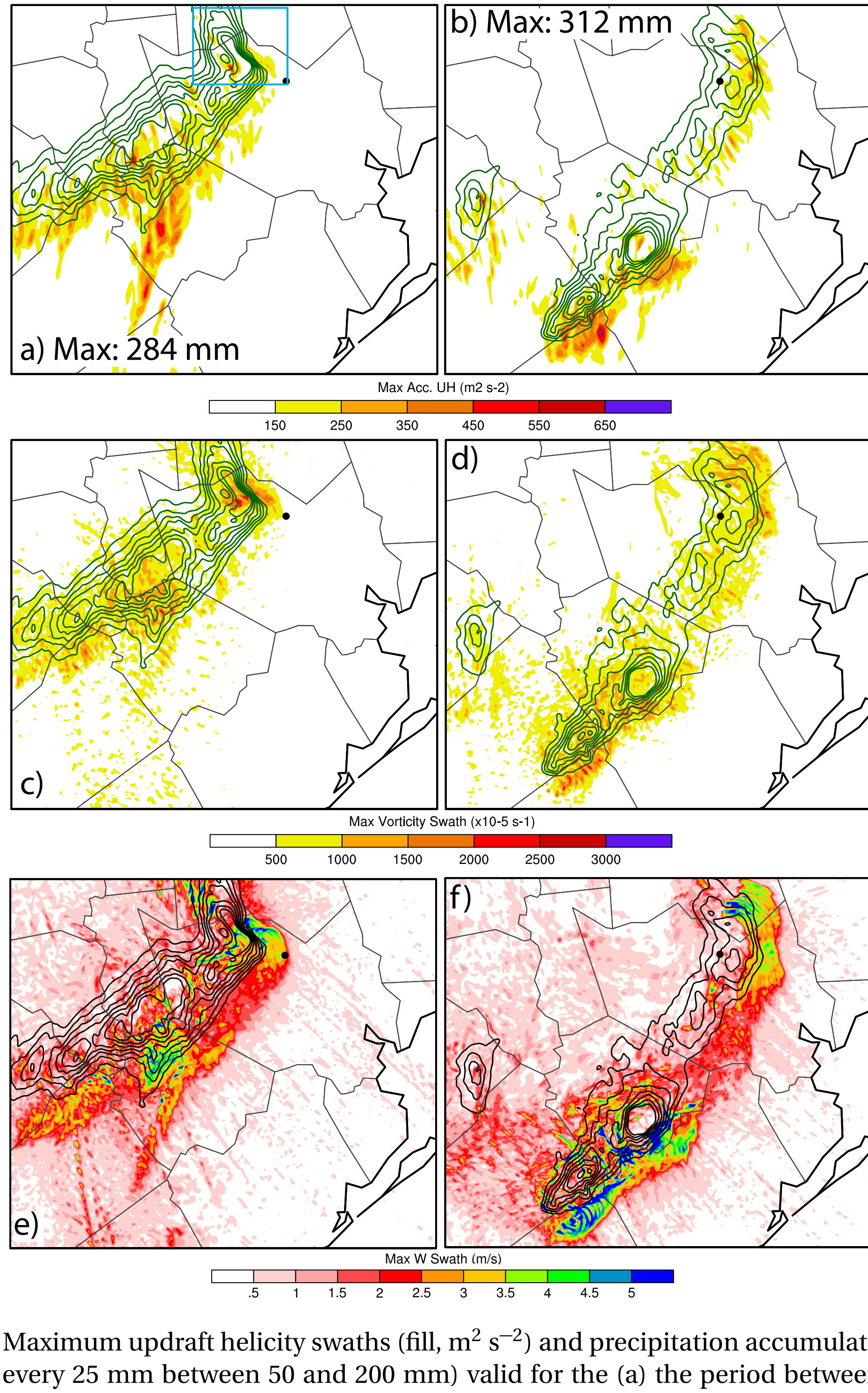

FIG. 5.14. Maximum updraft helicity swaths (fill, m^2 s^{-2}) and precipitation accumulations (green contours; every 25 mm between 50 and 200 mm) valid for the (a) the period between 0430 and 0620 UTC and (b) the 90-min between 0730 and 0900 UTC of the 0000 UTC 18 April 2016 initialization over the analysis domain. Maximum rainfall accumulations over each period are marked in (a) and (b). (c) and (d) same as in (a) and (b), respectively, except fill now represents swaths of maximum vorticity (x10^{-5} s^{-1}) at 1.5 km above ground level. (e) and (f), same as in (a) and (b), respectively, except fill now represents swaths of maximum 500 m AGL vertical velocity (m s^{-1}) and precipitation contours are now in black. Black dot denotes the location of George H.W. Bush Intercontinental Airport (KIAH). Note spatial extend is zoomed in, compared to Fig. 5.13.

The analysis simulation, as with the observed radar data, shows a spatial correlation between the highest rainfall accumulations and the regions of most intense UH (Fig. 5.13). The most intense accumulations are located north of the most intense rotating updrafts, which makes sense given the environmental kinematic profile for this simulation (Fig. 5.12). Additionally, this spatial correlation is seen both with rotation embedded in the convective line (Fig. 5.13a-c,f) and with isolated rotation features, in this case supercells, that develop out ahead of the main convection (Fig. 5.13d-e). This spatial correlation between maximum UH and the most intense hourly precipitation accumulations is seen during both periods, except at the northern part of the convection between 0400 and 0600 UTC, where the hourly maximum of hourly accumulation of 194 mm was recorded (Region enclosed by blue box in Fig. 5.13c). The lack of maximum updraft helicity in this region, compared to the other regions of large hourly rainfall accumulation, implies that either the updrafts are not rotating in the mid-level part of the storm (since this metric is calculated over the 2-5 km AGL layer in the model output) or the updrafts are not very strong. The latter of which seems unlikely, given the associated rainfall accumulation.

Examining these two periods of intense rainfall as events, as opposed over pre-defined hours, continues to show a pattern maximum UH being spatially correlated just upstream of the most intense rainfall accumulations (fig. 5.14a-b). The exception still remains in the region at the northern extent of the convection line in the first period (Region enclosed by blue box in Fig. 5.14a). In the low-levels, a similar spatial correlation is seen between intense 1.5 km AGL vorticity and the regions of most-intense rainfall (Fig. 5.14c-d) for both events. Further, the maximum rainfall accumulation in the first period that previously was not correlated with large maximum UH (i.e., blue box in Fig. 5.14a) is spatially correlated with very intense values of low-level vorticity (i.e., $\sim$0.02 s^{-1}, Fig. 5.14c). This shows that the updrafts that produced the most intense rainfall accumulations are intensely rotating at the low-levels, while only some are also rotating at the mid-levels. Additionally, the regions of maximum 1.5 km vorticity correspond to the regions of 4+ m s^{-1} updrafts at 500 m AGL over the same period (Fig. 5.14e-f), which is also spatially correlated to regions of most intense rainfall accumulation. This implies that the strong updrafts at 500 m are associated with strong rotation at a higher altitude and, presumably, influenced by the dynamical accelerations associated with that rotation. These bulk results agree with the idealized simulations in Nielsen and Schumacher (2018), which found that the enhancement of low-level (i.e., 500 m) updrafts by the dynamical accelerations associated with rotation were the main mechanisms by which rain rates could be enhanced compared to non-rotating convection.

On the individual storm scale during both of these periods, a similar relationship between low-level rotation and intense rain rates is seen in the analysis simulation. At the beginning of the simulation (i.e., 40-min from initialization), when the convection was more isolated in nature, the most intense convection is associated with rotating features (Fig. 5.15a). It is also clearly seen that the convection producing the most intense 5-minute rainfall rates at the time are associated with these rotation portions of the system (Fig. 5.15e). This pattern continues as the system begins to organize into the linear convective mode that is seen through the end of the simulation (Fig. 5.15).

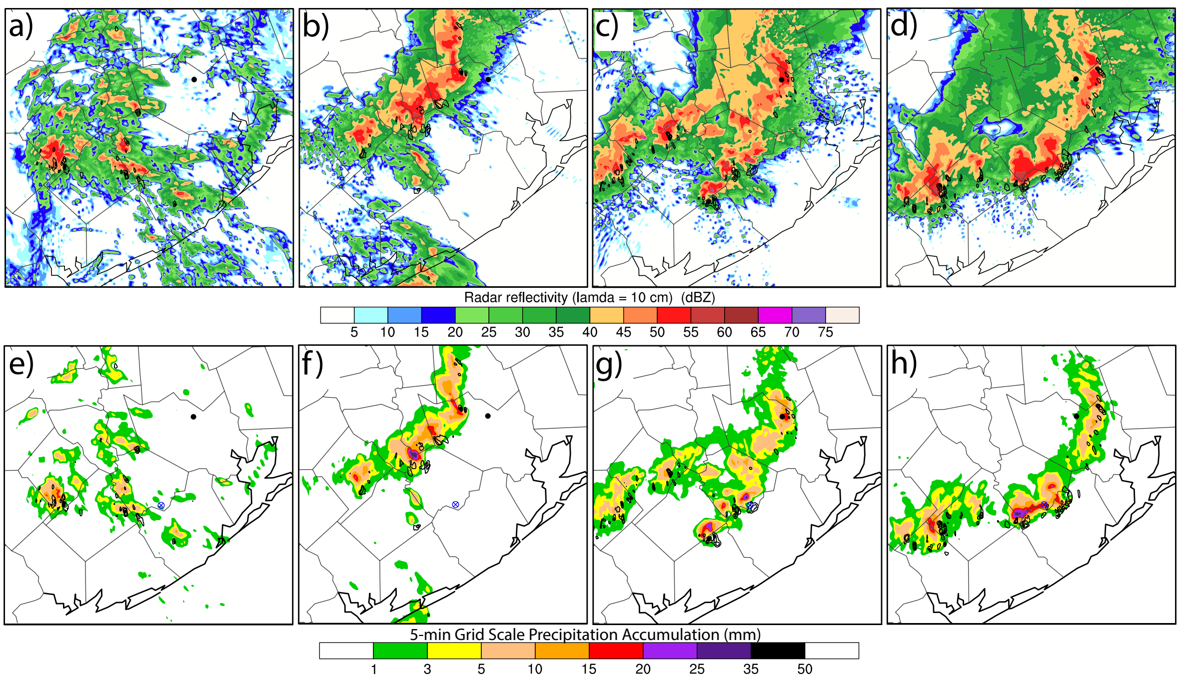

FIG. 5.15. (a-d) Simulated 1 km radar reflectivity (fill; dBz) and maximum updraft helicity (black contours; every 100 m^2 s^{-2} starting at 150 m^2 s^{-2}). (e-h) 5-minute accumulated precipitation (fill, mm) and maximum updraft helicity (black contours; every 100 m^2 s^{-2} starting at 150 m^2 s^{-2}). Panels show a zoomed in subset of the analysis domain valid (a,e) 40-min, (b,f) 4-hr 40-min, (c,g) 7-hr 55-minute, and (d,h) 9-hr 30-min into the simulation initialized at 0000 UTC 18 April 2016. Black dot in all panel denotes the location of George H.W. Bush Intercontinental Airport (KIAH). Blue x enclosed by circle in bottom panels denotes location of Prairie Aire Airfield (K4TAO).

During the first period discussed above (i.e., between 0300 to 0600 UTC), a clear spatial correlation is again seen at individual times between the embedded rotation features and the most intense short-term rainfall rates (Fig. 5.15b,f). The convection produces 5-minute rainfall accumulations in the 5-10 mm (~0.2-0.4 inch) range throughout the convective line, but these values increase to the 15-25 mm (~0.6-1.0 inch) range in the rotating regions (Fig. 5.15f). These modeled values are similar to those observed in rotating and non-rotating regions by the HCFWS gauges discussed in the previous section, respectively. The same spatial relationship between rotation and intense 5-minute rainfall accumulations are seen in the second period described above (i.e., between 0700 and 1000 UTC) associated with supercellular convection (Fig. 5.15c,d,g,h). Five-minute rainfall accumulations in the 15-25 mm (∼0.6-1.0 inch) range are modeled for the supercells, both when isolated ahead of and, embedded, in the main convective line (Fig. 5.15c,d,g,h).

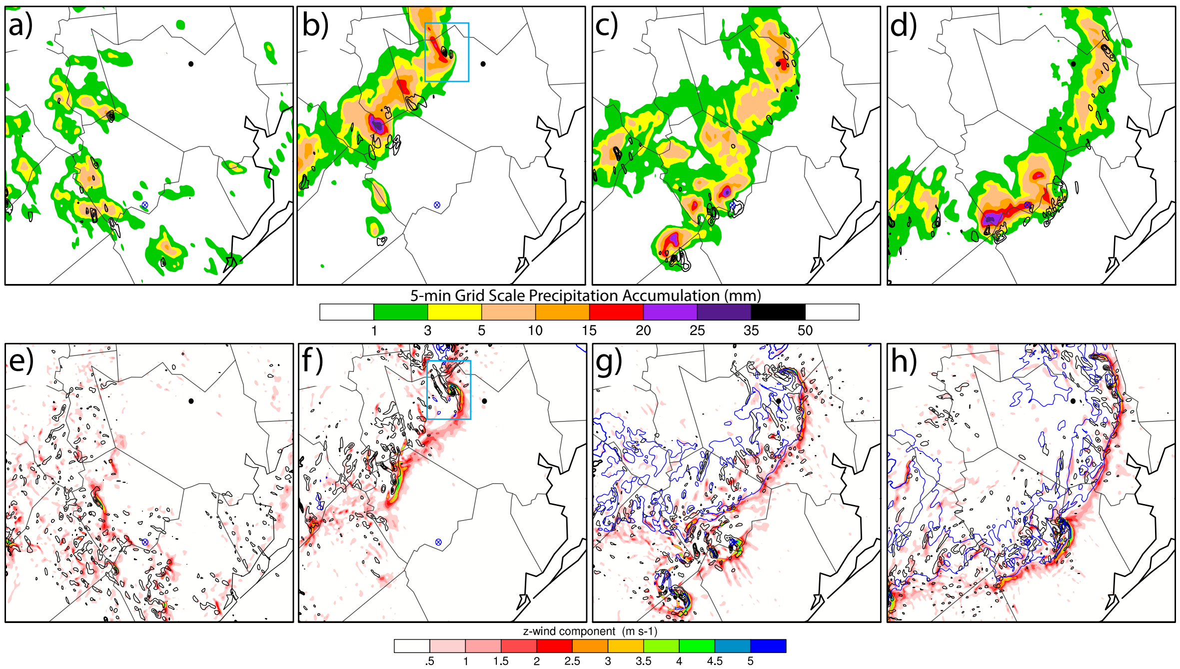

FIG. 5.16. (a-b) 5-minute accumulated precipitation (fill, mm) and maximum updraft helicity (black contours; every 100 m^2 s^{-2} starting at 150 m^2 s^{-2}). (e-h) 500 m vertical velocity (fill, m s^{-1}), 1.5 km vorticity (black contours; every 0.005 s^{-1} starting at 0.003 s^{-1}), and model perturbation potential temperature (blue contours at -5 and -10 K). Panels are valid at (a,e) 40-min, (b,f) 4-hr 40-min, (c,g) 7-hr 55-minute, and (d,h) 9-hr 30-min into the simulation initialized at 0000 UTC 18 April 2016, same as in Fig. 5.15. Note, however, spatial extent is further zoomed in than Fig. 5.15. Black dot in all panel denotes the location of George H.W. Bush Intercontinental Airport (KIAH). Blue x enclosed by circle in all panels denotes location of Prairie Aire Airfield (K4TAO).

Assessing the 500 m vertical velocity and 1500 m vertical vorticity at the same individual times as presented in Fig. 5.15, shows the same relationship between low-level updraft strength, vorticity, and 5-minute precipitation accumulation as seen from a bulk sense (Fig. 5.16). The most intense rainfall rates are seen associated with convective cells that have the most intense vertical motion (i.e., >2.5 m s^{-1}) at 500 m (cf. fill colors in Fig. 5.16a-d and fill colors in Fig. 5.16e-h).

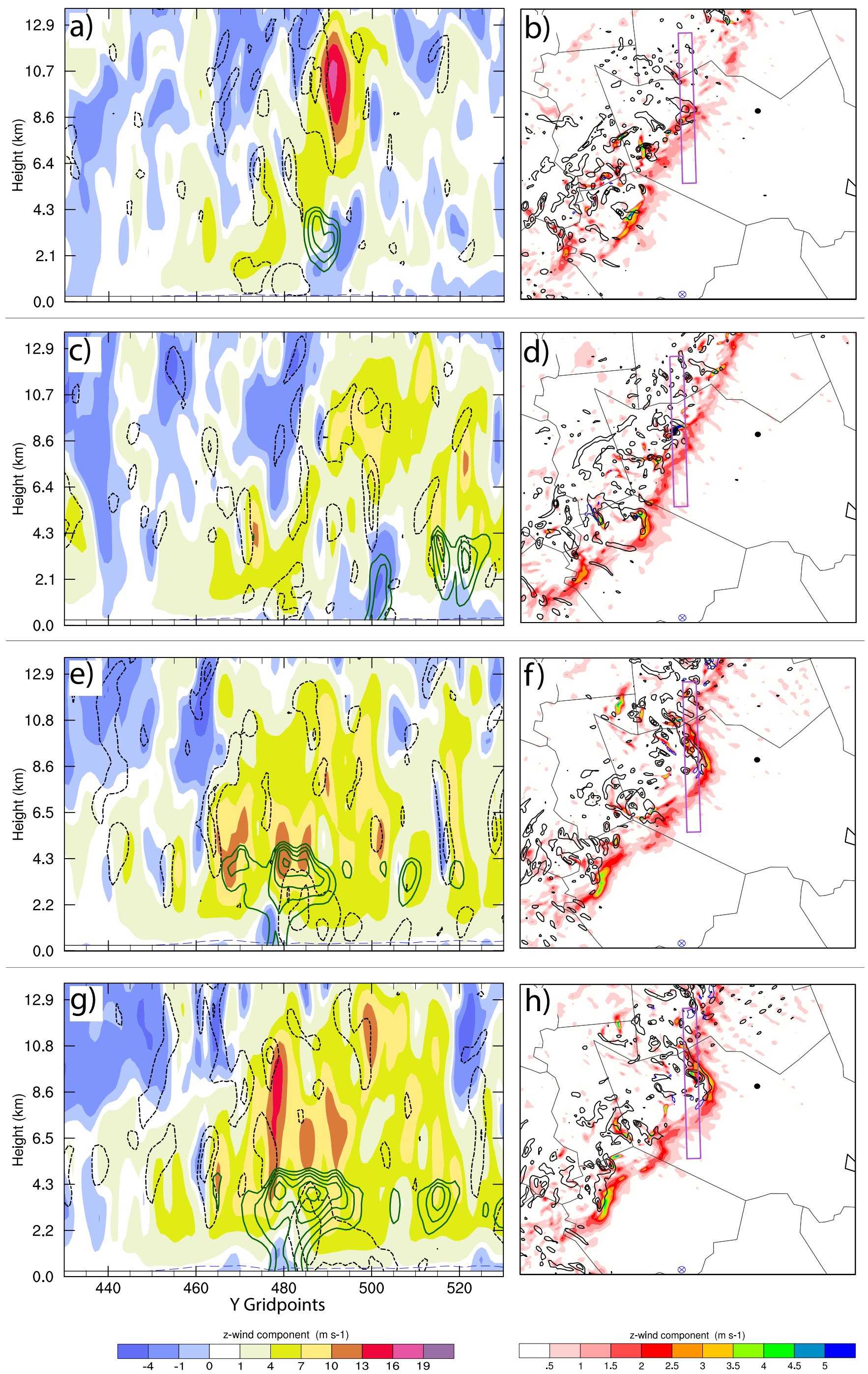

FIG. 5.17. (a,c,e,g) mean north-south vertical cross sections of vertical velocity (fill, m s^{-1}), vertical vorticity (dashed black contours, every 0.005 s^{-1} starting at 0.003 s^{-1}), model perturbation potential temperature (dashed blue contours at -5 and -10 K), and rain water mixing ratio (green contours, every 0.001 kg kg^{-1} starting at 0.004 kg kg^{-1}) over the purple box shown in (b,d,f,h) valid at (a,b) 0335 UTC, (c,d) 0350 UTC, (e,f) 0425 UTC, and (g,h) 0430 UTC 18 April 2016 from the analysis simulation. (b,d,f,h) same as in Fig. 5.16e-h, except now valid at the aforementioned times. Black dot in all panel denotes the location of George H.W. Bush Intercontinental Airport (KIAH). Blue x enclosed by circle in all panels denotes location of Prairie Aire Airfield (K4TAO).

The regions that sustain >2.5 m s^{-1} updrafts at 500 m are almost exclusively associated with rotation at 1.5 km AGL (cf. fill and black contours in Fig. 5.16e-h), which can be seen throughout the simulation (Fig. 5.16e-h). Vertical motion at 500 m does exist outside of the regions of rotation along the cold pool boundary, but these values are weaker and associated with weaker 5-minute rainfall totals (see blue line in Fig. 5.16f-h).

By following a specific region of low-level rotation in the vertical, the life cycle of the rotation and its effect on the system updraft structure and rainfall production can be seen. Initially as the low-level rotation begins to develop, it is quite confined to the lowest 2 km and little change in the overall structure of the storm is seen (Fig. 5.17a). There is possibly some slight rotationally induced enhancement and lowering of a shallow updraft structure that is originally initiated along the developing cold pool boundary (see dashed blue line Fig. 5.17a and linear structure in Fig. 5.17b). Additionally, the rain water production at this time is associated with the elevated mid-level updraft (Fig. 5.17a). As the low-level rotation intensifies, a more clear lowering and enhancement of the low-level updrafts, compared to those not associated with rotation, is seen (Fig. 5.17c). A 4+ m s^{-1} mean updraft over the cross section area is seen below 1 km AGL in the center of the rotation (Fig. 5.17c), with little to no reduction in this value above the level of maximum rotation in the updraft core.

The vertical depth and strength of the low-level rotation increases as the vortex continues to move east (Fig. 5.17e,f). A broad lowering of the updraft base is still seen, corresponding to the region of low-level rotation, under a further developed mid-level updraft (Fig. 5.17e). Additionally, a clearly defined region of rain water has now formed below the freezing level (green contours in Fig. 5.17e). Higher values of rain water mixing ratio are seen at lower altitudes in the regions associated with low-level rotation, compared to regions of similar mid-level updraft strength without low-level rotation (Fig. 5.17e). This implies more rain water is being created in the low-level rotation regions compared to non-rotating low-level regions. Furthermore, the updraft enhancement and lowering is still maintained in the regions of low-level rotation, despite the increased hydrometeor loading associated with these increased rain water mixing ratio values (Fig. 5.17e,g), which likely further speaks to the effects of the dynamical forcing associated with the rotation. These trends continue as the mean mid-level updraft continues to intensify, even though there is little change in the strength of the low-level rotation (Fig. 5.17g,h).

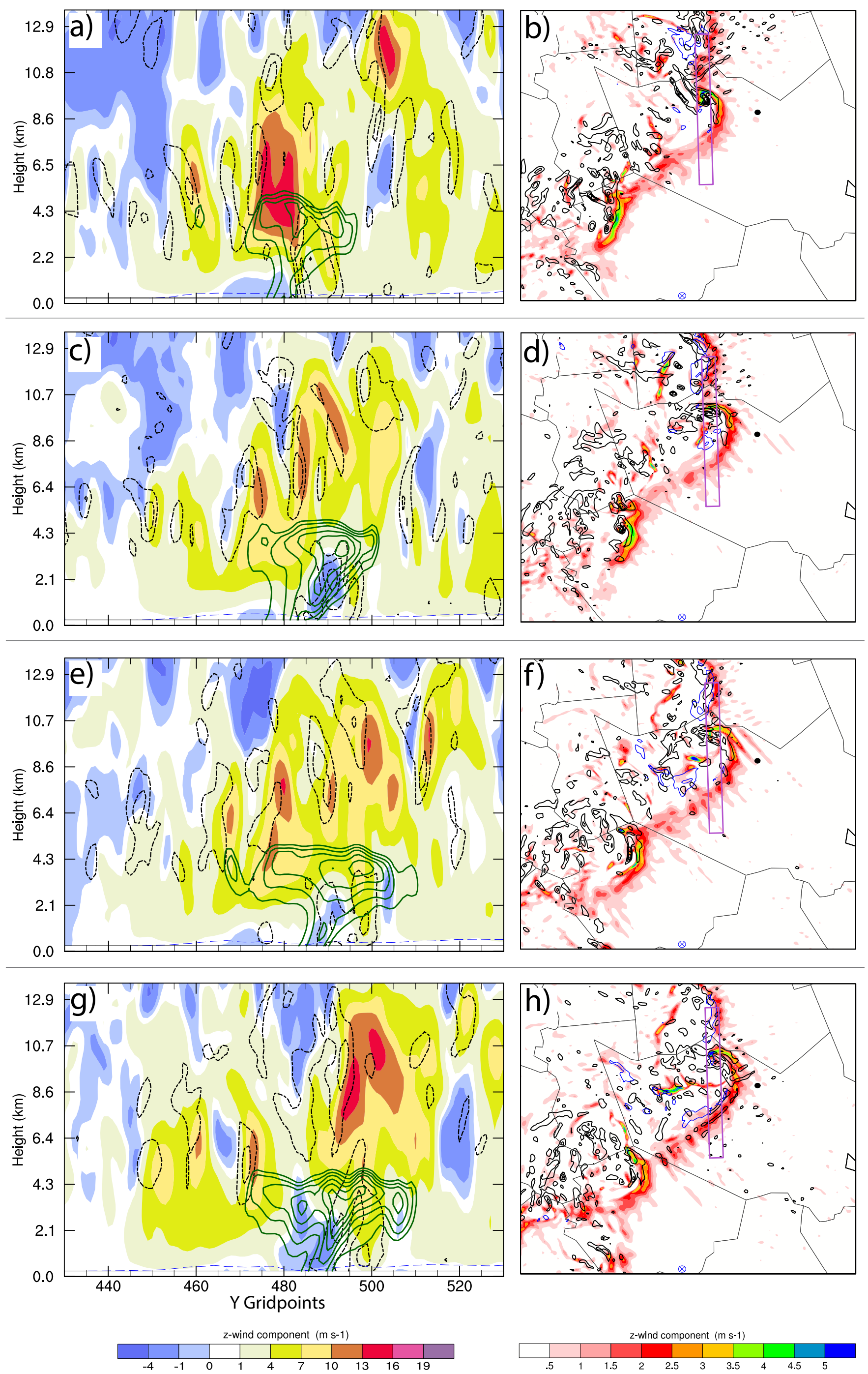

FIG. 5.18. As in Fig. 5.17 except valid at (a,b) 0440 UTC, (c,d) 0455 UTC, (e,f) 0505 UTC, and (g,h) 0515 UTC 18 April 2016 from the analysis simulation.

As the low-level rotation for this particular region of the storm reaches its local temporal maximum, a marked lowering of the updraft base combine with a large increase in low-level updraft strength is seen within the low-level rotation (Fig. 5.18a,b). This also corresponds to the period of most intense mid-level updraft strength and vertical alignment between the mid-level updraft and low-level rotation (Fig. 5.18a), which likely aided in the intensification of the low-level rotation (i.e., by stretching). Rain water mixing ratios are, again, enhanced at lower altitudes in the region of low-level rotation, which corresponds to the most intense low-level updrafts (Fig. 5.18a). This is even true at the edges of the low-level rotation that are vertically aligned with the fringes of the mid-level updraft (north side of green contours in Fig. 5.18a). The low-level updrafts in the rotation region are still positive, despite the hydrometeor loading, and are just to the north of the main precipitation shaft (Fig. 5.18a).

A short time later, the region of low-level rotation is now collocated with the main precipitation shaft and downward motion, likely associated with a significant increase in hydrometeor loading (Fig. 5.18c,d). This period shows a substantial increase in total rain water mixing ratio, compared to 15 minutes earlier (Fig. 5.18a,b), when the low-level rotation, low-level updraft, and mid-level updraft were maximized. Given that a lag between the surface rainfall magnitude and associated precipitation formation mechanisms is expected, this is not surprising. While low-level rotation is still present at this time, it has weakened and does not possess the same level or organization as seen previously (cf. Fig. 5.18a,c). The mid-level updraft has also weakened and become less organized (Fig. 5.18c). At this time the rain water mixing ratios that are now reaching the surface undercut, to a degree, the storm inflow and disrupt the low-level rotation structure (Fig. 5.18c), which signals a restart of the precipitation life cycle of this particular cell.

As the rainfall at the surface decreases and narrow in areal coverage, the low-level rotation is able to reform (Fig. 5.18e,f). Similarly to the the previous time periods, a lowering and enhancement of the low-level updraft is seen in the low-level rotation (Fig. 5.18e). This in turn leads to increased rain water mixing ratios at lower heights, compared to regions without the low-level updraft enhancement/rotation (Fig. 5.18e). As the mid and low-level updrafts become vertically aligned, the low-level rotation shows signs of enhancement and extends farther into the mid-levels (Fig. 5.18g), similar to what was seen earlier (Fig. 5.18a). The increase in updraft strength, lowering of the updraft base, and significant increase in rain water mixing ratios are again seen in the region of low-level rotation (Fig. 5.18g), despite the largest rain water mixing ratio values seen to this point. Further, the enhancement in rain water mixing ratio is increased from (Fig. 5.18e) to (Fig. 5.18g), as the low-level rotation strengthens. The reformation of the low-level rotation and the continuation of the same trends seen previously, imply that the life cycle and characteristics of these rotating, heavily precipitating regions are similar across the system and repeated as the storm system moves south and east through the simulation.

5.6 Discussion and Conclusions

The results of the observational and model analyses both show that extreme rain rates during the Houston Tax Day flood were associated with regions of meso-γ-scale rotation in an intensely sheared low-level environment. The observational analysis, based upon radar and the HCFWS rain gauge network, showed that 15-25 mm (∼.60-1.0 inch) 5-minute observed rain rates were sustained over the course of the event just upstream of locally intense regions of low-level rotation (Fig. 5.6). Intense 5-minute rainfall accumulations (5-10 mm (∼.20-.40 inch)) rates were seen throughout the the non-rotating convective region, which is not surprising given how conducive the environment was to convection and rainfall (Fig. 5.12). The analysis simulation also produced similar 5-minute rainfall accumulations as the observations in most intensely rotating features, both in discrete and embedded convective cells (Fig. 5.14), and modeled non-rotating features. Furthermore, these observed and modeled 5-minute rain rates agree with other short term rain rates observed in supercells (e.g., Smith et al. 2001). The maximum hourly rain rate seen in the HCWFS for the event of ∼120 mm (4.7 inch) was quite a bit lower than those seen in the model (i.e., >200 mm, Fig. 5.13). However, these differences could be a result of local storm motion differences, as noted in the previous section, and rain gauge sampling deficiencies. Overall, these results provide further evidence, similar to those presented in Chapter 3, that storms with meso-γ-scale can produce and maintain extreme rainfall rates, despite what is believed to be low-precipitation efficiency (e.g., Marwitz 1972; Foote and Fankhauser 1973; Browning 1977).

Nielsen and Schumacher (2018) showed that the presence of rotation associated with intense 0–1 km shear can serve to enhance rain rates, and overcome a presumed lack of precipitation efficiency, by providing a dynamical source of positive vertical momentum to the low-level updrafts that is not present in non-rotating storms (see Section 2.5.3 of Markowski and Richardson 2010). The rain rates are then enhanced by the increased updraft speed and ability to ingest thermodynamically stable parcels that still contain moisture and CAPE. Despite the inability in the analysis simulation to numerically solve for the dynamical accelerations as was done in Nielsen and Schumacher (2018), evidence of the dynamics behind the rotational precipitation enhancement mechanism proposed in Nielsen and Schumacher (2018) are seen. In a bulk sense, the simulation showed a spatial correlation between the most intense rainfall accumulations/rates and the vertical vorticity at 1.5 km (Fig. 5.13). Furthermore, the regions of most intense rainfall also corresponded to regions of most intense 500 m vertical velocity, which are in turn directly associated with the maximums in 1.5 km vorticity (Fig. 5.13). This yields the same bulk results as seen in Nielsen and Schumacher (2018, their Fig. 15) where the maximum rotation was seen near 1.5 km and the maximum acceleration due to the rotation was seen near 500 m. This is additionally shown in the mean vertical cross sections following a rotating feature in the analysis simulation (Fig. 5.17-5.18), where a lowering of the updraft base and a corresponding enhancement of low-level (i.e., 500 m and below) vertical velocities is seen in the regions of low-level rotation. This lowering and updraft enhancement in turn allows the updrafts to decrease the level of storm inflow, thereby, increasing the water vapor mixing ratio of the rising air (e.g., Fig. 5.12). These effects also appear to take place in this simulation despite the relatively shallow nature of the rotation at some points (Fig. 5.17-5.18). While downward acceleration is expected above the level of maximum rotation, it appears, at least in the analysis simulation, that it does not substantially affect the lowering of the updraft base. This is likely because the parcels, even with relatively little vertical displacement, are able to reach their LFCs (e.g., Fig. 5.12). Overall, these common characteristics between the analysis simulation and Nielsen and Schumacher (2018) imply that the same mechanisms for rain rate enhancement seen in the idealized simulations of Nielsen and Schumacher (2018) are at work in the horizontally heterogeneous simulation of the Houston Tax Day flood.

The analysis simulation, in addition to the dynamical signals for rotational enhancement of rain rates just discussed, also provided insights into how these dynamical changes associated with rotation might affect the rainfall production mechanisms and microphysical characteristics of the convection. As pointed out in section 5.5, an enhancement is seen in the rain water mixing ratios in the lower levels of the convection in rotating regions over non-rotating regions (Fig. 5.17-5.18). This implies that the ability for the rotation to lower the updraft base and increase the low-level vertical motion leads to quicker formation of rain water in the vertical well below the freezing level. Furthermore, the values increase rapidly as the low-level rotation intensifies (Fig. 5.17-5.18). This also explains why the local enhancements by rotation are seen in the radar K_{dp} because it is proportional to the amount of liquid water, which the model shows is being enhanced in the low-levels by the rotation. The increase in rain water mixing ratio in the lower parts of the storm in rotating regions could also serve to increase the propensity for warm rain precipitation formation mechanisms to dominate, which yield higher precipitation efficiencies compared to ice phased dominated processes (e.g., Tripoli 1982; Levy and Cotton 1984; Lamb 2001; Gochis et al. 2015). The enhancement of the low-level updrafts in the regions of low-level rotation is maintained even with an increase in hydrometeor loading associated with the increase in rain water mixing ratios in these regions (Fig. 5.17-5.18). The ability to overcome this fairly significant increase in resistance to vertical motion was not expected *a priori* by the author. However, it again points to the likely importance of the dynamical lift associated with the rotation in maintaining the low-level updrafts in this simulation and other such events.

On a similar note, given the maintenance of extreme short-term rain rates and resulting longer timescale rainfall accumulations in rotating, extreme precipitation events such as this, the hydrostatic pressure decrease associated with the reduction of total-column mass due to precipitation might be an important physical process. The impact of this mechanism is discussed in Lackmann and Yablonsky (2004) in regards to tropical cyclones. The study is motivated by the fact that pressure changes due to sources and sinks of mass from precipitation, evaporation, sublimation, and deposition are ignored in general because the effects are negligible compared to other processes. However, this assumption may not be correct in heavily precipitating systems. For example, Lackmann and Yablonsky (2004) discuss how the hydrostatic pressure equivalent of 25 mm of rain is approximately 2.5 hPa. While Lackmann and Yablonsky (2004) focus mainly on longer duration accumulations, such as 250 mm per day, the Tax Day flood produced 5-minute rain rates of 25 mm (Fig. 5.6) and much greater sub-daily accumulations. The results of the experiments of Lackmann and Yablonsky (2004), in potential vorticity (PV) space, showed that the mass sink due to precipitation was responsible for a large positive PV tendency near the melting level for a modeled tropical cyclone. Furthermore, mass lost due to precipitation was found to be non-negligible in regards to the storm average mass budget and enhanced convergence. Given that the heaviest precipitating storms in potential vorticity space are associated with convective-scale PV monopoles (e.g., rotating; Chagnon and Gray 2009; Weijenborg et al. 2015, 2017) and the Tax Day flood produced 5-minute rainfall observations of 25 mm, it is not unreasonable to expect that such a mass sink mechanism would be important, or at the very least, non-negligible. Additionally, the connection of extreme precipitation to PV space, and, thus, rotation, provides an additional pathway for positive feedback mechanisms to occur between extreme precipitation and rotation, as discussed in Nielsen and Schumacher (2018). Additional work is warranted to investigate these potential influences further.

The increase in warm rain mixing ratio in regions of low-level rotation is important to note because it implies that the presence of low-level rotation can increase (or at the very least affect), in certain scenarios, all three terms in Equation 3.2 that determine the rain rate of a particular storm. The dynamically induced positive (or negative) accelerations associated with the rotation can serve to directly increase (or decrease) w. The lowering of the updraft base and ability to lift thermodynamically stable parcels that contain moisture and CAPE can serve to directly increase q. Lastly, as in this case, these combine effects can serve to increase rain water formation in the lower parts of the storm and increase the presence/importance of warm rain precipitation formation mechanisms, which is associated with a higher precipitation efficiency, E. The exact influence on the three-term parameter space, of course, depends on many factors, especially the environmental thermodynamic profile and the characteristics of the ingested parcels (i.e., environmental in nature or storm modified). However, situations, such as this case and the ones presented in Nielsen and Schumacher (2018), with significant boundary layer and column moisture, slight stability at low-levels, very large values of 0–1 km shear, moderate CAPE values distributed through the entire troposphere, and deep warm cloud layers might be represent situations where the rotational enhancement effects are greatest.

In conclusion, this case study shows how meso-γ-scale rotation associated with intense 0–1 km shear can lead to the development and maintenance of extreme short-term rainfall rates in a horizontal heterogeneous modeling framework and in an observational analysis of the event. As in the idealized simulations of Nielsen and Schumacher (2018), the rotation was found to lead to increases in low-level updraft strength, compared to non-rotating regions, and lift parcels that were thermodynamically inhibited that still contained moisture and CAPE. Additionally, the case study presented here showed a corresponding increase, in regions of low-level rotation, of rain water mixing ratio as the rotation increased, which can lead to an increase in the precipitation efficiency by increasing the presence of warm rain formation. The results of this study offer further evidence of the ability for, even shallow, meso-γ-scale rotation to dynamically enhance the development and maintenance of extreme rainfall rates in convective scenarios with large values of 0–1 km shear.

CHAPTER 6

Conclusions

Overall this manuscript presents a holistic look at the frequency and influence of concurrent and collocated meso-γ-scale rotation with extreme rainfall producing convection. A specific subset of such events where tornadoes were concurrent and collocated with flash flooding, known as TORFF events, were also examined, since the recommended life-saving actions for each individual threat type are contradictory. Rainfall and flash flooding observations were used to examine the commonality of rotation in extreme rainfall events, compared to extreme rainfall events without rotation (Chapter 4), and a climatology of verified TORFF events in the United States was developed (Chapter 2). Further, idealized (Chapter 3) and real-time (Chapter 5) model simulations were used to investigate the influence that rotational dynamics have on the precipitation processes in such extreme rainfall events.

The TORFF climatology presented in Chapter 2 found, with the addition of a spatial buffer between the flash flood and tornado observations, that on average 25 to 75 "verified" TOFFF events occurred each year in the U.S. between 2003 and 2017, depending on the spatial buffer chosen. This presents a substantial increase in event frequency over the results of Nielsen et al. (2015). Little change was seen in the geographic distribution of the "verified" events compared to the results of Nielsen et al. (2015) with the majority occurring in the southeastern U.S. and Mississippi valley, which, not surprisingly, matches the spatial distribution of overlapping tornado and flash flood warnings. Additionally, ~30% of TORFF events had a component that involved nocturnal tornadoes, which elevates the warning communication challenges beyond that associated with the aforementioned contradictory recommended life-saving actions. Further, two TORFF events sampled as part of the VORTEX-SE field experiment illustrate the importance and potential sensitivity of 0–1 km shear in the development and evolution of the TORFF events. It was seen how complex interactions between the environmental moisture profile, 0–1 km shear, induced rotation, and the resulting rotationally induced dynamical accelerations can serve to enhance both the tornado and precipitation potential of a particular event. These convective scale interactions, which are dependent on convective scale storm specifics not easily (or at all) resolved by operational models, limit the ability for forecasters to accurately predict the event evolution with sufficient lead time. These results reiterate the need for further social science and physical science research to improve communication and forecasting practices in such common, multi-threat, and dangerous events.

The results of Chapter 2 and Nielsen et al. (2015) showed that the collocated of rotation and rainfall capable of producing a flash flood occurred across many storm modes and in varying environmental conditions. This motivated the investigation into any possible interactions between the baseline commonality in all cases: the rainfall production processes capable of producing a flash flood and the collocated meso-γ-scale rotation. In the idealized simulations, presented in Chapter 3, environments with more intense 0–1 km shear produced higher precipitation accumulations in the mean, point maximum, and domain coverage of the highest accumulations. Further, the strength and longevity of the low-level rotation increased with 0–1 km shear magnitude. The resulting nonlinear dynamical accelerations associated with the rotation were able to enhance the rain rates by enhancing low-level updrafts, over non-rotating convection, and, depending on the environmental thermodynamic profile, by tapping into sources of moisture and instability that are thermodynamically inhibited. These precipitation enhancements could also potentially be more pronounced in situations where thermodynamic buoyancy is limited and moisture is abundant. Further, the ability for rotation to form in environments with intense 0–1 km shear (e.g., Craven et al. 2004; Sherburn and Parker 2014), in both discrete and embedded convection, implies that the precipitation enhancement described here could occur in many different storm morphologies, including tropical cyclone rain bands. Additionally, the results show that 0–1 km shear might serve as a forecast predictor of a convective system's potential to produce both tornadoes and extreme rain rates. The enhancement of vertical momentum and, thus, precipitation by these mechanisms does not, in principle, preclude the formation of a tornado, since the same mechanisms (i.e., intense, dynamically induced updrafts near the surface) are favorable for tornadogenesis (e.g., Markowski and Richardson 2014). This simultaneous ability for mesoscale rotation to produce tornadoes and enhance precipitation processes also provides a dynamical mechanism that explains the frequency of TORFF events (Nielsen et al. 2015) in the United States without any clear dependence on storm motion (e.g., Bunkers and Doswell 2016; Nielsen et al. 2016a).

Given it was found in Chapter 3 that rotation is able to enhance precipitation through dynamic accelerations, Chapter 4 investigated the frequency that extreme short term rain rates, defined as hourly observations of >75 mm, were associated with meso-γ-scale rotation. Using a subjective radar analysis on events identified by rain gauge and Stage-IV rainfall accumulations that match the defined criteria, events were found to be collocated with rotation just under half the time in the United States. The spatial distribution of those extreme rainfall events with and without rotation were similar, with events occurring along the Atlantic and Gulf coasts and extending north into the Great Plans and lower Mississippi valley. An additional objective analysis on a subset (i.e., 29) of the events, showed that ~93% of the events were associated with meso-γ-scale rotation in the low-levels. Slight, but important, differences were seen in between the meteorological characteristics of each event subclass. Rotation events occurred more clearly in the warm sector and were associated with higher low-level shear, PWAT, 850 hPa warm air advection, and slightly weaker winds aloft; however, these results were dependent upon the individual events used in the composite. The results of Chapter 3 agree with previous studies (e.g., Smith et al. 2001; Duda and Gallus 2010; Hitchens and Brooks 2013; Weijenborg et al. 2017; Smith et al. 2018) that identify rotating storms as under-representative producers of extreme rainfall. Further, it provides observational support for the ability for rotationally induced dynamical accelerations to enhance rain rates, as shown in Chapter 3, and that such accelerations, at the very least, should not be ignored when it comes to precipitation processes.

Chapter 5 expanded on the horizontally homogeneous experiments in Chapter 3 by examining a real-time, horizontally heterogeneous, and high resolution simulation of the Houston, Texas Tax Day flood in April of 2016, which was classified as a TORFF event in Chapter 2 and occurred in an environment with intense 0–1 km shear. Additionally, an observational analysis was undertaken, using the Harris County Flood Warning System rain gauge network and local radar data, to determine rain rates associated with rotating and non-rotating features. The rain gauge data showed that 15-25 mm (~.60-1.0 inch) 5-min observed rain rates were sustained over the course of the event in convective regions with locally high K_{dp} values, which were spatially correlated with upstream regions of the most intense rotation. Furthermore, the overall K_{dp} values of the region increased as the strength of the broad rotation along the leading edge of the convective line increased, with locally high values of K_{dp} associated with the regions of most-intense upstream rotation. As seen in the observations, the analysis simulation of the event produced similar 5-minute rainfall accumulations associated with the most intensely rotating features. This was seen both in a bulk sense (i.e., throughout the simulation) and at individual times in varying convective modes. Similarly to the idealized results of Chapter 3, the analysis simulation of the event showed the most-intense rainfall was spatially correlated with rotation at 1.5 km, which was directly related to an increase in 500 m vertical velocity. By following a particular low-level rotating feature, a lowering of the updraft base and increase in the low-level updraft speed was seen in the regions of low-level rotation. Additionally, an increase in rain water mixing ratio is seen in the lower levels of the convection in regions of low-level rotation over regions without. This implies that the ability for the rotation to lower the updraft base and increase the low-level vertical motion leads to quicker formation of rain water in the vertical well below the freezing level. This also explains why the local enhancements by rotation are seen in the radar K_{dp} because it is proportional to the amount of liquid water, which the model shows is being enhanced in the low-levels by the rotation. The low-level updraft enhancement in regions of low-level rotation is also maintained in the simulation despite the increase hydrometeor loading associated with the increase in rain water mixing ratio, which further indicates, as shown in Chapter 3, the importance of the dynamical lift associated with the rotation in maintaining the low-level updrafts and driving the precipitation enhancement. The increase in warm rain mixing ratio in regions of low-level rotation is important to note because it implies that the presence of low-level rotation can increase (or at the very least affect), in certain scenarios, the precipitation efficiency of a convection system, and, thus, effect all three terms in Equation 3.2 that determine the rain rate of a particular storm, as opposed to just the two terms (i.e., w and q) discussed in Chapter 3. Overall, the case study showed how meso-γ-scale rotation associated with intense 0–1 km shear can lead to the development and maintenance of extreme short-term rainfall rates in a horizontal heterogeneous modeling framework and in an observational analysis of the event, adding further evidence that the mechanisms for rotational enhancement discussed in an idealized manner in Chapter 3 regularly affect the production of extreme rainfall.

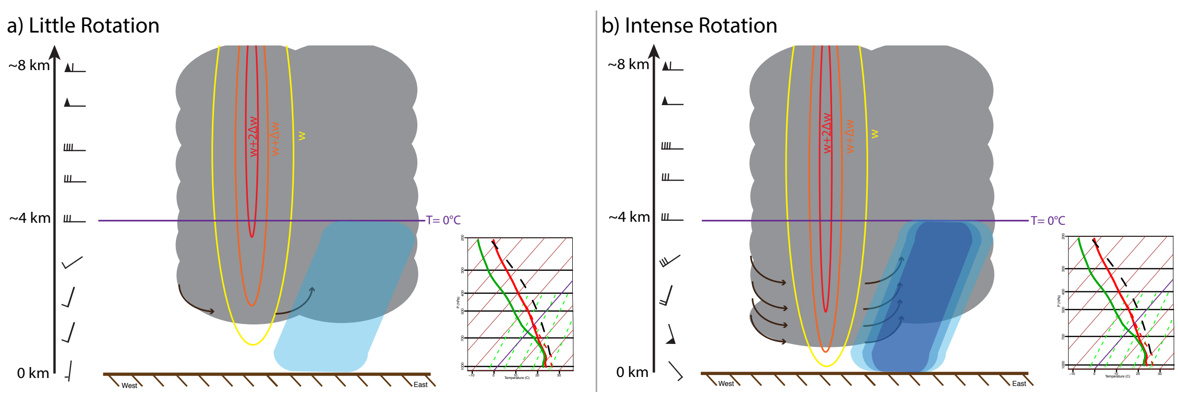

FIG. 6.1. Idealized schematic showing an idealized storm system slight (a) and significant rotation (b) in the same thermodynamic environment, which is denoted by the inset Skew-T Log-P in each panel and has the same plotting scheme as Fig. 5.12. Representative kinematic profile for each case is depicted by the wind barbs following the normal convention on the left side of each panel. Rotation is indicated by arrows, with the strength proportionate to number of arrows. Blue shading represents precipitation intensity, which increases as the blue shade darkens. Warm contours represent updraft velocity contours, and purple contour represents freezing level.

In conclusion, the results of this manuscript show that meso-γ-scale rotation is often associated with the production of extreme rainfall in the United States (i.e., Chapter 2 and 4) and is regularly concurrent and collocated with the production of tornadoes (i.e., TORFF events), which leads to complicated, contradictory recommendations of life-saving action. Idealized (Chapter 3) and real-time (Chapter 5) numerical modeling simulations show that rotationally induced dynamical accelerations can serve to enhance the convective rain rates by enhancing the low-level updrafts, lifting parcels that are thermodynamically stable but still contain moisture and instability, and increasing the production of rain water in the low-levels of the storm (Fig. 6.1). In total, rotation should no longer be looked upon from purely a tornadogensis point of view, but as a potential enhancement mechanism for rainfall and a risk to induce flash flooding.

Future work aims to further evaluate the effects of rotation on the three term parameter space that is related to the determination of instantaneous rain rate (i.e., $R = Ewq$). The research within this manuscript focused mainly on the direct dynamical effects of the rotation on updraft and inflow characteristics; however, other convective storm processes, such as those surrounding actual precipitation formation, were not directly examined. The most immediate need involves determining the effects that rotation has on the ice and liquid phases microphysical processes, as these processes directly involve the create of rain water. Further, the events examined in both Chapter 3 and Chapter 5 were associated with similar thermodynamic profiles. Thus, a need exists to test the sensitivity of the results to the thermodynamic profile, especially at low-to-mid levels. Varying low-to-mid level thermodynamic profiles would also have an effect on the nature of the low-level rotation, mid-level entrainment, and any cold pool development. The ability of a cold pool to effect the rotation (i.e., baroclinic development of horizontal vorticity) and the storm inflow moisture characteristics (i.e., modification of negatively buoyant inflow) are especially important points to examine. Lastly, additional investigation into the temporal variance associated with “verified” TORFF events is warranted, despite the uncertainties present in the verification datasets.

REFERENCES

Acevedo, O. C. and D. R. Fitzjarrald, 2001: The early evening surface-layer transition: Temporal and spatial variability. *J. Atmos. Sci.*, **58 (17)**, 2650–2667, doi: 10.1175/1520-0469(2001)058<2650:TEESLT>2.0.CO;2.

Adlerman, E. J., K. K. Droegemeier, and R. Davies-Jones, 1999: A numerical simulation of cyclic mesocyclogenesis. *J. Atmos. Sci.*, **56 (13)**, 2045–2069, doi: 10.1175/1520-0469(1999)056<2045:ANSOCM>2.0.CO;2.

Agee, E. and S. Childs, 2014: Adjustments in tornado counts, f-scale intensity, and path width for assessing significant tornado destruction. *J. Appl. Meteor. Climatol.*, **53 (6)**, 1494–1505, doi: 10.1175/JAMC-D-13-0235.1.

Anderson-Frey, A. K., Y. P. Richardson, A. R. Dean, R. L. Thompson, and B. T. Smith, 2016: Investigation of near-storm environments for tornado events and warnings. *Wea. Forecasting*, **31 (6)**, 1771–1790, doi: 10.1175/WAF-D-16-0046.1.

Ashley, S. T. and W. S. Ashley, 2008: Flood fatalities in the United States. *J. Appl. Meteor. Climatol.*, **47 (3)**, 805–818, doi: 10.1175/2007JAMC1611.1.

Ashley, W. S., 2007: Spatial and temporal analysis of tornado fatalities in the United States: 1880–2005. *Wea. Forecasting*, **22 (6)**, 1214–1228, doi: 10.1175/2007WAF2007004.1.

Ashley, W. S., A. J. Krmenec, and R. Schwantes, 2008: Vulnerability due to nocturnal tornadoes. *Wea. Forecasting*, **23 (5)**, 795–807, doi: 10.1175/2008WAF2222132.1.

Atkins, N. T. and M. St. Laurent, 2009: Bow echo mesovortices. Part I: Processes that influence their damaging potential. *Mon. Wea. Rev.*, **137 (5)**, 1497–1513, doi: 10.1175/2008MWR2649.1.

Baker, A. K., M. D. Parker, and M. D. Eastin, 2009: Environmental ingredients for supercells and tornadoes within Hurricane Ivan. *Wea. Forecasting*, **24 (1)**, 223–244, doi: 10.1175/2008WAF2222146.1.

Barthold, F. E., T. E. Workoff, B. A. Cosgrove, J. J. Gourley, D. R. Novak, and K. M. Mahoney, 2015: Improving flash flood forecasts: The HMT-WPC flash flood and intense rainfall experiment. *Bull. Amer. Meteor. Soc.*, **96 (11)**, 1859–1866, doi: 10.1175/BAMS-D-14-00201.1.

Beatty, K., E. Rasmussen, and J. Straka, 2008: The supercell spectrum. Part I: A review of research related to supercell precipitation morphology. *Electronic J. Severe Storms Meteor.*, **3 (4)**.

Benjamin, S. G., et al., 2016: A North American hourly assimilation and model forecast cycle: The rapid refresh. *Mon. Wea. Rev.*, **144 (4)**, 1669–1694, doi: 10.1175/MWR-D-15-0242.1.

Benoit, M. D., C. J. Nowotarski, D. T. Conlee, and L. Wood, 2018: Impacts of a university-led, on-demand sounding program on human and numerical weather prediction model forecasts in an upper-air observation hole. *J. Operational Meteor.*, **6 (7)**, doi: 10.15191/nwajom.2018.0607.

Beven, K. J., 2011: *Rainfall-runoff modelling: The primer.* John Wiley & Sons.

Blake, E. S. and D. A. Zelinsky, 2018: National Hurricane Center Tropical Cyclone Report: Hurricane Harvey (AL092017). Tech. Rep. AL092017, NOAA/National Hurricane Center, 76 pp. [Available online at `http://www.nhc.noaa.gov/data/tcr/AL092017_Harvey.pdf`].

Bluestein, H. B. and M. H. Jain, 1985: Formation of mesoscale lines of precipitation: Severe squall lines in Oklahoma during the spring. *J. Atmos. Sci.*, **42 (16)**, 1711–1732, doi: 10.1175/1520-0469(1985)042<1711:FOMLOP>2.0.CO;2.

Bonin, T., P. Chilson, B. Zielke, and E. Fedorovich, 2013: Observations of the early evening boundary-layer transition using a small unmanned aerial system. *Bound.-Layer Meteor.*, 1–14, doi: 10.1007/s10546-012-9760-3.

Bonner, W. D., 1968: Climatology of the low level jet. *Mon. Wea. Rev.*, **96 (12)**, 833–850, doi: 10.1175/1520-0493(1968)096<0833:COTLLJ>2.0.CO;2.

Bosart, L. F. and F. Sanders, 1981: The Johnstown flood of July 1977: A long-lived convective system. *J. Atmos. Sci.*, **38 (8)**, 1616–1642, doi: 10.1175/1520-0469(1981)038<1616:TJFOJA>2.0.CO;2.

Bouwer, L. M., 2011: Have disaster losses increased due to anthropogenic climate change? *Bull. Amer. Meteor. Soc.*, **92 (1)**, 39–46, doi: 10.1175/2010BAMS3092.1.

Brooks, H. E. and C. A. Doswell, III, 2002: Deaths in the 3 May 1999 Oklahoma City tornado from a historical perspective. *Wea. Forecasting*, **17 (3)**, 354–361, doi: 10.1175/1520-0434(2002)017<0354:DITMOC>2.0.CO;2.

Brooks, H. E., C. A. Doswell III, and M. P. Kay, 2003: Climatological estimates of local daily tornado probability for the United States. *Wea. Forecasting*, **18 (4)**, 626–640, doi: 10.1175/1520-0434(2003)018<0626:CEOLDT>2.0.CO;2.

Browning, K. A., 1977: The structure and mechanism of hailstorms. *Hail: A Review of Hail Science and Hail Suppression, Meteor. Mongr.*, **38**, 1–43.

Bryan, G. H. and J. M. Fritsch, 2002: A benchmark simulation for moist nonhydrostatic numerical models. *Mon. Wea. Rev.*, **130 (12)**, 2917–2928, doi: 10.1175/1520-0493(2002)130<2917:ABSFMN>2.0.CO;2.

Bunkers, M. J. and C. A. Doswell, III, 2016: Comments on “Double Impact: When both tornadoes and flash floods threaten the same place at the same time”. *Weather and Forecasting*, **31 (5)**, 1715–1721, doi: 10.1175/WAF-D-16-0116.1.

Bunkers, M. J., B. A. Klimowski, J. W. Zeitler, R. L. Thompson, and M. L. Weisman, 2000: Predicting supercell motion using a new hodograph technique. *Wea. Forecasting*, **15 (1)**, 61–79, doi: 10.1175/1520-0434(2000)015<0061:PSMUAN>2.0.CO;2.

Carbone, R., J. Tuttle, D. Ahijevych, and S. Trier, 2002: Inferences of predictability associated with warm season precipitation episodes. *J. Atmos. Sci.*, **59 (13)**, 2033–2056, doi: 10.1175/1520-0469(2002)059<2033:IOPAWW>2.0.CO;2.

Chagnon, J. M. and S. L. Gray, 2009: Horizontal potential vorticity dipoles on the convective storm scale. *Quart. J. Roy. Meteor. Soc.*, **135 (643)**, 1392–1408, doi: 10.1002/qj.468.

Changnon, S. A., R. A. Pielke Jr, D. Changnon, R. T. Sylves, and R. Pulwarty, 2000: Human factors explain the increased losses from weather and climate extremes*. *Bull. Amer. Meteor. Soc.*, **81 (3)**, 437–442, doi: 10.1175/1520-0477(2000)081<0437:HFETIL>2.3.CO;2.

Chappell, C. F., 1986: Quasi-stationary convective events. *Mesoscale Meteorology and Forecasting*, P. S. Ray, Ed., Amer. Meteor. Soc., 289–309.

Clark, A. J., J. Gao, P. T. Marsh, T. Smith, J. S. Kain, J. Correia Jr, M. Xue, and F. Kong, 2013: Tornado pathlength forecasts from 2010 to 2011 using ensemble updraft helicity. *Wea. Forecasting*, **28 (2)**, 387–407, doi: 10.1175/WAF-D-12-00038.1.

Coffer, B. E. and M. D. Parker, 2015: Impacts of increasing low-level shear on supercells during the early evening transition*. *Mon. Wea. Rev.*, **143 (5)**, 1945–1969, doi: 10.1175/MWR-D-14-00328.1.

Costa, J. E., 1987: Hydraulics and basin morphometry of the largest flash floods in the conterminous United States. *J. Hydrol.*, **93 (3)**, 313–338, doi: 10.1016/0022-1694(87)90102-8.

Craven, J. P., H. E. Brooks, and J. A. Hart, 2004: Baseline climatology of sounding derived parameters associated with deep, moist convection. *Natl. Wea. Dig*, **28 (1)**, 13–24.

Creutin, J. D., M. Borga, C. Lutoff, A. Scolobig, I. Ruin, and L. Créton-Cazanave, 2009: Catchment dynamics and social response during flash floods: the potential of radar rainfall monitoring for warning procedures. *Meteorological Appl.*, **16 (1)**, 115–125, doi: 10.1002/met.128.

Dalrymple, T., 1937: *Major Texas floods of 1935.* U.S. Geological Survey Water Supply Paper 796-G, 287 pp.

Davenport, C. E. and M. D. Parker, 2015: Observations of the 9 June 2009 dissipating supercell from VORTEX2. *Wea. Forecasting*, **30 (2)**, 368–388, doi: 10.1175/WAF-D-14-00087.1.

Davis, R. S., 2001: Flash flood forecast and detection methods. *Severe Convective Storms*, Springer, 481–525.

Demuth, J. L., et al., 2018: "sometimes da# beachlife ain't always da wave": Understanding people's evolving hurricane risk communication, risk assessments, and responses using twitter narratives. **10 (7)**, 537–560, doi: 10.1175/WCAS-D-17-0126.1.

Doswell, C. A., III, 1994: Flash flood producing convective storms: current understanding and research. *Proceedings, Spain-US Joint Workshop on Natural Hazards, Barcelona, Spain.*

Doswell, C. A., III, 2001: Severe convective storms—an overview. *Meteor. Mongr.*, **28**, 1–26.

Doswell, C. A., III, 2007: Small sample size and data quality issues illustrated using tornado occurrence data. *Electron. J. Severe Storms Meteor*, **2 (5)**, 1–16.

Doswell, C. A., III, H. E. Brooks, and R. A. Maddox, 1996: Flash flood forecasting: An ingredients-based methodology. *Wea. Forecasting*, **11 (4)**, 560–581, doi: 10.1175/1520-0434(1996)011<0560:FFFAIB>2.0.CO;2.

Doswell, C. A., III, C. Ramis, R. Romero, and S. Alonso, 1998: A diagnostic study of three heavy precipitation episodes in the western mediterranean region. *Wea. Forecasting*, **13 (1)**, 102–124, doi: 10.1175/1520-0434(1998)013<0102:ADSOTH>2.0.CO;2.

Duda, J. D. and W. A. Gallus, Jr, 2010: Spring and summer midwestern severe weather reports in supercells compared to other morphologies. *Wea. Forecasting*, **25 (1)**, 190–206, doi: 10.1175/2009WAF2222338.1.

Durran, D. R. and J. B. Klemp, 1983: A compressible model for the simulation of moist mountain waves. *Mon. Wea. Rev.*, **111 (12)**, 2341–2361, doi: 10.1175/1520-0493(1983)111<2341:ACMFTS>2.0.CO;2.

Edwards, R., A. R. Dean, R. L. Thompson, and B. T. Smith, 2012: Convective modes for significant severe thunderstorms in the contiguous United States. Part III: Tropical cyclone tornadoes. *Wea. Forecasting*, **27 (6)**, 1507–1519, doi: 10.1175/WAF-D-11-00117.1.

Ester, M., H.-P. Kriegel, J. Sander, X. Xu, et al., 1996: A density-based algorithm for discovering clusters in large spatial databases with noise. *Kdd*, Vol. 96, 226–231.

Foote, G. and J. Fankhauser, 1973: Airflow and moisture budget beneath a northeast Colorado hailstorm. *J. Appl. Meteor. Climatol.*, **12 (8)**, 1330–1353, doi: 10.1175/1520-0450(1973)012<1330:AAMBBA>2.0.CO;2.

Fritsch, J., R. Kane, and C. Chelius, 1986: The contribution of mesoscale convective weather systems to the warm-season precipitation in the United States. *J. Climate Appl. Meteor.*, **25 (10)**, 1333–1345, doi: 10.1175/1520-0450(1986)025<1333:TCOMCW>2.0.CO;2.

Fritsch, J., J. Murphy, and J. Kain, 1994: Warm core vortex amplification over land. *J. Atmos. Sci.*, **51 (13)**, 1780–1807, doi: 10.1175/1520-0469(1994)051<1780:WCVAOL>2.0.CO;2.

Fritsch, J. M. and R. Carbone, 2004: Improving quantitative precipitation forecasts in the warm season: A USWRP research and development strategy. *Bull. Amer. Meteor. Soc.*, **85 (7)**, 955–965, doi: 10.1175/BAMS-85-7-955.

Gill, S. E., J. F. Handley, A. R. Ennos, and S. Pauleit, 2007: Adapting cities for climate change: the role of the green infrastructure. *Built environment*, **33 (1)**, 115–133.

Gochis, D., et al., 2015: The great Colorado flood of september 2013. *Bull. Amer. Meteor. Soc.*, **96 (9)**, 1461–1487, doi: 10.1175/BAMS-D-13-00241.1.

Gourley, J. J., et al., 2013: A unified flash flood database across the United States. *Bull. Amer. Meteor. Soc.*, **94 (6)**, 799–805, doi: 10.1175/BAMS-D-12-00198.1.

Gourley, J. J., et al., 2017: The FLASH project: Improving the tools for flash flood monitoring and prediction across the United States. *Bull. Amer. Meteor. Soc.*, **98 (2)**, 361–372, doi: 10.1175/BAMS-D-15-00247.1.

Hapuarachchi, H., Q. Wang, and T. Pagano, 2011: A review of advances in flash flood forecasting. *Hydrological Processes*, **25 (18)**, 2771–2784, doi: 10.1002/hyp.8040.

Haynes, P. and M. McIntyre, 1987: On the evolution of vorticity and potential vorticity in the presence of diabatic heating and frictional or other forces. *J. Atmos. Sci.*, **44 (5)**, 828–841, doi: 10.1175/1520-0469(1987)044<0828:OTEOVA>2.0.CO;2.

HCFCD, 2019: Harris County Flood Warning System. [Available online at `https://www.harriscountyfws.org/`].

Herman, G. R., E. R. Nielsen, and R. S. Schumacher, 2018: Probabilistic verification of storm prediction center convective outlooks. *Wea. Forecasting*, **33 (1)**, 161–184, doi: 10.1175/WAF-D-17-0104.1.

Herman, G. R. and R. S. Schumacher, 2016: Extreme precipitation in models: An evaluation. *Wea. Forecasting*, **31**, 1853–1879, doi: 10.1175/WAF-D-16-0093.1.

Herman, G. R. and R. S. Schumacher, 2018a: Money doesn't grow on trees, but forecasts do: Forecasting extreme precipitation with random forests. *Mon. Wea. Rev.*, **146**, 1571–1600, doi: 10.1175/MWR-D-17-0250.1.

Herman, G. R. and R. S. Schumacher, 2018b: Perplexing problems with flash flood verification: Pondering precipitation proxies. *J. Hydrometeor.*, **19 (11)**, 1753–1776, doi: 10.1175/JHM-D-18-0092.1.

Herman, G. R. and R. S. Schumacher, 2018c: "Dendrology" in numerical weather prediction: What random forests and logistic regression tell us about forecasting extreme precipitation. *Mon. Wea. Rev.*, **146 (6)**, 1785–1812, doi: 10.1175/MWR-D-17-0307.1.

Hertenstein, R. F. and W. H. Schubert, 1991: Potential vorticity anomalies associated with squall lines. *Mon. Wea. Rev.*, **119 (7)**, 1663–1672, doi: 10.1175/1520-0493(1991)119<1663:PVAAWS>2.0.CO;2.

Hitchens, N. M. and H. E. Brooks, 2012: Evaluation of the Storm Prediction Center's day 1 convective outlooks. *Wea. Forecasting*, **27**, 1580–1585, doi: 10.1175/WAF-D-12-00061.1.

Hitchens, N. M. and H. E. Brooks, 2013: Preliminary investigation of the contribution of supercell thunderstorms to the climatology of heavy and extreme precipitation in the United States. *Atmos. Res.*, **123**, 206–210, doi: 10.1016/j.atmosres.2012.06.023.

Hitchens, N. M. and H. E. Brooks, 2014: Evaluation of the Storm Prediction Center's convective outlooks from day 3 through day 1. *Wea. Forecasting*, **29**, 1134–1142, doi: 10.1175/WAF-D-13-00132.1.

Hitchens, N. M. and H. E. Brooks, 2017: Determining criteria for missed events to evaluate significant severe convective outlooks. *Wea. Forecasting*, **32**, 1321–1328, doi: 10.1175/WAF-D-16-0170.1.

IEM, 2017: Iowa Environmental Mesonet COW: NWS storm based warning verification. Cited: 2017-09-27, [Available online at `https://mesonet.agron.iastate.edu/cow/`].

IEM, 2018a: Iowa Environmental Mesonet: ASOS-AWOS-METAR data download. Cited: 2018-04-05, [Available online at `https://mesonet.agron.iastate.edu/request/download.phtml`].

IEM, 2018b: Iowa Environmental Mesonet: GIS archive. [Available online at `https://mesonet.agron.iastate.edu/GIS/`].

James, E. P. and R. H. Johnson, 2010: Patterns of precipitation and mesolow evolution in midlatitude mesoscale convective vortices. *Mon. Wea. Rev.*, **138 (3)**, 909–931, doi: 10.1175/2009MWR3076.1.

Jones, T. A., K. M. McGrath, and J. T. Snow, 2004: Association between NSSL mesocyclone detection algorithm-detected vortices and tornadoes. *Wea. Forecasting*, **19 (5)**, 872–890, doi: 10.1175/1520-0434(2004)019<0872:ABNMDA>2.0.CO;2.

Kandel, D., A. Western, R. Grayson, and H. Turral, 2004: Process parameterization and temporal scaling in surface runoff and erosion modelling. *Hydrological Processes*, **18 (8)**, 1423–1446, doi: 10.1002/hyp.1421.

Kelsch, M., 2001: Hydrometeorological characteristics of flash floods. *Coping with flash floods*, Springer, 181–193.

Kelsch, M., E. Caporali, and L. G. Lanza, 2001: Hydrometeorology of flash floods. *Coping with flash floods*, Springer, 19–35.

Klemp, J. B., 1987: Dynamics of tornadic thunderstorms. *Ann. Rev. of Fluid Mech.*, **19 (1)**, 369–402.

Klemp, J. B., W. C. Skamarock, and J. Dudhia, 2007: Conservative split-explicit time integration methods for the compressible nonhydrostatic equations. *Mon. Wea. Rev.*, **135 (8)**, 2897–2913, doi: 10.1175/MWR3440.1.

Kumjian, M. R., 2013a: Principles and applications of dual-polarization weather radar. part I: Description of the polarimetric radar variables. *Journal of Operational Meteorology*, **1**, doi: 10.15191/nwajom.2013.0119.

Kumjian, M. R., 2013b: Principles and applications of dual-polarization weather radar. part II: Warm-and cold-season applications. *Journal of Operational Meteorology*, **1**, doi: 10.15191/nwajom.2013.0120.

KWTV, cited 2015: Understanding storm shelters could save Oklahomans' lives. [Available online at http://www.newson6.com/story/29010877/understanding-storm-shelters-could-save-oklahomans-lives].

Lackmann, G. M. and R. M. Yablonsky, 2004: The importance of the precipitation mass sink in tropical cyclones and other heavily precipitating systems. *J. Atmos. Sci.*, **61 (14)**, 1674–1692, doi: 10.1175/1520-0469(2004)061<1674:TIOTPM>2.0.CO;2.

Lamb, D., 2001: Rain production in convective storms. *Meteor. Mongr.*, **28**, 299–321.

LCRA, 2017: Lower Colorado River Authority: Historical data by gauge. Cited: 2017-09-28, [Available online at `https://hydromet.lcra.org/HistoricalData`].

Leary, M. R., R. Bednarski, D. Hammon, and T. Duncan, 1997: Blowhards, snobs, and narcissists. *Aversive interpersonal behaviors*, Springer, 111–131.

Legates, D. and T. Deliberty, 1993: Precipitation measurement biases in the United States. *Water . Resources . Bulletin*, **29 (5)**, 855–861.

Levy, G. and W. R. Cotton, 1984: A numerical investigation of mechanisms linking glaciation of the ice-phase to the boundary layer. *J. Climate Appl. Meteor.*, **23 (11)**, 1505–1519, doi: 10.1175/1520-0450(1984)023<1505:ANIOML>2.0.CO;2.

Lin, Y. and K. E. Mitchell, 2005: The NCEP Stage II/IV hourly precipitation analyses: development and applications. *Preprints, 19th Conference on Hydrology*, San Diego, CA, Amer. Meteor. Soc., [Available online at `http://ams.confex.com/ams/pdfpapers/83847.pdf`].

Linder, J. and S. Fitzgerald, 2016: Harris Country Flood Control District: Tax day flood immediate report. Tech. memo., 34 pp.

Loftus, A. M., D. B. Weber, and C. A. Doswell III, 2008: Parameterized mesoscale forcing mechanisms for initiating numerically simulated isolated multicellular convection. *Mon. Wea. Rev.*, **136 (7)**, 2408–2421, doi: 10.1175/2007MWR2133.1.

Lorenz, E. N., 1969: The predictability of a flow which possesses many scales of motion. *Tellus A*, **21 (3)**.

Maddox, R. A., C. F. Chappell, and L. R. Hoxit, 1979: Synoptic and meso-α scale aspects of flash flood events. *Bull. Amer. Meteor. Soc.*, 115–123, doi: 10.1175/1520-0477-60.2.115.

Maddox, R. A. and W. Deitrich, 1982: Meteorological settings associated with simultaneous occurrences of severe thunderstorms and flash floods. *Natl. Wea. Dig*, **7 (3)**, 36–43.

Maples, L. Z. and J. P. Tiefenbacher, 2009: Landscape, development, technology and drivers: The geography of drownings associated with automobiles in Texas floods, 1950–2004. *Applied geography*, **29 (2)**, 224–234, doi: 10.1016/j.apgeog.2008.09.004.

Markowski, P. and Y. Richardson, 2010: *Mesoscale meteorology in midlatitudes*. John Wiley & Sons.

Markowski, P., et al., 2012: The pretornadic phase of the Goshen County, Wyoming, supercell of 5 June 2009 intercepted by VORTEX2. Part II: Intensification of low-level rotation. *Mon. Wea. Rev.*, **140 (9)**, 2916–2938, doi: 10.1175/MWR-D-11-00337.1.

Markowski, P. M. and Y. P. Richardson, 2014: The influence of environmental low-level shear and cold pools on tornadogenesis: Insights from idealized simulations. *J. Atmos. Sci.*, **71 (1)**, 243–275, doi: 10.1175/JAS-D-13-0159.1.

Marwitz, J. D., 1972: Precipitation efficiency of thunderstorms on the high plains. *J. Rech. Atmos*, **6**, 367–370.

McCaul, E. W., Jr and M. L. Weisman, 2001: The sensitivity of simulated supercell structure and intensity to variations in the shapes of environmental buoyancy and shear profiles. *Mon. Wea. Rev.*, **129 (4)**, 664–687, doi: 10.1175/1520-0493(2001)129<0664:TSOSSS>2.0.CO;2.

Melhauser, C. and F. Zhang, 2012: Practical and intrinsic predictability of severe and convective weather at the mesoscales. *J. Atmos. Sci.*, **69 (11)**, 3350–3371, doi: 10.1175/JAS-D-11-0315.1.

Mellor, G. L. and T. Yamada, 1982: Development of a turbulence closure model for geophysical fluid problems. *Reviews of Geophysics*, **20 (4)**, 851–875, doi: 10.1029/RG020i004p00851.

Mercer, A. E., C. M. Shafer, C. A. Doswell, III, L. M. Leslie, and M. B. Richman, 2009: Objective classification of tornadic and nontornadic severe weather outbreaks. *Mon. Wea. Rev.*, **137 (12)**, 4355–4368, doi: 10.1175/2009MWR2897.1.

Mlawer, E. J., S. J. Taubman, P. D. Brown, M. J. Iacono, and S. A. Clough, 1997: Radiative transfer for inhomogeneous atmospheres: RRTM, a validated correlated-k model for the longwave. *J. Geophys. Res.*, **102 (D14)**, 16 663–16 682.

Mohamadi, M. A. and A. Kavian, 2015: Effects of rainfall patterns on runoff and soil erosion in field plots. *International Soil and Water Conservation Research*, **3 (4)**, 273–281, doi: 10.1016/j.iswcr.2015.10.001.

Moller, A. R., C. A. Doswell III, M. P. Foster, and G. R. Woodall, 1994: The operational recognition of supercell thunderstorm environments and storm structures. *Wea. Forecasting*, **9 (3)**, 327–347, doi: 10.1175/1520-0434(1994)009<0327:TOROST>2.0.CO;2.

Moore, J. T., F. H. Glass, C. E. Graves, S. M. Rochette, and M. J. Singer, 2003: The environment of warm-season elevated thunderstorms associated with heavy rainfall over the central United States. *Wea. Forecasting*, **18 (5)**, 861–878, doi: 10.1175/1520-0434(2003)018<0861:TEOWET>2.0.CO;2.

Morales, A., R. S. Schumacher, and S. M. Kreidenweis, 2015: Mesoscale vortex development during extreme precipitation: Colorado, September 2013. *Mon. Wea. Rev.*, **143 (12)**, 4943–4962, doi: 10.1175/MWR-D-15-0086.1.

Morin, M. J. and M. D. Parker, 2011: A numerical investigation of supercells in landfalling tropical cyclones. *Geophys. Res. Lett.*, **38 (10)**, doi: 10.1029/2011GL047448.

Morrison, H. G., G. Thompson, and V. Tatarskii, 2009: Impact of cloud microphysics on the development of trailing stratiform precipitation in a simulated squall line: Comparison of one- and two-moment schemes. *Mon. Wea. Rev.*, **137**, 991–1007, doi: 10.1175/2008MWR2556.1.

Morss, R. E., O. V. Wilhelmi, G. A. Meehl, and L. Dilling, 2011: Improving societal outcomes of extreme weather in a changing climate: an integrated perspective. *Annu. Rev. Environ. Resour.*, **36 (1)**, 1, doi: 10.1146/annurev-environ-060809-100145.

Morss, R. E., et al., 2017: Hazardous weather prediction and communication in the modern information environment. *Bull. Amer. Meteor. Soc.*, **98 (12)**, 2653–2674, doi: 10.1175/BAMS-D-16-0058.1.

Nakanish, M., 2001: Improvement of the Mellor–Yamada turbulence closure model based on large-eddy simulation data. *Boundary-layer meteorology*, **99 (3)**, 349–378, doi: 10.1023/A:1018915827400.

Nakanishi, M. and H. Niino, 2004: An improved Mellor–Yamada level-3 model with condensation physics: Its design and verification. *Boundary-Layer Meteorology*, **112 (1)**, 1–31, doi: 10.1023/B:BOUN.0000020164.04146.98.

NCEI, 2017: Storm events database. NOAA, [Available online at `http://www.ncdc.noaa.gov/stormevents/`].

Nelson, B. R., O. P. Prat, D.-J. Seo, and E. Habib, 2016: Assessment and implications of NCEP Stage IV quantitative precipitation estimates for product intercomparisons. *Wea. Forecasting*, **31 (2)**, 371–394, doi: 10.1175/WAF-D-14-00112.1.

Nielsen, E. R., 2016: Using convection-allowing ensembles to understand the predictability of extreme rainfall. M.S. thesis, Department of Atmospheric Sciences, Colorado State University, Fort Collins, CO.

Nielsen, E. R., G. R. Herman, and R. S. Schumacher, 2017: An updated U.S. geographic distribution of concurrent, collocated tornado and flash flood events and a look at those observed during the first year of VORTEX-SE. *Special symposium on severe local storms: observation need to advance research, prediction, and communication, Seattle, WA, Amer. Meteor. Soc., 923*, [Available online at https://ams.confex.com/ams/97Annual/webprogram/Handout/Paper305034/TORFF_VORTEX_SE_AMS_poster2017.pdf].

Nielsen, E. R., G. R. Herman, R. C. Tournay, J. M. Peters, and R. S. Schumacher, 2015: Double impact: When both tornadoes and flash floods threaten the same place at the same time. *Wea. Forecasting*, **30 (6)**, 1673–1693, doi: 10.1175/WAF-D-15-0084.1.

Nielsen, E. R., G. R. Herman, R. C. Tournay, J. M. Peters, and R. S. Schumacher, 2016a: Reply to "comments on 'Double impact: When both tornadoes and flash floods threaten the same place at the same time'". *Weather and Forecasting*, **31 (5)**, 1723–1727, doi: 10.1175/WAF-D-16-0151.1.

Nielsen, E. R. and R. S. Schumacher, 2016: Using convection-allowing ensembles to understand the predictability of an extreme rainfall event. *Mon. Wea. Rev.*, **144 (10)**, doi: 10.1175/MWR-D-16-0083.1.

Nielsen, E. R. and R. S. Schumacher, 2018: Dynamical insights into extreme short-term precipitation associated with supercells and mesovortices. *J. Atmos. Sci.*, **75 (9)**, 2983–3009, doi: 10.1175/JAS-D-18-0385.1.

Nielsen, E. R., R. S. Schumacher, and A. M. Keclik, 2016b: The effect of the Balcones Escarpment on three cases of extreme precipitation in central Texas. *Mon. Wea. Rev.*, **144 (1)**, 119–138, doi: 10.1175/MWR-D-15-0156.1.

NOAA, 2011: Value of a weather-ready nation. [Available online at http://www.ppi.noaa.gov/wp-content/uploads/PPI-Weather-Econ-Stats-10-13-11.pdf].

NOAA, 2016a: *Storm Data*, Vol. 58, No. 3. 350 pp.

NOAA, 2016b: *Storm Data*, Vol. 58, No. 4. 377 pp.

Novak, D. R., C. Bailey, K. Brill, M. Eckert, D. Petersen, R. Rausch, and M. Schichtel, 2011: Human improvement to numerical weather prediction at the Hydrometeorological Prediction Center. *91th Annual AMS Meeting, AMS 24th Conference on Weather and Forecasting/20th Conference on Numerical Weather Prediction*, [Available online at https://ams.confex.com/ams/91Annual/webprogram/Manuscript/Paper181989/HumanNWP_final.pdf].

Nowotarski, C. J., P. M. Markowski, and Y. P. Richardson, 2011: The characteristics of numerically simulated supercell storms situated over statically stable boundary layers. *Mon. Wea. Rev.*, **139 (10)**, 3139–3162, doi: 10.1175/MWR-D-10-05087.1.

NWS, 1999: Service assessment: South Texas Floods October 17-22, 1998. National Weather Service, [Available online at http://www.nws.noaa.gov/om/assessments/pdfs/txflood.pdf].

NWS, 2011: Service assessment: Record floods of greater Nashville: Including flooding in middle Tennessee and western Kentucky, May 1-4, 2010. National Weather Service, [Available online at http://www.nws.noaa.gov/om/assessments/pdfs/Tenn_Flooding.pdf] pp.

NWS, 2014: Service assessment: May 2013 Oklahoma Tornadoes and Flash Flooding. National Weather Service, [Available online at http://www.nws.noaa.gov/om/assessments/pdfs/13oklahoma_tornadoes.pdf] pp.

NWS, 2017: National Weather Service manual 10-950. Hydrologic Services Program, NWSPD 10-9, National Weather Service, [Available online at http://www.nws.noaa.gov/directives/sym/pd01009050curr.pdf].

NWS, 2018a: Service assessment: August/September 2017 hurricane Harvey. National Weather Service, [Available online at https://www.weather.gov/media/publications/assessments/harvey6-18.pdf] pp.

NWS, 2018b: Summary of natural hazard statistics in the United States. Climate, Weather, and Water Services, National Weather Service, [Available online at http://www.nws.noaa.gov/om/hazstats.shtml].

Parker, M. D. and D. A. Ahijevych, 2007: Convective episodes in the east-central United States. *Mon. Wea. Rev.*, **135 (11)**, 3707–3727, doi: 10.1175/2007MWR2098.1.

Parker, M. D. and R. H. Johnson, 2000: Organizational modes of midlatitude mesoscale convective systems. *Mon. Wea. Rev.*, **128 (10)**, 3413–3436, doi: 10.1175/1520-0493(2001)129<3413:OMOMMC>2.0.CO;2.

Parker, M. D. and R. H. Johnson, 2004: Structures and dynamics of quasi-2D mesoscale convective systems. *J. Atmos. Sci.*, **61 (5)**, 545–567, doi: 10.1175/1520-0469(2004)061<0545:SADOQM>2.0.CO;2.

Pedregosa, F., et al., 2011: Scikit-learn: Machine learning in python. *J. Mach. Learn. Res.*, **12**, 2825–2830, URL http://dl.acm.org/citation.cfm?id=1953048.2078195.

Peters, J. M., E. R. Nielsen, M. D. Parker, S. M. Hitchcock, and R. S. Schumacher, 2017: The impact of low-level moisture errors on model forecasts of an MCS observed during PECAN. *Mon. Wea. Rev.*, **145 (9)**, 3599–3624, doi: 10.1175/MWR-D-16-0296.1.

Potvin, C. K., C. Broyles, P. S. Skinner, H. E. Brooks, and E. Rasmussen, 2019: A bayesian hierarchical modeling framework for correcting reporting bias in the U.S. tornado database. *Wea. Forecasting*, **34 (1)**, 15–30, doi: 10.1175/WAF-D-18-0137.1.

Potvin, C. K., K. L. Elmore, and S. J. Weiss, 2010: Assessing the impacts of proximity sounding criteria on the climatology of significant tornado environments. *Wea. Forecasting*, **25 (3)**, 921–930, doi: 10.1175/2010WAF2222368.1.

Raymond, D. and H. Jiang, 1990: A theory for long-lived mesoscale convective systems. *J. Atmos. Sci.*, **47 (24)**, 3067–3077, doi: 10.1175/1520-0469(1990)047<3067:ATFLLM>2.0.CO;2.

Rhodes, B. C., 2011: PyEphem: Astronomical Ephemeris for Python. Astrophysics Source Code Library, `1112.014`.

Rogash, J. A. and J. Racy, 2002: Some meteorological characteristics of significant tornado events occurring in proximity to flash flooding. *Wea. Forecasting*, **17 (1)**, 155–159, doi: 10.1175/1520-0434(2002)017<0155:SMCOST>2.0.CO;2.

Rogash, J. A. and R. D. Smith, 2000: Multiscale overview of a violent tornado outbreak with attendant flash flooding. *Wea. Forecasting*, **15 (4)**, 416–431, doi: 10.1175/1520-0434(2000)015<0416:MOOAVT>2.0.CO;2.

Rotunno, R. and J. B. Klemp, 1982: The influence of the shear-induced pressure gradient on thunderstorm motion. *Mon. Wea. Rev.*, **110 (2)**, 136–151, doi: 10.1175/1520-0493(1982)110<0136:TIOTSI>2.0.CO;2.

Saharia, M., P.-E. Kirstetter, H. Vergara, J. J. Gourley, Y. Hong, and M. Giroud, 2017: Mapping flash flood severity in the United States. *J. Hydrometeor.*, **18 (2)**, 397–411, doi: 10.1175/JHM-D-16-0082.1.

Schroeder, A., J. Basara, J. M. Shepherd, and S. Nelson, 2016: Insights into atmospheric contributors to urban flash flooding across the United States using an analysis of rawinsonde data and associated calculated parameters. *J. Appl. Meteor. Climatol.*, **55 (2)**, 313–323, doi: 10.1175/JAMC-D-14-0232.1.

Schumacher, R. S., 2009: Mechanisms for quasi-stationary behavior in simulated heavy-rain-producing convective systems. *J. Atmos. Sci.*, **66 (6)**, 1543–1568, doi: 10.1175/2008JAS2856.1.

Schumacher, R. S., 2015a: Resolution dependence of initiation and upscale growth of deep convection in convection-allowing forecasts of the 31 May–1 June 2013 supercell and MCS. *Mon. Wea. Rev.*, **143 (11)**, 4331–4354, doi: 10.1175/MWR-D-15-0179.1.

Schumacher, R. S., 2015b: Sensitivity of precipitation accumulation in elevated convective systems to small changes in low-level moisture. *J. Atmos. Sci.*, **72 (6)**, 2507–2524, doi: 10.1175/JAS-D-14-0389.1.

Schumacher, R. S., 2017: Heavy rainfall and flash flooding. *Natural Hazard Science, Oxford Research Encyclopedias*, **132**, doi: 10.1093/acrefore/9780199389407.013.

Schumacher, R. S., A. J. Clark, M. Xue, and F. Kong, 2013: Factors influencing the development and maintenance of nocturnal heavy-rain-producing convective systems in a storm-scale ensemble. *Mon. Wea. Rev.*, **141 (8)**, 2778–2801, doi: 10.1175/MWR-D-12-00239.1.

Schumacher, R. S. and R. H. Johnson, 2005: Organization and environmental properties of extreme-rain-producing mesoscale convective systems. *Mon. Wea. Rev.*, **133**, 961–976, doi: 10.1175/MWR2899.1.

Schumacher, R. S. and R. H. Johnson, 2006: Characteristics of United States extreme rain events during 1999–2003. *Wea. Forecasting*, **21**, 69–85, doi: 10.1175/WAF900.1.

Schumacher, R. S. and R. H. Johnson, 2009: Quasi-stationary, extreme-rain-producing convective systems associated with midlevel cyclonic circulations. *Wea. Forecasting*, **24**, 555–574, doi: 10.1175/2008WAF2222173.1.

Schumacher, R. S. and E. R. Nielsen, 2018: CSU mobile radiosonde data. version 2.0. Cited: 2018-10-22, [Available online at `https://data.eol.ucar.edu/dataset/541.020`], doi: 10.5065/d62j69kp.

Schwartz, B. E., C. F. Chappell, W. E. Togstad, and X.-P. Zhong, 1990: The Minneapolis flash flood: Meteorological analysis and operational response. *Wea. Forecasting*, **5 (1)**, 3–21, doi: 10.1175/1520-0434(1990)005<0003:TMFFMA>2.0.CO;2.

Schwartz, C. S., G. S. Romine, R. A. Sobash, K. R. Fossell, and M. L. Weisman, 2015: NCAR's experimental real-time convection-allowing ensemble prediction system. *Wea. Forecasting*, **30 (6)**, 1645–1654, doi: 10.1175/WAF-D-15-0103.1.

Sharif, H. O., T. L. Jackson, M. M. Hossain, and D. Zane, 2015: Analysis of flood fatalities in Texas. *Natural Hazards Rev.*, **16 (1)**, doi: 10.1061/(ASCE)NH.1527-6996.0000145.

Sherburn, K. D. and M. D. Parker, 2014: Climatology and ingredients of significant severe convection in high-shear, low-cape environments. *Wea. Forecasting*, **29 (4)**, 854–877, doi: 10.1175/WAF-D-13-00041.1.

Skamarock, W., et al., 2008: A description of the advanced research WRF version 3. NCAR Tech. Note NCAR/TN–475+STR, [Available online at `http://www.mmm.ucar.edu/wrf/users/docs/arw_v3.pdf`] pp.

Skamarock, W. C. and J. B. Klemp, 2008: A time-split nonhydrostatic atmospheric model for weather research and forecasting applications. *J. Comput. Phys.*, **227 (7)**, 3465–3485.

Smirnova, T. G., J. M. Brown, and S. G. Benjamin, 1997: Performance of different soil model configurations in simulating ground surface temperature and surface fluxes. *Mon. Wea. Rev.*, **125 (8)**, 1870–1884, doi: 10.1175/1520-0493(1997)125<1870:PODSMC>2.0.CO;2.

Smirnova, T. G., J. M. Brown, S. G. Benjamin, and J. S. Kenyon, 2016: Modifications to the rapid update cycle land surface model (RUC LSM) available in the weather research and forecasting (WRF) model. *Mon. Wea. Rev.*, **144 (5)**, 1851–1865, doi: 10.1175/MWR-D-15-0198.1.

Smirnova, T. G., J. M. Brown, S. G. Benjamin, and D. Kim, 2000: Parameterization of cold-season processes in the maps land-surface scheme. *J. Geophys. Res.*, **105 (D3)**, 4077–4086, doi: 10.1029/1999JD901047.

Smith, B., J. Smith, M. Baeck, G. Villarini, and D. Wright, 2013: Spectrum of storm event hydrologic response in urban watersheds. *Water Resources Research*, **49 (5)**, 2649–2663, doi: 10.1002/wrcr.20223.

Smith, B. T., 2006: SVRGIS: Geographic information system (GIS) graphical database of tornado, large hail, and damaging wind reports in the United States (1950-2005). *Preprints, 23rd Conf. Severe Local Storms, St. Louis, MO, Amer. Meteor. Soc., P2.6*, [Available online at `https://ams.confex.com/ams/pdfpapers/115381.pdf`].

Smith, B. T., R. L. Thompson, J. S. Grams, C. Broyles, and H. E. Brooks, 2012: Convective modes for significant severe thunderstorms in the contiguous United States. Part I: Storm classification and climatology. *Wea. Forecasting*, **27 (5)**, 1114–1135, doi: 10.1175/WAF-D-11-00115.1.

Smith, J. A., M. L. Baeck, Y. Zhang, and C. A. Doswell III, 2001: Extreme rainfall and flooding from supercell thunderstorms. *J. Hydrometeor.*, **2 (5)**, 469–489, doi: 10.1175/1525-7541(2001)002<0469:ERAFFS>2.0.CO;2.

Smith, J. A., A. A. Cox, M. L. Baeck, L. Yang, and P. Bates, 2018: Strange floods: The upper tail of flood peaks in the U.S. *Water Resources Research*, **(54)**, doi: 10.1029/2018WR022539.

Smith, T. L., S. G. Benjamin, J. M. Brown, S. Weygandt, T. Smirnova, and B. Schwartz, 2008: Convection forecasts from the hourly updated, 3-km high resolution rapid refresh model. *Preprints, 24th Conf. on Severe Local Storms*, Savannah, GA, Amer. Meteor. Soc., 11.1, [Available online at `Availableonlineathttp://ams.confex.com/ams/24SLS/techprogram/paper_142055.htm.]`].

Smith, T. M., et al., 2016: Multi-radar multi-sensor (MRMS) severe weather and aviation products: Initial operating capabilities. *Bull. Amer. Meteor. Soc.*, **97 (9)**, 1617–1630, doi: 10.1175/BAMS-D-12-00173.1.

SPC, 2018: Storm Prediction Center: Archive national sector hourly mesoscale analysis. Cited: 2018-09-28, [Available online at `www.spc.noaa.gov/exper/ma_archive/images_s4`].

Špitalar, M., J. J. Gourley, C. Lutoff, P.-E. Kirstetter, M. Brilly, and N. Carr, 2014: Analysis of flash flood parameters and human impacts in the US from 2006 to 2012. *J. Hydrol.*, **519, Part A (0)**, 863 – 870, doi: 10.1016/j.jhydrol.2014.07.004.

Stevenson, S. N. and R. S. Schumacher, 2014: A 10-year survey of extreme rainfall events in the central and eastern United States using gridded multisensor precipitation analyses. *Mon. Wea. Rev.*, **142 (9)**, 3147–3162, doi: 10.1175/MWR-D-13-00345.1.

Sui, C.-H., X. Li, and M.-J. Yang, 2007: On the definition of precipitation efficiency. *J. Atmos. Sci.*, **64 (12)**, 4506–4513, doi: 10.1175/2007JAS2332.1.

Sutter, D. and S. Erickson, 2010: The time cost of tornado warnings and the savings with storm-based warnings. **2 (2)**, 103–112, doi: 10.1175/2009WCAS1011.1.

Sweeney, T. L., 1992: Modernized areal flash flood guidance. NOAA Tech. Memo. NWS HYDRO 44, 32 pp.

Terti, G., I. Ruin, S. Anquetin, and J. J. Gourley, 2017: A situation-based analysis of flash flood fatalities in the United States. *Bull. Amer. Meteor. Soc.*, **98 (2)**, 333–345, doi: 10.1175/BAMS-D-15-00276.1.

Thompson, G. and T. Eidhammer, 2014: A study of aerosol impacts on clouds and precipitation development in a large winter cyclone. *J. Atmos. Sci.*, **71 (10)**, 3636–3658, doi: 10.1175/JAS-D-13-0305.1.

Thompson, R. L., B. T. Smith, J. S. Grams, A. R. Dean, and C. Broyles, 2012: Convective modes for significant severe thunderstorms in the contiguous United States. Part II: Supercell and QLCS tornado environments. *Wea. Forecasting*, **27 (5)**, 1136–1154, doi: 10.1175/WAF-D-11-00116.1.

Trapp, R. J. and M. L. Weisman, 2003: Low-level mesovortices within squall lines and bow echoes. Part II: Their genesis and implications. *Mon. Wea. Rev.*, **131 (11)**, 2804–2823, doi: 10.1175/1520-0493(2003)131<2804:LMWSLA>2.0.CO;2.

Trier, S., C. Davis, and D. Ahijevych, 2010: Environmental controls on the simulated diurnal cycle of warm-season precipitation in the continental United States. *J. Atmos. Sci.*, **67 (4)**, 1066–1090, doi: 10.1175/2009JAS3247.1.

Trier, S. B., C. A. Davis, and W. C. Skamarock, 2000a: Long-lived mesoconvective vortices and their environment Part II: Induced thermodynamic destabilization in idealized simulations. *Mon. Wea. Rev.*, **128**, 3396–3412, doi: 10.1175/1520-0493(2000)128<3396:LLMVAT>2.0.CO;2.

Trier, S. B., C. A. Davis, and J. D. Tuttle, 2000b: Long-lived mesoconvective vortices and their environment Part I: Observations from the central United States during the 1998 warm season. *Mon. Wea. Rev.*, **128**, 3376–3395, doi: 10.1175/1520-0493(2000)128<3376:LLMVAT>2.0.CO;2.

Tripoli, G., 1982: The colorado state university three-dimensional cloud/mesoscale model-1982. part I: General theoretical framework and sensitivity experiments. *J. Rech. Atmos.*, **16**, 185–219.

Tuttle, J. D. and C. A. Davis, 2006: Corridors of warm season precipitation in the central United States. *Mon. Wea. Rev.*, **134 (9)**, 2297–2317, doi: 10.1175/MWR3188.1.

Unidata, 2018: THREDDS data server (TDS) version 4.6.2 [software]. Boulder, CO: UCAR/Unidata. [http://doi.org/10.5065/D6N014KG].

Verbout, S. M., H. E. Brooks, L. M. Leslie, and D. M. Schultz, 2006: Evolution of the U.S. tornado database: 1954–2003. *Wea. Forecasting*, **21 (1)**, 86–93, doi: 10.1175/WAF910.1.

Wang, C.-C., H.-C. Kuo, R. H. Johnson, C.-Y. Lee, S.-Y. Huang, and Y.-H. Chen, 2015: A numerical study of convection in rainbands of typhoon Morakot (2009) with extreme rainfall: roles of pressure perturbations with low-level wind maxima. *Atmospheric Chemistry and Physics*, **15 (19)**, 11 097–11 115, doi: 10.5194/acp-15-11097-2015.

Weijenborg, C., J. Chagnon, P. Friederichs, S. Gray, and A. Hense, 2017: Coherent evolution of potential vorticity anomalies associated with deep moist convection. *Quart. J. Roy. Meteor. Soc.*, **143 (704)**, 1254–1267, doi: 10.1002/qj.3000.

Weijenborg, C., P. Friederichs, and A. Hense, 2015: Organisation of potential vorticity on the mesoscale during deep moist convection. *Tellus A*, **67 (1)**, 25 705, doi: 10.3402/tellusa.v67.25705.

Weisman, M. L. and J. B. Klemp, 1984: The structure and classification of numerically simulated convective storms in directionally varying wind shears. *Mon. Wea. Rev.*, **112 (12)**, 2479–2498, doi: 10.1175/1520-0493(1984)112<2479:TSACON>2.0.CO;2.

Weisman, M. L. and R. J. Trapp, 2003: Low-level mesovortices within squall lines and bow echoes. Part I: Overview and dependence on environmental shear. *Mon. Wea. Rev.*, **131 (11)**, 2779–2803, doi: 10.1175/1520-0493(2003)131<2779:LMWSLA>2.0.CO;2.

Wilhelmson, R. and Y. Ogura, 1972: The pressure perturbation and the numerical modeling of a cloud. *J. Atmos. Sci.*, **29 (7)**, 1295–1307, doi: 10.1175/1520-0469(1972)029<1295:TPPATN>2.0.CO;2.

Woolhiser, D. and D. Goodrich, 1988: Effect of storm rainfall intensity patterns on surface runoff. *Journal of Hydrology*, **102 (1-4)**, 335–354, doi: 10.1016/0022-1694(88)90106-0.

Wurman, J., P. Robinson, C. Alexander, and Y. Richardson, 2007: Low-level winds in tornadoes and potential catastrophic tornado impacts in urban areas. *Bull. Amer. Meteor. Soc.*, **88 (1)**, 31–46, doi: 10.1175/BAMS-88-1-31.

Yang, D., B. E. Goodison, J. R. Metcalfe, V. S. Golubev, R. Bates, T. Pangburn, and C. L. Hanson, 1998: Accuracy of NWS 8" standard nonrecording precipitation gauge: Results and application of WMO intercomparison. *J. Atmos. Sci.*, **15 (1)**, 54–68, doi: 10.1175/1520-0426(1998)015<0054:AONSNP>2.0.CO;2.

Zhang, F., A. M. Odins, and J. W. Nielsen-Gammon, 2006: Mesoscale predictability of an extreme warm-season precipitation event. *Wea. Forecasting*, **21 (2)**, 149–166, doi: 10.1175/WAF909.1.

Zhang, J., et al., 2016: Multi-radar multi-sensor (MRMS) quantitative precipitation estimation: Initial operating capabilities. *Bull. Amer. Meteor. Soc.*, **97 (4)**, 621–638, doi: 10.1175/BAMS-D-14-00174.1.